WITS
UNIVERSITY

The microwave assisted synthesis of doped carbon dot/carbon nano-onion composites: A novel all-carbon counter electrode for dye-sensitized solar cells

A dissertation submitted to the Faculty of Science, University of the Witwatersrand, in fulfilment of Master of Science degree in chemistry

by

Ms Khanyisile Masemola

Student Number: 1098477

BSc (Hons in Chemistry)

Supervisors: Dr. M.S. Maubane-Nkadimeng
Prof. N. J Coville
Prof. N Moloto

Molecular Sciences Institute, School of Chemistry

University of the Witwatersrand, Johannesburg, South Africa, 2022

DECLARATION

I declare that this dissertation, which is hereby submitted to obtain the degree of Master of Science in the Faculty of Science, School of Chemistry, University of the Witwatersrand, Johannesburg is my own unaided work with all parts that stem from external sources referenced and cited appropriately and has not been submitted for examination at any institution or any other university.

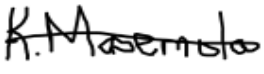

Khanyisile Masemola

On this 1st of August 2022

DEDICATION

I dedicate this work to God, my Lord and Saviour who carried me through. *Ngiyathokoza Kakaramba yeZulu!*

This work is also a special dedication to my loving parents:

My father Mr J. M Masemola and My mother Mrs. N. V Masemola

ACKNOWLEDGEMENTS

I would love to greatly thank the almighty God, the author and finisher of my faith, for all He has done for me. He has brought me this far and stood by my side the entire time.

To my amazing supervisors, Dr. Manoko S. Maubane-Nkadimeng, Prof. Neil J. Coville and Prof. Nosipho Moloto. To you, I say thank you so much for being the rock stars that provided me with invaluable insight, knowledge, and for giving me an opportunity to learn under your mentorship. I would love to thank them for their exceptional guidance, patience and generosity.

To my mentors Prof. Daniel Wamwangi and Dr. Orlette Mkhari. Thank you so much for going above and beyond to assist me till we reached the completion of this research project. For taking me under your wing, I would love to extend my appreciation for all your efforts you have put to educate and motivate me.

A very special acknowledgement also goes to the microscopy and microanalysis unit (MMU) and the powder X-ray diffraction spectroscopy unit (PXRDU) for allowing me to use their valuable facilities and instruments in their respective units. With great pleasure, I would love to extend my gratitude and acknowledge Dr. Rudolph Erasmus for his kind assistance during Raman spectroscopy and for time-correlated single photon counting (TCSPC) analysis.

A very warm thank you to Ms. Petra Dinham for granting me a chance to do field emission scanning electron microscopy (FESEM) analysis at the School of Chemical & Metallurgical Engineering (CHEMET), Dr. Sanele Nyembe for atomic force microscopy (AFM) images at Mintek facility and Ms. Louise Mostert for X-ray photoelectron spectrposcopy (XPS) analysis through the National Metrology Institute of South Africa (NMISA) characterization facility.

A big thank you to the School of Chemistry and all CATOMAT group members at the University of the Witwatersrand for being great colleagues and friendly fellow staff members throughout my study period. Your welcoming spirit will stay with me forever.

To the DST-National Research Foundation (NRF) and to the DST-NRF Centre of Excellence in Strong Materials (COE-SM) for the financial assistance you have provided. I am truly thankful. I truly appreciate each and every one of you from the deepest apex of my heart.

Psalms 73:26 [ESV]: *"My flesh and my heart may fail, but God is the strength of my heart and my portion forever"*

PRESENTATIONS AND AWARDS

PRESENTATIONS

- RCS Chemical Nanosciences and Nanotechnology Early Career Virtual Poster Symposium: Poster presentation "*Microwave-assisted synthesis of carbon dots/PEDOT composites for use as counter electrode material in dye-sensitized solar cells*", Zoom (24 March 2021)
- 2021 Wits Famelab International Science Communication Competition: Oral presentation "*Black out*", Zoom (5 - 7 May 2021)
- SACI YCS Symposium 2021: Grad flash "*Construction of nitrogen doped carbon dots/nano-onions composites for use as counter electrode material in dye sensitized solar cells*", Microsoft Team (8 – 9 July 2021)
- 12th PG Cross Faculty Symposium: Grad flash "*Nitrogen-doped carbon nano-dots decorated on carbon nano-onions network: A novel all-carbon composite counter electrode for dye-sensitized solar cell*", Zoom (26 July 2021)
- Catalysis-Materials (CATMAT) group meeting: Oral presentation, Zoom (20 August 2020)
- ACS Fall 2021: Poster presentations "*One-step microwave assisted synthesis of nitrogen doped carbon dots for use as electrode material in dye sensitized solar cell*", Zoom (22 – 26 August 2021)
- Carbon dots/onions group meeting: Oral presentation, Zoom (16 September 2021)
- 2nd Commonwealth Chemistry Posters: Poster presentation "*Efforts to sustainable energy using nitrogen doped composites as counter electrode material in dye sensitized solar cells*", Microsoft Team (30 September – 01 October 2021)
- SANI NYRS 2020/1: Poster presentation "Efforts to sustainable energy: A novel all-carbon composite counter electrode for dye-sensitized solar cell", Zoom (7 – 8 October 2021)
- CoSAAMI Symposium: Oral presentation "*Tuning the physiochemical properties of carbon dots via heteroatom doping: Effect of the concentration of nitrogen-containing precursor*", Microsoft Teams (18 – 22 October)
- AFInMic PG Symposium (MSSA): Oral presentation "*Microscopy in the service of sustainable energy*", Zoom (29 November – 03 December 2021)

WORKSHOPS

- AFInMic EA Microscopy Workshop, Zoom (24 - 27 May 2021)
- AMRS Nanotechnology Research and Innovation Bootcamp, Zoom (10 - 13 August 2021)
- AFInMic WA International Microscopy Workshop, Zoom (9 – 12 May 2022)

AWARDS

- Received certificate for passing the regional round: 2021 Wits Famelab International Science Communication Competition
- Third place student participation award certificate: AFInMic EA Microscopy Workshop
- Received a certificate of participation: SACI YCS Symposium 2021
- Received a certificate of participation: 2nd Commonwealth Chemistry Posters
- Received a certificate of participation: SANI NYRS 2020/1
- Won first prize for oral presentation, and received a certificate of participation: AFInMic PG Symposium (MSSA)
- Received a certificate of participation: AFInMic WA International Microscopy Workshop

ABSTRACT

Human society's development is heavily reliant on stable energy supply, and fossil energy sources have long been a very reliable energy source for this objective. However, being a non-renewable energy source, fossil fuel depletion is unavoidable and impending in this or future generations. To solve this issue, renewable energy, particularly solar energy, has received a lot of attention since it directly turns solar energy into electrical power with no environmental consequences. Various photovoltaic technologies based on organic, inorganic, and hybrid solar cells have been successfully manufactured to date. However, much study has been concentrated on organic solar cells for household and other commercial uses due to its inherent cheap module cost and ease of production. But dye-sensitized solar cells (DSSCs) have been reported to be the most efficient and simplest applied organic solar cell technology. In this study, carbon dot: onion-like carbon nanomaterial composites (Cdots: OLCNs) were synthesized for possible future application in electronic devices with particular attention to dye-sensitized solar cells. The nitrogen-doped carbon dots (NCdots) and functionalized onion-like carbon nanomaterials (OLCNs) were synthesized using a one-step hydrothermal microwave assisted irradiation method and flame pyrolysis method using liquid fuels, respectively. The as-synthesized OLCNs where purified and washed using an organic solvent *n*-pentane to obtain pristine OLCNs (p-OLCNs) which were further functionalized with N_2 gas to obtained nitrogen-doped CNOs (N- OLCNs) and H_2O_2 to give oxygenated OLCNs (ox-OLCNs). For the synthesis of NCdots, various precursors (ethylenediamine, urea and fumaronitrile) were used to evaluate the effect of different nitrogen sources on the properties of these materials. Photoluminescence spectroscopy showed that the resulting NCdots exhibited the conventional excitation-dependency behavior. The NCdots which presented with the highest fluorescence quantum yield (made from ethylenediamine) were used to make the subsequent NCdot: OLCNs composites. The as-prepared p-/ox-/N-OLCNs all showed similar morphologies typical of chain-like carbon nanostructures, according to transmission and scanning electron microscopy studies, but with varying particle sizes of 42 nm, 125nm and 85 nm, respectively.

The corresponding nanocomposites were used as counter electrode materials in DSSCs. The application of all the nanocomposites in the DSSCs resulted in cell efficiencies, current densities, open circuit voltages and fill factors that were lower than that of a conventional platinum (Pt) electrode. All nanocomposites tested presented with cell efficiencies <1%.

Furthermore, the cells displayed some photovoltaic effect of minimal activity in the absence of light, under dark field conditions implying it is still a photovoltaic material. This photocurrent generated by the cell in the dark is suggested to be a dominant contributor to the low performance of the cells. However, what was remarkable was that this photovoltaic effect, primarily due to the thermal activity from the long lasting glow of the NCdots specifically, was found to be stable and efficient in response as infrared radiation even without being illuminated with light for 5 minutes. This suggests that the NCdots: OLCNs composites have potential application, possibly as efficient diodes rather than for use in DSSCs.

TABLE OF CONTENTS

Chapter 3 Characterization techniques

LIST OF FIGURES

Chapter 2

Chapter 4

Chapter 5

Chapter 6

Chapter 7

Appendix A: Supplementary information

No table of figures entries found.

LIST OF SCHEMES

Chapter 4

Chapter 5

No table of figures entries found.

Chapter 6

LIST OF TABLES

Chapter 4

Chapter 5

No table of figures entries found.

Chapter 6

Chapter 7

No table of figures entries found.

Appendix A: Supplementary information

Chapter 1
Introduction to the study

1.1. Introduction

The development of alternative energy sources to fossil fuel has been driven by a variety of interests, including economic considerations, along with healthcare and environmental concerns. The sun provides most of the energy that is used on earth (direct/indirect) to sustain life. Solar cells, which turn sunlight directly into electricity, can give methods for converting solar energy into usable energy. Solar cells are used in many applications that include calculators, solar lights, spaceships, and satellites. This dissertation is taken up with the use of dye-sensitized solar cells (DSSCs) as an electricity generating device by converting solar energy. The dissertation's first chapter discusses the study's background and motivation, including the study's aim and objectives.

1.1.1 Study background

In recent years, a great emphasis on renewable energy sources has emerged in response to rising energy demands and concerns about global warming. One of the breakthroughs that can replace fossil fuels in the generation of large amounts of energy is projected to play a big role in the future of solar energy conversion [1]. Both the availability, and the storage and supply of energy have a significant influence on human life quality. Unless sustainable renewable energy supplies can be created fast, human life quality is in peril. Through the synthesis and analysis of materials for application in energy conversion devices, the multidisciplinary discipline of chemistry may significantly contribute to the discovery of environmentally acceptable energy solutions [2]. The world's energy demands are predicted to more than quadruple in the next 50 years, putting further strain on the existing global crisis unless renewable energies can fill the hole left by fossil fuels, and Chemistry can play a role in solving this pertinent issue [3].

The devastating environmental contamination produced by common oil pollution, and even the alarming climatic effects of the greenhouse effect induced by the burning of fossil fuels, have recently heightened worldwide concern on energy sources [4]. Fortunately, the sun provides tremendous amounts of energy to the world, estimated to be 3×10^{24} J per year, or around 10^4 times what humankind currently consumes [5, 6]. Additionally, it might be

claimed that in order to meet our current needs, around 0.1% of the earth's surface would need to be covered with solar cells, each of which would need to have an output efficiency of at least 10% [7, 8] to provide all of humanity's energy needs. These upbeat statistics inspire the scientific community to work even harder on improving solar energy conversion technology and to offer novel solutions to the energy issues we face. To date, nonetheless, tapping further into sun's immense energy reservoir has proven to be difficult.

Solar energy conversion is one of the innovations that might result in a new source of energy for large-scale power generation since it is expected to be crucial in future scenarios. On the other hand, inorganic solar panels are still unreasonably expensive [9]. Unquestionably, the huge rise in the lookout for commercial energy and power transmission technology lies at the root of this dilemma. As a result, low-cost solar energy options are being thoroughly investigated.

1.1.2 Motivation to the study

Current energy research has been focused on discovering and investigating alternative sources to non-renewable carbon sources of energy, as well as producing durable, affordable, and dependable equipment with great applicability and practicality, in order to fulfill rising global energy demands [10 – 12]. These technologies must be able to allow more sustainable and efficient energy usage or the dependable use of renewable energy when fossil fuels run out (become exhausted) or become too rare and costly to utilize [13]. Along with its availability and the fact that it largely employs green technology, solar energy has been recognized as one of safest and most probable methods to solving energy concerns [11, 12].

Photovoltaic (PV) solar cells have been shown to be successful in harvesting solar energy. With its ability to convert sunlight into power, photovoltaics has great potential for assisting humanity in resolving its ongoing energy problems [14]. A number of photovoltaic modules have been produced and researched as a workable solution. One of the most thoroughly studied methods for transforming solar radiation into energy, dye-sensitized solar cells are especially well suited for use in low-cost, high-performance gadgets [15].

In terms of performance and manufacturing simplicity, DSSCs are by far one of the most promising replacements to silicon solar cells. Crystalline silicon (Si), which makes up 80% of the industry for semiconductor solar cells, now dominates commercial markets. The

remaining 20% is mostly composed of thin film solar energy technologies, using Ga_xSe_2 and CdTe $CuIn_{(1-x)}$ films [16]. The aforementioned complex is a semiconductor with an indirect bandgap that typically requires a 300-mm thick absorbance layer and has incredibly high manufacturing and production costs. The latter complex comprises the use of dangerous and rare elements found on the planet [14]. Compared to these solid-state systems, the DSSC provides a low-cost, ecologically beneficial alternative. The DSSCs are simple to construct, and thus the thin-film constructs are lightweight enough to be employed in automated production [17, 18]. One of the most important nodes in the DSSC is the counter electrode (CE), which is in charge of transferring electrons from the cathode circuit to the electrolyte. To create a successful DSSC, a counter electrode's structural, electromechanical, electrical, and electrochemical durability are some of the aspects that must be improved [19].

Since carbon is extremely stable and is thought to have properties similar to silicon, it is appealing in the hunt for substitute materials to utilize in a DSSC. A fascinating chemical called carbon may be found in a number of stable allotropes [20], exhibiting a wide range of intriguing optoelectronic, mechanical, and chemical features Owing to its unique structure, characteristics, and potential uses in energy storage applications, many forms of nano-structured carbons have attracted attention in recent years [21–24].

Carbon dots (Cdots) are a novel form of a light - harvesting nano-carbonaceous material that has aroused much interest in a range of sectors since its discovery. These Cdots show quantum properties and have been shown to be superior to semiconductor quantum dots (and organic dyes) due to their good photodegradation resistance, excellent stability, and low toxicity [25]. Based on these benefits, Cdots have been recommended as a greener alternative to standard semiconductor quantum dots that employ hazardous metallic components [26, 27]. Due to their unique properties, onion-like carbon nanoparticles (OLCNs) have also become a substitute counter electrode material for usage in solar cells. Due to their multiple surface-active spots/defects and large surface area, they have been used in DSSCs [28]. This study's foundation is the creation of a composite of carbon nanomaterials that resemble onions and have been enhanced with carbon dots for usage in DSSCs.

The study is driven by the knowledge that nanostructured materials electrodes have been proposed to have a large conversion efficiency due to a strong electrode-electrolyte contact, resulting in enhanced electrode electrochemical activity. Owing to this, we report a novel all

carbon based Cdots: OLCNs counter electrode for application in a DSSC. The Cdots are predicted to increase the composites' catalytic activity, while the OLCNs' high surface area is predicted to increase the Cdots': OLCNs collective activity. The composite will be a less expensive alternative to a platinum (Pt) counter electrode, opening new possibilities for electrochemical DSSC devices.

1.1.3 Problem statement

The counter electrode, one of the essential parts of the DSSC, is in charge of moving electrons from the external circuit to the electrolyte. The following qualities must be present in an efficient counter electrode: stability in the mechanical, chemical, and electrochemical realms; robustness; and excellent catalytic activity [19]. Due to its excellent conductivity, Pt is the favored material for counter electrodes. However, the high cost of Pt prevents its widespread application in solar cells [29].

To address this issue, scientists have been exploring carbon compounds in DSSCs to develop photovoltaic cells with acceptable performance. Because of some of its similarities to Si, carbon has been shown to be quite appealing in the hunt for alternative material to Si. Up to this point, many multipurpose carbon-based compounds have been reported as counter electrodes, such carbon black (CB) [30], activated carbon [31, 32], graphite [32], carbon nanotubes [33, 34], graphene [35] and fullerene (C60) [36]. To enhance the capacity of all carbon-based CEs for DSSCs, the current density, electrocatalytic activity, electrical conductivity and device stability must all be improved [37-39]. In an attempt to accomplish these benefits, an all-carbon based nanocomposites containing two distinct carbon allotropes will be synthesized.

In this study, we have synthesized and studied a unique all-carbon-based carbon dot: onion-like carbon nanomaterials (Cdot: OLCNs) nanocomposite material as a high-performance CE material. To boost the electrocatalytic activity, the Cdots are expected to behave as active catalytic sites. The OLCNs network is expected to create a favourable pathway for electrolyte transport and an electrically conductive passageways for rapid electron charge transfer, while the large surface area of the OLCNs may help disperse the Cdots and avoid particle aggregation. There have been few publications on the use of all-carbon based materials as CE materials, and to date no studies on Cdot: OLCNs composites, to our knowledge.

1.2 Purpose of the study

1.2.1. Aim of the study

In order to establish a connection between energy conversion devices and carbon nanomaterials, this study aimed to create N-doped Cdots: functionalized-OLCNs composites and analyze their characteristics, as well as test the counter electrode in DSSC.

1.2.2. Objectives

The following objectives helped to achieve the study's aim:

- To synthesize nitrogen doped Cdots (NCdots) from various precursors using the microwave irradiation method.
- To synthesize OLCNs using the flame pyrolysis method.
- To functionalize the OLCNs with ammonia gas to obtain nitrogen-doped OLCNs (N-OLCNs), and H_2O_2 to obtain oxygenated- OLCNs (ox- OLCNs).
- To synthesize doped Cdots; OLCNs composites using the as-synthesized doped Cdots and the pristine, as well as functionalized OLCNs.
- Adding doped Cdots: OLCN composites as a counter electrode component to the dye-sensitized photovoltaic device.
- To create Cdot-coated counter electrodes (CE) for dye-sensitized solar cells (DSSCs): composite OLCNs.
- To compare the performance of the Pt-based DSSCs with results from literature using carbon nanocomposites as the basis.

A variety of characterization methods were used to examine the synthesized materials, including scanning electron microscopy (SEM), transmission electron microscopy (TEM), thermal gravimetric analysis (TGA), Fourier transform infrared (FTIR) spectroscopy, laser Raman spectroscopy, X-ray photoelectron spectroscopy (XPS), Brunauer-Emmett-Teller (BET) surface analysis, elemental (CHN-S) analysis, powder X-ray diffraction spectroscopy (PXRD), the cyclic voltammetry (CV), electrochemical impedance spectroscopy (EIS), linear sweep voltammetry (LSV), and current density-voltage (J-V) measurements were used to examine the solar devices.

1.2.3. Research questions and hypothesis

The issue under investigation was how the structure of the carbonaceous material would change if heteroatoms were included into the matrix of carbon dots. The physical and chemical characteristics of the nanocomposites, the solar cell, and the ensuing photoluminescence features of a DSSC would all be affected by the addition of nitrogen doped Cdots to the matrix of the OLCNs. How would the functionalized-OLCNs: NCdots composites compare in terms of performance to the unfunctionalized-OLCNs: NCdots composites?

- Can conductive composites be utilized in dye-sensitized solar cells to capture solar energy and provide clean, plentiful electricity?
- Are the variously doped Cdots a perfect composite material to be employed in a counter electrode in dye-sensitized solar cells when combined with pure and functionalized OLCNs?
- Will the OLCNs' performance be enhanced by the addition of doped Cdots?

1.3. Outline of dissertation

Chapter 1: Qutlines the general introduction, context, and purpose of the study as well as the goals and objectives of the research on the usage of carbon/carbon composites in dye-sensitized solar cells to increase their efficiency.

Chapter 2: The literature on carbon dots, carbon nano-onions, and carbon composites is thoroughly reviewed in this chapter, along with information on how these materials were found, how they differ from non-carbon nanomaterials, how they are made, and how they are used. Additionally, it gives background information on the designs and operation of DSSCs.

Chapter 3: Explains the characterisation methods and tools utilized in this work and provides detailed descriptions of each. Additionally, several of the example preparations are explained in this chapter.

Chapter 4: The outcomes of the microwave-irradiation approach used for the synthesis and characterisation of nitrogen doped carbon dots made from several precursors (citric acid, ethylenediamine, urea, and fumaronitrile) are presented. In this

chapter, the characteristics of the Cdots made from various predecessors were compared, along with their discussion and interpretation.

Chapter 5: Describes the synthesis, results and discussion on the synthesis of OLCNs using the flame pyrolysis method. The discussion and interpretation of the functionalization of the pristine OLCNs to obtained N- OLCNs and ox- OLCNs are presented in this chapter.

Chapter 6: Presents the synthesis procedure to make doped Cdots: OLCNs nanocomposites. Different ratios of Cdots: OLCNs, their optical properties together with their physical properties were discussed.

Chapter 7: Demonstrates the fabrication and characterisation of customized DSSCs made with various Cdots: OLCNs composites. Their electrocatalytic activities were investigated and the chapter also presents how the incorporation of the nanocomposites as counter electrode material affected the performance of the devices.

Chapter 8: General conclusions and recommendations.

References

1. Robertson, N. (2006). Optimizing Dyes for Dye-Sensitized Solar Cells. *Angewandte Chemie International Edition*, *45*(15), 2338–2345. https://doi.org/10.1002/anie.200503083
2. Grätzel, M. (2005). Solar Energy Conversion by Dye-Sensitized Photovoltaic Cells. *Inorganic Chemistry*, *44*(20), 6841–6851. https://doi.org/10.1021/ic0508371
3. Bella, F., Gerbaldi, C., Barolo, C., & Grätzel, M. (2015). Aqueous dye-sensitized solar cells. *Chemical Society Reviews*, *44*(11), 3431–3473. https://doi.org/10.1039/c4cs00456f
4. Little, D. I., Sheppard, S. R., & Hulme, D. (2021). A perspective on oil spills: What we should have learned about global warming. *Ocean & Coastal Management*, *202*, 105509. https://doi.org/10.1016/j.ocecoaman.2020.105509
5. Brabec, C. J., Heeney, M., McCulloch, I., & Nelson, J. (2011). Influence of blend microstructure on bulk heterojunction organic photovoltaic performance. *Chem. Soc. Rev.*, *40*(3), 1185–1199. https://doi.org/10.1039/c0cs00045k
6. Li, J., & Grimsdale, A. C. (2010). Carbazole-based polymers for organic photovoltaic devices. *Chemical Society Reviews*, *39*(7), 2399. https://doi.org/10.1039/b915995a
7. Bessette, A., & Hanan, G. S. (2014). Design, synthesis and photophysical studies of dipyrromethene-based materials: insights into their applications in organic photovoltaic devices. *Chem. Soc. Rev.*, *43*(10), 3342–3405. https://doi.org/10.1039/c3cs60411j
8. Dang, M. T., & Wuest, J. D. (2013). Using volatile additives to alter the morphology and performance of active layers in thin-film molecular photovoltaic devices incorporating bulk heterojunctions. *Chemical Society Reviews*, *42*(23), 9105. https://doi.org/10.1039/c3cs35447d
9. Grätzel, M. (2001). Photoelectrochemical cells. *Nature*, *414*(6861), 338–344. https://doi.org/10.1038/35104607
10. Essner, J. B., & Baker, G. A. (2017). The emerging roles of carbon dots in solar photovoltaics: a critical review. *Environmental Science: Nano*, *4*(6), 1216–1263. https://doi.org/10.1039/c7en00179g
11. Ranabhat, K., Patrikeev, L., Antal'evna-Revina, A., Andrianov, K., Lapshinsky, V., & Sofronova, E. (2016). An introduction to solar cell technology. *Istrazivanja i Projektovanja Za Privredu*, *14*(4), 481–491. https://doi.org/10.5937/jaes14-10879
12. Wöhrle, D., & Meissner, D. (1991). Organic Solar Cells. *Advanced Materials*, *3*(3), 129–138. https://doi.org/10.1002/adma.19910030303

13. Chen, G. Z. (2013). Understanding supercapacitors based on nano-hybrid materials with interfacial conjugation. *Progress in Natural Science: Materials International*, *23*(3), 245–255. https://doi.org/10.1016/j.pnsc.2013.04.001
14. Chung, I., Lee, B., He, J., Chang, R. P. H., & Kanatzidis, M. G. (2012). All-solid-state dye-sensitized solar cells with high efficiency. *Nature*, *485*(7399), 486–489. https://doi.org/10.1038/nature11067
15. Sugathan, V., John, E., & Sudhakar, K. (2015). Recent improvements in dye sensitized solar cells: A review. *Renewable and Sustainable Energy Reviews*, *52*, 54–64. https://doi.org/10.1016/j.rser.2015.07.076
16. Bisquert, J. (2011). Dilemmas of Dye-Sensitized Solar Cells. *ChemPhysChem*, *12*(9), 1633–1636. https://doi.org/10.1002/cphc.201100248
17. Hagfeldt, A., Boschloo, G., Sun, L., Kloo, L., & Pettersson, H. (2010). Dye-Sensitized Solar Cells. *Chemical Reviews*, *110*(11), 6595–6663. https://doi.org/10.1021/cr900356p
18. Grätzel, M. (2009). Recent Advances in Sensitized Mesoscopic Solar Cells. *Accounts of Chemical Research*, *42*(11), 1788–1798. https://doi.org/10.1021/ar900141y
19. Ge, C., Rahman, M. M., Nath, N. C. D., Ju, M. J., Noh, K. M., & Lee, J. J. (2015). Graphene-incorporated Photoelectrodes for Dye-sensitized Solar Cells. *Bulletin of the Korean Chemical Society*, *36*(3), 762-771.
20. Zhu, H., Wei, J., Wang, K., & Wu, D. (2009). Applications of carbon materials in photovoltaic solar cells. *Solar Energy Materials and Solar Cells*, *93*(9), 1461–1470. https://doi.org/10.1016/j.solmat.2009.04.006
21. Che, G., Lakshmi, B. B., Fisher, E. R., & Martin, C. R. (1998). Carbon nanotubule membranes for electrochemical energy storage and production. Nature, 393(6683), 346–349. https://doi.org/10.1038/30694
22. Yoshio, M., Wang, H., Fukuda, K., Hara, Y., & Adachi, Y. (2000). Effect of Carbon Coating on Electrochemical Performance of Treated Natural Graphite as Lithium-Ion Battery Anode Material. *Journal of The Electrochemical Society*, *147*(4), 1245. https://doi.org/10.1149/1.1393344
23. Wang, C., Waje, M., Wang, X., Tang, J. M., Haddon, R. C., & Yan. (2003). Proton Exchange Membrane Fuel Cells with Carbon Nanotube Based Electrodes. Nano Letters, 4(2), 345–348. https://doi.org/10.1021/nl034952p
24. Stewart, D. A., & Léonard, F. (2005). Energy Conversion Efficiency in Nanotube Optoelectronics. *Nano Letters*, *5*(2), 219–222. https://doi.org/10.1021/nl048410z

25. Becquerel, A. E. (1839). Electrode Effect under the Influence of Solar Radiation. *Acad. Sci., Paris*, *9*, 561-567.
26. Mohammad Bagher, A. (2015). Types of Solar Cells and Application. *American Journal of Optics and Photonics*, *3*(5), 94. https://doi.org/10.11648/j.ajop.20150305.17
27. Halme, J., Vahermaa, P., Miettunen, K., & Lund, P. (2010). Device Physics of Dye Solar Cells. *Advanced Materials*, *22*(35), 210–234. https://doi.org/10.1002/adma.201000726
28. Pang, B., Zhang, M., Zhou, C., Dong, H., Ma, S., Shi, Y., Sun, Q., Li, F., Yu, L., & Dong, L. (2020). Nitrogen-Doped Carbon Nano-Onions Decorated on Graphene Network: A Novel All-Carbon Composite Counter Electrode for Dye-Sensitized Solar Cell with a 10.28% Power Conversion Efficiency. *Solar RRL*, *4*(9), 2000263. https://doi.org/10.1002/solr.202000263
29. Robertson, N. (2006b). Optimizing Dyes for Dye-Sensitized Solar Cells. *ChemInform*, *37*(27). https://doi.org/10.1002/chin.200627273
30. Murakami, T. N., Ito, S., Wang, Q., Nazeeruddin, M. K., Bessho, T., Cesar, I., Liska, P., Humphry-Baker, R., Comte, P., PéChy, P., & GräTzel, M. (2006). Highly Efficient Dye-Sensitized Solar Cells Based on Carbon Black Counter Electrodes. *Journal of The Electrochemical Society*, *153*(12), A2255. https://doi.org/10.1149/1.2358087
31. Imoto, K., Takahashi, K., Yamaguchi, T., Komura, T., Nakamura, J. I., & Murata, K. (2003). High-performance carbon counter electrode for dye-sensitized solar cells. *Solar Energy Materials and Solar Cells*, *79*(4), 459–469. https://doi.org/10.1016/s0927-0248(03)00021-7
32. Chen, J., Li, K., Luo, Y., Guo, X., Li, D., Deng, M., Huang, S., & Meng, Q. (2009). A flexible carbon counter electrode for dye-sensitized solar cells. *Carbon*, *47*(11), 2704–2708. https://doi.org/10.1016/j.carbon.2009.05.028
33. Suzuki, K., Yamaguchi, M., Kumagai, M., & Yanagida, S. (2003). Application of Carbon Nanotubes to Counter Electrodes of Dye-sensitized Solar Cells. *Chemistry Letters*, *32*(1), 28–29. https://doi.org/10.1246/cl.2003.28
34. Han, J., Kim, H., Kim, D. Y., Jo, S. M., & Jang, S. Y. (2010). Water-Soluble Polyelectrolyte-Grafted Multiwalled Carbon Nanotube Thin Films for Efficient Counter Electrode of Dye-Sensitized Solar Cells. *ACS Nano*, *4*(6), 3503–3509. https://doi.org/10.1021/nn100574g
35. Roy-Mayhew, J. D., Bozym, D. J., Punckt, C., & Aksay, I. A. (2010). Functionalized Graphene as a Catalytic Counter Electrode in Dye-Sensitized Solar Cells. *ACS Nano*, *4*(10), 6203–6211. https://doi.org/10.1021/nn1016428

36. Wu, M., Lin, X., Hagfeldt, A., & Ma, T. (2011). Low-Cost Molybdenum Carbide and Tungsten Carbide Counter Electrodes for Dye-Sensitized Solar Cells. *Angewandte Chemie International Edition*, *50*(15), 3520–3524. https://doi.org/10.1002/anie.201006635
37. Meng, X., Yu, C., Zhang, X., Huang, L., Rager, M., Hong, J., Qiu, J., & Lin, Z. (2018). Active sites-enriched carbon matrix enables efficient triiodide reduction in dye-sensitized solar cells: An understanding of the active centers. *Nano Energy*, *54*, 138–147. https://doi.org/10.1016/j.nanoen.2018.09.070
38. Yu, F., Shi, Y., Yao, W., Han, S., & Ma, J. (2019). A new breakthrough for graphene/carbon nanotubes as counter electrodes of dye-sensitized solar cells with up to a 10.69% power conversion efficiency. *Journal of Power Sources*, *412*, 366–373. https://doi.org/10.1016/j.jpowsour.2018.11.066
39. Kim, C. K., Zhou, H., Kowalewski, T., Matyjaszewski, K., & Kim, H. K. (2018). Soft-Templated Tellurium-Doped Mesoporous Carbon as a Pt-Free Electrocatalyst for High-Performance Dye-Sensitized Solar Cells. *ACS Applied Materials & Interfaces*, *11*(2), 2093–2102. https://doi.org/10.1021/acsami.8b19223

Chapter 2

Literature review

2. Background and introduction

The direct solar energy harvesting technology known as photovoltaic (PV) is recognised as a key factor in the future provision of the world's energy sources. Solar cell technology is now dominated by silicon (Si) and semiconductor-based technologies. However, the price cost of these photovoltaics is expensive. Silicon has the disadvantage of deterioration when used under light, limiting its longevity and reliability [1].

Large scale solar electrical conversion systems in the future will require materials that are readily available and easy to handle. As a result, finding new types of clean and affordable energy resources is critical. Carbon is one of these elements and is appealing in the pursuit for new materials since it is predicted to have qualities comparable to silicon. Indeed, carbon-based solar cells have been made and studied [2]. This chapter provides a review of the relevant literature and historical context for carbon materials used in dye-sensitized solar cells (DSSCs), which are related to the driving forces, goals, and objectives of this study.

2.1 Carbon based nanomaterials

Material science (especially materials chemistry) has emerged as an active scientific topic [3]. Material science is preoccupied with the synthesis and properties of materials as well as the alteration of material surfaces to enable new materials (with new qualities) to be applied in practical applications [4]. In this multidisciplinary field, nanomaterials, the building blocks to construct bigger micro- and macroscale structures, have in the past five decades received a lot of interest. One of these nanomaterials is based on carbon [5, 6]. Nanoscale carbon structures have characteristics that differ significantly from bulk carbon. Carbon nanoparticles are carbon-based compounds with sizes ranging from 1 to 100 nm [7] and include fullerenes [8], carbon nanotubes [9, 10], graphene [11], carbon onions [12], and carbon dots [13], and these nanomaterials are currently studied worldwide and have been used in a variety of applications.

2.1.2 Carbon nano-dots

Carbon nanodots (Cdots) are zero-dimensional (0-D) carbon nanoparticles with high oxygen and hydrogen percentages [14]. They are one of the carbon allotropes [15]. Cdots, due to their

unique optical characteristics, and especially fluorescence emission have been used in many applications.

Cdots can readily be dispersed in water, have outstanding optical characteristics, and also photobleaching resistance [16]. Furthermore, employing a variety of one-step techniques, highly fluorescent Cdots may be generated on a large scale at cheap cost [17]. As a consequence, they may be employed as a novel type of fluorescent material that can be used to replace the existing inorganic quantum dots (QDs), also known as compound semiconductors, in a number of applications while eliminating the use of heavy metals, which can create poisoning and environmental impacts.

Cdots can be made from many carbon-based sources and this permits for the generation of a tunable surface chemistry, chemical versatility, competitive prices, fast chemical modification, high photostability, environmental friendliness, and excellent biocompatibility [18 - 20]. Due to their particular emission dependency on the excitation source, Cdots differ from more prevalent inorganic semiconductor quantum dots or metallic nanoparticles in terms of their unique physical and chemical characteristics [21]. In reality, their fluorescence properties are influenced by the precursors used, the reaction conditions, and the synthesis processes [22, 23]. Their optical characteristics may be tuned to encompass the whole electromagnetic spectrum, from ultraviolet to the near - infrared region.

2.1.3 Synthesis techniques to make carbon nano-dots

Over time, many techniques for the synthesis of carbon nanoparticles, including Cdots, have been developed [24]. The structural, chemical, and optical features (such as size and crystalline structure), as well as luminescence qualities (such as quantum yield) of Cdots are frequently influenced by the synthesis method and precursors [25]. The top-down and bottom-up methodologies [26], which are briefly explained here, are the two basic ways used to synthesize Cdots.

2.1.3.1 Top-down approach

Cdots were originally produced via the top-down approach, which involves dissolving huge carbon structures into smaller carbon nanoparticles. These bigger compounds can be reduced physically, chemically, or even electrochemically until the appropriate particle size is reached [27]. This method has the disadvantage of requiring long, and possibly complicated reactions that demand purification steps and specialist equipment [28]. The arc-discharge technique

[29], laser ablation [30], and electrochemical oxidation methods are examples of synthetic procedures that come under this paradigm. [31].

Larger carbon structures, such as nano diamonds [33], graphite [34], carbon nanotubes [35], carbon soot [36], activated carbon [37], and graphite oxide [38], are examples of carbon that have been broken down using these processes.

2.1.3.2 Bottom-up approach

Because it is easier to use than the top-down method, this strategy has gained a lot of attention. In this method, Cdots are made up from small organic carbon structures [39, 40]. This method has the advantage of using low-cost, commonly available carbon containing ingredients. As a result, the bottom-up approach is preferred over the top-down method because it avoids many of the problems that the top-down method has, including carbonaceous aggregation, poor size control, poor homogeneity, and undesired surface qualities of the product. This technique includes synthetic approaches that use the hydrothermal method [41], pyrolysis method [42], ultrasonic method or combustion method [43, 44], acid dehydration method [45], and the microwave-irradiation method [46].

Bottom-up techniques create carbon quantum dots (CQDs) from chemical precursors such as citrate [46], carbohydrates [47, 48] and polymer–silica nanocomposites [49] through combustion/ thermal treatments and microwave synthetic routes [50].

The top-down approach is used to make graphitic quantum dots (GQDs), whereas the bottom-up method is used to make carbon quantum dots (CQDs) [51, 52]. The flexibility to add a dopant (nitrogen, sulphur, silica, phosphorus, etc.) or surface passivating agents throughout the process allows the bottom-up approach to frequently give good shape and size control of the resulting Cdots [53].

2.1.3.2.1 Microwave-assisted irradiation synthesis method

One of the most popular bottom-up approaches for Cdot synthesis is microwave-assisted reactions. Microwaves are electromagnetic waves with frequencies between 300 MHz and 300 GHz and wavelengths between 1 mm and 1 m [54, 55]. During microwave treatment, precursor molecules absorb electromagnetic fields produced by microwaves and transform them into heat energy [56, 57]. Dielectric solvents like methanol, butanol, nitrobenzene, formic acid, and notably water absorb electromagnetic irradiation and transform it into reaction heat [56, 57]. In comparison to more traditional heating techniques such using a

heating mantle, an oil bath, or a hotplate, microwave heating offers the benefit of providing consistent heating, a rapid synthesis time, and reproducible performance. In addition to being an ecologically responsible method of synthesis, microwave heating frequently results in fewer by-products and permits accurate particle size monitoring [58, 59].

Microwave-assisted procedures have successfully created carbon nanoparticles like graphene, fullerene, and carbon nanotubes (CNTs) [60–63]. Numerous studies have been done on microwave-based Cdot synthesis [64]. In particular, post-functionalization of graphene, fullerene, and CNTs with organic and inorganic functional groups has also been accomplished by microwave irradiation [60, 65-66].

The microwave-assisted irradiation synthesis is a particularly important way to create Cdots when compared to other synthesis methods since it is a straightforward, clean, adaptable, and effective method [67]. The capacity of polar molecules to absorb microwave radiation and convert it to heat via dielectric heating is the key to microwave-assisted chemistry's effectiveness and efficiency. When polar molecules having an electrical dipole moment are bombarded with microwaves, they experience molecular rotation as they try to orient themselves in the electric field [68]. This process offers a number of advantages, notably cost effectiveness, short reaction speed, and operability, and also the prevention of harsh traditional treatments such raised temperatures, strong acids, and extended reaction times [69], rendering it a green preparative method.

Another noteworthy feature of microwave irradiation is the utilization of uniform heating and fast reaction times, which enables large-scale Cdots production [70]. The microwave method has also been used to make doped Cdots. For instance, Christé and colleagues examined the productivity and dependability of several nitrogen doping (N-doping) processes in their research on the synthesis of nitrogen-doped Cdots utilizing microwave-assisted hydrothermal and solvothermal techniques [64].

2.1.4 Doping carbon nano-dots

Cdots are a novel form of a photoluminescent carbonaceous material [71]. Cdot functionalization allows for the alteration of the Cdot surface state and intrinsic structure. Various functionalization strategies enable the photophysical effectiveness of the Cdots to be boosted to widen the spectrum of applications of fluorescent Cdots [72].

Atomic impurities create n-type or p-type carriers when they combine with carbon cores, altering the Cdots' electronic structure. Fluorescent Cdots with various active sites or surface functional groups are produced through surface modifications (due to a particular functional ligand). Surface states can be formed or modified by conjugating polymers or functional molecules with surface functional groups [73]. This approach has piqued academics' interest due to its simplicity and capacity to alter the inherent structure of Cdots. Dehydration, condensation, polymerization, and carbonization are steps used in the doping process [72].

Doping of Cdots has certain advantages. Cdot surface passivation has been shown to greatly enhance photoluminescence, lifetimes, and quantum yields [74]. Physical qualities such as solubility in aqueous and non-aqueous solvents are also altered by surface doping. [75].

2.1.4.1 Nitrogen-doped carbon dots

Nitrogen doping is among the most well-studied heteroatom-doping techniques for Cdots, resulting in the synthesis of nitrogen-doped Cdots (NCdots). Doping can improve the efficiency of dye-sensitized solar cells (DSSCs) by altering their optical properties and raising their Fermi level since nitrogen may function as an n-type impurity. Various nitrogen sources, including ethylenediamine [76], urea [77], and ammonia [78], have been employed to dope Cdots. In addition to the aforementioned chemicals, other carbon containing chemicals that contain N can also be employed to make nitrogen doped Cdots. These include natural products such as silk [79], milk [80], and even wool [81].

Doping nitrogen into carbon can produce pyrrolic-N, graphitic-N, and pyridinic-N structures [82] and elaborating on the function of these N configurations in Cdots is crucial for comprehending their photoluminescence (PL) process. **Fig 2.1** shows these types of nitrogen configurations. The pyridinic and pyrrolic nitrogen atoms in NCdots, can be thought of as defective structures since they alter the conjugated carbon structure. This explains why the emission efficiency is somewhat influenced by the nitrogen concentration of NCdots [83].

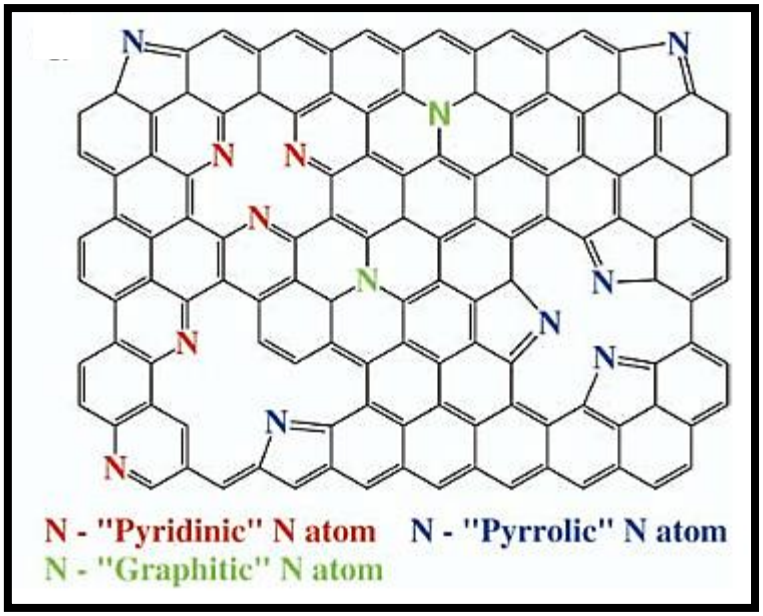

Figure 2.1: Schematic structure representing the three types of nitrogen configurations [84].

The N-state, which is brought about by nitrogen, is a new surface state that traps electrons, lowers non-radiative recombination, and increases radiative recombination. After surface passivation, nitrogen doping has been found to greatly improve fluorescence and quantum yield (QY_{FL}) of Cdots [85, 86]. Additionally, nitrogen doping is the most efficient strategy for improving the QY_{FL} of NCdots among non-metallic doping techniques because of the high fluorescence yield of electrons trapped by the new N-state.

To dope the NCdots employed in this investigation: citric acid and ethylenediamine, citric acid and urea, and fumaronitrile were used. The synthesis of Cdots relied heavily on their precursors.

2.1.5 Properties and applications of carbon nano-dots

Because of their various physical, optical, and chemical features, carbon dots have attracted a lot of curiosity. The fact that these luminous nanomaterials may be made from very affordable sources, such as simple organic compounds like citric acid [78] or more heterogeneous sources such as orange juice [87], rice [88], coffee beans [89], ashes [90] or even waste [91] has given rise to the extensive studies on the properties of Cdots. Cdots are primarily composed of carbon (largely sp^2 with some sp^3 character) with small amounts of hydrogen, oxygen, and nitrogen [92, 93]. These products have a high fluorescence quantum yield QY_{FL} [14]. As a result, Cdots have established themselves as a low-cost, ecologically acceptable nanomaterial class for new technological innovations.

Furthermore, they offer an intriguing alternative to typical fluorescent materials and are now hailed as having significant potential for use in displays [94], lighting [95], sensing [96] biological processing [97, 98] chemical monitoring [99, 100], catalysis [101], drug delivery [102], imaging [103 - 105] and solar cells [106].

It is difficult to remove fluorescent Cdots from solution because of their tiny size, which causes them to aggregate in the solid state [107, 108]. This agglomeration may cause aggregation-induced luminescence suppression, in which case the application of their photoluminescence emissions is compromised. To overcome these difficulties, a support might be decorated with Cdots.

2.2 Onion-like carbon nanomaterials

Following Iijima's work on carbon nanotubes (CNTs) in 1991 [109], chemists, material scientists, and physicists etc. have been fascinated by these and associated carbon nanomaterials, resulting in the study of a wide range of carbon nanostructures. Carbon nano-onions are one such carbon. They were initially identified by Ugarte in 1992 [110] by exposing carbon soot to an intense electron beam. Carbon nano-onions (CNOs) are nanoparticles made up of spherically closed carbon shells that get their name from their graphitic concentric multi-layered structure that resembles much like an onion [111].

They are an allotrope nanophase of carbon [112]. Onion-like carbon nanomaterials (OLCNs) is the name given to CNOs when the layers do not give a complete onion-like structure. They have a polyhedral nanostructure with diameters of 100 nanometers. CNOs (and OLCNs) can have one of two structures: 1) a densely packed core that is not empty since it includes the carbonaceous nanomaterial produced, or 2) a core-filled with a metal nanoparticle (mostly from the metal catalyst employed in the carbon synthesis) [113].

2.2.1 Synthesis techniques to make carbon nano-onions

Carbon nanoparticles, including CNOs and OLCNs, have been made by a variety of synthesis methods that have been established over time. Over the last few decades, numerous preparation procedures, such as ferrocene chlorination [114], heat treatment of carbon black [115] and the chemical vapor deposition method (CVD) [116 -119] have been used to create chain-like carbon nanostructures.

They have been found to show potential application in drug delivery [120], super-capacitors [121], lithium-ion batteries [122 - 124], point-source electron field emittance [125] and solar cells due to their unique interior void space [126, 127]. An example of a synthetic procedure that produces large OLCNs involves pyrolyzing wood wool and then treating the product formed with a strong acid (e.g., nitric acid). This yields OLCNs with distinct fluorescence emissions [128] and that show chemical functionalization that allow the OLCNs to be dispersed in organic solvents [129].

The flame pyrolysis method, also known as the innovative open flame-assisted synthesis methodology, is a cutting-edge technique utilized for the continuous production of catalyst-free solid OLCNs under ambient conditions [130, 131]. The carbon supply is broken down into atomic or radical carbon moieties in the flame pyrolysis process, which react to produce OLCNs clumps, from which a compacted structure can be produced [132]. The auto curling mechanism initiates the development of OLCNs layers from the inside out [133, 134]. Among the carbon-containing liquids and/or oils that have been employed in the flame pyrolysis procedure are flaxseed oil, paraffin oil, and naphthalene [135, 136]. Furthermore, this approach is low-cost and produces large amounts of clean (i.e., free of metal catalyst) OLCNs [137, 138]. In this study, olive oil was employed as a carbon precursor to create chain-like OLCNs using the flame pyrolysis process.

It's vital to note that this approach can create a wide variety of nanoparticles. The product morphology is dependent on the synthesis process used to make the OLCNs. These methods give rise to onion-like structures with highly variable nanosize [139, 140], and different shapes (spherical [141 - 144], quasi-spherical [145], or polyhedral [42, 143, 146]). The carbon cores/interior void space can be dense [132, 133, 135] or hollow [143, 144, 147]). CNOs created by nanodiamonds, or electron radiation are very small (approximately 5-8 carbon shells) [148]. This can result in CNOs of various sizes and chemical and physical characteristics [149].

2.2.2 Functionalization of OLCNs

Since all carbon nanostructures aggregate, which is facilitated by intermolecular interactions like van der Waals forces, it has been demonstrated that all carbon nanostructures have low solubility in both aqueous and organic fluids [147]. The functionalization of carbon nanostructures is a way to solve this tendency. One strategy is to modify the carbons with

heteroatoms like F, B, S, P, O, as well as N [150 - 155]. So far, two basic tactics have been used to achieve this goal. The first technique relies on heteroatoms modifying carbon nanomaterials during their synthesis [149, 150]. The second technique includes treating previously formed carbon structures with various oxidizing or reducing chemicals after they have been synthesized [155, 158 - 160].

OLCNs are particularly appealing as materials for numerous applications due to their unique mix of very favourable physicochemical features. Despite their advantages, OLCNs have to date not garnered much attention as an electrode material for DSSCs, although they have been used in supercapacitor (SC) and battery applications [161 - 163]. Additionally, OLCNs have been demonstrated to be excellent materials for and can be doped by ion implantation [164, 165]. The OLCNs structures enables quick charge transfer processes. Further, the OLCNs structures may be modified or doped to increase their electrochemical and electrocatalytic capabilities.

In this study, OLCNs have been modified i) nitrogen doping to make N- OLCNs and ii) functionalized with an oxidizing agent to produce ox- OLCNs. This functionalization could enhance the long-term operating stability when they are utilized as counter electrodes [166]. The capacitance of OLCNs might be improved by making internal shells receptive to electrolytes, therefore increasing the specific surface area of the OLCNs while maintaining facile ion transport. The usage of these materials in solar cells might give a potential answer to issues with DSSC manufacture.

2.3. Overview of photovoltaic cells

2.3.1 History of photovoltaic cells

In 1839, French scientist Alexandre Edmond Becquerel was studying the effects of light on metal electrodes submerged in an electrolyte when he made the discovery of the optical and electrical (photovoltaic) phenomena [167]. Following this early work, new materials have been employed in optoelectronic technology.

William Adams and Richard Day observed the PV effect in solid selenium in 1877, and Wilhelm Ludwig Franz Hallwachs produced a semiconductor-junction photovoltaic cell with copper and copper oxide in 1904 [168]. However, there was still a lack of knowledge of the science underpinning the functioning of these early PV systems at the time.

The second phase in the history of the topic, which lasted from 1905 to 1950, provided the theoretical foundation for the use of PV devices [169]. The progress of band theory for highly pure single crystal semiconductors, as well as Einstein's photon theory and the adaption of the Czochralski crystal growth process for single crystal silicon and germanium growth, marked the second phase of this story. For highly tuned photovoltaic cells, the developed PVs hypothesis highlighted the significance of using high grade single – crystal semiconductors.

These breakthroughs paved the way for the third phase of PV device development, which occurred between 1950 and 1959 and yielded the first practical silicon single-crystal PV devices. The unveiling of the PV effect by Bell Labs in 1954, followed by the patent for an 8% effective silicon photovoltaic cell by Pearson, Chapin, and Fuller in 1957, was an important development in the generation of PV technology [169].

2.3.2 Chemistry of solar cells and solar cell architecture

In 1991, Grätzel and O'Regan constructed the first DSSC, and in 1992, they published the first study on energy transformations and photoelectric energy production utilizing this technology [170]. DSSCs are a simple device to create organic solar cells [171]. DSSCs are noted for being transparent and adaptable, have cheap manufacturing costs, low raw material prices, and have good commercial energy conversion [172]. For solar photovoltaic cells to operate, light must be absorbed in order to generate exactions/electron holes, and the various charge carriers of opposing types must be separated and extracted independently from the external circuit [173].

The DSSC systems consist of a number of segments that ensure that the cell works properly [171]:

- a transparent, highly conductive oxide coating has been applied on a sheet of glass to create a translucent anode
- Application of a mesoporous oxide layer to the anode to initiate electrical conduction
- A single layer charge transfer dye that increases optical absorption by being covalently bonded to the surface of the mesoporous oxide layer.

- A dye regeneration-influencing electrolyte that contains a redox mediator dissolved in an organic liquid
- A cathode, which is often a glass sheet coated with a catalyst to promote easier electron accumulation

DSSCs include optically clear electrodes, coordination compounds, nanoparticulate semiconductors, inorganic salts, solvents, and metallic catalysts, which altogether contribute to the goal of absorbing incident radiation and turning it into generated electricity [174]. Because the performance of the individual components determines the overall efficiency of the DSSC, constant development of these components will enhance the cell and boost the device's overall quality.

2.3.3 Working principle of a DSSC

Photoelectric cells called dye-sensitized solar cells are similar to artificial photosynthesis in that they imitate both the process by which plant cells produce their own energy and the results of sustainable solar power absorption by plants. When the electrons are produced by the impact of photon energy and all chemical processes are considered, DSSCs are classified as photo-electrochemical cells [175].

A DSSC's core working principle begins with light incidence generating dye excitation. The semiconductor material's conduction band is then formed by stimulating the electrons from the dye state [176, 177]. Through a porous, thin film layer, the electrons go to the transparent conducting oxide (TCO) in the cell. The trapping and de-trapping effect, as well as the incidence rate, have an impact on electron flow [178 - 181]. Whenever an oxidized dye receives electrons from a redox mediator, the dye is regenerated, but the mediators are oxidized as well [175]. The oxidized redox mediators are also replenished after diffusing to the counter electrode through reduction owing to the electrons entering the counter electrode (CE) through the use of an external circuit. The operational process is now complete [182].

The frequent counter electrode used in DSSCs is Pt placed on a TCO substrate [175]. Researchers have been working to develop new low-cost materials and methods to effectively replace Pt and TCOs in counter electrodes due to the high expense of employing both of these materials (Pt and TCOs). Studies on the use of flat electrodes and liquid electrolyte in DSSCs for dye sensitization of semiconductors causes problems for photo-electrochemical research have also been undertaken [183]. Potential substitutes include carbon nanoparticles with a

high specific surface area and strong electrical conductivity [184, 185]. We also suggest a unique, entirely carbon-based composite material for high-performance counter electrode materials in this study.

2.4. The use of carbon dots and onion-like carbon as electrode materials in DSSCs

Pt has significant electric conductivity and excellent catalytic activity for the reduction of triiodide, but it is extremely expensive and there aren't enough reserves to support its widespread application [185, 186]. So far, low-cost carbonaceous materials have been used as the catalytic materials on FTO (fluorine-doped tin oxide) or ITO (indium tin oxide) glass for the CEs in DSSCs. These materials include graphite [187], carbon black [188], activated carbon [189], hard carbon spheres [190], carbon nanotubes [191, 192], fullerene [193], and graphene [194]. Both smoothness and conductance are two essential elements that influence the functionality of CEs [186, 189 ,190]. Nevertheless, the DSSCs' performance with any of these substrates has been shown to be modest, and long-term durability enhancements are also required for future large-scale manufacturing.

Carbon nano-materials (e.g., carbon nano-tubes, graphene or graphene nano-plates, and carbon composites) have been studied since they have large surface areas and strong electrical conductance [195]. It is critical to concurrently increase conductance, electrical properties, and device durability to boost the effectiveness of an all-carbon-based CE for use in a DSSC. Moreover, the CE materials seldom have strong electrical conductivity and electrocatalytic activity. Pang and co-workers were some of the first to synthesize and test an all-carbon composite CE comprised of modified reduced graphene and nitrogen-doped carbon nano-onions in a DSSC [196] and they obtained an impressive power cell efficiency > 10%.

2.5 All carbon composite material

The small size of Cdots can cause problems with their use. They can create carbonaceous clusters when they are dry (after being taken out of a solvent), which can lead to aggregation-induced luminescence quenching, which impairs their photoluminescence emissions [197]. Low insufficient quantum yields and poor transduction of light energy into chemical/electrical energy can result from a suppressed photoelectrochemical spectrum [198]. Supporting Cdots on an insoluble solid surface is one way to deal with the problems that come with them [199, 200]. When contrasted to other graphic carbon materials, OLCNs with multi-layered lamellar structures have appealing properties, such as size [201, 202].

Consequently, as a composite, these carbon compounds can possibly give intriguing catalytic properties as new electrode materials for electrical and chemical energy storage applications [203, 204]

Utilizing Cdot: functionalized OLCNs composites with nitrogen doping might provide important insight into how co-doping affects the optical properties of carbonaceous materials utilized in DSSCs.

2.7 Conclusion

Carbon dots can be produced utilizing a number of precursors and synthetic preparation processes. This makes them exciting materials to synthesize because of their nonporous outer shells, which are readily available to electrolyte ion. To date, carbon nano-onions have gained increased attention as a promising solar electrode material with enhanced power density. They may be the perfect counter electrode for DSSCs due to their excellent electrical conductivity, low charge-transfer resistance, outstanding electrocatalytic activity, affordable price, and stability for large-scale manufacture. To evaluate this proposal, the investigation of a hybrid composite material composing of NCdots/functionalized OLCNs (p- OLCNs, ox-OLCNs, and N- OLCNs) to achieve these merits desired has been undertaken.

References

1. Grätzel, M. (2003). Dye-sensitized solar cells. *Journal of Photochemistry and Photobiology C: Photochemistry Reviews*, *4*(2), 145–153. https://doi.org/10.1016/s1389-5567(03)00026-1
2. Zhu, H., Wei, J., Wang, K., & Wu, D. (2009). Applications of carbon materials in photovoltaic solar cells. *Solar Energy Materials and Solar Cells*, *93*(9), 1461–1470. https://doi.org/10.1016/j.solmat.2009.04.006
3. Alagarasi, A. (2011). Introduction to Nanomaterials. *National Centre for Catalysis Research, Chennai, India: Indian Institute of Technology Madras*, 1–76. https://nccr.iitm.ac.in/2011.pdf
4. Hutagalung, S. D. (2012). Materials Science and Technology. *InTech. Rijeka, Croatia*, 1–5.
5. Wang, C., Waje, M., Wang, X., Tang, J. M., Haddon, R. C., & Yan. (2003b). Proton Exchange Membrane Fuel Cells with Carbon Nanotube Based Electrodes. *Nano Letters*, *4*(2), 345–348. https://doi.org/10.1021/nl034952p
6. Stewart, D. A., & Léonard, F. (2005). Energy Conversion Efficiency in Nanotube Optoelectronics. *Nano Letters*, *5*(2), 219–222. https://doi.org/10.1021/nl048410z
7. Singh, M., Manikandan, S., & Kumaraguru, A. (2011). Nanoparticles: A New Technology with Wide Applications. *Research Journal of Nanoscience and Nanotechnology*, *1*(1), 1–11. https://doi.org/10.3923/rjnn.2011.1.11
8. Jeevanandam, J., Barhoum, A., Chan, Y. S., Dufresne, A., & Danquah, M. K. (2018). Review on nanoparticles and nanostructured materials: history, sources, toxicity and regulations. *Beilstein Journal of Nanotechnology*, *9*, 1050–1074. https://doi.org/10.3762/bjnano.9.98
9. McDonough, J. K., Frolov, A. I., Presser, V., Niu, J., Miller, C. H., Ubieto, T., Fedorov, M. V., & Gogotsi, Y. (2012). Influence of the structure of carbon onions on their electrochemical performance in supercapacitor electrodes. *Carbon*, *50*(9), 3298–3309. https://doi.org/10.1016/j.carbon.2011.12.022
10. Bollmann, W., & Spreadborough, J. (1960). Action of Graphite as a Lubricant. *Nature*, *186*(4718), 29–30. https://doi.org/10.1038/186029a0
11. Iijima, S. (1991). Helical microtubules of graphitic carbon. *Nature*, *354*(6348), 56–58. https://doi.org/10.1038/354056a0

12. Iijima, S., & Ichihashi, T. (1993). Single-shell carbon nanotubes of 1-nm diameter. *Nature*, *363*(6430), 603–605. https://doi.org/10.1038/363603a0
13. Novoselov, K. S., Geim, A. K., Morozov, S. V., Jiang, D., Zhang, Y., Dubonos, S. V., Grigorieva, I. V., & Firsov, A. A. (2004). Electric Field Effect in Atomically Thin Carbon Films. *Science*, *306*(5696), 666–669. https://doi.org/10.1126/science.1102896
14. Zhang, C., Li, J., Liu, E., He, C., Shi, C., Du, X., Hauge, R. H., & Zhao, N. (2012). Synthesis of hollow carbon nano-onions and their use for electrochemical hydrogen storage. *Carbon*, *50*(10), 3513–3521. https://doi.org/10.1016/j.carbon.2012.03.019
15. Zuo, P., Lu, X., Sun, Z., Guo, Y., & He, H. (2015). A review on syntheses, properties, characterization and bioanalytical applications of fluorescent carbon dots. *Microchimica Acta*, *183*(2), 519–542. https://doi.org/10.1007/s00604-015-1705-3
16. Baker, S. N., & Baker, G. A. (2010). ChemInform Abstract: Luminescent Carbon Nanodots: Emergent Nanolights. *ChemInform*, *42*(3), no. https://doi.org/10.1002/chin.201103270
17. de Medeiros, T. V., Manioudakis, J., Noun, F., Macairan, J. R., Victoria, F., & Naccache, R. (2019). Microwave-assisted synthesis of carbon dots and their applications. *Journal of Materials Chemistry C*, *7*(24), 7175–7195. https://doi.org/10.1039/c9tc01640f
18. Baker, S., & Baker, G. (2010). Luminescent Carbon Nanodots: Emergent Nanolights. *Angewandte Chemie International Edition*, *49*(38), 6726–6744. https://doi.org/10.1002/anie.200906623
19. Goryacheva, I. Y., Sapelkin, A. V., & Sukhorukov, G. B. (2017). Carbon nanodots: Mechanisms of photoluminescence and principles of application. *TrAC Trends in Analytical Chemistry*, *90*, 27–37. https://doi.org/10.1016/j.trac.2017.02.012
20. Mondal, S., Yucknovsky, A., Akulov, K., Ghorai, N., Schwartz, T., Ghosh, H. N., & Amdursky, N. (2019). Efficient Photosensitizing Capabilities and Ultrafast Carrier Dynamics of Doped Carbon Dots. *Journal of the American Chemical Society*, *141*(38), 15413–15422. https://doi.org/10.1021/jacs.9b08071
21. Bottini, M., & Mustelin, T. (2007). Nanosynthesis by candlelight. *Nature Nanotechnology*, *2*(10), 599–600. https://doi.org/10.1038/nnano.2007.316
22. Sun, Y. P., Zhou, B., Lin, Y., Wang, W., Fernando, K. A. S., Pathak, P., Meziani, M. J., Harruff, B. A., Wang, X., Wang, H., Luo, P. G., Yang, H., Kose, M. E., Chen, B., Veca, L. M., & Xie, S. Y. (2006). Quantum-Sized Carbon Dots for Bright and Colorful Photoluminescence. *Journal of the American Chemical Society*, *128*(24), 7756–7757. https://doi.org/10.1021/ja062677d

23. Wen, Z. H., & Yin, X. B. (2016). Excitation-independent carbon dots, from photoluminescence mechanism to single-color application. *RSC Advances*, *6*(33), 27829–27835. https://doi.org/10.1039/c5ra27172j
24. Li, X., Zhang, S., Kulinich, S. A., Liu, Y., & Zeng, H. (2014). Engineering surface states of carbon dots to achieve controllable luminescence for solid-luminescent composites and sensitive Be2+ detection. *Scientific Reports*, *4*(1). https://doi.org/10.1038/srep04976
25. Zhu, S., Song, Y., Zhao, X., Shao, J., Zhang, J., & Yang, B. (2015). The photoluminescence mechanism in carbon dots (graphene quantum dots, carbon nanodots, and polymer dots): current state and future perspective. *Nano Research*, *8*(2), 355–381. https://doi.org/10.1007/s12274-014-0644-3
26. Xu, Y., Liu, J., Gao, C., & Wang, E. (2014). Applications of carbon quantum dots in electrochemiluminescence: A mini review. *Electrochemistry Communications*, *48*, 151–154. https://doi.org/10.1016/j.elecom.2014.08.032
27. Zuo, P., Lu, X., Sun, Z., Guo, Y., & He, H. (2015). A review on syntheses, properties, characterization and bioanalytical applications of fluorescent carbon dots. *Microchimica Acta*, *183*(2), 519–542. https://doi.org/10.1007/s00604-015-1705-3
28. Reyes, D., Camacho, M., Camacho, M., Mayorga, M., Weathers, D., Salamo, G., Wang, Z., & Neogi, A. (2016). Laser Ablated Carbon Nanodots for Light Emission. *Nanoscale Research Letters*, *11*(1). https://doi.org/10.1186/s11671-016-1638-8
29. Sun, Y. P., Zhou, B., Lin, Y., Wang, W., Fernando, K. A. S., Pathak, P., Meziani, M. J., Harruff, B. A., Wang, X., Wang, H., Luo, P. G., Yang, H., Kose, M. E., Chen, B., Veca, L. M., & Xie, S. Y. (2006). Quantum-Sized Carbon Dots for Bright and Colorful Photoluminescence. *Journal of the American Chemical Society*, *128*(24), 7756–7757. https://doi.org/10.1021/ja062677d
30. Cao, L., Wang, X., Meziani, M. J., Lu, F., Wang, H., Luo, P. G., Lin, Y., Harruff, B. A., Veca, L. M., Murray, D., Xie, S. Y., & Sun, Y. P. (2007). Carbon Dots for Multiphoton Bioimaging. *Journal of the American Chemical Society*, *129*(37), 11318–11319. https://doi.org/10.1021/ja073527l
31. Ramirez, A., Sun, X., & Collum, D. B. (2006). Lithium Diisopropylamide-Mediated Enolization: Catalysis by Hemilabile Ligands. *Journal of the American Chemical Society*, *128*(31), 10326–10336. https://doi.org/10.1021/ja062147h
32. Zhou, J., Booker, C., Li, R., Zhou, X., Sham, T. K., Sun, X., & Ding, Z. (2007). An Electrochemical Avenue to Blue Luminescent Nanocrystals from Multiwalled Carbon

Nanotubes (MWCNTs). *Journal of the American Chemical Society*, *129*(4), 744–745. https://doi.org/10.1021/ja0669070

33. Yu, S. J., Kang, M. W., Chang, H. C., Chen, K. M., & Yu, Y. C. (2005). Bright Fluorescent Nanodiamonds: No Photobleaching and Low Cytotoxicity. *Journal of the American Chemical Society*, *127*(50), 17604–17605. https://doi.org/10.1021/ja0567081
34. Sun, Y. P., Zhou, B., Lin, Y., Wang, W., Fernando, K. A. S., Pathak, P., Meziani, M. J., Harruff, B. A., Wang, X., Wang, H., Luo, P. G., Yang, H., Kose, M. E., Chen, B., Veca, L. M., & Xie, S. Y. (2006). Quantum-Sized Carbon Dots for Bright and Colorful Photoluminescence. *Journal of the American Chemical Society*, *128*(24), 7756–7757. https://doi.org/10.1021/ja062677d
35. Zhou, J., Booker, C., Li, R., Zhou, X., Sham, T. K., Sun, X., & Ding, Z. (2007). An Electrochemical Avenue to Blue Luminescent Nanocrystals from Multiwalled Carbon Nanotubes (MWCNTs). *Journal of the American Chemical Society*, *129*(4), 744–745. https://doi.org/10.1021/ja0669070
36. Liu, H., Ye, T., & Mao, C. (2007). Fluorescent Carbon Nanoparticles Derived from Candle Soot. *Angewandte Chemie International Edition*, *46*(34), 6473–6475. https://doi.org/10.1002/anie.200701271
37. Dong, Y., Zhou, N., Lin, X., Lin, J., Chi, Y., & Chen, G. (2010). Extraction of Electrochemiluminescent Oxidized Carbon Quantum Dots from Activated Carbon. *Chemistry of Materials*, *22*(21), 5895–5899. https://doi.org/10.1021/cm1018844
38. Wang, Q., Zheng, H., Long, Y., Zhang, L., Gao, M., & Bai, W. (2011). Microwave–hydrothermal synthesis of fluorescent carbon dots from graphite oxide. *Carbon*, *49*(9), 3134–3140. https://doi.org/10.1016/j.carbon.2011.03.041
39. Zhu, S., Song, Y., Zhao, X., Shao, J., Zhang, J., & Yang, B. (2015). The photoluminescence mechanism in carbon dots (graphene quantum dots, carbon nanodots, and polymer dots): current state and future perspective. *Nano Research*, *8*(2), 355–381. https://doi.org/10.1007/s12274-014-0644-3
40. Lim, S. Y., Shen, W., & Gao, Z. (2015). Carbon quantum dots and their applications. *Chemical Society Reviews*, *44*(1), 362–381. https://doi.org/10.1039/c4cs00269e
41. Hsu, P. C., Shih, Z. Y., Lee, C. H., & Chang, H. T. (2012b). Synthesis and analytical applications of photoluminescent carbon nanodots. *Green Chemistry*, *14*(4), 917. https://doi.org/10.1039/c2gc16451e
42. Shen, L. M., & Liu, J. (2016). New development in carbon quantum dots technical applications. *Talanta*, *156–157*, 245–256. https://doi.org/10.1016/j.talanta.2016.05.028

43. Lim, S. Y., Shen, W., & Gao, Z. (2015). Carbon quantum dots and their applications. *Chemical Society Reviews*, *44*(1), 362–381. https://doi.org/10.1039/c4cs00269e
44. Li, H., He, X., Liu, Y., Huang, H., Lian, S., Lee, S. T., & Kang, Z. (2011). One-step ultrasonic synthesis of water-soluble carbon nanoparticles with excellent photoluminescent properties. *Carbon*, *49*(2), 605–609. https://doi.org/10.1016/j.carbon.2010.10.004
45. Preview: Angew. Chem. Int. Ed. (2007). *Angewandte Chemie International Edition*, *46*(45), 8717. https://doi.org/10.1002/anie.200790232
46. Moon, B. J., Oh, Y., Shin, D. H., Kim, S. J., Lee, S. H., Kim, T. W., Park, M., & Bae, S. (2016). Facile and Purification-Free Synthesis of Nitrogenated Amphiphilic Graphitic Carbon Dots. *Chemistry of Materials*, *28*(5), 1481–1488. https://doi.org/10.1021/acs.chemmater.5b04915
47. Zhu, H., Wang, X., Li, Y., Wang, Z., Yang, F., & Yang, X. (2009). Microwave synthesis of fluorescent carbon nanoparticles with electrochemiluminescence properties. *Chemical Communications*, *34*, 5118. https://doi.org/10.1039/b907612c
48. Bourlinos, A. B., Stassinopoulos, A., Anglos, D., Zboril, R., Karakassides, M., & Giannelis, E. P. (2008). Surface Functionalized Carbogenic Quantum Dots. *Small*, *4*(4), 455–458. https://doi.org/10.1002/smll.200700578
49. Peng, H., & Travas-Sejdic, J. (2009). Simple Aqueous Solution Route to Luminescent Carbogenic Dots from Carbohydrates. *Chemistry of Materials*, *21*(23), 5563–5565. https://doi.org/10.1021/cm901593y
50. Liu, R., Wu, D., Liu, S., Koynov, K., Knoll, W., & Li, Q. (2009). An Aqueous Route to Multicolor Photoluminescent Carbon Dots Using Silica Spheres as Carriers. *Angewandte Chemie International Edition*, *48*(25), 4598–4601. https://doi.org/10.1002/anie.200900652
51. Lim, S. Y., Shen, W., & Gao, Z. (2015). Carbon quantum dots and their applications. *Chemical Society Reviews*, *44*(1), 362–381. https://doi.org/10.1039/c4cs00269e
52. Tuerhong, M., Xu, Y., & Yin, X. B. (2017). Review on Carbon Dots and Their Applications. *Chinese Journal of Analytical Chemistry*, *45*(1), 139–150. https://doi.org/10.1016/s1872-2040(16)60990-8
53. Lim, C. S., Hola, K., Ambrosi, A., Zboril, R., & Pumera, M. (2015). Graphene and carbon quantum dots electrochemistry. *Electrochemistry Communications*, *52*, 75–79. https://doi.org/10.1016/j.elecom.2015.01.023

54. Dong, Y., Lin, J., Chen, Y., Fu, F., Chi, Y., & Chen, G. (2014). Graphene quantum dots, graphene oxide, carbon quantum dots and graphite nanocrystals in coals. *Nanoscale*, *6*(13), 7410–7415. https://doi.org/10.1039/c4nr01482k
55. Wang, Q., Liu, X., Zhang, L., & Lv, Y. (2012). Microwave-assisted synthesis of carbon nanodots through an eggshell membrane and their fluorescent application. *The Analyst*, *137*(22), 5392. https://doi.org/10.1039/c2an36059d
56. Li, H., Shao, F. Q., Zou, S. Y., Yang, Q. J., Huang, H., Feng, J. J., & Wang, A. J. (2015). Microwave-assisted synthesis of N,P-doped carbon dots for fluorescent cell imaging. *Microchimica Acta*, *183*(2), 821–826. https://doi.org/10.1007/s00604-015-1714-2
57. Hong, E., Lee, K. H., Oh, S., & Park, C. G. (2003). Synthesis of Carbon Nanotubes Using Microwave Radiation. *Advanced Functional Materials*, *13*(12), 961–966. https://doi.org/10.1002/adfm.200304396
58. Kappe, C. O., & Dallinger, D. (2009). Controlled microwave heating in modern organic synthesis: highlights from the 2004–2008 literature. *Molecular Diversity*, *13*(2), 71–193. https://doi.org/10.1007/s11030-009-9138-8
59. Liu, Y., Xiao, N., Gong, N., Wang, H., Shi, X., Gu, W., & Ye, L. (2014). One-step microwave-assisted polyol synthesis of green luminescent carbon dots as optical nanoprobes. *Carbon*, *68*, 258–264. https://doi.org/10.1016/j.carbon.2013.10.086
60. Bhaisare, M. L., Talib, A., Khan, M. S., Pandey, S., & Wu, H. F. (2015). Synthesis of fluorescent carbon dots via microwave carbonization of citric acid in presence of tetraoctylammonium ion, and their application to cellular bioimaging. *Microchimica Acta*, *182*(13–14), 2173–2181. https://doi.org/10.1007/s00604-015-1541-5
61. Economopoulos, S. P., Rotas, G., Miyata, Y., Shinohara, H., & Tagmatarchis, N. (2010). Exfoliation and Chemical Modification Using Microwave Irradiation Affording Highly Functionalized Graphene. *ACS Nano*, *4*(12), 7499–7507. https://doi.org/10.1021/nn101735e
62. Hetzel, R., Manning, T., Lovingood, D., Strouse, G., & Phillips, D. (2012). Production of Fullerenes by Microwave Synthesis. *Fullerenes, Nanotubes and Carbon Nanostructures*, *20*(2), 99–108. https://doi.org/10.1080/1536383x.2010.533300
63. Schwenke, A. M., Hoeppener, S., & Schubert, U. S. (2015). Synthesis and Modification of Carbon Nanomaterials utilizing Microwave Heating. *Advanced Materials*, *27*(28), 4113–4141. https://doi.org/10.1002/adma.201500472

64. Christé, Esteves Da Silva, & Pinto Da Silva. (2020). Evaluation of the Environmental Impact and Efficiency of N-Doping Strategies in the Synthesis of Carbon Dots. *Materials*, *13*(3), 504. https://doi.org/10.3390/ma13030504
65. P. Economopoulos, S., Karousis, N., Rotas, G., Pagona, G., & Tagmatarchis, N. (2011). Microwave-assisted Functionalization of Carbon Nanostructured Materials. *Current Organic Chemistry*, *15*(8), 1121–1132. https://doi.org/10.2174/138527211795203031
66. Vázquez, E., & Prato, M. (2009). Carbon Nanotubes and Microwaves: Interactions, Responses, and Applications. *ACS Nano*, *3*(12), 3819–3824. https://doi.org/10.1021/nn901604j
67. Kim, S., Yoo, B. K., Choi, Y., Kim, B. S., & Kwon, O. H. (2018). Time-resolved spectroscopy of the ensembled photoluminescence of nitrogen- and boron/nitrogen-doped carbon dots. *Physical Chemistry Chemical Physics*, *20*(17), 11673–11681. https://doi.org/10.1039/c8cp01619d
68. de Medeiros, T. V., Manioudakis, J., Noun, F., Macairan, J. R., Victoria, F., & Naccache, R. (2019). Microwave-assisted synthesis of carbon dots and their applications. *Journal of Materials Chemistry C*, *7*(24), 7175–7195. https://doi.org/10.1039/c9tc01640f
69. Choi, Y., Kang, B., Lee, J., Kim, S., Kim, G. T., Kang, H., Lee, B. R., Kim, H., Shim, S. H., Lee, G., Kwon, O. H., & Kim, B. S. (2016). Integrative Approach toward Uncovering the Origin of Photoluminescence in Dual Heteroatom-Doped Carbon Nanodots. *Chemistry of Materials*, *28*(19), 6840–6847. https://doi.org/10.1021/acs.chemmater.6b01710
70. Gong, X., Lu, W., Paau, M. C., Hu, Q., Wu, X., Shuang, S., Dong, C., & Choi, M. M. (2015). Facile synthesis of nitrogen-doped carbon dots for Fe3+ sensing and cellular imaging. *Analytica Chimica Acta*, *861*, 74–84. https://doi.org/10.1016/j.aca.2014.12.045
71. Wang, K., Gao, Z., Gao, G., Wo, Y., Wang, Y., Shen, G., & Cui, D. (2013). Systematic safety evaluation on photoluminescent carbon dots. *Nanoscale Research Letters*, *8*(1). https://doi.org/10.1186/1556-276x-8-122
72. Chen, B. B., Liu, M. L., Li, C. M., & Huang, C. Z. (2019). Fluorescent carbon dots functionalization. *Advances in Colloid and Interface Science*, *270*, 165–190. https://doi.org/10.1016/j.cis.2019.06.008
73. Park, Y., Yoo, J., Lim, B., Kwon, W., & Rhee, S. W. (2016). Improving the functionality of carbon nanodots: doping and surface functionalization. *Journal of Materials Chemistry A*, *4*(30), 11582–11603. https://doi.org/10.1039/c6ta04813g

74. Shamsipur, M., Barati, A., & Karami, S. (2017). Long-wavelength, multicolor, and white-light emitting carbon-based dots: Achievements made, challenges remaining, and applications. *Carbon*, *124*, 429–472. https://doi.org/10.1016/j.carbon.2017.08.072
75. Abdullah Issa, M., Z. Abidin, Z., Sobri, S., Rashid, S., Adzir Mahdi, M., Azowa Ibrahim, N., & Y. Pudza, M. (2019). Facile Synthesis of Nitrogen-Doped Carbon Dots from Lignocellulosic Waste. *Nanomaterials*, *9*(10), 1500. https://doi.org/10.3390/nano9101500
76. Zhu, S., Meng, Q., Wang, L., Zhang, J., Song, Y., Jin, H., Zhang, K., Sun, H., Wang, H., & Yang, B. (2013). Highly Photoluminescent Carbon Dots for Multicolor Patterning, Sensors, and Bioimaging. *Angewandte Chemie International Edition*, *52*(14), 3953–3957. https://doi.org/10.1002/anie.201300519
77. Liu, X., Liu, J., Zheng, B., Yan, L., Dai, J., Zhuang, Z., Du, J., Guo, Y., & Xiao, D. (2017). N-Doped carbon dots: green and efficient synthesis on a large-scale and their application in fluorescent pH sensing. *New Journal of Chemistry*, *41*(19), 10607–10612. https://doi.org/10.1039/c7nj01889d
78. Liu, Y., & Han, S. (2018). A chemiluminescence resonance energy transfer for the determination of indolyl acetic acid using luminescent nitrogen-doped carbon dots as acceptors. *New Journal of Chemistry*, *42*(1), 388–394. https://doi.org/10.1039/c7nj04215a
79. Wu, Z. L., Zhang, P., Gao, M. X., Liu, C. F., Wang, W., Leng, F., & Huang, C. Z. (2013). One-pot hydrothermal synthesis of highly luminescent nitrogen-doped amphoteric carbon dots for bioimaging from Bombyx mori silk – natural proteins. *Journal of Materials Chemistry B*, *1*(22), 2868. https://doi.org/10.1039/c3tb20418a
80. Wang, L., & Zhou, H. S. (2014). Green Synthesis of Luminescent Nitrogen-Doped Carbon Dots from Milk and Its Imaging Application. *Analytical Chemistry*, *86*(18), 8902–8905. https://doi.org/10.1021/ac502646x
81. Wang, L., Bi, Y., Hou, J., Li, H., Xu, Y., Wang, B., Ding, H., & Ding, L. (2016). Facile, green and clean one-step synthesis of carbon dots from wool: Application as a sensor for glyphosate detection based on the inner filter effect. *Talanta*, *160*, 268–275. https://doi.org/10.1016/j.talanta.2016.07.020
82. Tang, L., Ji, R., Li, X., Teng, K. S., & Lau, S. P. (2013). Energy-level structure of nitrogen-doped graphene quantum dots. Journal of Materials Chemistry C, 1(32), 4908. https://doi.org/10.1039/c3tc30877d
83. Qian, Z., Ma, J., Shan, X., Feng, H., Shao, L., & Chen, J. (2014). Highly Luminescent N-Doped Carbon Quantum Dots as an Effective Multifunctional Fluorescence Sensing

Platform. Chemistry - A European Journal, 20(8), 2254–2263. https://doi.org/10.1002/chem.201304374

84. Zhang, C., Fu, L., Liu, N., Liu, M., Wang, Y., & Liu, Z. (2011). Synthesis of Nitrogen-Doped Graphene Using Embedded Carbon and Nitrogen Sources. Advanced Materials, 23(8), 1020–1024. https://doi.org/10.1002/adma.201004110
85. Dong, Y., Pang, H., Yang, H. B., Guo, C., Shao, J., Chi, Y., Li, C. M., & Yu, T. (2013). Carbon-Based Dots Co-doped with Nitrogen and Sulfur for High Quantum Yield and Excitation-Independent Emission. *Angewandte Chemie International Edition*, *52*(30), 7800–7804. https://doi.org/10.1002/anie.201301114
86. Qu, D., Zheng, M., Zhang, L., Zhao, H., Xie, Z., Jing, X., Haddad, R. E., Fan, H., & Sun, Z. (2014). Formation mechanism and optimization of highly luminescent N-doped graphene quantum dots. *Scientific Reports*, *4*(1). https://doi.org/10.1038/srep05294
87. Sahu, S., Behera, B., Maiti, T. K., & Mohapatra, S. (2012). Simple one-step synthesis of highly luminescent carbon dots from orange juice: application as excellent bio-imaging agents. *Chemical Communications*, *48*(70), 8835. https://doi.org/10.1039/c2cc33796g
88. Kalita, H., Mohapatra, J., Pradhan, L., Mitra, A., Bahadur, D., & Aslam, M. (2016). Efficient synthesis of rice based graphene quantum dots and their fluorescent properties. *RSC Advances*, *6*(28), 23518–23524. https://doi.org/10.1039/c5ra25706a
89. Hsu, P. C., Shih, Z. Y., Lee, C. H., & Chang, H. T. (2012). Synthesis and analytical applications of photoluminescent carbon nanodots. *Green Chemistry*, *14*(4), 917. https://doi.org/10.1039/c2gc16451e
90. Wei, J., Shen, J., Zhang, X., Guo, S., Pan, J., Hou, X., Zhang, H., Wang, L., & Feng, B. (2013). Simple one-step synthesis of water-soluble fluorescent carbon dots derived from paper ash. *RSC Advances*, *3*(32), 13119. https://doi.org/10.1039/c3ra41751d
91. Sharma, V., Tiwari, P., & Mobin, S. M. (2017). Sustainable carbon-dots: recent advances in green carbon dots for sensing and bioimaging. *Journal of Materials Chemistry B*, *5*(45), 8904–8924. https://doi.org/10.1039/c7tb02484c
92. Wang, Y., & Hu, A. (2014). Carbon quantum dots: synthesis, properties and applications. *Journal of Materials Chemistry C*, *2*(34), 6921. https://doi.org/10.1039/c4tc00988f
93. Hu, S. (2016). Tuning optical properties and photocatalytic activities of carbon-based "quantum dots" through their surface groups. *The Chemical Record*, *16*(1), 219-230.
94. Zhou, J., Zhou, H., Tang, J., Deng, S., Yan, F., Li, W., & Qu, M. (2016). Carbon dots doped with heteroatoms for fluorescent bioimaging: a review. *Microchimica Acta*, *184*(2), 343–368. https://doi.org/10.1007/s00604-016-2043-9

95. Yuan, F., Li, S., Fan, Z., Meng, X., Fan, L., & Yang, S. (2016). Shining carbon dots: Synthesis and biomedical and optoelectronic applications. *Nano Today*, *11*(5), 565–586. https://doi.org/10.1016/j.nantod.2016.08.006
96. Lu, S., Sui, L., Liu, J., Zhu, S., Chen, A., Jin, M., & Yang, B. (2017). Near-Infrared Photoluminescent Polymer-Carbon Nanodots with Two-Photon Fluorescence. *Advanced Materials*, *29*(15), 1603443. https://doi.org/10.1002/adma.201603443
97. Sun, X., & Lei, Y. (2017). Fluorescent carbon dots and their sensing applications. *TrAC Trends in Analytical Chemistry*, *89*, 163–180. https://doi.org/10.1016/j.trac.2017.02.001
98. Macairan, J. R., Jaunky, D. B., Piekny, A., & Naccache, R. (2019). Intracellular ratiometric temperature sensing using fluorescent carbon dots. *Nanoscale Advances*, *1*(1), 105–113. https://doi.org/10.1039/c8na00255j
99. Kong, B., Zhu, A., Ding, C., Zhao, X., Li, B., & Tian, Y. (2012). Carbon Dot-Based Inorganic-Organic Nanosystem for Two-Photon Imaging and Biosensing of pH Variation in Living Cells and Tissues. *Advanced Materials*, *24*(43), 5844–5848. https://doi.org/10.1002/adma.201202599
100. Liu, Q., Zhang, N., Shi, H., Ji, W., Guo, X., Yuan, W., & Hu, Q. (2018). One-step microwave synthesis of carbon dots for highly sensitive and selective detection of copper ions in aqueous solution. *New Journal of Chemistry*, *42*(4), 3097–3101. https://doi.org/10.1039/c7nj05000c
101. Li, X., Zheng, Y., Tang, Y., Chen, Q., Gao, J., Luo, Q., & Wang, Q. (2019). Efficient and visual monitoring of cerium (III) ions by green-fluorescent carbon dots and paper-based sensing. *Spectrochimica Acta Part A: Molecular and Biomolecular Spectroscopy*, *206*, 240–245. https://doi.org/10.1016/j.saa.2018.08.021
102. Zhang, J., Yuan, Y., Liang, G., & Yu, S. H. (2015). Scale-Up Synthesis of Fragrant Nitrogen-Doped Carbon Dots from Bee Pollens for Bioimaging and Catalysis. *Advanced Science*, *2*(4), 1500002. https://doi.org/10.1002/advs.201500002
103. Yuan, Y., Guo, B., Hao, L., Liu, N., Lin, Y., Guo, W., Li, X., & Gu, B. (2017). Doxorubicin-loaded environmentally friendly carbon dots as a novel drug delivery system for nucleus targeted cancer therapy. *Colloids and Surfaces B: Biointerfaces*, *159*, 349–359. https://doi.org/10.1016/j.colsurfb.2017.07.030
104. Yang, S. T., Cao, L., Luo, P. G., Lu, F., Wang, X., Wang, H., Meziani, M. J., Liu, Y., Qi, G., & Sun, Y. P. (2009). Carbon Dots for Optical Imaging in Vivo. *Journal of the American Chemical Society*, *131*(32), 11308–11309. https://doi.org/10.1021/ja904843x

105. Ding, H., Cheng, L. W., Ma, Y. Y., Kong, J. L., & Xiong, H. M. (2013). Luminescent carbon quantum dots and their application in cell imaging. *New Journal of Chemistry*, *37*(8), 2515. https://doi.org/10.1039/c3nj00366c

106. Angamuthu, R., Rajendran, R., & Vairamuthu, R. (2018). Quick Microwave Assisted Synthesis and In Vitro Imaging Application of Oxygen Doped Fluorescent Carbon Dots. *Journal of Fluorescence*, *28*(4), 959–966. https://doi.org/10.1007/s10895-018-2259-7

107. Synthesis of carbon quantum dots by chemical vapor deposition approach for use in polymer solar cell as the electrode buffer layer. (2016). *Carbon N.Y*, *109*, 598–607. https://doi.org/10.1016/j.carbon.2016.08.058.

108. Essner, J. B., Kist, J. A., Polo-Parada, L., & Baker, G. A. (2018). Artifacts and Errors Associated with the Ubiquitous Presence of Fluorescent Impurities in Carbon Nanodots. *Chemistry of Materials*, *30*(6), 1878–1887. https://doi.org/10.1021/acs.chemmater.7b04446

109. Iijima, S. (1991). Helical microtubules of graphitic carbon. *Nature*, *354*(6348), 56–58. https://doi.org/10.1038/354056a0

110. Ugarte, D. (1992). Curling and closure of graphitic networks under electron-beam irradiation. *Nature*, *359*(6397), 707–709. https://doi.org/10.1038/359707a0

111. Medranda, D., Borowiec, J., Zhang, X., Wang, S., Yan, K., Zhang, J., He, Y., Ivaturi, S., & Boi, F. S. (2018). Ferromagnetically filled carbon nano-onions: the key role of sulfur in dimensional, structural and electric control. *Royal Society Open Science*, *5*(1), 170981. https://doi.org/10.1098/rsos.170981

112. Han, F. D., Yao, B., & Bai, Y. J. (2011). Preparation of Carbon Nano-Onions and Their Application as Anode Materials for Rechargeable Lithium-Ion Batteries. *The Journal of Physical Chemistry C*, *115*(18), 8923–8927. https://doi.org/10.1021/jp2007599

113. Mohapatra, D., Badrayyana, S., & Parida, S. (2016). Facile wick-and-oil flame synthesis of high-quality hydrophilic onion-like carbon nanoparticles. *Materials Chemistry and Physics*, *174*, 112–119. https://doi.org/10.1016/j.matchemphys.2016.02.057

114. Katcho, N. A., Urones-Garrote, E., Avila-Brande, D., Gomez-Herrero, A., Urbonaite, S., Csillag, S., Lomba, E., Agullo-Rueda, F., Landa-Canovas, A. R., & Otero-Diaz, L. C. (2007). Carbon Hollow Nanospheres from Chlorination of Ferrocene. *ChemInform*, *38*(30). https://doi.org/10.1002/chin.200730192

115. Lian, W., Song, H., Chen, X., Li, L., Huo, J., Zhao, M., & Wang, G. (2008). The transformation of acetylene black into onion-like hollow carbon nanoparticles at 1000°C

using an iron catalyst. *Carbon*, *46*(3), 525–530. https://doi.org/10.1016/j.carbon.2007.12.024

116. Ma, Y., Hu, Z., Huo, K., Lu, Y., Hu, Y., Liu, Y., Hu, J., & Chen, Y. (2005). A practical route to the production of carbon nanocages. *Carbon*, *43*(8), 1667–1672. https://doi.org/10.1016/j.carbon.2005.02.004

117. Zhang, C., Li, J., Liu, E., He, C., Shi, C., Du, X., Hauge, R. H., & Zhao, N. (2012). Synthesis of hollow carbon nano-onions and their use for electrochemical hydrogen storage. *Carbon*, *50*(10), 3513–3521. https://doi.org/10.1016/j.carbon.2012.03.019

118. Chen, X., Deng, F., Wang, J., Yang, H., Wu, G., Zhang, X., Peng, J., & Li, W. (2001). New method of carbon onion growth by radio-frequency plasma-enhanced chemical vapor deposition. *Chemical Physics Letters*, *336*(3–4), 201–204. https://doi.org/10.1016/s0009-2614(01)00085-9

119. Du, J., Zhao, R., & Zhu, Z. (2011). A facile approach for synthesis and *in situ* modification of onion-like carbon with molybdenum carbide. *Physica Status Solidi (a)*, *208*(4), 878–881. https://doi.org/10.1002/pssa.201026646

120. Donath, E., Sukhorukov, G. B., Caruso, F., Davis, S. A., & Möhwald, H. (1998). Novel Hollow Polymer Shells by Colloid-Templated Assembly of Polyelectrolytes. *Angewandte Chemie International Edition*, *37*(16), 2201–2205. https://doi.org/10.1002/(sici)1521-3773(19980904)

121. Lei, Z., Chen, Z., & Zhao, X. S. (2010). Growth of Polyaniline on Hollow Carbon Spheres for Enhancing Electrocapacitance. *The Journal of Physical Chemistry C*, *114*(46), 19867–19874. https://doi.org/10.1021/jp1084026

122. Han, F. D., Yao, B., & Bai, Y. J. (2011). Preparation of Carbon Nano-Onions and Their Application as Anode Materials for Rechargeable Lithium-Ion Batteries. *The Journal of Physical Chemistry C*, *115*(18), 8923–8927. https://doi.org/10.1021/jp2007599

123. Wang, Y., Yan, F., Liu, S. W., Tan, A. Y. S., Song, H., Sun, X. W., & Yang, H. Y. (2013). Onion-like carbon matrix supported Co3O4 nanocomposites: a highly reversible anode material for lithium ion batteries with excellent cycling stability. *Journal of Materials Chemistry A*, *1*(17), 5212. https://doi.org/10.1039/c3ta10559h

124. Wang, Y., Han, Z. J., Yu, S. F., Song, R. R., Song, H. H., Ostrikov, K. K., & Yang, H. Y. (2013). Core-leaf onion-like carbon/MnO2 hybrid nano-urchins for rechargeable lithium-ion batteries. *Carbon*, *64*, 230–236. https://doi.org/10.1016/j.carbon.2013.07.057

125. Wang, M. S., Golberg, D., & Bando, Y. (2010). Carbon "Onions" as Point Electron Sources. *ACS Nano*, *4*(8), 4396–4402. https://doi.org/10.1021/nn1013353

126. Dissertation Summaries and Abstracts; The Seymour Fisher Outstanding Body Image Dissertation Annual Award. (2010). *Body Image*, *7*(1), 94. https://doi.org/10.1016/s1740-1445(09)00124-7

127. McDonough, J. K., & Gogotsi, Y. (2013). Carbon Onions: Synthesis and Electrochemical Applications. *Interface Magazine*, *22*(3), 61–66. https://doi.org/10.1149/2.f05133if

128. Ghosh, M., Sonkar, S. K., Saxena, M., & Sarkar, S. (2011). Life Cycle Imaging: Carbon Nano-onions for Imaging the Life Cycle of Drosophila Melanogaster (Small 22/2011). *Small*, *7*(22), 3169. https://doi.org/10.1002/smll.201190085

129. Georgakilas, V., Guldi, D. M., Signorini, R., Bozio, R., & Prato, M. (2003). Organic Functionalization and Optical Properties of Carbon Onions. *Journal of the American Chemical Society*, *125*(47), 14268–14269. https://doi.org/10.1021/ja0342805

130. Singh, V. (2018). Natural source derived carbon nano-onions as electrode material for sensing applications. *Diamond and Related Materials*, *87*, 202–207. https://doi.org/10.1016/j.diamond.2018.06.007

131. Mohapatra, D., Badrayyana, S., & Parida, S. (2016). Facile wick-and-oil flame synthesis of high-quality hydrophilic onion-like carbon nanoparticles. *Materials Chemistry and Physics*, *174*, 112–119. https://doi.org/10.1016/j.matchemphys.2016.02.057

132. Dhand, V., Prasad, J. S., Rao, M. V., Bharadwaj, S., Anjaneyulu, Y., & Jain, P. K. (2013). Flame synthesis of carbon nano onions using liquefied petroleum gas without catalyst. *Materials Science and Engineering: C*, *33*(2), 758–762. https://doi.org/10.1016/j.msec.2012.10.029

133. Levy, L., Chaudhuri, I. S., Krueger, N., & McCunney, R. J. (2012). Does Carbon Black Disaggregate in Lung Fluid? A Critical Assessment. *Chemical Research in Toxicology*, *25*(10), 2001–2006. https://doi.org/10.1021/tx300160z

134. Mohapatra, J., Ananthoju, B., Nair, V., Mitra, A., Bahadur, D., Medhekar, N., & Aslam, M. (2018). Enzymatic and non-enzymatic electrochemical glucose sensor based on carbon nano-onions. *Applied Surface Science*, *442*, 332–341. https://doi.org/10.1016/j.apsusc.2018.02.124

135. Tripathi, K. M., Tran, T. S., Kim, Y. J., & Kim, T. (2017). Green Fluorescent Onion-Like Carbon Nanoparticles from Flaxseed Oil for Visible Light Induced Photocatalytic Applications and Label-Free Detection of Al(III) Ions. *ACS Sustainable Chemistry & Engineering*, *5*(5), 3982–3992. https://doi.org/10.1021/acssuschemeng.6b03182

136. Tripathi, K. M., Bhati, A., Singh, A., Gupta, N. R., Verma, S., Sarkar, S., & Sonkar, S. K. (2016). From the traditional way of pyrolysis to tunable photoluminescent water soluble carbon nano-onions for cell imaging and selective sensing of glucose. *RSC Advances*, *6*(44), 37319–37329. https://doi.org/10.1039/c6ra04030f

137. Choucair, M., & Stride, J. A. (2012). The gram-scale synthesis of carbon onions. *Carbon*, *50*(3), 1109–1115. https://doi.org/10.1016/j.carbon.2011.10.023

138. Ghosh, M., Sonkar, S. K., Saxena, M., & Sarkar, S. (2011). Carbon Nano-onions for Imaging the Life Cycle of Drosophila Melanogaster. *Small*, *7*(22), 3170–3177. https://doi.org/10.1002/smll.201101158

139. Sano, N., Wang, H., Alexandrou, I., Chhowalla, M., Teo, K. B. K., Amaratunga, G. A. J., & Iimura, K. (2002). Properties of carbon onions produced by an arc discharge in water. *Journal of Applied Physics*, *92*(5), 2783–2788. https://doi.org/10.1063/1.1498884

140. Alexandrou, I., Wang, H., Sano, N., & Amaratunga, G. A. J. (2004). Structure of carbon onions and nanotubes formed by arc in liquids. *The Journal of Chemical Physics*, *120*(2), 1055–1058. https://doi.org/10.1063/1.1629274

141. Kuznetsov, V. L., Chuvilin, A. L., Butenko, Y. V., Mal'kov, I. Y., & Titov, V. M. (1994). Onion-like carbon from ultra-disperse diamond. *Chemical Physics Letters*, *222*(4), 343–348. https://doi.org/10.1016/0009-2614(94)87072-1

142. Tomita, S., Sakurai, T., Ohta, H., Fujii, M., & Hayashi, S. (2001). Structure and electronic properties of carbon onions. *The Journal of Chemical Physics*, *114*(17), 7477–7482. https://doi.org/10.1063/1.1360197

143. Street, K., Marchetti, M., Vander Wal, R., & Tomasek, A. (2004). Evaluation of the Tribological behavior of Nano-Onions in Krytox 143AB. *Tribology Letters*, *16*(1/2), 143–149. https://doi.org/10.1023/b:tril.0000009724.01711.f4

144. Gan, Y., & Banhart, F. (2008). The Mobility of Carbon Atoms in Graphitic Nanoparticles Studied by the Relaxation of Strain in Carbon Onions. *Advanced Materials*, *20*(24), 4751–4754. https://doi.org/10.1002/adma.200800574

145. Terrones, H., & Terrones, M. (1997). The transformation of polyhedral particles into graphitic onions. *Journal of Physics and Chemistry of Solids*, *58*(11), 1789–1796. https://doi.org/10.1016/s0022-3697(97)00067-x

146. Ugarte, D. (1995). Onion-like graphitic particles. *Carbon*, *33*(7), 989–993. https://doi.org/10.1016/0008-6223(95)00027-b

147. Khoei, A. R., & Khorrami, M. S. (2016). Mechanical properties of graphene oxide: A molecular dynamics study. *Fullerenes, Nanotubes and Carbon Nanostructures*, *24*(9), 594–603. https://doi.org/10.1080/1536383x.2016.1208180

148. Bartelmess, J., & Giordani, S. (2014). Carbon nano-onions (multi-layer fullerenes): chemistry and applications. *Beilstein Journal of Nanotechnology*, *5*, 1980–1998. https://doi.org/10.3762/bjnano.5.207

149. Mongwe, T. H., Matsoso, B. J., Mutuma, B. K., Coville, N. J., & Maubane, M. S. (2018). Synthesis of chain-like carbon nano-onions by a flame assisted pyrolysis technique using different collecting plates. *Diamond and Related Materials*, *90*, 135–143. https://doi.org/10.1016/j.diamond.2018.10.002

150. Schiros, T., Nordlund, D., Palova, L., Zhao, L., Levendorf, M., Jaye, C., Reichman, D., Park, J., Hybertsen, M., & Pasupathy, A. (2016). Atomistic Interrogation of B–N Co-dopant Structures and Their Electronic Effects in Graphene. *ACS Nano*, *10*(7), 6574–6584. https://doi.org/10.1021/acsnano.6b01318

151. Wang, G., Ling, Y., Wang, H., Xihong, L., & Li, Y. (2014). Chemically modified nanostructures for photoelectrochemical water splitting. *Journal of Photochemistry and Photobiology C: Photochemistry Reviews*, *19*, 35–51. https://doi.org/10.1016/j.jphotochemrev.2013.10.006

152. Zhu, J., Holmen, A., & Chen, D. (2013). Carbon Nanomaterials in Catalysis: Proton Affinity, Chemical and Electronic Properties, and their Catalytic Consequences. *ChemCatChem*, *5*(2), 378–401. https://doi.org/10.1002/cctc.201200471

153. Panchakarla, L., Govindaraj, A., & Rao, C. (2010). Boron- and nitrogen-doped carbon nanotubes and graphene. *Inorganica Chimica Acta*, *363*(15), 4163–4174. https://doi.org/10.1016/j.ica.2010.07.057

154. Zhang, Y., Reed, A., & Kim, D. Y. (2018). Nitrogen doped carbon nano-onions as efficient and robust electrocatalysts for oxygen reduction reactions. *Current Applied Physics*, *18*(4), 417–423. https://doi.org/10.1016/j.cap.2018.02.001

155. Chatterjee, K., Ashokkumar, M., Gullapalli, H., Gong, Y., Vajtai, R., Thanikaivelan, P., & Ajayan, P. M. (2018). Nitrogen-rich carbon nano-onions for oxygen reduction reaction. *Carbon*, *130*, 645–651. https://doi.org/10.1016/j.carbon.2018.01.052

156. Yang, Y., Zhang, J., Zhuang, J., & Wang, X. (2015). Synthesis of nitrogen-doped carbon nanostructures from polyurethane sponge for bioimaging and catalysis. *Nanoscale*, *7*(29), 12284–12290. https://doi.org/10.1039/c5nr03481g

157. Wang, L., Yu, P., Zhao, L., Tian, C., Zhao, D., Zhou, W., Yin, J., Wang, R., & Fu, H. (2014). B and N isolate-doped graphitic carbon nanosheets from nitrogen-containing ion-exchanged resins for enhanced oxygen reduction. *Scientific Reports*, *4*(1). https://doi.org/10.1038/srep05184

158. Jain, D., Mamtani, K., Gustin, V., Gunduz, S., Celik, G., Waluyo, I., Hunt, A., Co, A. C., & Ozkan, U. S. (2018). Enhancement in Oxygen Reduction Reaction Activity of Nitrogen-Doped Carbon Nanostructures in Acidic Media through Chloride-Ion Exposure. *ChemElectroChem*, *5*(14), 1966–1975. https://doi.org/10.1002/celc.201800134

159. Sa, Y. J., Park, C., Jeong, H. Y., Park, S. H., Lee, Z., Kim, K. T., Park, G. G., & Joo, S. H. (2014). Carbon Nanotubes/Heteroatom-Doped Carbon Core-Sheath Nanostructures as Highly Active, Metal-Free Oxygen Reduction Electrocatalysts for Alkaline Fuel Cells. *Angewandte Chemie International Edition*, *53*(16), 4102–4106. https://doi.org/10.1002/anie.201307203

160. Mamtani, K., & Ozkan, U. S. (2014). Heteroatom-Doped Carbon Nanostructures as Oxygen Reduction Reaction Catalysts in Acidic Media: An Overview. *Catalysis Letters*, *145*(1), 436–450. https://doi.org/10.1007/s10562-014-1434-y

161. Chmiola, J., Yushin, G., Gogotsi, Y., Portet, C., Simon, P., & Taberna, P. L. (2006). Anomalous Increase in Carbon Capacitance at Pore Sizes Less Than 1 Nanometer. *Science*, *313*(5794), 1760–1763. https://doi.org/10.1126/science.1132195

162. Pandolfo, A., & Hollenkamp, A. (2006). Carbon properties and their role in supercapacitors. *Journal of Power Sources*, *157*(1), 11–27. https://doi.org/10.1016/j.jpowsour.2006.02.065

163. Pech, D., Brunet, M., Durou, H., Huang, P., Mochalin, V., Gogotsi, Y., Taberna, P. L., & Simon, P. (2010). Ultrahigh-power micrometre-sized supercapacitors based on onion-like carbon. *Nature Nanotechnology*, *5*(9), 651–654. https://doi.org/10.1038/nnano.2010.162

164. Simon, P., & Gogotsi, Y. (2008). Materials for electrochemical capacitors. *Nature Materials*, *7*(11), 845–854. https://doi.org/10.1038/nmat2297

165. Simon, P., & Gogotsi, Y. (2010). Charge storage mechanism in nanoporous carbons and its consequence for electrical double layer capacitors. *Philosophical Transactions of the Royal Society A: Mathematical, Physical and Engineering Sciences*, *368*(1923), 3457–3467. https://doi.org/10.1098/rsta.2010.0109

166. Yu, D., Nagelli, E., Du, F., & Dai, L. (2010). Metal-Free Carbon Nanomaterials Become More Active than Metal Catalysts and Last Longer. *The Journal of Physical Chemistry Letters*, *1*(14), 2165–2173. https://doi.org/10.1021/jz100533t

167. Becquerel, A. E. (1839). Electrode Effect under the Influence of Solar Radiation. *Acad. Sci., Paris, 9*, 561-567.

168. Jordan, D. C., & Kurtz, S. R. (2011). Photovoltaic Degradation Rates-an Analytical Review. *Progress in Photovoltaics: Research and Applications*, *21*(1), 12–29. https://doi.org/10.1002/pip.1182

169. Fraas, L. M. (2014). Low-Cost Solar Electric Power. *Springer Cham Heidelberg New York Dordrecht London*, 1–12. https://doi.org/10.1007/978-3-319-07530-3

170. O'Regan, B., & Grätzel, M. (1991). A low-cost, high-efficiency solar cell based on dye-sensitized colloidal TiO2 films. *Nature*, *353*(6346), 737–740. https://doi.org/10.1038/353737a0

171. Gong, J., Liang, J., & Sumathy, K. (2012). Review on dye-sensitized solar cells (DSSCs): Fundamental concepts and novel materials. *Renewable and Sustainable Energy Reviews*, *16*(8), 5848–5860. https://doi.org/10.1016/j.rser.2012.04.044

172. Nogueira, A., Longo, C., & de Paoli, M. A. (2004). Polymers in dye sensitized solar cells: overview and perspectives. *Coordination Chemistry Reviews*, *248*(13–14), 1455–1468. https://doi.org/10.1016/j.ccr.2004.05.018

173. Mohammad Bagher, A. (2015). Types of Solar Cells and Application. *American Journal of Optics and Photonics*, *3*(5), 94. https://doi.org/10.11648/j.ajop.20150305.17

174. Mir, N., & Salavati-Niasari, M. (2012). Photovoltaic properties of corresponding dye sensitized solar cells: Effect of active sites of growth controller on TiO2 nanostructures. *Solar Energy*, *86*(11), 3397–3404. https://doi.org/10.1016/j.solener.2012.08.016

175. Sugathan, V., John, E., & Sudhakar, K. (2015). Recent improvements in dye sensitized solar cells: A review. *Renewable and Sustainable Energy Reviews*, *52*, 54–64. https://doi.org/10.1016/j.rser.2015.07.076

176. Franco, G., Gehring, J., Peter, L. M., Ponomarev, E. A., & Uhlendorf, I. (1999). Frequency-Resolved Optical Detection of Photoinjected Electrons in Dye-Sensitized Nanocrystalline Photovoltaic Cells. *The Journal of Physical Chemistry B*, *103*(4), 692–698. https://doi.org/10.1021/jp984060r

177. Cherepy, N. J., Smestad, G. P., Grätzel, M., & Zhang, J. Z. (1997). Ultrafast Electron Injection: Implications for a Photoelectrochemical Cell Utilizing an Anthocyanin Dye-

Sensitized TiO_2 Nanocrystalline Electrode. *The Journal of Physical Chemistry B*, *101*(45), 9342–9351. https://doi.org/10.1021/jp972197w

178. Peter, L. (1999). Intensity dependence of the electron diffusion length in dye-sensitised nanocrystalline TiO2 photovoltaic cells. *Electrochemistry Communications*, *1*(12), 576–580. https://doi.org/10.1016/s1388-2481(99)00120-4

179. Peter, L., & Wijayantha, K. (2000). Electron transport and back reaction in dye sensitised nanocrystalline photovoltaic cells. *Electrochimica Acta*, *45*(28), 4543–4551. https://doi.org/10.1016/s0013-4686(00)00605-8

180. Fredin, K., Nissfolk, J., & Hagfeldt, A. (2005). Brownian dynamics simulations of electrons and ions in mesoporous films. *Solar Energy Materials and Solar Cells*, *86*(2), 283–297. https://doi.org/10.1016/j.solmat.2004.07.010

181. Papageorgiou, N., Grätzel, M., & Infelta, P. (1996). On the relevance of mass transport in thin layer nanocrystalline photoelectrochemical solar cells. *Solar Energy Materials and Solar Cells*, *44*(4), 405–438. https://doi.org/10.1016/s0927-0248(96)00050-5

182. Wei, D. (2010). Dye Sensitized Solar Cells. *International Journal of Molecular Sciences*, *11*(3), 1103–1113. https://doi.org/10.3390/ijms11031103

183. Oelhafen, P., & Schüler, A. (2005). Nanostructured materials for solar energy conversion. *Solar Energy*, *79*(2), 110–121. https://doi.org/10.1016/j.solener.2004.11.004

184. Brennan, L. J., Byrne, M. T., Bari, M., & Gun'ko, Y. K. (2011). Carbon Nanomaterials for Dye-Sensitized Solar Cell Applications: A Bright Future. *Advanced Energy Materials*, *1*(4), 472–485. https://doi.org/10.1002/aenm.201100136

185. Kay, A., & Grätzel, M. (1996). Low cost photovoltaic modules based on dye sensitized nanocrystalline titanium dioxide and carbon powder. *Solar Energy Materials and Solar Cells*, *44*(1), 99–117. https://doi.org/10.1016/0927-0248(96)00063-3

186. Murakami, T. N., Ito, S., Wang, Q., Nazeeruddin, M. K., Bessho, T., Cesar, I., Liska, P., Humphry-Baker, R., Comte, P., PéChy, P., & GräTzel, M. (2006). Highly Efficient Dye-Sensitized Solar Cells Based on Carbon Black Counter Electrodes. *Journal of The Electrochemical Society*, *153*(12), A2255. https://doi.org/10.1149/1.2358087

187. Novoselov, K. S., Geim, A. K., Morozov, S. V., Jiang, D., Zhang, Y., Dubonos, S. V., Grigorieva, I. V., & Firsov, A. A. (2004). Electric Field Effect in Atomically Thin Carbon Films. *Science*, *306*(5696), 666–669. https://doi.org/10.1126/science.1102896

188. Yue, G., Wu, J., Xiao, Y., Lin, J., Huang, M., Fan, L., & Yao, Y. (2013). A dye-sensitized solar cell based on PEDOT:PSS counter electrode. *Chinese Science Bulletin*, *58*(4–5), 559–566. https://doi.org/10.1007/s11434-012-5352-3

189. Huang, Z., Liu, X., Li, K., Li, D., Luo, Y., Li, H., Song, W., Chen, L., & Meng, Q. (2007). Application of carbon materials as counter electrodes of dye-sensitized solar cells. *Electrochemistry Communications*, *9*(4), 596–598. https://doi.org/10.1016/j.elecom.2006.10.028

190. Li, H., Tang, Q., Meng, Y., He, B., & Yu, L. (2016). Dissolution-resistant platinum alloy counter electrodes for stable dye-sensitized solar cells. *Electrochimica Acta*, *190*, 409–418. https://doi.org/10.1016/j.electacta.2015.12.168

191. Suzuki, K., Yamaguchi, M., Kumagai, M., & Yanagida, S. (2003). Application of Carbon Nanotubes to Counter Electrodes of Dye-sensitized Solar Cells. *Chemistry Letters*, *32*(1), 28–29. https://doi.org/10.1246/cl.2003.28

192. Trancik, J. E., Barton, S. C., & Hone, J. (2008). Transparent and Catalytic Carbon Nanotube Films. *Nano Letters*, *8*(4), 982–987. https://doi.org/10.1021/nl071945i

193. Hino, T., Ogawa, Y., & Kuramoto, N. (2006). Preparation of functionalized and non-functionalized fullerene thin films on ITO glasses and the application to a counter electrode in a dye-sensitized solar cell. *Carbon*, *44*(5), 880–887. https://doi.org/10.1016/j.carbon.2005.10.027

194. Hong, W., Xu, Y., Lu, G., Li, C., & Shi, G. (2008). Transparent graphene/PEDOT–PSS composite films as counter electrodes of dye-sensitized solar cells. *Electrochemistry Communications*, *10*(10), 1555–1558. https://doi.org/10.1016/j.elecom.2008.08.007

195. Sugathan, V., John, E., & Sudhakar, K. (2015b). Recent improvements in dye sensitized solar cells: A review. *Renewable and Sustainable Energy Reviews*, *52*, 54–64. https://doi.org/10.1016/j.rser.2015.07.076

196. Pang, B., Zhang, M., Zhou, C., Dong, H., Ma, S., Shi, Y., Sun, Q., Li, F., Yu, L., & Dong, L. (2020). Nitrogen-Doped Carbon Nano-Onions Decorated on Graphene Network: A Novel All-Carbon Composite Counter Electrode for Dye-Sensitized Solar Cell with a 10.28% Power Conversion Efficiency. *Solar RRL*, *4*(9), 2000263. https://doi.org/10.1002/solr.202000263

197. Essner, J. B., Kist, J. A., Polo-Parada, L., & Baker, G. A. (2018). Artifacts and Errors Associated with the Ubiquitous Presence of Fluorescent Impurities in Carbon Nanodots. *Chemistry of Materials*, *30*(6), 1878–1887. https://doi.org/10.1021/acs.chemmater.7b04446

198. Yuan, F., Li, S., Fan, Z., Meng, X., Fan, L., & Yang, S. (2016). Shining carbon dots: Synthesis and biomedical and optoelectronic applications. Nano Today, 11(5), 565–586. https://doi.org/10.1016/j.nantod.2016.08.00.

199. Innocenzi, P., Malfatti, L., & Carboni, D. (2015). Graphene and carbon nanodots in mesoporous materials: an interactive platform for functional applications. *Nanoscale*, *7*(30), 12759–12772. https://doi.org/10.1039/c5nr03773e

200. D. Zhou, D. Li, P. Jing, Y. Zhai, D. Shen, S. Qu, A.L. Rogach, (2017). Conquering aggregation-induced solid-state luminescence quenching of carbon dots through a carbon dots-triggered silica gelation process. *29(4)*, 1779–1787.

201. Liu, S., Yang, B., Zhou, J., & Song, H. (2019). Nitrogen-rich carbon-onion-constructed nanosheets: an ultrafast and ultrastable dual anode material for sodium and potassium storage. *Journal of Materials Chemistry A*, *7*(31), 18499–18509. https://doi.org/10.1039/c9ta04699b

202. Gu, D., Bongard, H., Deng, Y., Feng, D., Wu, Z., Fang, Y., Mao, J., Tu, B., Schüth, F., & Zhao, D. (2010). An Aqueous Emulsion Route to Synthesize Mesoporous Carbon Vesicles and Their Nanocomposites. *Advanced Materials*, *22*(7), 833–837. https://doi.org/10.1002/adma.200902550

203. Meng, X., Yu, C., Song, X., Liu, Y., Liang, S., Liu, Z., Hao, C., & Qiu, J. (2015). Nitrogen-Doped Graphene Nanoribbons with Surface Enriched Active Sites and Enhanced Performance for Dye-Sensitized Solar Cells. *Advanced Energy Materials*, *5*(11), 1500180. https://doi.org/10.1002/aenm.201500180

204. Balamurugan, J., Thanh, T. D., Kim, N. H., & Lee, J. H. (2015). Nitrogen-Doped Graphene Nanosheets with FeN Core-Shell Nanoparticles as High-Performance Counter Electrode Materials for Dye-Sensitized Solar Cells. *Advanced Materials Interfaces*, *3*(1), 1500348. https://doi.org/10.1002/admi.201500348

Chapter 3

Characterization techniques

3.1 Introduction

The methods utilized to characterize the materials produced for this research project are presented in this chapter.

Almost all characterisation techniques require sample preparation prior to analysis. The optical, physical, and chemical properties of the products were examined in terms of morphology, photoluminescence, absorption, elemental composition, thermal stability, surface functional groups, and crystallinity.

3.2. Characterization techniques used for the prepared NCdots, OLCNs and NCdots: OLCNs composites synthesized in this study.

3.2.1. Scanning electron microscopy analysis

SEM was used to examine the external structural morphology of the CNOs as they were created (SEM) [1].

The ZEISS Sigma 300 VP with a field emission gun was used to examine the morphological structure of as-synthesised CNOs in this investigation. The instrument was run at 30 kV with a 0.63 nA spot size. To prepare the samples for analysis, a spatula tip (2 mg) of CNOs sample was deposited onto a carbon tape mounted to a metallic sample stub. The samples were sputter coated with gold palladium to reduce the interference of the sample with electron beam (charging).

3.2.2. Transmission electron microscopy analysis

Transmission electron microscopy (TEM) was used to study the synthetic materials' inherent structural characteristics. When using TEM, a high-powered electron beam is used, and magnification may reach 0.5 nm when the beam is accelerated at 120 kV [2].

The FEI Tecnai T12 transmission electron microscope was used in this study to examine the intrinsic morphological traits and characteristics of NCdots, OLCNs, and NCdots: OLCNs composites. The following steps were used to prepare the sample for analysis. First, 5 mL of distilled water and 1 milligram of the material were combined in a glass container. To obtain

a homogeneous sample suspension, the mixture was then sonicated for 10 minutes, which disseminated the sample's contents throughout the solvent. The suspension was then pipetted onto a copper grid with a 200-mesh size (provided by Structure Probe, Inc. (SPI)). The grid was dried at room temperature in air.

3.2.3. Powder X-ray diffraction analysis

All materials synthesized (NCdots, OLCNs, and NCdots: OLCNs composites) were analysed using a Bruker D2 Phaser powder X-ray diffraction (PXRD), which employed Cu-Kα irradiation and a 30 kV X-ray tube at a current of 30 mA across a $10° \leq 2\theta \leq 90°$ range. The samples were contained in a zero-background holder.

3.2.4. Laser Raman spectroscopy analysis

Laser Raman spectroscopy analysis (LRS) is a technique for characterizing materials that utilises unique vibrational and crystallographic information by comparing the relative intensities of the defective bands. One of the most effective techniques for characterizing carbonaceous material is Raman spectroscopy, which provides precise data on the size and level of functionalization of the as-prepared material. Photon energy dispersion in an electrochemical system and electronic states in the material provide this information [3-5]. With this information, it is possible to examine the material's photons and electrons more thoroughly. Characterization of sp^2 hybridized carbons such 0D fullerenes, 1D carbon nanotubes, 2D graphene, and 3D graphite is frequently done using LRS [6].

The D and D′ bands, which occur at 1350 cm^{-1} and 1620 cm^{-1}, respectively, including the G and G′ bands, which show at 1582 cm^{-1} and 2700 cm^{-1}, are commonly employed to characterize the Raman spectra of graphitic materials [7]. The G band is created by vibrations in the sp^2-hybridized framework, whereas the D band is caused by defects in the OLCNs lattice (sp^3-hybridized carbon) [8]. The structural characterization of graphitic materials can provide useful information concerning flaws, finite sizes of crystallites parallel and perpendicular to the hexagonal axis, and graphene layer stacking. Using an Olympus BX41 microscope attachment and a Lexel Model 95-SHG argon ion laser, Raman spectra were taken at 785 nm (red line laser) for NCdots and 514.5 nm (blue line laser) for the various as-synthesized OLCNs. The incident beam was focused onto the sample using a 100x objective (N.A = 0.90). The backscattered light was directed onto a liquid nitrogen-cooled CCD

detector using a 600 lines/mm grating. Software called LabSpec v5 was utilized to record the signal. All samples took about 90 seconds to acquire.

3.2.5. Fourier transform infrared spectroscopy analysis

Quantifying a range of infrared-absorbing components is made a lot easier with Fourier transform infrared spectroscopy (FTIR). This study employed a Bruker Tensor 27 FT-IR analyzer to monitor the presence of unique functional groups in each sample. These investigations produced spectra that functioned as distinct chemical fingerprints that could be recognized from other compounds' absorption patterns.

3.2.6. Thermo-gravimetric analysis

In a controlled setting with a gaseous atmosphere, thermogravimetric analysis (TGA) measures the change in mass of a material as a function of temperature (air and nitrogen).

Thermal stability data was obtained using a Perkin Elmer TGA Simultaneous Analyzer STA 6000 Pyris Series for TGA and Differential Thermogravimetric Analysis (DTA) 6000. The TGA data was utilized to identify any residual mass from the as-synthesised NCdots, OLCNs, and NCdots: OLCNs composites after heating in air. In each standard run, an estimated quantity of roughly 10 mg was added into a high-temperature alumina sample cup. In the furnace chamber of the analyzer, the alumina sample cup was supported and kept in place while being heated in air at a rate of 10°C per minute from 35 to 900°C. The machine was purged with N_2 gas (20 mL/min) to generate an inert atmosphere while flushing at 35°C for 2 minutes. All samples were then tested in the open air.

3.2.7. Ultraviolet visible absorption analysis

Ultraviolet visible (UV-vis) spectroscopy is a spectroscopic method for determining solution concentrations, chemical structures, purity, and nanoparticle sizes [9]. The UV-vis spectrophotometer (Agilent Technologies Cary (100) Series) was used to examine the synthesised materials' absorption wavelength. For measurements, a precise mass (mg) of the substance to be examined was dispersed in distilled water to produce a defined concentration, which was then studied at 350 nanometers (nm) and measurements collected between 275 and 800 nm. A Varian UV-vis 50 conc. spectrophotometer was used to assess the absorption characteristics of the as-prepared OLCNs generated.

3.2.8. Photoluminescence spectroscopy analysis

The fluorescence characteristics of the as-synthesised compounds were investigated using photoluminescence spectroscopy (PL). With a 5 nm slit width in solution and a wavelength range of 300-700 nm, the emission spectra were acquired using Cary Eclipse software in 10 mm fluorescent quartz cells. Varian Cary Eclipse fluorescence spectrophotometer provided the PL data.

3.2.9. Time-correlated single-photon counting analysis

The simultaneous measurement character of a molecule's radiative emission of light from a sample following stimulation was measured. A steady-state measurement of fluorescence emission (intensity vs wavelength) yielded the relative and average values. The fluorescence lifespan provided an absolute (concentration-independent) metric and enables for the creation of a dynamic image of the fluorescence, both of which contribute to its popularity [10]. Time-correlated single-photon counting is the method that is the most accurate for calculating fluorescence lifetimes. Unlike certain analogue measuring techniques, it is a digital methodology with well-defined (Poisson) statistics that is unaffected by variations in source intensity. Time-correlated single-photon counting (TCSPC) is based on detecting individual photons arriving after optical stimulation of a material.

A pulsed excitation source was employed (laser or LED) [11]. A double-exponential function was used to fit the PL decay curves for the NCdots in the aqueous phase, and average decay periods were computed. Additionally, steady-state PL measurements were made as a function of excitation wavelength using a CHIMERA spectrometer (Light Conversion) with an excitation wavelength of 377 nm.

3.2.10. Elemental Analyser analysis

The PerkinElmer 2400 Series II CHNS Elemental Analyzer (CHNS) System was used to analyze materials in this investigation, and the EA Data Manager software was employed herein to help streamline data collection and analysis.

3.2.11. X-ray photoelectron spectroscopy analysis

Using X-ray photoelectron spectroscopy (XPS), it was possible to determine the surface composition, elemental composition, and chemical bonding of the as-synthesised materials based on the electrons' binding energies. This method involves bombarding the material's

surface with X-rays to remove the photoelectrons. The spectra were analyzed using a Physical Electronics Quantum 2000 scanning ESCAlab 250Xi microprobe equipment with monochromatic Al k operating at 300 W. (1486.7 eV). For C 1s, N 1s, and O 1s, survey and high-resolution spectra were obtained at 285, 80, and 40, respectively.

The CasaXPS program was used to analyze and quantify the spectra, with the manufacturer's sensitivity factors. Subtraction of a linear background was used in the analysis, as well as charge reference to the 285 eV carbon signal. The spectra were matched using a set of line shapes with a width of 0.5-12.5 eV that are 70% Gaussian and 30% Lorentzian (GL30). The sample preparation and analysis were done at National Metrology Institute of South Africa (NMISA), CSIR. Using a 0.026 ° step size, samples were scanned throughout the 2 range from 10 to 90 °.

3.2.12. Brunauer-Emmett-Teller surface area analysis

Before analysis, 100 mg of the sample were degassed in nitrogen for 4 hours at 150 °C using a Micromeritics Flow Prep 060 sample degasser. The gas sorption was carried out in liquid nitrogen (-195 °C).

3.2.13. Atomic Force Microscopy analysis

To measure the NCdots' surface topology, height, and roughness, atomic force microscopy (AFM) pictures were collected using a Multi-Mode v8 scanning probe microscope from Bruker. The AFM had a resolution of less than 1 nm [12–15]. In comparison to SEM and TEM, AFM not only gives two-dimensional (2D) pictures of Cdots from which the Cdots dimension may be estimated by counting the height of particles on the images at random, but also offers three-dimensional (3D) details about the material's surface shape.

A drop of the nanoparticle dispersion was applied to a freshly cut piece of mica substrate to take measurements. The surface topography was photographed following the evaporation of the water. The sample preparation and analysis were done at Mintek, Randburg.

3.2.14. Olympus fluorescent microscope analysis

An Olympus BX63 fluorescent microscope (OFM) was used to take the fluorescence microscopy pictures. The light source for fluorescence microscopy observations was a mercury lamp with a fluorescent filter. All experiments were performed at room temperature. For single particle imaging, NCdots were dropped with a spatula onto a polished microscope

glass petri dish. A modified wide field epifluorescence microscope was used to image single particles. A 500 nm long-pass dichroic mirror (Chroma 500 DCLP) was used to reflect a 488 nm argon laser beam that was directed onto the epi-illumination port of an inverted fluorescence microscope. The laser beam was then focused onto the rear aperture of a high numerical aperture objective inside the microscope.

3.2.15. Cyclic Voltammetry analysis

Using the electrochemical workstation and a three-electrode electrochemical cell, samples were measured using cyclic voltammetry (CV). In this study, the current was measured by sweeping the potential back and forth between the selected limits (from positive to negative and negative to positive).

3.2.16. Electrochemical impedance spectroscopy analysis

An effective method for examining interfacial characteristics connected to events at the electrode surface is electrochemical impedance spectroscopy (EIS). EIS is one of the most important electrochemical techniques, and ohms are the unit of measurement for a circuit's impedance (as resistance unit). Unlike the other electrochemical approach, the potentiometric technique's potential variations (vs. a reference electrode) at zero current are related to changes in the concentration of a target analyte. EMF, or electromotive force, is a measure of a cell's concentration. In a typical electrochemical cell, matter-electrode interactions (redox species) include the concentration of electroactive species, charge transfer, mass transfer, and resistance of the electrolyte from the bulk solution to the electrode surface. As illustrated in, each of these characteristics is represented by an electrical circuit consisting of resistances, capacitors, or constant phase components coupled in parallel or series to make an equivalent circuit [16]. Therefore, investigations into mass, charge, and diffusion processes might make use of the EIS. As a result, the EIS may examine innate material properties or specific processes that may have an impact on the conductance, resistance, or capacitance of an electrochemical system.

EIS has various benefits since it is a steady-state approach that uses tiny signal analysis and can explore signal relaxations across a wide range of applied frequency, from less than 1 mHz to larger than 1 MHz, utilizing commercially accessible electrochemical working stations (potentiostat) [17].

3.2.17. Linear sweep voltammetry analysis

Through linear sweep experiments, linear sweep voltammetry (LSV) voltammograms of the three-electrode system in electrolyte were produced. Then the Tafel plots were created.

In this study, all CV, EIS and LSV voltammograms were recorded by a potentiostat/galvanostat (BioLogic SP-300). Data acquisition EC Lab software was used in the instrument. The system is outfitted with a three-electrode system that includes a glassy carbon counter electrode, a platinum auxiliary electrode, and an Ag/AgCl reference electrode.

3.2.18. Photocurrent density-voltage analysis

Photovoltaic testing was performed on all produced DSSCs by measuring photocurrent and voltage (J-V) characteristics. The FF, which is a factor that is directly connected to the power conversion efficiency, was used to assess the overall performance of the cell (PCE or ɳ). The PCE is directly proportional to the FF and is hence directly related at a given incident light power (P_{light}) related by the equation below **(Eq. 1)**. A lower fill factors result in the cell's poor performance for the given incident light power [18].

$$\eta(\%) \equiv \frac{J_{mp}V_{mp}}{P_{light}} = \frac{FF J_{sc} V_{oc}}{P_{light}} x100, \ (\varepsilon \alpha FF) \ldots\ldots (1)$$

The photocurrent density-voltage (J-V) properties of each solar cell were assessed under 100 mW.cm^{-2} illumination using a solar simulator (150 W Xe lamp with 1.5 air mass filters and a source/measure unit) (HP 4141B DC). All testing and measurements were performed in typical settings at room temperature.

References

1. Reed, S. (2002). Optimization of wavelength daspersive x-ray spectrometry analysis conditions. *Journal of Research of the National Institute of Standards and Technology*, *107*(6), 497. https://doi.org/10.6028/jres.107.042
2. Masunda, H. (2015). Paper. *InTech World Journal.*, 3–34.
3. White, S. N. (2009). Laser Raman spectroscopy as a technique for identification of seafloor hydrothermal and cold seep minerals. *Chemical Geology*, *259*(3–4), 240–252. https://doi.org/10.1016/j.chemgeo.2008.11.008
4. Dresselhaus, M., Jorio, A., & Saito, R. (2010). Characterizing Graphene, Graphite, and Carbon Nanotubes by Raman Spectroscopy. *Annual Review of Condensed Matter Physics*, *1*(1), 89–108. https://doi.org/10.1146/annurev-conmatphys-070909-103919
5. Pimenta, M. A., Dresselhaus, G., Dresselhaus, M. S., Cançado, L. G., Jorio, A., & Saito, R. (2007). Studying disorder in graphite-based systems by Raman spectroscopy. *Phys. Chem. Chem. Phys.*, *9*(11), 1276–1290. https://doi.org/10.1039/b613962k
6. Saito, R., Hofmann, M., Dresselhaus, G., Jorio, A., & Dresselhaus, M. S. (2011). Raman spectroscopy of graphene and carbon nanotubes. *Advances in Physics*, *60*(3), 413–550. https://doi.org/10.1080/00018732.2011.582251
7. Dresselhaus, M. S., Dresselhaus, G., & Jorio, A. (2007). Raman Spectroscopy of Carbon Nanotubes in 1997 and 2007. *The Journal of Physical Chemistry C*, *111*(48), 17887–17893. https://doi.org/10.1021/jp071378n
8. Wajs, E., Molina-Ontoria, A., Nielsen, T. T., Echegoyen, L., & Fragoso, A. (2014). Supramolecular Solubilization of Cyclodextrin-Modified Carbon Nano-Onions by Host–Guest Interactions. *Langmuir*, *31*(1), 535–541. https://doi.org/10.1021/la504065r
9. Haiss, W., Thanh, N. T. K., Aveyard, J., & Fernig, D. G. (2007). Determination of Size and Concentration of Gold Nanoparticles from UV−Vis Spectra. *Analytical Chemistry*, *79*(11), 4215–4221. https://doi.org/10.1021/ac0702084
10. Li, W., Wu, S., Xu, X., Zhuang, J., Zhang, H., Zhang, X., Hu, C., Lei, B., Kaminski, C. F., & Liu, Y. (2019). Carbon Dot-Silica Nanoparticle Composites for Ultralong Lifetime Phosphorescence Imaging in Tissue and Cells at Room Temperature. *Chemistry of Materials*, *31*(23), 9887–9894. https://doi.org/10.1021/acs.chemmater.9b04120
11. Mondal, S., Yucknovsky, A., Akulov, K., Ghorai, N., Schwartz, T., Ghosh, H. N., & Amdursky, N. (2019). Efficient Photosensitizing Capabilities and Ultrafast Carrier

Dynamics of Doped Carbon Dots. *Journal of the American Chemical Society*, *141*(38), 15413–15422. https://doi.org/10.1021/jacs.9b08071

12. Huang, J. J., Zhong, Z. F., Rong, M. Z., Zhou, X., Chen, X. D., & Zhang, M. Q. (2014). An easy approach of preparing strongly luminescent carbon dots and their polymer based composites for enhancing solar cell efficiency. *Carbon*, *70*, 190–198. https://doi.org/10.1016/j.carbon.2013.12.092
13. Gao, Z., Shen, G., Zhao, X., Dong, N., Jia, P., Wu, J., Cui, D., Zhang, Y., & Wang, Y. (2013). Carbon dots: a safe nanoscale substance for the immunologic system of mice. *Nanoscale Research Letters*, *8*(1). https://doi.org/10.1186/1556-276x-8-276
14. Dai, H., Shi, Y., Wang, Y., Sun, Y., Hu, J., Ni, P., & Li, Z. (2014). A carbon dot based biosensor for melamine detection by fluorescence resonance energy transfer. *Sensors and Actuators B: Chemical*, *202*, 201–208. https://doi.org/10.1016/j.snb.2014.05.058
15. Wang, W., Kim, T., Yan, Z., Zhu, G., Cole, I., Nguyen, N. T., & Li, Q. (2015). Carbon dots functionalized by organosilane with double-sided anchoring for nanomolar Hg2+ detection. *Journal of Colloid and Interface Science*, *437*, 28–34. https://doi.org/10.1016/j.jcis.2014.09.013
16. Gao, X., Ding, C., Zhu, A., & Tian, Y. (2014). Carbon-Dot-Based Ratiometric Fluorescent Probe for Imaging and Biosensing of Superoxide Anion in Live Cells. *Analytical Chemistry*, *86*(14), 7071–7078. https://doi.org/10.1021/ac501499y
17. Magar, H. S., Hassan, R. Y. A., & Mulchandani, A. (2021). Electrochemical Impedance Spectroscopy (EIS): Principles, Construction, and Biosensing Applications. *Sensors*, *21*(19), 6578. https://doi.org/10.3390/s21196578
18. Narayan, M. R. (2011). Review: Dye sensitized solar cells based on natural photosensitizers. *Renewable and Sustainable Energy Reviews*. https://doi.org/10.1016/j.rser.2011.07.148

Chapter 4

Effect of the nitrogen source on the synthesis of nitrogen doped carbon dots using the microwave-assisted irradiation method

4.1.Introduction

Since Scrivens and co-workers synthesized fluorescent carbon dots (Cdots) in 2004, the field has grown extensively [1]. Based on their crystal structure and quantum confinement, different types of Cdots have since been synthesized viz. carbon quantum dots (CQDs), graphene quantum dots (GQDs), carbon nanodots (CNDs) may be characterized [2] and carbonized polymer dots (CPDs) [3]. Different carbon dots are depicted in Figure.4.1.

The edge effect and quantum confinement effect are two examples of the distinctive properties of the GQDs, which are tiny units of graphene made up of one or more sheets that include chemical groups on the edge or within the interlayer hole. They are often anisotropic and have lateral dimensions. Without the quantum confinement effect of particle size, the defect/surface state and subdomain state inside the graphitic carbon core are the principal sources of photoluminescence in CNDs. Although CNDs include a significant amount of surface chemical groups and carbonization, they often lack pronounced polymer and crystal lattice characteristics.

The CQDs are typically spherical with an obvious crystalline lattice and chemical groups on the surface, and they display intrinsic state luminescence and the quantum confinement effect due to their size. The CPDs also have a hybrid polymer/carbon structure with a carbon core and several surface functional groups and polymer chains. The two varieties of completely carbonized cores that resemble CNDs or CQDs, a para-crystalline carbon structure made up of tiny carbon clusters surrounding by polymer frames, and a dehydrated cross-linkage and linked polymer frame structure are the four subclasses of the carbon core [3]. As a result, the photoluminescence centre differs significantly amongst the various Cdot kinds.

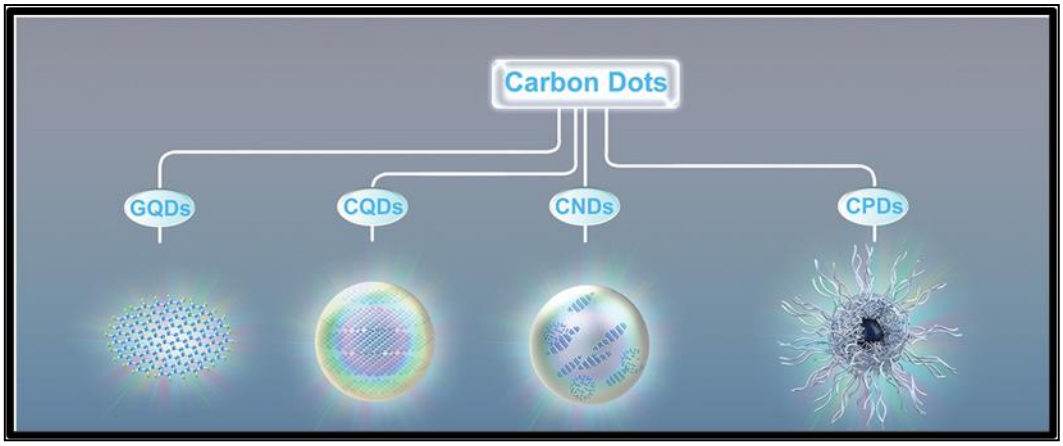

Figure 4.1: The proposed representative structures of graphene quantum dots (GQDs), carbon quantum dots (CQDs), carbon nanodots (CNDs), and carbonized polymer dots (CPDs) [3].

The top-down or bottom-up procedures are the most often used techniques to create these carbons, as explained in **Section 2.1.3, Ch. 2**. The top-down synthesis is known as cutting from/breaking down various carbon sources to smaller carbon-based compounds [4], whereas the bottom-up synthesis utilises tiny organic molecules [5, 6]. The top-down and bottom-up approaches are referred to as "nano-methods" to make carbons [7, 8]. Although the top-down and bottom-up techniques produce Cdots with comparable luminous capabilities, their structures and properties differ to some degree [9]. The production of polydisperse Cdots is difficult to manage.

Regarding their physicochemical characteristics, Cdots are different from metallic nanoparticles or inorganic semiconductor quantum dots. They are helpful in chemo sensing, biosensing, imaging, cancer therapy, catalysis, light emitting diodes, and solar cells because to properties including controlled fluorescence, no optical blinking, nontoxicity, long-term photobleaching resistance, and water dispersibility [10–19]. Carbon, oxygen, and/or nitrogen-based groups and their polymeric aggregates make up the structure of Cdots. Cdots, unlike semiconductor quantum dots, have an unusual emission dependency on the excitation wavelength [20].

The intrinsic structure and optical characteristics of Cdots requires a thorough understanding of surface functionalization. Carbon and oxygen are the dominant elements found in non-functionalized Cdots [21]. Unfunctionalized Cdots have poor luminous performance [fluorescence quantum yield (QY_{FL}) <5%]. The addition of oxygen (or other element) surface

functional groups is used to modify the efficiency. The nonradioactive recombination of localized electron-hole pairs generated by oxygen groups like epoxy and carboxylic groups on the Cdots surface reduces the pristine emission [22]. Non-functionalized Cdots frequently exhibit blue fluorescence and have a constrained number of active sites due to the singularity of surface functional groups, which limits their use. As a result, functionalized Cdots show improved photophysical and photochemical capabilities. Doping has also been suggested as a possible way to fine-tune Cdot emission features [23]. Since nitrogen and carbon atoms are similar in size, nitrogen-doping (N-doping) is possibly the most common heteroatom employed for doping. Additionally, nitrogen has five valence electrons available for joining carbon atoms together [24]. N-doping often increases the quantum yield of Cdots [25-27], rendering it one of the most prevalent techniques to improve Cdot photoluminescence [28, 29]. A nitrogen-rich tiny organic molecule is often added to the carbon precursor as a nitrogen precursor in hydrothermal-based bottom-up synthesis procedures to accomplish nitrogen doping.

Small molecules containing heteroatoms and other precursors can be pyrolyzed or carbonized to produce heteroatom-doped Cdots in a single step, whereas surface-modified Cdots often need two or more steps. Cdots with functional ligands may be modified by physical blending or chemical bonding, such as amidation reaction, N-ethyl-N′-(3-(dimethylamino) propyl) carbodiimide/N-hydroxysuccinimide, and electrostatic contact [21]. The intrinsic structure and electron distribution of Cdots can be altered by non-metal, metal, and heteroatom doping. Among the several non-metals, nitrogen doping is, as previously mentioned, a particularly effective method for increasing the QY_{FL} of Cdots because electrons trapped by the newly created N-state can exhibit high fluorescence yield [30]. Additionally, the fluorescence may be adjusted via N-doping, and excitation independence behaviour caused by passivated surface states can be identified [31-33]. They can determine how basic or acidic carbons are, as well as their various surface chemical and/or physical reactivity [34].

In this study, several nitrogen precursors have been used to make doped Cdots. Citric acid was used in solid-state microwave-assisted process to synthesize N-doped carbon dot [35-39] and polymers, for change of surface functionality or passivation, are two of the most widely employed small organic compounds in the manufacture of Cdots, to name a few. Citric acid was employed in this study a carbon source while ethylenediamine, fumaronitrile and urea

were used as N sources. Because of its chemical makeup, fumaronitrile serves as a source of both carbon and nitrogen. The structures of the reactants are shown in **Figure 4.2**.

The study optimized experimental parameters such as microwave power, heating time, and reactant ratio. Thus, a 1:1 mole ratio of citric acid to dopants, a microwave power of 700 W, and 5 minutes irradiation reaction time were employed as the optimal synthesis conditions.

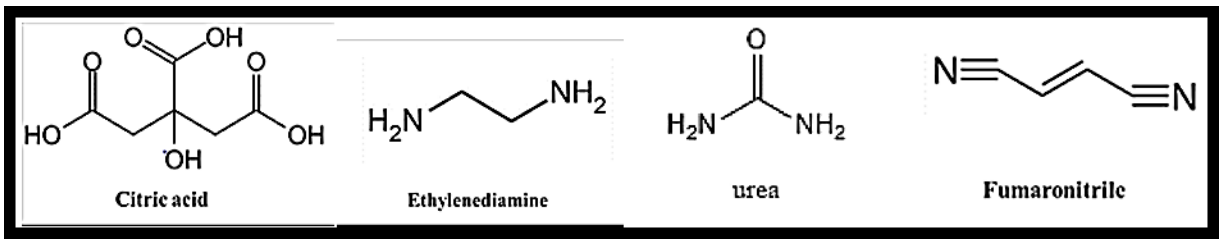

Figure 4.2: The structures of precursors used to prepare NCdots.

4.2.Starting materials

All of the compounds were readily accessible on the market and of analytical purity. The reagents did not require further purification. Citric acid was employed as a source of carbon, ethylenediamine, urea, and fumaronitrile were used as N-dopants, and distilled water served as the solvent in the precursor process. They are shown in **Table 4.1**.

Table 4.1: Materials and reagents used in this study.

Reagents and materials	Purity and speciation	Supplier
Citric acid	(C.A) ≥ 99.5 %	Sigma-Alrich
Ethylenediammine (EDA)	$C_2H_4(NH_2)_2$, ≥ 99.5 %	Sigma-Alrich
Urea	$CO(NH_2)_2$, ≥ 99.6 %	Sigma-Alrich
Fumaronitrile (FN)	NCCH=CHCN, ≥ 98.0 %	Sigma-Alrich
Quinine sulfate	QS, Bioreagent, ≥ 98.0 %	Sigma-Alrich

4.2.1. Experimental procedure

N-doped carbon dots (NCdots) were prepared from different precursors. The intention was to synthesise the three types of NCdots using three different types of nitrogen-containing precursors and to evaluate their physical, electronic, optical, and physiochemical properties for comparison purposes. These were:

i) citric acid + ethylenediamine to obtain NCdots (EDA)

ii) citric acid + urea to obtain NCdots (Urea)

iii) fumaronitrile to obtain NCdots (FN)

to observe the change in properties of NCdots synthesized using a microwave-irradiation method.

Various experiments were conducted to synthesize the nitrogen doped carbon dots. Using the hydrothermal microwave-assisted irradiation procedure. This method has been used by other researchers viz. Christé et al. [33] for NCdots (EDA), Kasprzyk et al. [39] for NCdots (Urea), and Moon et al. and Hou et al. [40, 46] for NCdots (FN).

Despite extensive investigation, the impact of N-doping techniques on the QY_{FL} still remains unknown [2]. As a result, the effectiveness of various nitrogen precursors on the QY_{FL} of the resultant Cdots is unknown. This makes logical creation of Cdots with high QY_{FL} difficult, which is a need for most (if not all) of these NCdots present uses.

4.2.2. Synthesis of nitrogen-doped carbon dots

The literature was consulted to determine the synthesis techniques that were used in this work (as stated in **Sec. 4.2** above). Using an Anton-Paar Multiwave 3000 SOLV microwave reactor system with a maximum output of 1400 W and a regulated pressure of 60 bars, NCdots were created. The temperature of carbonization of precursors to Cdots was manually set as the highest temperature (or infrared temperature limit on the microwave) of the reaction mixture, and the microwave power was manually set to 700 W for all reactions. All reactions took place for 5 minutes at a fixed microwave power, and during that period, the power was scaled up gradually (at a ramping rate of 100W/min) for all processes. Reaction conditions are summarized in **Table 4.2** below.

Table 4.2: NCdots microwave-assisted synthesis conditions used in this study.

Sample Name	Carbon source	Nitrogen source	Solvent
NCdots (EDA)	C.A/EDA (1 g)	EDA (1 g)	Water (20 mL)
NCdots (Urea)	C.A/Urea (1 g)	Urea (1 g)	Water (20 mL)
NCdots (FN)	FN (1 g)	FN -	Water (20 mL)

The following steps were used when performing the response procedures:

The standard procedure implemented included adding the different precursors into a beaker and mixing them with distilled water. An amount of about 1.0 g of precursor (with ratio 1:1 by weight) was mixed with 20 mL of water – for the preparation of the differently doped Cdots. After that, the mixture was put into a Teflon 100 mL microwave jar with a pressure jacket and cooked there for 5 minutes at 700 W. The carbonized materials were allowed to cool to room temperature when the reaction was finished. The aqueous doped Cdots were then purified by high-speed centrifugation at 18000 rpm for 20 minutes to remove large particles or unreacted starting materials. Using a thin 0.22 m filter membrane, the collected supernatant was filtered to remove any suspended contaminants while rejecting any unsuspended or insoluble aggregates. Upon completion of filtering, a rotary evaporator was then used to evaporate off the water from the doped Cdots solution at moderate speed at a temperature of 70 ºC. The finished product was then allowed to dry for 24 hours in a vacuum oven at 60 ºC. All doped NCdots were prepared this same way (**Scheme 4.1**). Equation 1 was used to compute the weight-by-weight synthesis yield taking into account the quantity of finished powder and quantity of beginning precursors employed.

$$\%\, Yield = \frac{Actual\ yield}{Theoretical\ yield}\ x\ 100 \quad \text{.....} \quad (1)$$

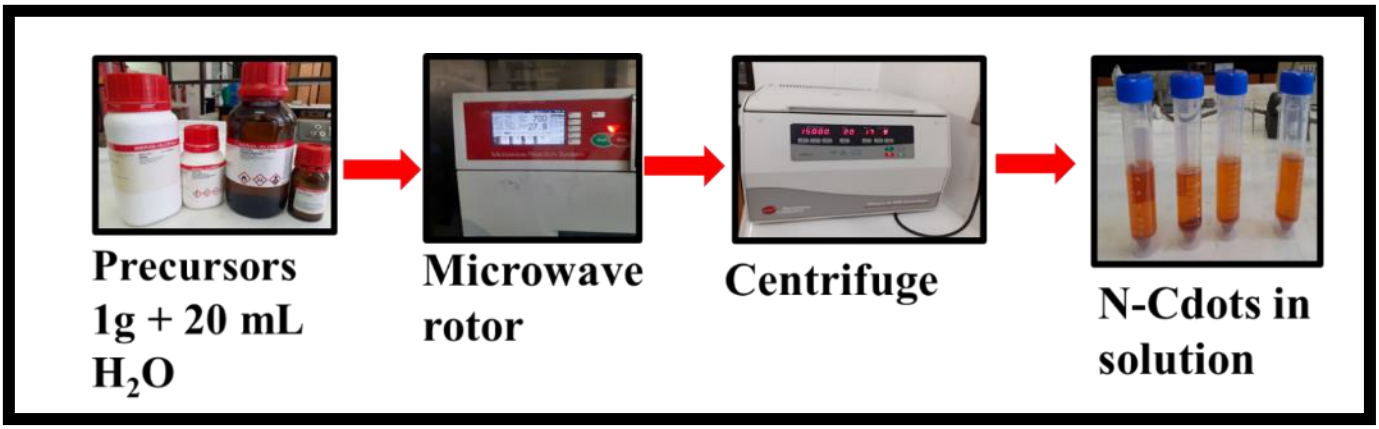

Scheme 4.1: Synthesis procedure followed in synthesizing the carbon dots.

4.2.3. Characterization techniques

- The synthesized materials were characterized using TEM, PXRD, Raman spectroscopy, UV-vis and PL spectroscopy, TCSPC, TGA/DTA analysis, FTIR analysis, XPS analysis, CHNS Elemental Analyzer, AFM and OFM microscopy.

4.3.Results and discussion

The outcomes and observations from the one-step microwave assisted NCdots synthesized are presented in this section. The preparation method used to make the carbon-based quantum particles has a significant impact on their characteristics. Because of this, the chemical structures of NCdots can differ substantially, and characterizing them is essential to knowing how to produce carbon-based quantum particles. The results and discussion sections below review the experimental findings and discuss them in the context of literature, while linking characterization techniques to each other and properties to performance, as per application in DSSCs.

4.3.1. Morphological analysis

TEM examination was used to examine the structure, morphological characteristics, and size distribution of NCdots produced under ideal synthetic circumstances (see explanation in **Supplementary Information,** (**SI**) **Sec. S1 and S1.1**). The spherical shape of all the NCdots was shown by TEM images, which are shown in **Fig. 4.3 a–c** below, and the particles were evenly dispersed without any aggregation. The synthesized Cdots' particle sizes were estimated using Image J software; the matching size distribution histogram is displayed next to each TEM image. The particle size of NCots (EDA) range from 4 to 10 nm with an average diameter of 6.5 nm ± 0.54 nm (**Fig. 4.3 a**). NCdots (Urea) ranged from 4 to 10 nm, with an average diameter of 7 nm ± 0.68 nm (**Fig. 4.3 b**). The NCdots (FN) were bigger in

size with a particle size range ranging from 15 – 60 nm and an average diameter of 35nm ± 0.49 nm (**Fig. 4.3 c**). These results vary slightly from those reported in literature using the same precursors due to the different reaction conditions employed. The large particle size of NCdots (FN) observed may be due to the reactivity of the precursor in the microwave oven, as the NCdots (FN) formed at a higher reaction temperature than the other NCdots synthesized using the strong microwave power (see **Table 4.3** below), under the same synthesis conditions using.

For example, NCdots reported by Mondal et al., were synthesized using ethylenedimine and citric acid had slightly smaller average particle sizes (~5 nm) using a domestic microwave oven (P= 300 W, T= 150 °C and t=10 min) [41]. Similarly, NCQDs prepared by Devi et al via hydrothermal synthesis at 140°C for 10 hours were found to have a ~6.7 nm diameter [42]. Using citric acid and urea in an aqueous solution, Sendao et al. created Cdots by microwave processing (5 minutes at 700 W in a home microwave). The average particle size of the Cdots was found to be 23.1 nm [43]. They said that whereas Cdots are normally less than 10 nm, larger versions of these nanoparticles are occasionally seen (up to 30 nm) [44, 45]. Hou et al., synthesized NCQDs by a hydrothermal method using fumaronitrile and the Cdots produced had an average diameter of ~4.5 nm via heating in an oven at 225 °C for 10 min. [46].

These findings reveal that there are many factors (i.e., microwave power, solvent volume, reaction time, type of precursor etc) that affect the properties of Cdots and that slight modifications on synthesis procedure have an impact on the physical properties of Cdots. Summary using the same precursors is given in **Table 4.3**.

The chemical make-up of the precursor molecules has long been recognized to influence the chemical characteristics of Cdots. The type of precursor and the method of synthesis can both affect the Cdots' particle sizes [47, 48]. Therefore, the structural, chemical, thermal, and optical characteristics of NCdots made from various precursors that included nitrogen were examined. The collected yield in this study after synthesis was 29 % for NCots (EDA), 29 % for NCdots (Urea) and 71 % for NCdots (FN).

Table 4.3: Comparison of particles size of NCdots synthesized in this study vs literature

Sample Name	Carbon source	Nitrogen source	Reaction time (mins)	Particle size (nm)	Microwave power (W)	Temperature (°C)	Reference
NCdots (EDA)	CA/EDA	EDA	7	6.5	700	174	This work
NCdots	CA/EDA	EDA	10	5	300	150	[41]
NCdots (Urea)	CA/Urea	Urea	7	7	700	184	This work
NCdots	CA/Urea	Urea	5	23.1	700	-	[43]
NCdots (FN)	FN	FN	7	35	700	190	This work
NCQDs	FN	FN	10	4.5	-	225	[46]

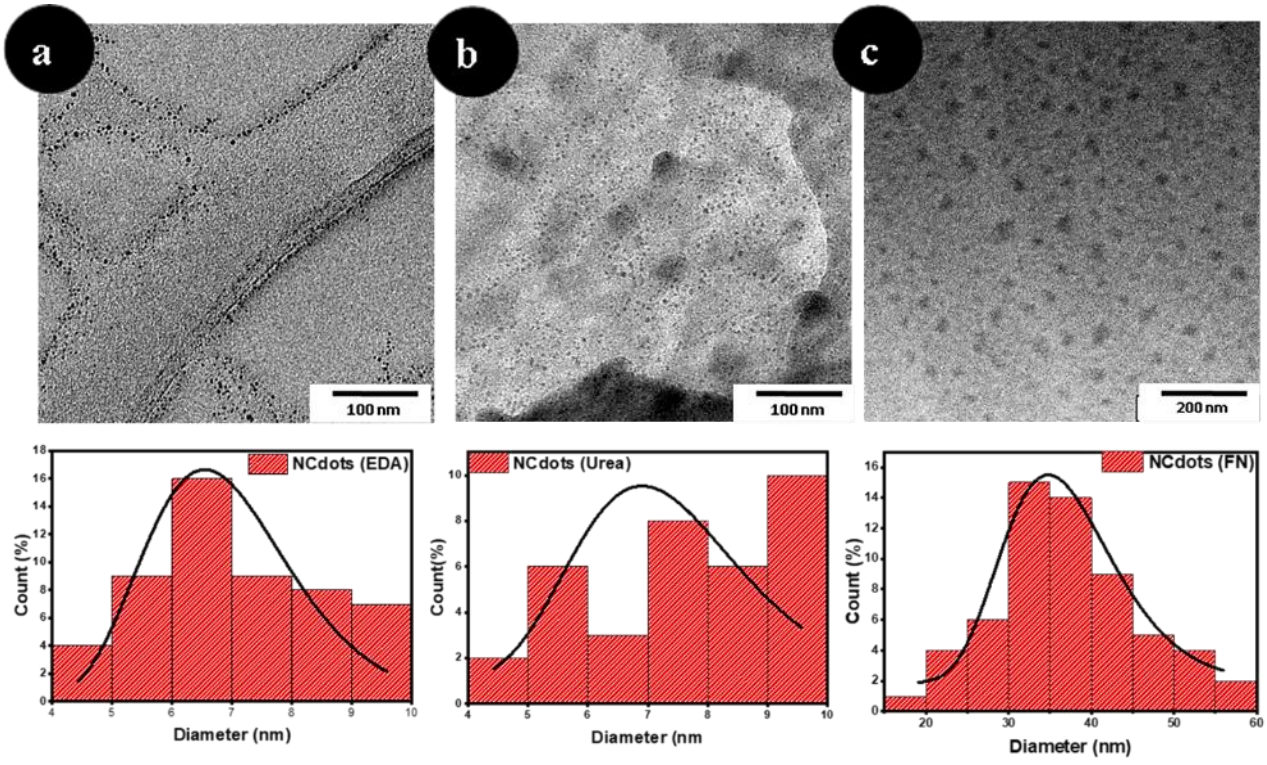

Figure 4.3: TEM images and their corresponding size distribution histograms below of a) NCdots (EDA), b) NCdots (Urea) and c) NCdots (FN).

4.3.2. Powder X-ray diffraction (PXRD) spectroscopy analysis

The PXRD patterns were measured for all nitrogen-doped carbon dots. **Figure 4.4. (a)** depicts the PXRD patterns of all NCdots while **Figures. 4.4 b, c and d** show the separate patterns, which present complete conversion to a graphite-like material. Broad carbon peaks are observed for the NCdots (EDA) and NCdots (Urea) consistent for small, disordered material. The PXRD pattern of the latter two samples demonstrated one broad peak centred at $2\theta = 24.7^{\circ}$ for NCdots (EDA) and $2\theta = 25.1^{\circ}$ for NCdots (Urea) which can be attributed to the 002 plane of carbon. The difference relates to the internal structure suggesting the carbon layers pack differently. They both also exhibited a small peak at $\sim 2\theta = 61.0^{\circ}$ (100 plane) which can be attributed to the highly disordered carbon atom with amorphous structure and a graphitic characteristic [49-52], respectively (circled in **Figs. 4.4 b and c**). The PXRD diffractogram of NCdots (FN) (**Fig. 4.4.d**), demonstrated a narrow peak centred at $2\theta = 27.2^{\circ}$ which is attributed to carbon material with more crystalline characteristics, [53] and no other secondary peak was observed for this particular sample.

The PXRD pattern of a graphitic carbon typically shows a diffraction peak at around $2\theta = 25.0^{\circ}$ or higher [53-56]. It is evident that the crystallinity of NCdots varied with the different N-precursors, similar to those reported by other researchers [57-59]. In addition, the PXRD pattern of NCdots (FN) demonstrated a sharper peak as compared to the diffraction peak of the other two sample, implying that NCdots (FN) might have a higher degree of graphitization [60]. As explained in **Sec. 4.3.2** that both the NCdots (EDA) and NCdots (Urea) exhibit broad carbon PXRD patterns which suggest that these NCdots are of a highly disordered amorphous carbon structure relatively, while NCdots (FN) exhibited a sharp, narrow PXRD structure which suggests rather more crystalline characteristics. Hence, the (001) plane is not observed in the NCdots (FN). The broader 002 peak of NCdots is a characteristic of Cdots with smaller sizes [59, 49]. These findings are consistent with the TEM study, which showed that NCdots (EDA) and NCdots (Urea) had smaller average particle sizes than NCdots (FN).

The XRD data from **Figure 4.4 b, c and d** below was used to determine the crystallite size and interplanar d-space on the various NCdots employing the Scherrer equation (1) and Bragg's law (2), respectively. From the XRD graph, we can calculate the full width and half

maximum (FWHM) and utilise the FWHM value obtained to calculate both the crystallite size and d-space.

$$D = \frac{K\lambda}{\beta cos\theta} \ldots \quad (1)$$

Where D is the average crystallite size (nm), K is the Scherrer constant (also called the shape factor or shape parameter) whose value is ~0.94 for spherical crystallites (with cubic symmetry), λ is the X-ray wavelength for the Cu-K_α X-ray source which has been experimentally deterimed and has value of 1.5406 Å (0.15406 nm), β is the line broadening at FWHM in radians and θ is the peak position/Bragg's angle in degrees at half of 2θ.

$$2dsin\theta = n\lambda \ldots \quad (2)$$

Here, d is the interplanar spacing (in Å or nm), θ is the Bragg's angle, n is the diffraction order (for first order, n=1) and λ is X-ray wavelength (Cu-K_α = 0.15406 nm).

The calculated (average) crystallite sizes for NCdots (EDA), NCdots (Urea) and NCdots (FN) were found to be 0.35 nm, 0.41 nm and 1.67 nm for NCdots (EDA), NCdots (Urea) and NCdots (FN), respectively. The interplanr spacing values were calculated to be $d_{(200)}$ = 0.36 and $d_{(100)}$ = 0.24 for NCdots (EDA), $d_{(200)}$ = 0.35 and $d_{(100)}$ = 0.22 for NCdots (Urea) and $d_{(200)}$ = 0.32 for NCdots (FN).

Furthermore, the dislocation density and micro strain values of the various NCdots were calculated using equation (3) and (4), respectively using parameters obtained above.

$$\delta = \frac{1}{D^2} \ldots \quad (3)$$

Where **δ** is the dislocation density (nm^{-2}) and D is the crystallite size.

$$\varepsilon = \frac{\beta}{4tan\theta} \ldots \quad (4)$$

Here ε is the micro strain, β is the line broadening at FWHM in radians and θ is the peak position/Bragg's angle in degrees at half of 2θ.

The dislocation densities were found to be 8.099 nm^{-2}, 6.039 nm^{-2} and 0.354 nm^{-2} for NCdots (EDA), NCdots (Urea) and NCdots (FN). The corresponding micro strain values were calculated to be 0.48, 0.41 and 0.09 for NCdots (EDA), NCdots (Urea) and NCdots (FN), respectively.

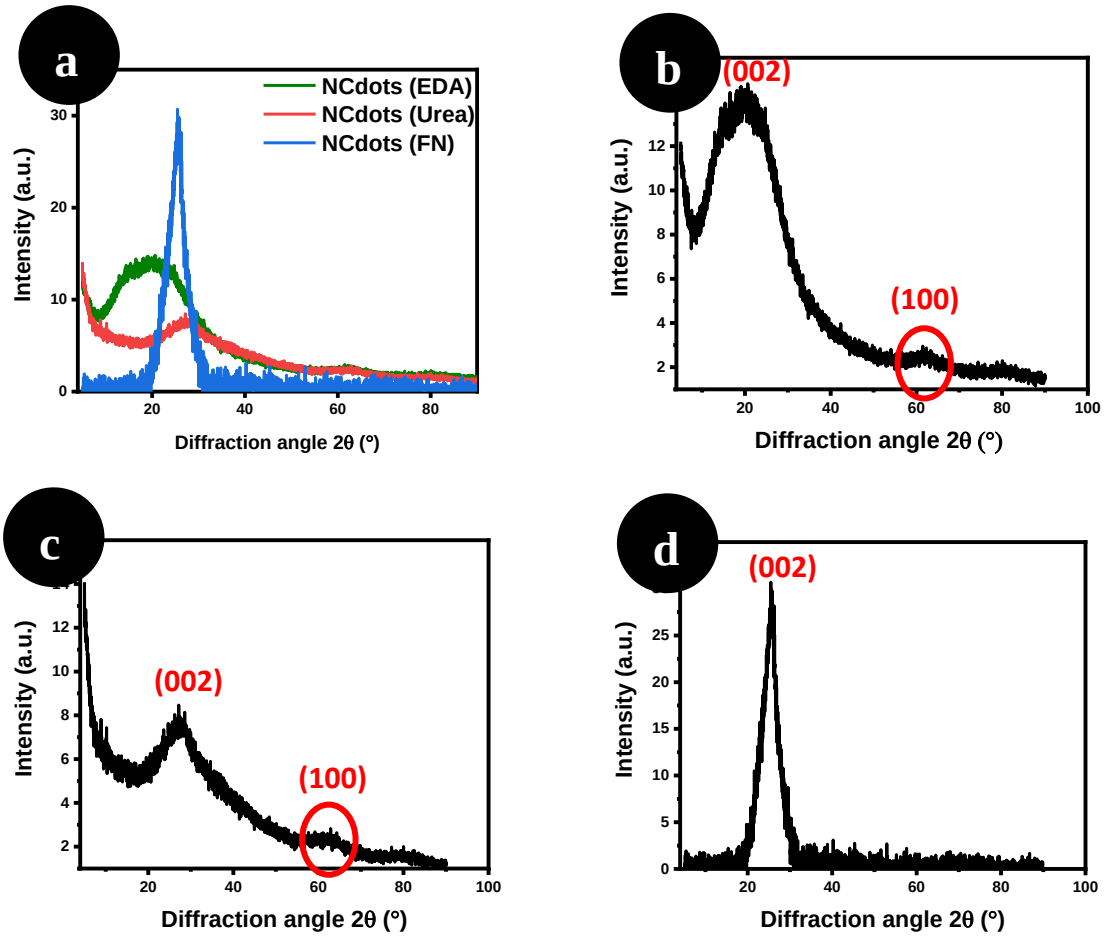

Figure 4.4: PXRD patterns of the as-synthesized a) all as-prepared NCdots, b) NCdots (EDA), c) NCdots (Urea) and d) NCdots (FN)

4.3.3. Raman spectroscopic analysis

The core of graphene quantum carbon dots, which are carbon-based nanoparticles, is believed to be made of sp^2 carbon atoms joined by sp^3 carbon atoms [61] **Fig 4.5**. This figure shows that at the extremes one can find a variety of carbon nanostructures with varying sp^2 /sp^3 ratios [62].

To learn more about the structural characteristics of the NCdots created in this work, Raman spectra were examined at 785 nm (red line laser), because the background fluorescence with

514.5 nm (green laser) was very intense. There was less fluorescence experienced with the red laser, hence it was chosen as the excitation soiurce. The D band, which is often centered at about 1300 cm^{-1} and is sp^3 hybridized, and the G band, which is typically centered at 1600 cm^{-1}, are the two primary characteristics of carbon nanomaterials. Other minor peaks include the 2D peak and the D+G overtones [63-67]. The D band is connected to the vibrations of carbon atoms in disordered graphite or glassy carbon with dangling bonds on the termination plane. The G band corresponds to the graphite E_{2g} mode and is related to the vibration of sp^2-hybridized carbon atoms in a two-dimensional hexagonal lattice [68, 69].

Heteroatom doping can cause Raman peaks to shift in location and strength. As an instance, Rogach's group [70] discovered that the G band blue moved to 1649 cm^{-1}, as opposed to the normal in-plane vibration G band, which occurs near to 1580 cm^{-1} when there is no doping of the carbon.

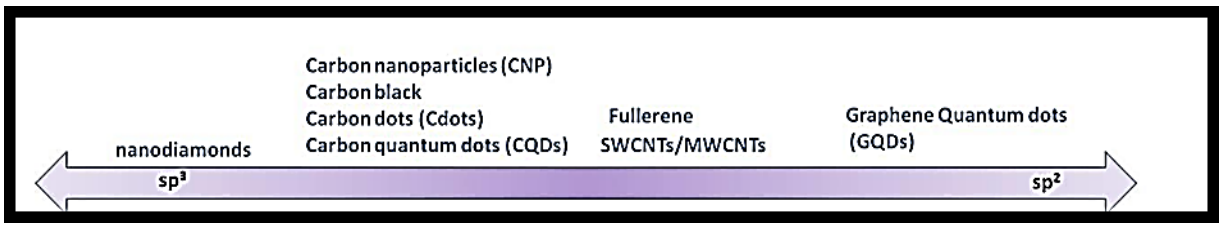

Figure 4.5: Carbon-based nanomaterials including carbon quantum particles [62].

It was difficult to get usable Raman data for the NCdots (EDA) and NCdots (Urea) because the Raman modes could not be described. This is associated with photoluminescence excitation of the carbon. The Raman analysis demonstrated the existence of a small G peak at ~1600 cm^{-1} for these two samples (**Fig. 4.6 a, and b**). The sloped baseline is consistent with the fluorescence properties associated with the Cdots, making Raman spectra measurement problematic. The fluorescent material could be analyzed with Fourier transform Raman (FT-Raman) at an excitation wavelength of ~1064 nm as a possible solution to this problem. This is due to the fact that FT-Raman can minimize materials' background fluorescence. UV-Raman analysis could also be used to investigate this issue although this option may be limited if the equipment has a wavelength of ~244 nm for excitation. This is not suitable for sp^2 carbon, and a longer wavelength of 325 nm would be more efficient.

For NCdots, the two distinctive D and G bands were observed (FN). At about 1350 cm^{-1}, the D band was noticed and the G band at about 1590 cm^{-1} (**Fig. 4.6 c**). The calculated I_D/I_G ratio

was found to be ~ 0.79. The Raman data is summarised in **Table 4.4** below. The data for NCdots (FN) is similar to that found by Moon et al [39]. According to reports, a big I_D/I_G number denotes expanding structural flaws or an increase in the quantity of disordered carbon inside Cdots, whereas a small I_D/I_G value implies a core of Cdots that is extremely crystalline. An I_D/I_G value of ca. 0.7 is typical of graphite [74]. If the I_D/ I_G ratio is equal to 1, it means there is an equal amount of both sp^3 and sp^2 carbons are present, while a ratio above one suggests a high degree of disorder and a ratio less than one suggests a high degree of graphitic carbon [71-73]. According to research by Ajayan's team, exposed edge sites and flaws in N-doping cause NGQDs to have an I_D/I_G = 1.05 [74].

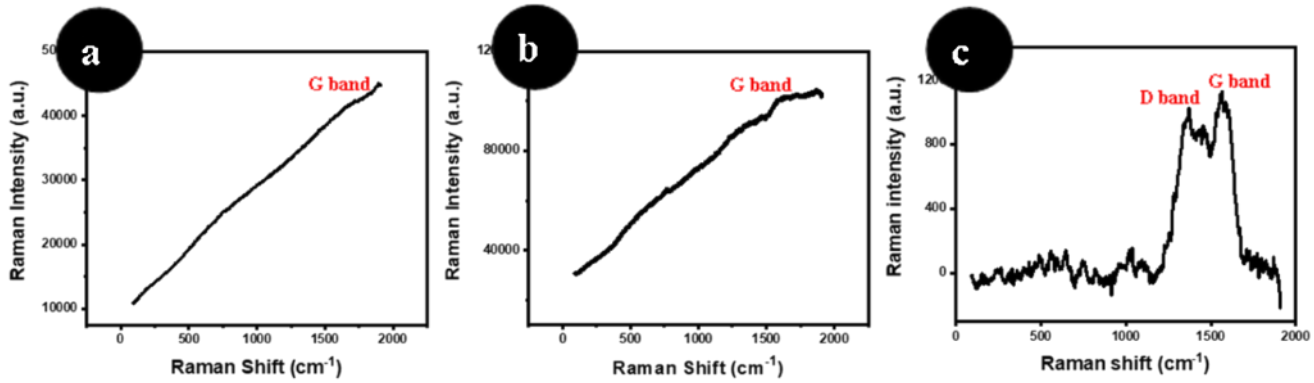

Figure 4.6: Raman spectra patterns of the as-synthesized a) NCdots (EDA), b) NCdots (Urea) and c) NCdots (FN) all recorded at λ_{ex} 785 nm.

Table 4.4: Summary of the Raman spectroscopy analysis results.

Sample name	D Band (cm^{-1})	Area	G Band (cm^{-1})	Area	I_D/I_G ratio
NCdots (EDA)	-	-	1689	-	-
NCdots (Urea)	-	-	1594	-	-
Ncdots (FN)	1380	1243.1	1556	1573.6	0.79

From TEM, PXRD and Raman data, it can be inferred that the NCdots (EDA) and NCdots (Urea) can be classified as CNDs and NCdots (FN) can be classified as either GQDs or CQDs [3, 62]. More information on their quantum confinement effect, rather than just crystal structure and spectroscopy, might improve the accuracy of the distinction between the two classes.

4.3.4 Optical properties (absorbance measurement and fluorescence studies analysis)

Utilizing spectrophotometry for photoluminescence (PL) and ultraviolet-visible (Uv-vis) absorption, the optical characteristics of both the as-synthesised NCdots were examined. **Figure 4.7** displays the NCdots' emission and absorption spectra, which were captured in water under ambient circumstances**.** Every spectrum displays band-to-band core transitions below 300 nm [75] and displays a shoulder at about 245 nm that may be caused by the C=C bond's π-π* transition [76]. An absorption peak at wavelengths 275 nm was observed for NCdots (EDA). The other two samples also showed two peaks ca. 283 and 598 nm for NCdots (Urea) and 280 and 325 nm for the NCdots (FN) (**Fig. 4.7 b and c)**, respectively. Poorly resolved bands may be the result of a bathochromic shift brought on by a high energy transition that originates from the quantum confinement of the carbogenic core (or the carbon π–π* transitions in the sp^2 domain transition). The secondary peaks resemble a broad low energy absorption band due to the n-π* transition of heteroatomic surface functionalities attached at the edge of the carbon core, respectively [77]. The findings demonstrate that the synthesized NCdots exhibit a broadband absorption for the PL emission mechanism and multiple emissive centers (in this case, dual emissive centers: core state and surface state). These absorption peaks in the Cdots structure suggest prolonged conjugation [78].

At an excitation energy of 350 nm, emission spectra were captured, as the NCdots did not exhibit any activity in region < 300 nm. The emission spectra showed maxima at 438 nm, 454 nm and 452 nm corresponding to NCdots (EDA), NCdots (Urea) and NCdots (FN) (see **Fig. 4.7 a, b and c**), respectively. The emission peaks of all types of NCdots were found to be broad, and this is a typical characteristic of fluorescent NCdots [79, 80].

UV absorption peaks of NCdots generated using traditional procedures are typically strong, but the locations of UV absorption peaks can vary. As shown in insets in **Fig. 4.7**, the NCdots dispersed in water were orange/brownish and transparent in daylight. When the sample was treated with UV light, the aqueous solution of NCdots emitted a bright blue fluorescence, showing that the NCdots have a high fluorescence. Furthermore, the sample solution is very clear, indicating that the NCdots have good aqueous dispersibility. Most reports on Cdots generated using the microwave-irradiation approach have been reported to exhibit blue fluorescence emissions when exposed to UV light [81, 82]. Tauc plots of these NCdots, ascwell as their determined bandgap energies, can be found in the **SI, Figure. S12**.

It is assumed that the emission and absorption data can be explained by proposals made in the literature. Traditional bandgap absorptions are absent in Cdots, and it is most likely that excited state energy trapping occurs between the defects that generate absorptions and those that induce emissions [83]. The Cdots surface may be modified using groups like amine and hydroxyl to fill in defects, stabilize surface energy traps after passivation, and then trap more emissive energy as a result of quantum confinement. As a result, the PL is more stable, and the fluorescence quantum yield is larger the smaller the Cdots are [84]. The distribution of unique emissive sites on each Cdot as well as impacts from particles of varying sizes in the sample might all contribute to the optical behavior of Cdots [85]. Studies of the optical characteristics of tiny Cdots, however, are still debatable, and the precise mechanisms underlying PL are yet unknown.

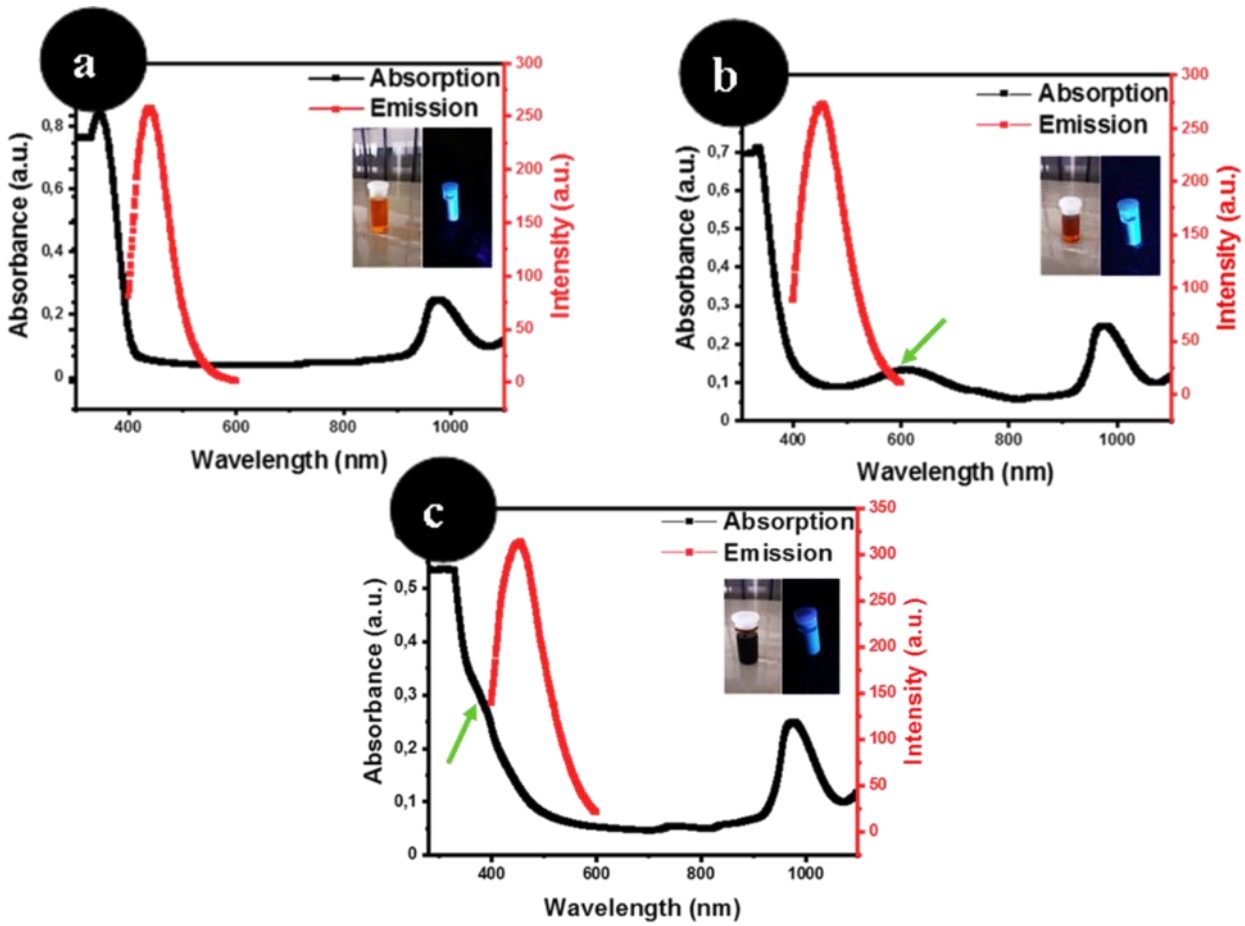

Figure 4.7: UV-vis absorption spectrum and PL emission spectra of a) NCdots (EDA), b) NCdots (Urea) and c) NCdots (FN). The inserts show the photographs of NCdots in water under visible light (brown solutions) and under UV lamp (blue solutions) at 365 nm excitation wavelength under irradiation.

Various excitation wavelengths were used to record the NCdots' emission spectra. As shown in **Fig. 4.8**, from 350 to 470 nm, in intervals of 20 nm, the emission intensity rose as the excitation wavelength was raised. All of the detected NCdots' emission strength, however, clearly decreased when the excitation wavelength was further increased. Additionally, a distinct red shift in the emission peak location for all samples was detected with an increase in the excitation wavelength from 410, 370, and 390 to 470 nm (**Fig. 4.8 a, b, and c**) for NCdots (EDA), NCdots (Urea), and NCdots (FN), respectively.

These findings imply that the NCdots defy Kasha's rule, which states that a fluorophore's emission peak location is independent of the excitation wavelength. According to reports, the photoluminescence characteristics change depending on how big the carbon quantum particles are. This is caused by the HOMO-LUMO gap's dependency on particle size, which causes redder-shifted emission as particle size increases [62]. NCdots synthesized in this study were seen to be bigger in size compared to the literature synthesis procedure (see **Sec 4.2.3** above). As a result, when λ_{ex} exceeds 400 nm, the location of λ_{em} shifts towards higher wavelengths and becomes excitation wavelength-dependent, which suggests that the NCdots as made contain two separate emissive species. This type of excitation-dependent emission is a distinguishing property of Cdots, allowing them to function as fluorescent probes [84].

The origin of this excitation-dependent nature is either due to the optical selection of various sized nanoparticles (quantum effect) and/or various emissive traps on their surface, or some other completely different mechanism; at the moment, this is an unresolved issue and a source of contention among scientists [85]. As a result, all as-synthesised NCdots are excitation dependent, which is to be expected. In our study, it appears that the PL features of the NCdots generated are due to distinct nanoparticle compositions and architectures, as well as variable particle sizes. These findings are in line with those made in prior investigations [86].

Although, the exact mechanism of Cdots photoluminescence is still a point of contention among researchers [87], four reliable PL processes have been established:

i) the carbon core's measurements of the quantum confinement effect and conjugated -domains
ii) the surface state, which is determined by chemical groups attached to the carbon backbone and their hybridization

iii) the fluorescent molecules attached to the surface or inside of the Cdots entirely control the molecular state

iv) the crosslink-enhanced emission (CEE) effect, which prevents materials from transitioning in nonradiative ways [88, 89].

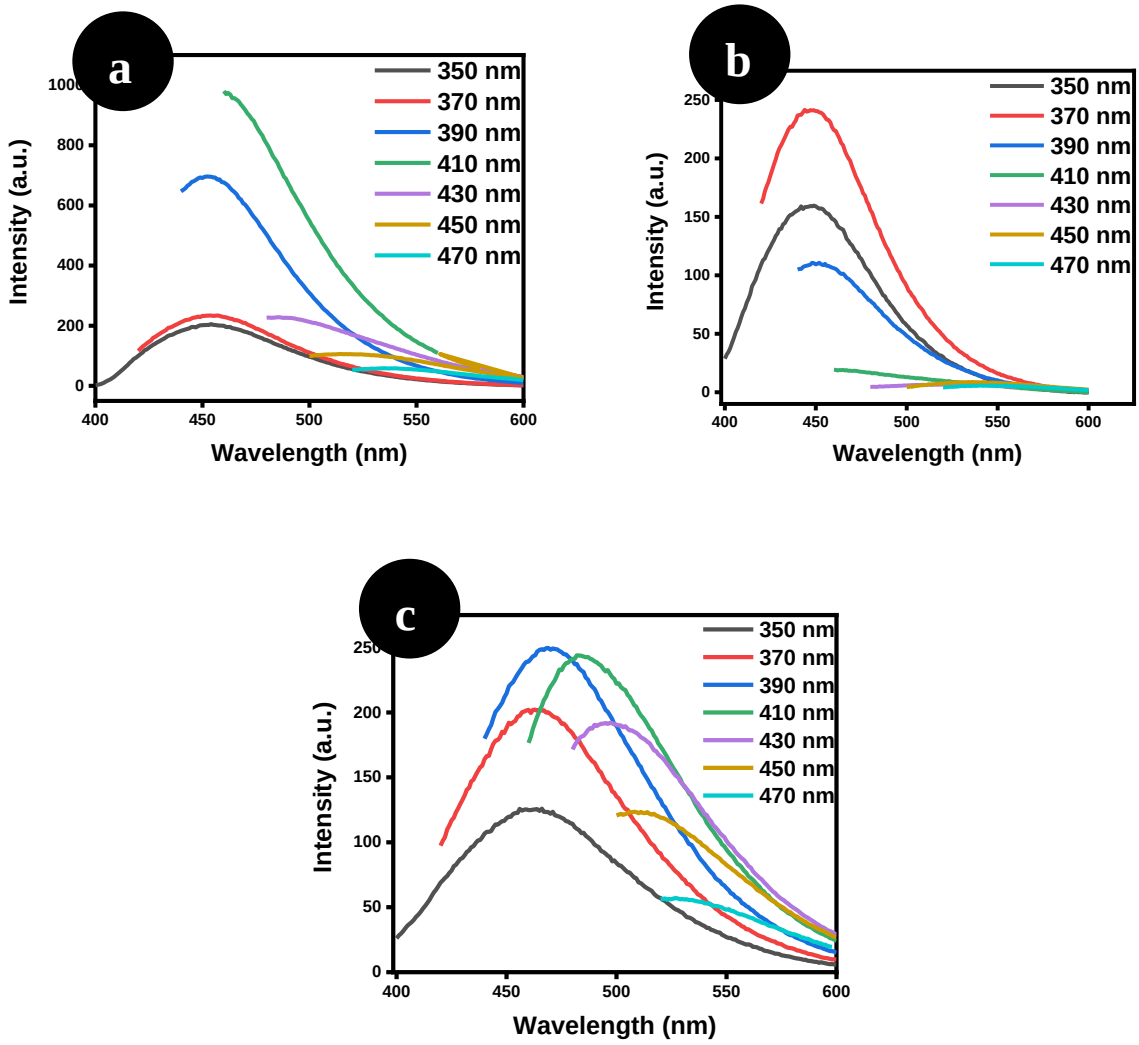

Figure 4.8: PL spectra of the aqueous solution of a) NCdots (EDA), b) NCdots (Urea) and c) NCdots (FN).

4.3.5. Quantum yield study and analysis

Fluorescence quantum yield (QY_{FL}) is the effectiveness of tuning absorbed energy into emitted light, which might take the form of fluorescence. Even at low concentrations, fluorophores having a high QY_{FL} frequently exhibit a bright fluorescence, thus this lowers the quantity of fluorophores needed for application which can minimize costs, of DSSC production in this case.

The QY_{FL} of the NCdots (**Table 4. 5**) was determined using quinone sulphate (QS) as a standard (QY_{FL} = 0.54, dissolved in water as a solvent) at the excitation wavelength of 350 nm [90, 91]. The integrated fluorescence intensity was calculated using the area under the fluorescence curve. The integrated fluorescence intensity was plotted against the absorbance, with the intercept set to zero. Finally, equation 2 was used to obtain QY_{FL} values (Equation 2):

$$\Phi = \Phi_R \frac{I}{I_R} x \frac{A_R}{A} x \frac{n^2}{n_R^2} \quad \text{..... (2)}$$

Where Φ is the quantum yield of the sample, I and I_R are the measured intensities of the fluorescent sample and the quinone sulphate reference, respectively. The A_R and A values are the measured absorbances of the reference and sample, respectively. The refractive index, n, was assumed to be 1 since the NCdots and QS were dispersed in the same solvent ($n_{(H2O)}$ = 1.33).

To avoid inner filter effects, there optical density of all samples was kept below 0,05. For all observations of fluorescence spectra, the excitation and emission slit widths were 5 nm. **Table 4.4** gives the QY_{FL} values for the three samples, and the NCdots (EDA) were observed to have the highest QY_{FL} compared to the other NCdots.

The quantum yields of these microwave-produced luminous Cdots are frequently reported to be < 10% [92]. Interestingly, the quantum yield of the NCdots (EDA) here was found to be 15%. If an electron in a molecule's singlet ground state (where electron spins are coupled) is stimulated to a high energy level, it has a chance of either being in the excited singlet state or the exciting triplet state. Due to the singlet ground state's presence of a spin zero, the spin quantum selection rule prevents excited triplet excitons from decaying into the ground state. In addition, photon absorption cannot ignite excited triplet excitons. Thus, the triplet state population is not a requirement for the DSSC material [93-95]. Hence, the NCdots with the highest quantum yield was chosen for application in dye-sensitized solar cell. The higher quantum yield is a result of nitrogen doping, which implies that ethylenediamine is more of a nitrogen-rich small organic molecule than a precursor to nitrogen [96].

Since nitrogen is an element that donates electrons, the nitrogen-doped carbon dots exhibit excellent electron conductivity due to the density of the electron cloud around the nitrogen atom. When exposed to UV light, electrons in Cdots travel from the ground state to the excited

state, and because the excited state is unstable, the electrons lose energy in the form of fluorescence before returning to the ground state [97]. For this reason, NCdots (EDA) were chosen, to be the material of choice for the fabrication of NCdots: OLCNs composites (see **Chapter 6**) for application as counter electrode material in DSSCs.

Table 4.5 Quantum yield calculations

Sample name	Integrated Emission Intensity	Abs@350 nm (A)	Quantum ratio	Quantum Yield (%)
QS ref	1507494	0,02863	0.54 (known)	-
NCdots (EDA)	654028,52	0.04384	0.1530	15.30
NCdots (Urea)	352028.51	0,04725	0,0764	7.64
NCdots (FN)	55830,76	0.01017	0,0563	5.63

Christé et al reported NCdots (EDA) with 3% QY a 350 nm excitation wavelength [33]. Zhao's group managed to synthesize NCdots (Urea) with 12.9% QY [98] and Moon et al found their NCdots (FN) to have a QY of ~47%.

4.3.6. Time-correlated single-photon counting (TCSPC) analysis

Unlike steady state intensity measurements, which is relative, the fluorescence lifespan provides an absolute (concentration-independent) metric that permits a dynamic image of the fluorescence spectrum to be created. The fluorescence lifetime is a chemical characteristic that is independent of concentration within specific restrictions. Thus, concentration variations, whether induced by photobleaching or diluting/concentrating the sample, have no effect on the lifespan value [99]. The greatest barrier to using carbon dots in the solid state is accumulation-induced luminescence quenching. In this study, analyses were done using a 377 nm pulsed diode laser source at the emission wavelength of 400 nm (**Fig 4.9 a, b and c** below). From time-resolved spectral data at the proper wavelengths, kinetic traces were constructed. Transient absorption and time-resolved fluorescence experiments were conducted in quartz cells with a 2 mm sample path length.

TSCPC as an analytical technique has relevance in relation to DSSC application in that enhanced power conversion efficiencies can be attributed to increased lifetimes of photo excited excitons due to strong spin-orbit coupling of the N electrons in NCdots which is required for good performance and electronic (and chemical) stability of the DSSC. Thus, longer decay lifetimes may enhance the performance of the DSSC.

For all the three as-synthesized NCdots, the plots followed bi-exponential decay patterns. The time-resolved fluorescence decay curves can be fitted into double exponential functions showing τ_1, and average lifetime (τ_{ave}). The average luminescence lifetime was found to be $8.28 \times 10^3 \pm 7.19 \times 10$ ns for NCdots (EDA), $3.46 \times 10^7 \pm 5.15 \times 10^6$ ns for NCdots (Urea) and $2.77 \times 10^7 \pm 2.72 \times 10^6$ ns for NCdots (FN). The NCdots (Urea) and NCdots (FN) were observed to have short average lifetimes (< 5 ns), and such short lifetime is similar to those found for graphene dots (QDs) [100, 101] whereas NCdots (EDA) exhibited a longer average lifetime (> 5 ns). Moreover, it was found that the varying emission durations for differently doped NCdots affected the radiative route due to the modification by heteroatom dopants. The highest QY_{FL} was found to be NCdots (EDA) and because of the fluorescence being dominated by a highly emissive molecular state with a relatively longer average lifetime, NCdots (EDA) exhibited a high QY_{FL}.

There have only been a few reports of strong fluorescence in Cdot-based solid-state materials [102]. Overall, the emission lifetimes of the various doped Cdots were somewhat diverse, demonstrating that doping and the various dopants utilized have an effect on the radiative route [103]. The effect of doping on Cdots and the dynamics of their excited states is consistent with the results of excitation wavelength dependent studies.

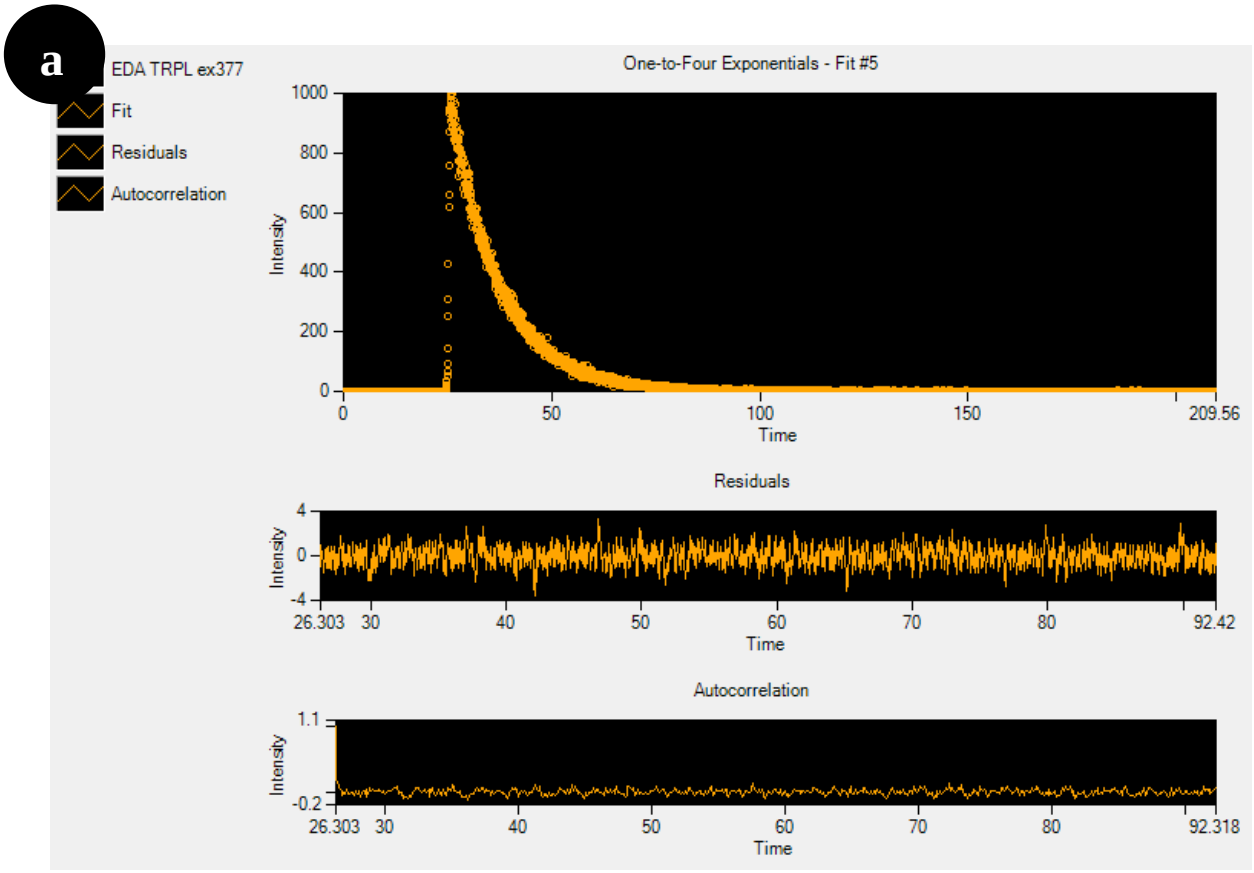
a
EDA TRPL ex377
Fit
Residuals
Autocorrelation
One-to-Four Exponentials - Fit #5
Intensity
Time
Residuals
Autocorrelation

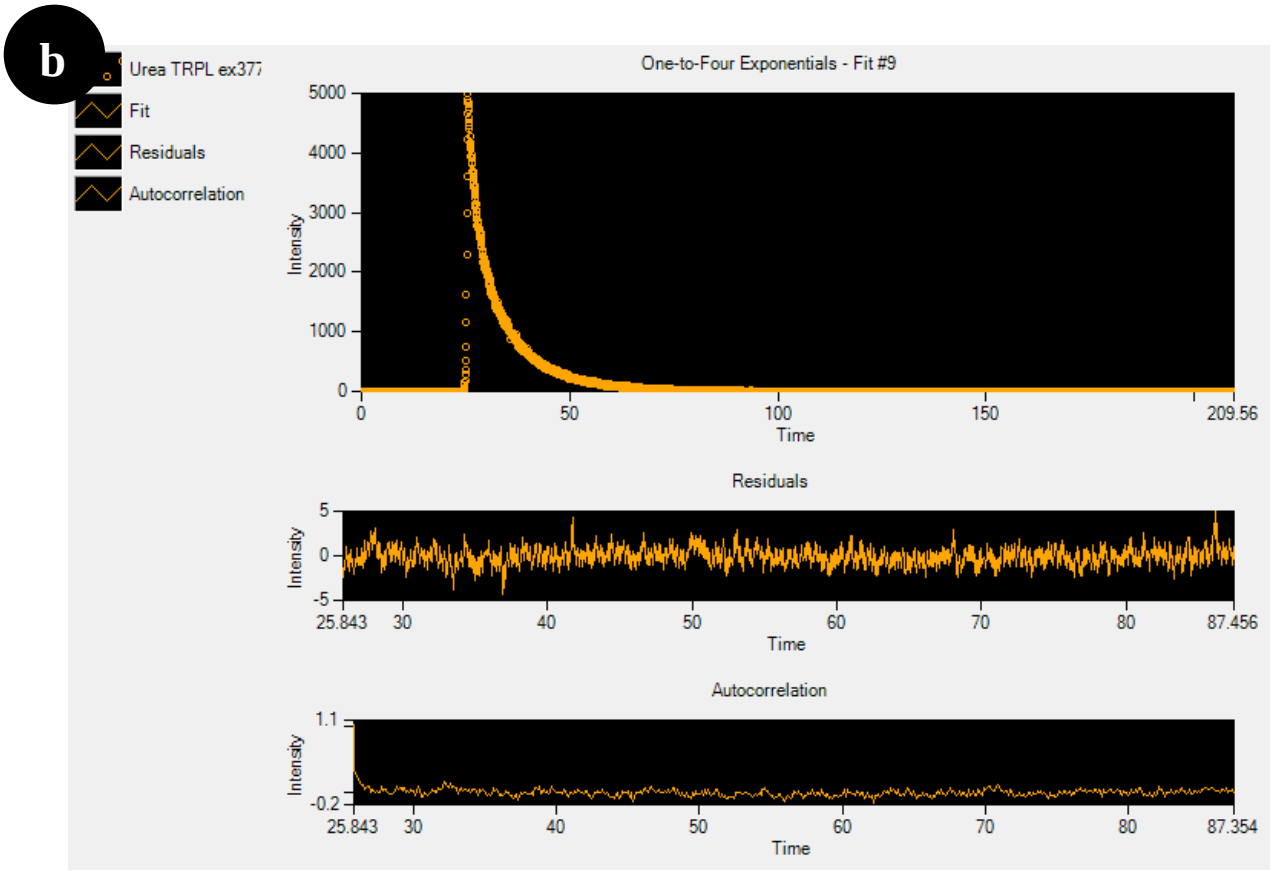
b
Urea TRPL ex377
Fit
Residuals
Autocorrelation
One-to-Four Exponentials - Fit #9
Intensity
Time
Residuals
Autocorrelation

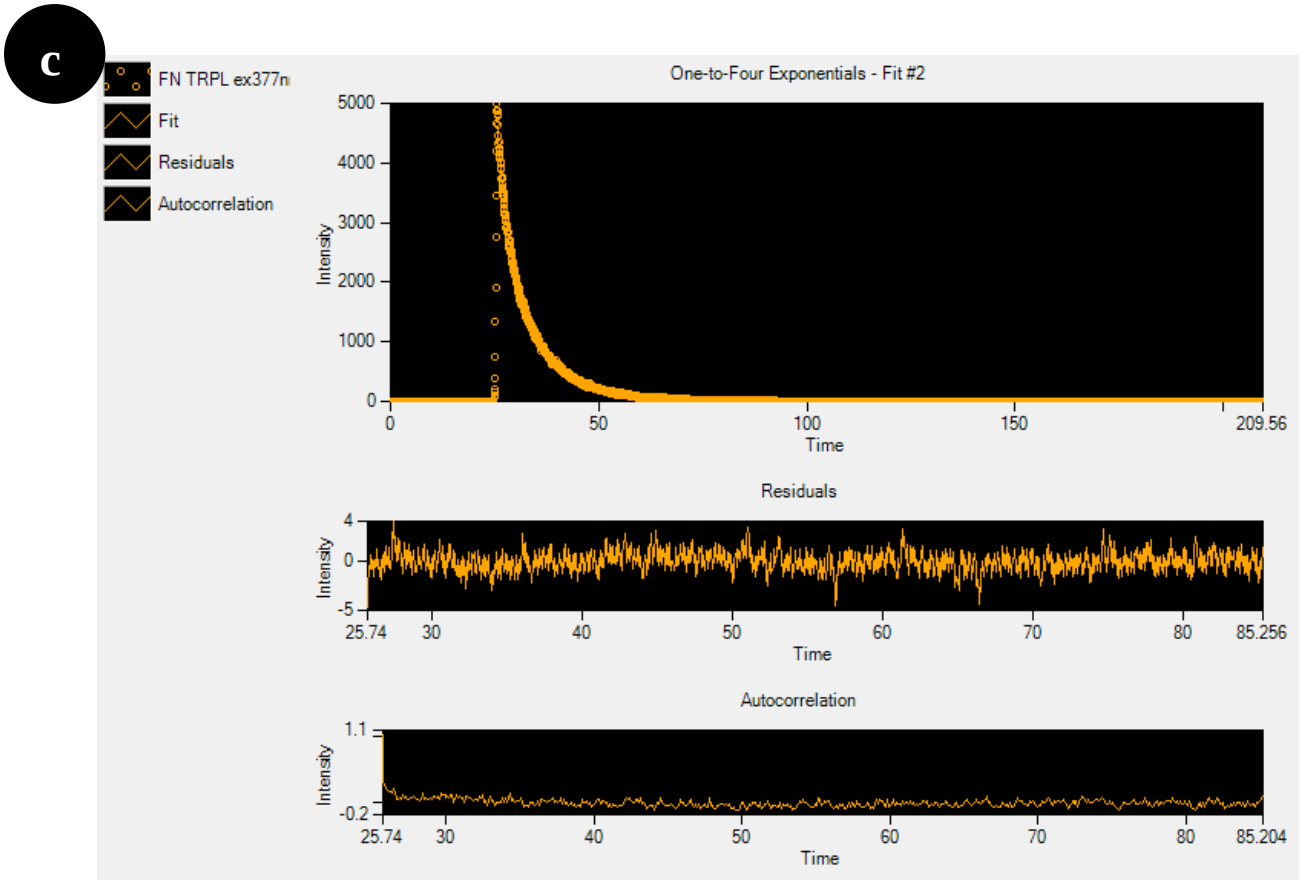

Figure 4.9: Decay studies of a) NCdots (EDA), b) NCdots (Urea) and c) NCdots (FN).

4.3.7. Thermogravimetric/differential thermal (TGA/DTA) analysis

TGA and DTA analyses were carried out to obtain the thermal stability and to get an estimate of the purity of the NCdots, recorded under ambient conditions (**Fig 4.10 a and b**). All the NCdots showed small decomposition peaks at temperatures around 180-190 ˚C which are due to moisture or adsorbed water by the NCdots [104], **Fig 4.10 a**. The NCdots also displayed several breakdown peaks at temperatures between 200 and 600 ˚C (circled), which may be related to various functional groups on their surface or various arrangements of the various types of nitrogen atoms [105]. At temperatures exceeding 500 °C, the NCdots showed a significant weight loss, which is caused by the disintegration of the graphitic carbon core of the NCdots [106]. The weight percentage of the residual nanoparticles after heating was found to be < 0.5 % for all NCdots. This indicates that the synthesized NCdots were fairly free of any impurities.

The DTA curves (**Fig 4.10 b**) showed numerous weight loss steps below 400 °C. The first step is up to 300 °C, where the weight loss is not substantial. The degradation in this region is due to the evolution of oxygen and nitrogen atoms, the lattermost likely from HCN and NH_3 functional groups [107]. The decomposition of the residual carbon core in the second stage is what causes the weight loss. The decomposition temperatures of the carbogenic backbone structure occur at 598, 610, and 638 °C for NCdots (EDA), NCdots (Urea) and NCdots (FN). From **Figure 4.10 b** the NCdots (FN) can be seen to present with a broader decomposition peak as compared to the other NCdots at temperatures above exceeding 500 °C. This relatively broader peak can be attributed to strong interaction of the N atoms to the Cdots, resulting in NCdots (FN) presenting with the highest thermal stability. These results are in agreement with Raman data.

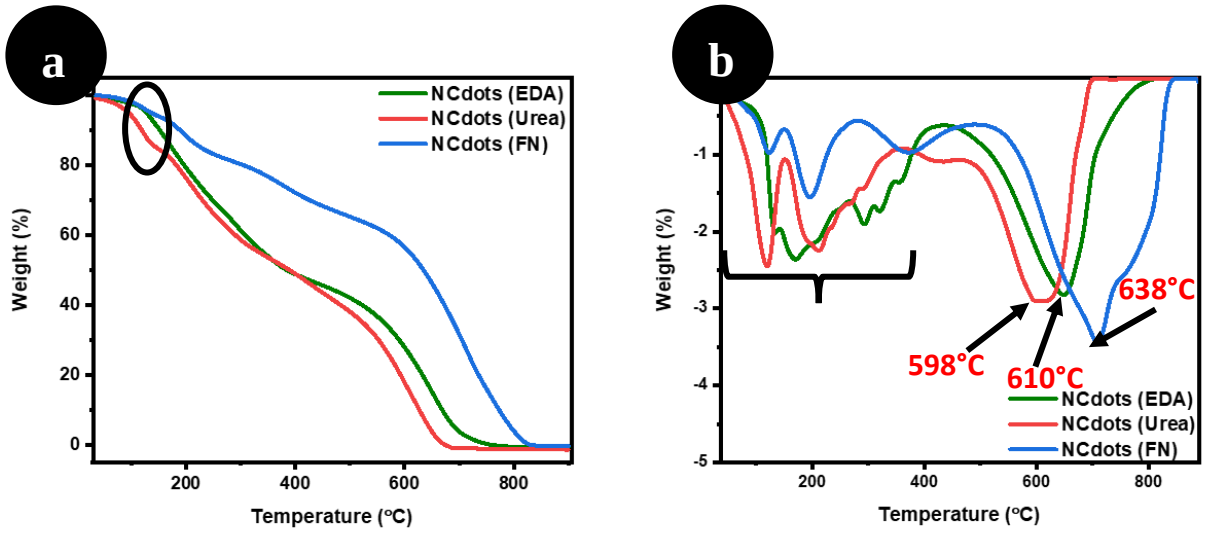

Figure 4.10: Shows the percentage weight loss as a function of temperature; a) TGA profiles for the produced NCdots, and b) DTA curves for NCdots.

4.3.8. Fourier transmission infrared spectroscopy (FTIR) analysis

Functional group types on the surface of NCdots have a crucial role in determining their chemical, physical, and optical properties [108] (**Fig 4.11**). The FTIR spectra of the NCdots were all similar. They showed extensive absorption bands in the 3235 cm^{-1} region, which may be attributed to the distinctive vibrations of O-H or/and N-H groups, while the peak at 2240 cm^{-1} can be attributed to a C≡N group [40]. While the peaks in the range of 1600 to 1400 cm^{-1} can be attributed to the C=C (ca. 1548 cm^{-1}) stretching vibrations of aromatic hydrocarbons, the peak at 1687 cm^{-1} indicates the C=O stretching band.[109]. The stretching and bending vibrations C-N

(1380 cm^{-1}), C-O (1467 cm^{-1}) and C-H (769 cm^{-1}) were also ascribed to the peaks below 1500 cm^{-1} [33, 39-40, 108-110].

To understand these results, a consideration by Li's group was adopted. The usage of the microwave method and the reactants have an impact on the existence of the different functional groups [110]. Urea includes -C=O and -NH_2 groups, while citric acid has -COOH and -OH polar groups (**Fig 4.2**). It was suggested that as citric acid and urea are both polar molecules, thus microwave radiation allows the O=C–NH links to be formed [110]. When exposed to microwave radiation, the various monomers will dehydrate one another, causing the polymerization of the amide species.

These findings demonstrate that the surface of the NCdots contains many functional groups, including O-H, N-H, and maybe -COOH, making them very soluble in water. Additionally, these functional groups can serve as linkers to bind biomolecules, resulting in the formation of NCdots as nano-carriers [39,111]. These outcomes are comparable to those obtained by Koteswararao et al. [112] who quickly microwave aided solid-state approach to synthesize highly fluorescent N-doped carbon dots, which is what was used in this investigation.

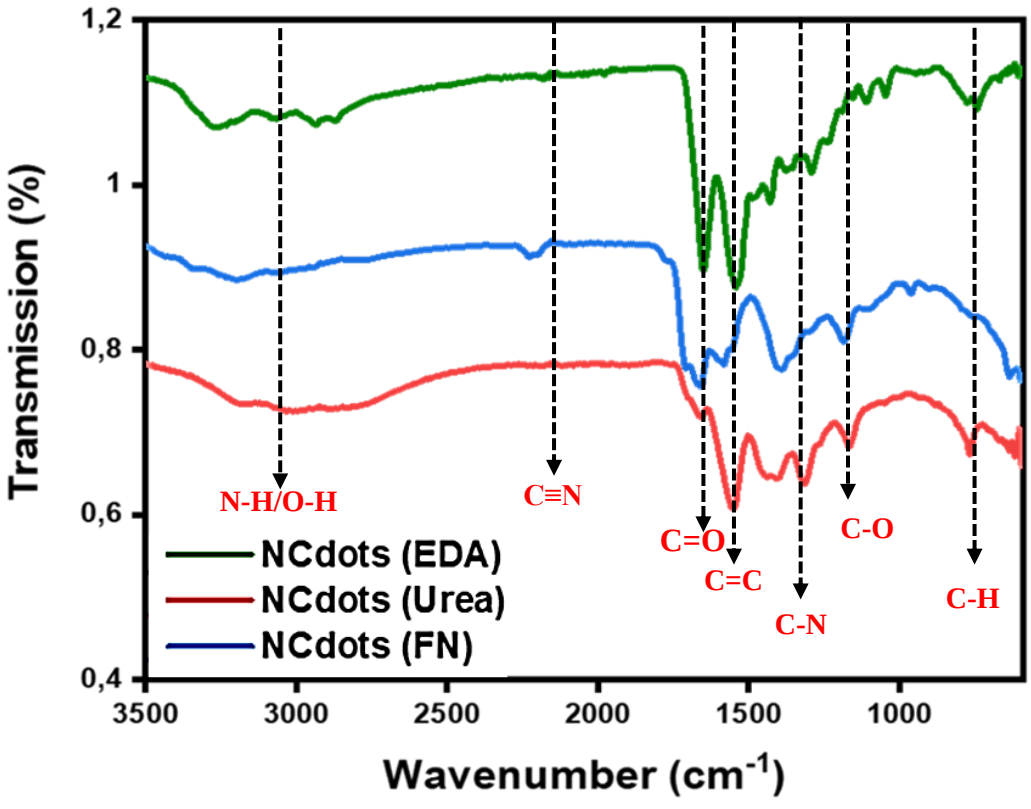

Figure 4.11: FTIR spectra of all as-prepared NCdots.

4.3.9. X-ray photoelectron spectroscopy (XPS) analysis

The three NCdots samples' surface composition was investigated using XPS analysis. The samples are mostly made up of the elements C (59–61 at. %) and N (17–26 at.%), with varying quantities of O (12–15 at.%) as shown in **Table 4.6** below. The interior levels of C 1s, O 1s, and N 1s were then scanned in great detail. Utilizing the CasaXPS program, data processing via peak fitting and deconvolution revealed potential chemical groupings and their relative contributions.

Figure. 4.12 below shows the XPS full scan spectrum of NCdots (EDA) as well as the high resolution spectra of C1s, N1s and O1s after deconvolution. **Figure. 4.12 a** presents three predominant peaks which are all attributed to the carbon (C1s), nitrogen (N1s) and oxygen (O1s) with atomic percentages of 61.9 %, 22.3 % and 15.7 % respectively. The high-resolution spectrum of C1s (**Figure 4.12 b**) revealed three different peaks at 285.0 eV (13.3 at. %), 286.3 eV (32.3 at. %) and 288.1 eV (15.6 at. %) which were assigned to C-C sp^2, C-O and C=O, respectively [113]. The high resolution spectrum of N1s (**Figure 4.12 c**) was deconvoluted into a single peak located at 400.1 which was assigned to an organic graphitic nitrogen, the pyrrolic N [114-116]. Furthermore, the deconvolution of the high-resolution spectrum of O1s (**Figure 4.12 d**) revealed two signals at 531.6 eV and 533.5 eV which are associated with C-O and C=O (or N-C=O group) with 15.5 % and 0.7 % atomic percentage, respectively [117]. Christe observed similar results [37].

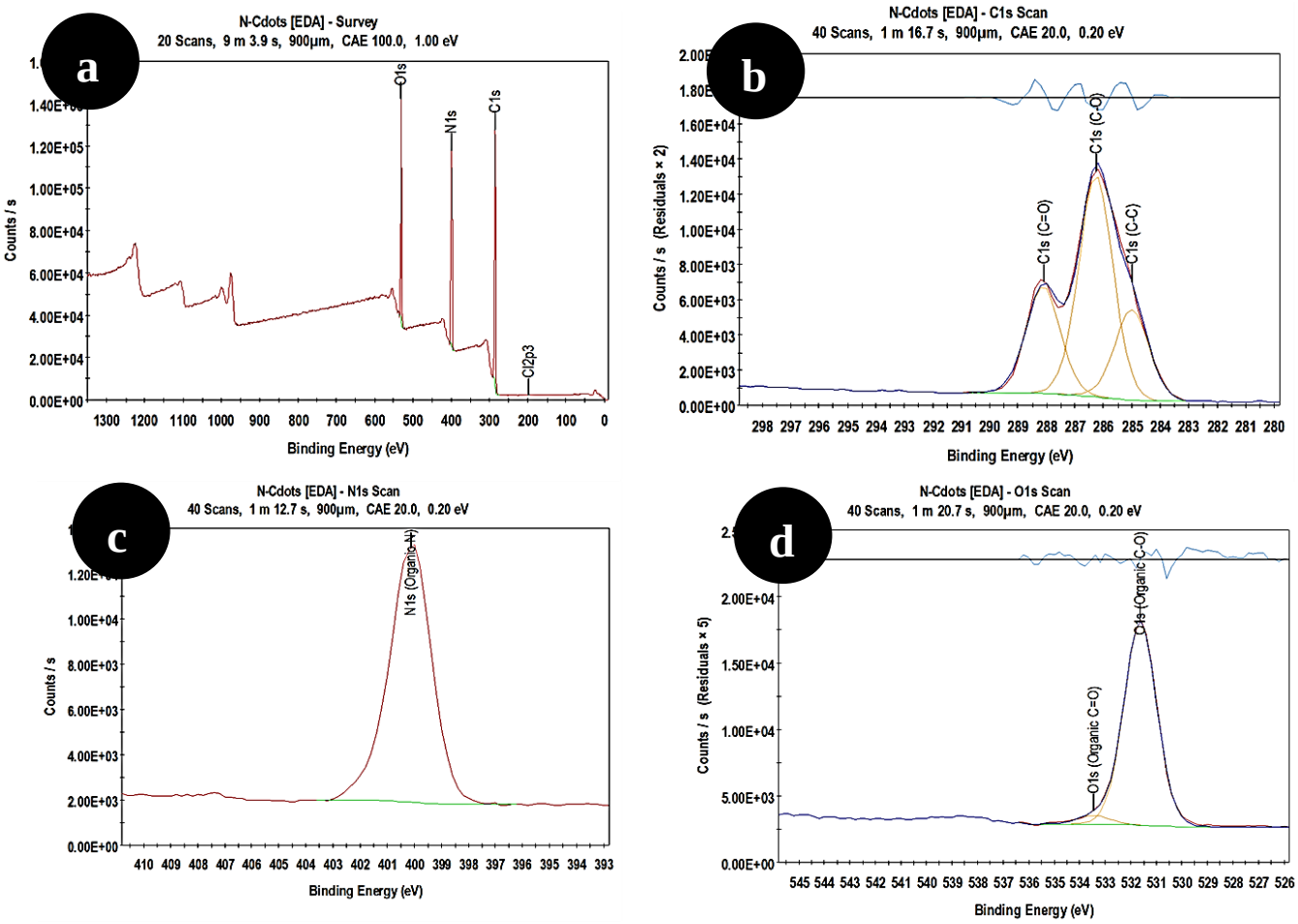

Figure 4.12: a) XPS full scan spectrum, and the corresponding high-resolution spectra of b) C1s, c) N1s, and d) O1s of the as-synthesized NCdots (EDA).

Three peaks at 285.1 eV, 400.3 eV, and 531.8 eV in the entire XPS scan spectra of NCdots (Urea), **Figure 4.13 a**, are assigned to the C1s, N1s, and O1s with atomic percentages of 61.5 percent, 26.2 percent, and 12.3 percent, respectively. Three separate forms of carbon were also seen in the high-resolution C1s spectra (**Figure 4.13 b**) at 284.7 eV, 286.5 eV, and 288.2 eV which were assigned to C-C sp^2, C-O and C=O, respectively. The deconvolution of the high resolution spectrum of N1s (**Figure 4.11 c**) resulted in two different types of nitrogen atoms located at 399.9 eV (9.2 at. %) and 401.1 eV (3.9 at. %) pyridinic and pyrrolic N, respectively. These results are similar to those reported previously [118]. The high resolution spectrum of O1s (**Figure 4.13 d**) revealed two peaks at 531.5 eV and 533.0 eV which are attributed to C-O (20.6 at. %) and C=O (6 at. %), respectively.

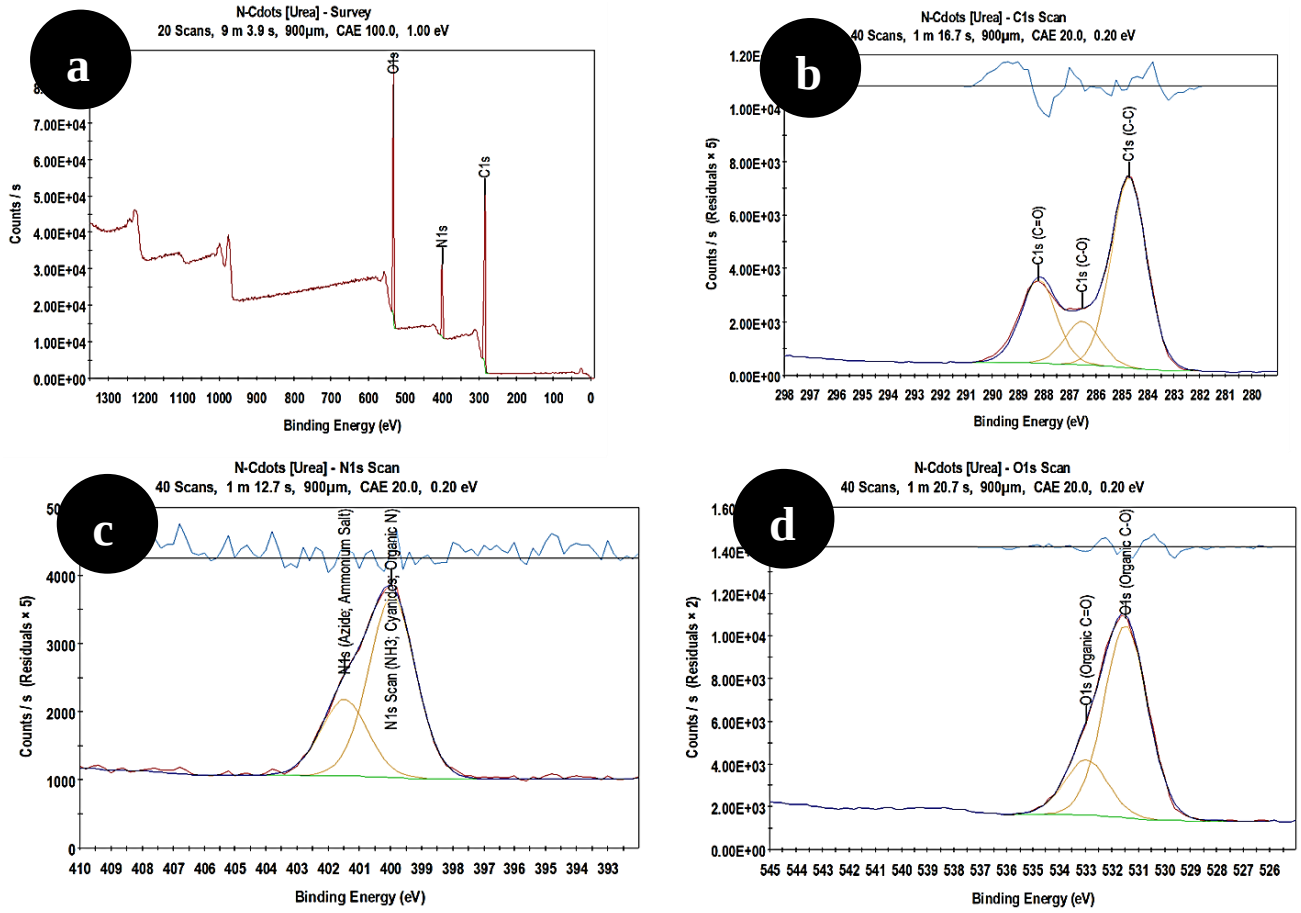

Figure 4.13: a) XPS full scan spectrum, and the corresponding high-resolution spectra of b) C1s, c) N1s, and d) O1s of the as-synthesized NCdots (Urea).

NCdots (FN) contained a different elemental composition and atomic percentages compared to the NCdots (EDA) and NCdots (Urea). As shown in **Figure 4.14 a** below, the XPS full scan spectrum of NCdots (FN) revealed three main peaks at 284.9 eV (59.1 at. %), 399.4 eV (14.2 at. %) and 531.9 eV (17.3 at. %) which are attributed to the C1s, N1s and O1s respectively. The atomic weight percentages were calculated to be 38.2 %, 14.8 % and 6 %, respectively. The high-resolution C1s peak (**Figure 4.14 b**) also showed three different types of carbon at 284.2 eV, 286.0 eV and 288.2 eV which were assigned to C-C sp^2 hybridisation, C-O and C=O, respectively. The deconvolution of high resolution spectrum of N1s (**Figure 4.14 c**) resulted in a single type of nitrogen atoms located at 399.2 eV was due to pyridinic N [119]. The high resolution spectrum of O1s (**Figure 4.14 d**) also revealed a single peak at 531.7 eV which was attributed to C-O. Even though, FN as the starting material for NCdots (FN) has no silicon containing groups, Si signals were observed assigned to Si2p at binding energy of 101.8 eV (at 9.4 at. %). The sample might have been contaminated during sample preparation. This is surface

SiO_2 (not observed in the TGA) and results from scraping of the carbon materials off the glass surfaces.

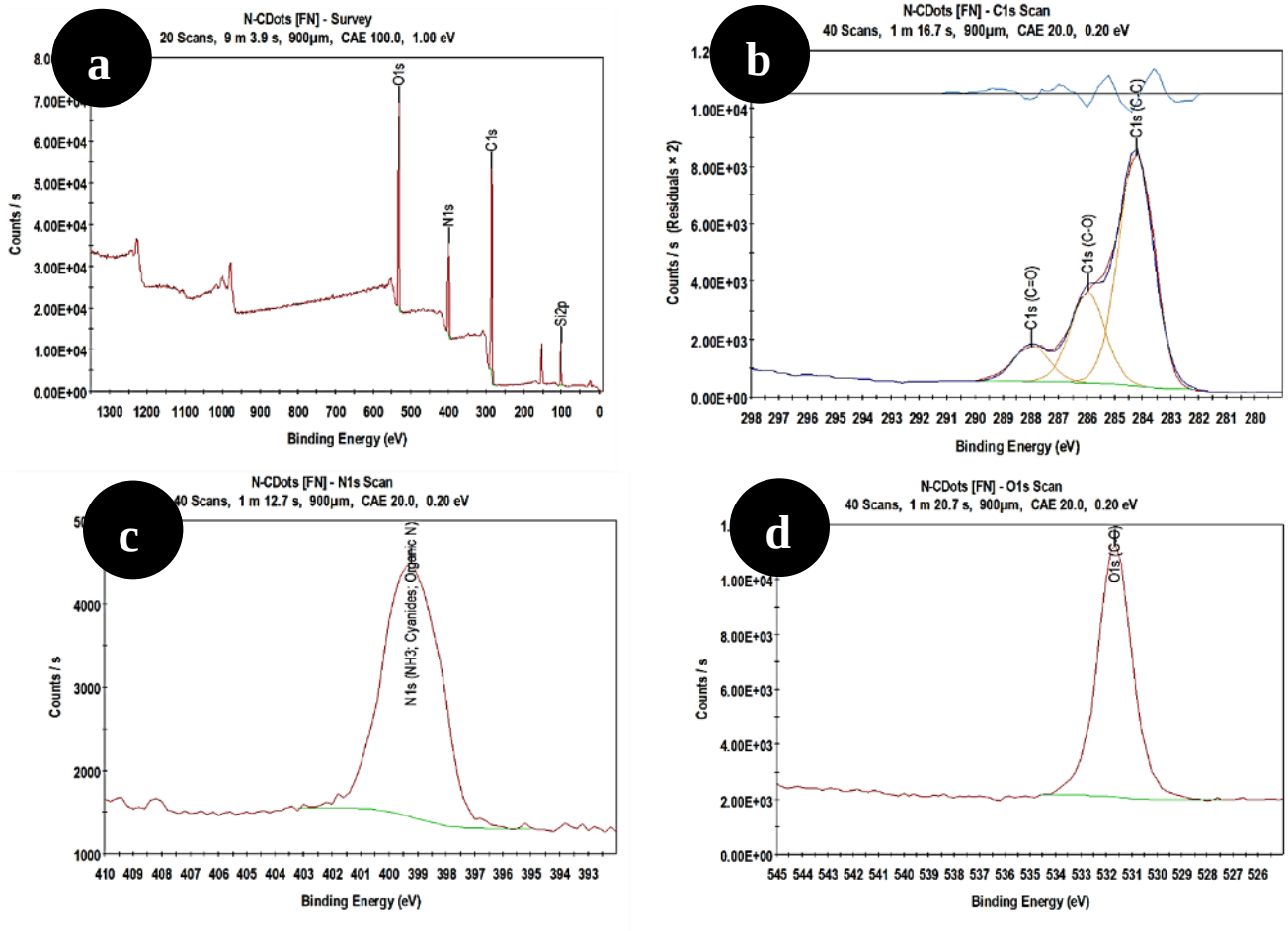

Figure 4.14: a) XPS full scan spectrum, and the corresponding high-resolution spectra of b) C1s, c) N1s, and d) O1s of the as-synthesized NCdots (FN).

Table 4.6 The relative percentage composition of the as-synthesized NCdots from XPS spectroscopy.

	Atomic percentage			
Sample name	C (%)	N (%)	O (%)	Impurities (%)
NCdots (EDA)	61.9	22.3	15.7	0.1
NCdots (Urea)	61.5	26.2	12.3	-
NCdots (FN)	59.1	17.3	14.2	9.4

The XPS results of all NCdots showed that nitrogen doping of the NCdots was successful during microwave synthesis. It is assumed that the surface concentration will be no different from that found in the bulk. The nitrogen concentration of NCdots (Urea) was the highest of the three NCdots varieties. The nitrogen content of all as-synthesised NCdots was greater than previously reported values for the identical NCdots in the literature. This might be due to the synthesis process used in this work, which indicated that the monomers experienced considerable carbonization during polymerization to generate nitrogen-doped carbon dots.

4.3.10. Elemental (CHNS) analysis

Elemental analysis of the NCdots in weight percentage (wt.%) are summarised in **Table 4.7**. The C wt.% across all three samples are above 40 %, thus indicating these dots are carbon rich nanodots. The H wt.% was below 10% for all Cdots and there was no significant variation in H composition observed between the various NCdots.

The NCdots have variable amounts of elemental nitrogen. Compared to NCdots (EDA) and NCdots (Urea), NCdots (FN) had the largest concentration of N atoms (CHNS analysis) and the lowest N atomic composition (XPS analysis). NCdots (Urea), was observed to present with the lowest N atom concentration and the greatest N atomic composition.

Despite the fact that both techniques can be used to determine the sample composition, the main signal in XPS comes from the surface (a few atomic layers at the surface, say a few nanometer) due to electron escape depth, whereas CHNS analysis effectively gives the "bulk" concentration of elements present in a sample, but very little information about the speciation or oxidation state of each element. CHNS analysis is an elemental analysis instrument, which means it can only detect elements, determine their composition, and determine sample purity. XPS, on the other hand, provides information on the sample's chemical composition at the surface and the binding energies that arise [120]. As a result, XPS and CHNS analyses give complimentary information about a sample, however the information is usually fairly different due to variances in surface and bulk chemical compositions.

Table 4.5: Summary of the CHN-S analysis results.

Elemental Composition (%)				
Sample reference	C	H	N	S
NCdots (EDA	48.89	7.061	22.44	-
NCdots (Urea)	42.69	5.292	14.01	-
NCdots (FN)	50.36	4.057	27.28	-

4.3.11. Atomic Force Microscopy (AFM) analysis

Using AFM tests, the surface roughness of all the freshly manufactured NCdots was assessed at room temperature. Drops of a dilute aqueous dispersion of the produced NCdots were placed on glass and silicon surfaces in a conventional process for AFM investigation. The surface roughness (RMS) and maximum roughness depth (R_{max}, which is the largest single roughness depth within the evaluation length) values were evaluated and compared to tapping mode AFM data using the 50-objective lens. The 10-objective lens was helpful in determining the diverse undulations by seeing the undulations (when observed) on a larger scale. The surface topography of the NCdots, the visualization of roughness morphology, and the link with the various nitrogen dopants utilized are discussed.

Figure 4.15 illustrates the two dimensional (2D) images of the synthesised NCdots which was randomly arranged on the silicon wafer substrate at low magnification (2 µm). The three dimensional (3D) images of NCdots were observed with corresponding two dimensional image analysis. **Fig. 4.15 a and b** (2D and 3D images) show pink 'blobs' of agglomerated substances on the surface of the NCdots (EDA) and NCdots (Urea), respectively. These sites of agglomeration are not visible for NCdots (FN) **Fig. 4.15 c**.

The RMS was found to be 0.802 nm, 2.235 nm, and 1.346 nm for NCdots (EDA), NCdots (Urea), and NCdots (FN), respectively. It was discovered that the R_{max} of NCdots (EDA), NCdots (Urea), and NCdots (FN) were, respectively, 2.295 nm, 2.096 nm, and 0.810 nm. More roughness was seen on the surface and in-depth investigation (R_{max} values). These findings suggest that NCdots (EDA) and NCdots (Urea) were agglomerated on the surface, with clusters of particles visible, as opposed to what was seen for the NCdots (FN) images, which were extremely smooth. It was possible to discern quite homogenous, practically spherical particles

that are devoid of any agglomeration. This could be because NCdots (FN) were more crystalline as confirmed by both PXRD and Raman data (**Figs 4.4 and 4.6**, respectively).

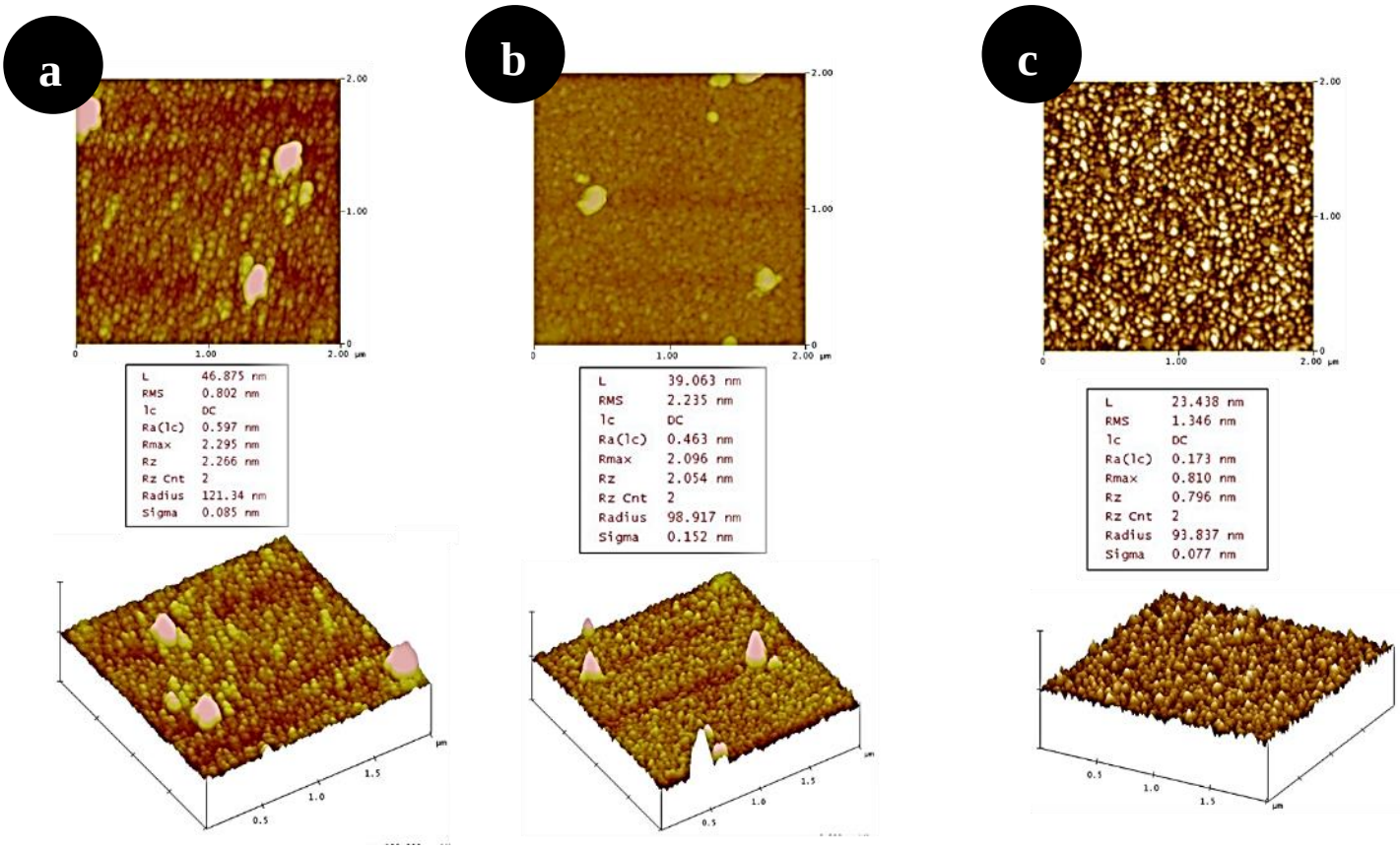

Figure 4.15: AFM images of a) NCdots (EDA), b) NCdots (Urea) and c) NCdots (FN) and their corresponding section analysis as well as 3D surface image analysis.

4.3.12. Olympus fluorescent microscope (OFM) analysis

In line with findings from Sec. 4.3.4, fluorescent microscope pictures were taken using an Olympus BX63 fluorescent microscope. The stimulation of fluorophores and subsequent detection of the fluorescent signal are both possible with OFM. The strong fluorescence characteristic of NCdots with varying bandwidths is revealed by fluorescence microscopic experiments.

The NCdots particles were seen with black emission under a UV-filter and green emission under a red filter as shown in **Fig.4.16 a-f**. Thus, a range of fluorescence emission was observed under green fluorescence [121]. This result is consistent with previous reports [122, 123].

Fig. 4.16 a and d show fluorescent images of NCdots (EDA) which had a different image morphology compared the other NCdots. The imaging looks like it has water molecules present and that is because NCdots (EDA) are very hygroscopic in ambient conditions when dried. All NCdots have relatively high avidity to moisture in the air, however for NCdots (EDA) have a higher affinity thus they were paste-like during analysis.

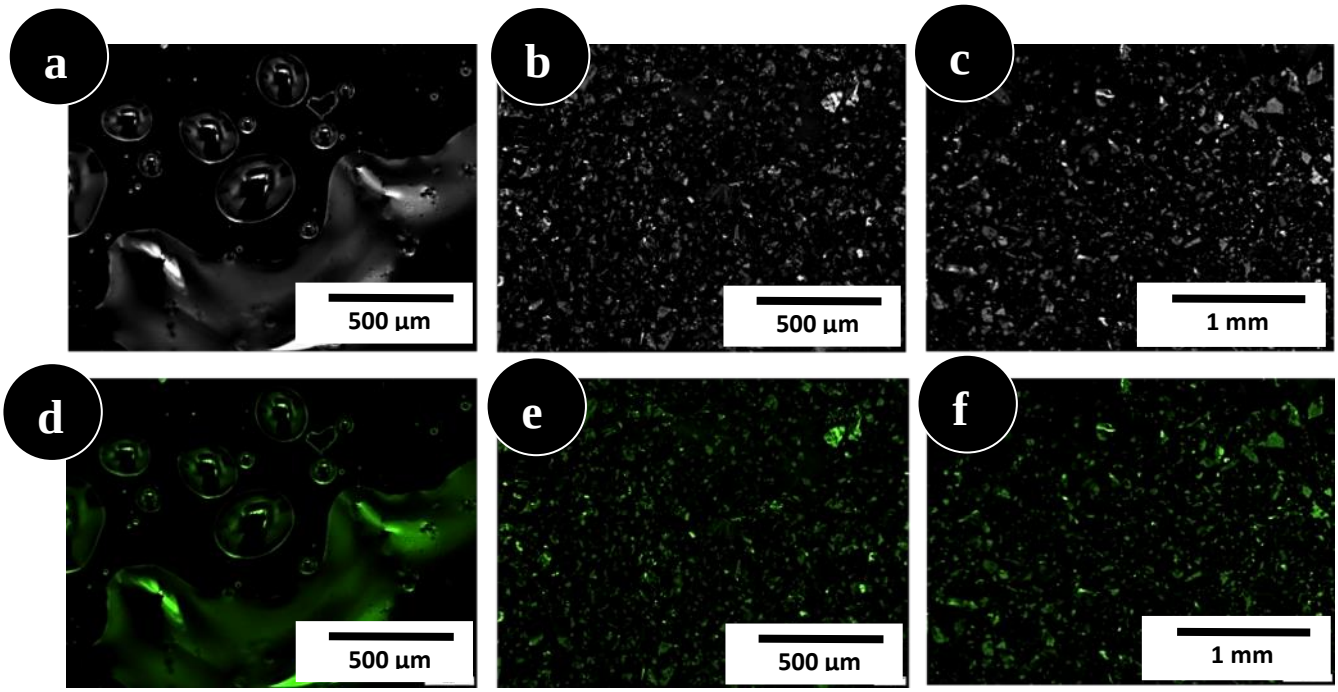

Figure 4.16: OFM images of a) NCdots (EDA), b) NCdots (Urea) and c) NCdots (FN).and their corresponding green field images d), e) and f), respectively.

4.4.Conclusion

In this study, the hydrothermal microwave irradiation process was used to synthesize NCdots with a high fluorescence. Three different N-precursors were used viz, citric acid and ethylenediamine, citric acid and urea, and fumaronitrile. The route proved to be a simple, cost-effective, one-step microwave synthesis pathway towards the production water-soluble luminous NCdots. The NCdots' highest quantum yield in aqueous solutions with persistent, excitation-wavelength-dependent PL features was 15% (EDA). According to FTIR, XPS, and CHNS tests, the NCdots all exhibited a high nitrogen-atom concentration both on the surface and in the bulk. Excitation wavelength dependent studies' findings are compatible with the effects of doping on Cdots and the dynamics of their excited states. The decay lifetime as well as quantum yield values obtained for NCdots (EDA) indicate a highly emissive molecular state with a long lifetime. This indicates that the additional intersystem crossover brought on by the

longer NCdot lifetime can improve the DSSC's efficiency (which would accelerate the dissociation of the excitons in the system). Furthermore, the data showed that the production of NCdots is dependent on the type of precursor used.

References

1. Xu, X., Ray, R., Gu, Y., Ploehn, H. J., Gearheart, L., Raker, K., & Scrivens, W. A. (2004). Electrophoretic Analysis and Purification of Fluorescent Single-Walled Carbon Nanotube Fragments. *Journal of the American Chemical Society*, 126(40), 12736–12737. https://doi.org/10.1021/ja040082h
2. Cayuela, A., Soriano, M. L., Carrillo-Carrión, C., & Valcárcel, M. (2016). Semiconductor and carbon-based fluorescent nanodots: the need for consistency. *Chemical Communications*, *52*(7), 1311–1326. https://doi.org/10.1039/c5cc07754k
3. Xia, C., Zhu, S., Feng, T., Yang, M., & Yang, B. (2019). Evolution and Synthesis of Carbon Dots: From Carbon Dots to Carbonized Polymer Dots. *Advanced Science*, *6*(23), 1901316. https://doi.org/10.1002/advs.201901316
4. Gonçalves, H., Jorge, P. A., Fernandes, J., & Esteves Da Silva, J. C. (2010). Hg(II) sensing based on functionalized carbon dots obtained by direct laser ablation. *Sensors and Actuators B: Chemical*, *145*(2), 702–707. https://doi.org/10.1016/j.snb.2010.01.031
5. Huang, D., Zhou, H., Wu, Y., Wang, T., Sun, L., Gao, P., Sun, Y., Huang, H., Zhou, G., & Hu, J. (2019). Bottom-up synthesis and structural design strategy for graphene quantum dots with tunable emission to the near infrared region. *Carbon*, *142*, 673–684. https://doi.org/10.1016/j.carbon.2018.10.047
6. Sharma, A., & Das, J. (2019). Small molecules derived carbon dots: synthesis and applications in sensing, catalysis, imaging, and biomedicine. *Journal of Nanobiotechnology*, *17*(1). https://doi.org/10.1186/s12951-019-0525-8
7. Feng, X., Wu, J., Ai, M., Pisula, W., Zhi, L., Rabe, J., & Müllen, K. (2007). Triangle-Shaped Polycyclic Aromatic Hydrocarbons. *Angewandte Chemie International Edition*, *46*(17), 3033–3036. https://doi.org/10.1002/anie.200605224
8. Yan, X., Cui, X., & Li, L. S. (2010). Synthesis of Large, Stable Colloidal Graphene Quantum Dots with Tunable Size. *Journal of the American Chemical Society*, *132*(17), 5944–5945. https://doi.org/10.1021/ja1009376
9. Preview: Angew. Chem. Int. Ed. 50/2010. (2010). *Angewandte Chemie International Edition*, *49*(49), 9537. https://doi.org/10.1002/anie.201090155
10. Zhou, Y., Benetti, D., Tong, X., Jin, L., Wang, Z. M., Ma, D., Zhao, H., & Rosei, F. (2018). Colloidal carbon dots based highly stable luminescent solar concentrators. *Nano Energy*, *44*, 378–387. https://doi.org/10.1016/j.nanoen.2017.12.017

11. Xu, J., Miao, Y., Zheng, J., Wang, H., Yang, Y., & Liu, X. (2018). Carbon dot-based white and yellow electroluminescent light emitting diodes with a record-breaking brightness. *Nanoscale*, *10*(23), 11211–11221. https://doi.org/10.1039/c8nr01834k
12. Hu, L., Li, H., Liu, C., Song, Y., Zhang, M., Huang, H., Liu, Y., & Kang, Z. (2018). Chiral evolution of carbon dots and the tuning of laccase activity. *Nanoscale, 10*(5), 2333–2340. https://doi.org/10.1039/c7nr08335a
13. Liu, C., Fu, Y., Xia, Y., Zhu, C., Hu, L., Zhang, K., Wu, H., Huang, H., Liu, Y., Xie, T., Zhong, J., & Kang, Z. (2018). Cascaded photo-potential in a carbon dot-hematite system driving overall water splitting under visible light. *Nanoscale*, *10*(5), 2454–2460. https://doi.org/10.1039/c7nr08000j
14. Ding, Z., Li, F., Wen, J., Wang, X., & Sun, R. (2018). Gram-scale synthesis of single-crystalline graphene quantum dots derived from lignin biomass. *Green Chemistry*, *20*(6), 1383–1390. https://doi.org/10.1039/c7gc03218h
15. Essner, J. B., & Baker, G. A. (2017). The emerging roles of carbon dots in solar photovoltaics: a critical review. *Environmental Science: Nano*, *4*(6), 1216–1263. https://doi.org/10.1039/c7en00179g
16. Wang, W. J., Xia, J. M., Hai, X., Chen, M. L., & Wang, J. H. (2017). A hybrid of carbon dots with 4-chloro-7-nitro-2,1,3-benzoxadiazole for selective detection of p-phenylenediamine. *Environmental Science: Nano*, *4*(5), 1037–1044. https://doi.org/10.1039/c7en00027h
17. Lu, X., Zhang, J., Xie, Y. N., Zhang, X., Jiang, X., Hou, X., & Wu, P. (2018). Ratiometric Phosphorescent Probe for Thallium in Serum, Water, and Soil Samples Based on Long-Lived, Spectrally Resolved, Mn-Doped ZnSe Quantum Dots and Carbon Dots. *Analytical Chemistry*, *90*(4), 2939–2945. https://doi.org/10.1021/acs.analchem.7b05365
18. Ren, J., Sun, X., Wang, Y., Song, R., Xie, Z., Zhou, S., & Chen, P. (2018). Controllable Photoluminescent and Nonlinear Optical Properties of Polymerizable Carbon Dots and Their Arbitrary Copolymerized Gel Glasses. *Advanced Optical Materials*, *6*(12), 1701273. https://doi.org/10.1002/adom.201701273
19. Li, S., Amat, D., Peng, Z., Vanni, S., Raskin, S., de Angulo, G., Othman, A. M., Graham, R. M., & Leblanc, R. M. (2016). Transferrin conjugated nontoxic carbon dots for doxorubicin delivery to target pediatric brain tumor cells. *Nanoscale*, *8*(37), 16662–16669. https://doi.org/10.1039/c6nr05055g

20. Sun, Y. P., Zhou, B., Lin, Y., Wang, W., Fernando, K. A. S., Pathak, P., Meziani, M. J., Harruff, B. A., Wang, X., Wang, H., Luo, P. G., Yang, H., Kose, M. E., Chen, B., Veca, L. M., & Xie, S. Y. (2006). Quantum-Sized Carbon Dots for Bright and Colorful Photoluminescence. *Journal of the American Chemical Society*, *128*(24), 7756–7757. https://doi.org/10.1021/ja062677d
21. Chen, B. B., Liu, M. L., Li, C. M., & Huang, C. Z. (2019). Fluorescent carbon dots functionalization. *Advances in Colloid and Interface Science*, *270*, 165–190. https://doi.org/10.1016/j.cis.2019.06.008
22. Zhou, J., Zhou, H., Tang, J., Deng, S., Yan, F., Li, W., & Qu, M. (2016). Carbon dots doped with heteroatoms for fluorescent bioimaging: a review. *Microchimica Acta*, *184*(2), 343–368. https://doi.org/10.1007/s00604-016-2043-9
23. Ferreyra, D. D., Rodríguez Sartori, D., Ezquerra Riega, S. D., Rodríguez, H. B., & Gonzalez, M. C. (2020). Tuning the nitrogen content of carbon dots in carbon nitride nanoflakes. *Carbon*, *167*, 230–243. https://doi.org/10.1016/j.carbon.2020.05.062
24. Martindale, B. C. M., Hutton, G. A. M., Caputo, C. A., & Reisner, E. (2015). Solar Hydrogen Production Using Carbon Quantum Dots and a Molecular Nickel Catalyst. *Journal of the American Chemical Society*, *137*(18), 6018–6025. https://doi.org/10.1021/jacs.5b01650
25. Liao, J., Cheng, Z., & Zhou, L. (2016). Nitrogen-Doping Enhanced Fluorescent Carbon Dots: Green Synthesis and Their Applications for Bioimaging and Label-Free Detection of Au^{3+} Ions. *ACS Sustainable Chemistry & Engineering*, *4*(6), 3053–3061. https://doi.org/10.1021/acssuschemeng.6b00018
26. Xu, M., He, G., Li, Z., He, F., Gao, F., Su, Y., Zhang, L., Yang, Z., & Zhang, Y. (2014). A green heterogeneous synthesis of N-doped carbon dots and their photoluminescence applications in solid and aqueous states. *Nanoscale*, *6*(17), 10307–10315. https://doi.org/10.1039/c4nr02792b
27. Du, Y., & Guo, S. (2016). Chemically doped fluorescent carbon and graphene quantum dots for bioimaging, sensor, catalytic and photoelectronic applications. *Nanoscale*, *8*(5), 2532–2543. https://doi.org/10.1039/c5nr07579c
28. Liu, Y., Jiang, L., Li, B., Fan, X., Wang, W., Liu, P., Xu, S., & Luo, X. (2019). Nitrogen doped carbon dots: mechanism investigation and their application for label free CA125 analysis. *Journal of Materials Chemistry B*, *7*(19), 3053–3058. https://doi.org/10.1039/c9tb00021f

29. Zhu, S., Zhang, J., Tang, S., Qiao, C., Wang, L., Wang, H., Liu, X., Li, B., Li, Y., Yu, W., Wang, X., Sun, H., & Yang, B. (2012). Surface Chemistry Routes to Modulate the Photoluminescence of Graphene Quantum Dots: From Fluorescence Mechanism to Up-Conversion Bioimaging Applications. *Advanced Functional Materials*, *22*(22), 4732–4740. https://doi.org/10.1002/adfm.201201499
30. Dong, Y., Pang, H., Yang, H. B., Guo, C., Shao, J., Chi, Y., Li, C. M., & Yu, T. (2013). Carbon-Based Dots Co-doped with Nitrogen and Sulfur for High Quantum Yield and Excitation-Independent Emission. *Angewandte Chemie International Edition*, *52*(30), 7800–7804. https://doi.org/10.1002/anie.201301114
31. Jiang, K., Sun, S., Zhang, L., Lu, Y., Wu, A., Cai, C., & Lin, H. (2015). Red, Green, and Blue Luminescence by Carbon Dots: Full-Color Emission Tuning and Multicolor Cellular Imaging. *Angewandte Chemie*, *127*(18), 5450–5453. https://doi.org/10.1002/ange.201501193
32. Xu, Q., Kuang, T., Liu, Y., Cai, L., Peng, X., Sreenivasan Sreeprasad, T., Zhao, P., Yu, Z., & Li, N. (2016). Heteroatom-doped carbon dots: synthesis, characterization, properties, photoluminescence mechanism and biological applications. *Journal of Materials Chemistry B*, *4*(45), 7204–7219. https://doi.org/10.1039/c6tb02131j
33. Christé, Esteves Da Silva, & Pinto Da Silva. (2020). Evaluation of the Environmental Impact and Efficiency of N-Doping Strategies in the Synthesis of Carbon Dots. *Materials*, *13*(3), 504. https://doi.org/10.3390/ma13030504
34. Titirici, M. M., White, R. J., & Zhao, L. (2012). Nitrogen-doped Hydrothermal Carbons. *Green*, *2*(1), 25–40. https://doi.org/10.1515/green-2011-0023
35. Sendão, R. M. S., Crista, D. M. A., Afonso, A. C. P., Martínez De Yuso, M. D. V., Algarra, M., Esteves Da Silva, J. C. G., & Pinto Da Silva, L. (2019). Insight into the hybrid luminescence showed by carbon dots and molecular fluorophores in solution. *Physical Chemistry Chemical Physics*, *21*(37), 20919–20926. https://doi.org/10.1039/c9cp03730f
36. Qu, D., Sun, Z., Zheng, M., Li, J., Zhang, Y., Zhang, G., Zhao, H., Liu, X., & Xie, Z. (2015). Three Colors Emission from S,N Co-doped Graphene Quantum Dots for Visible Light H_2Production and Bioimaging. *Advanced Optical Materials*, *3*(3), 360–367. https://doi.org/10.1002/adom.201400549
37. Zeng, Q., Shao, D., He, X., Ren, Z., Ji, W., Shan, C., Qu, S., Li, J., Chen, L., & Li, Q. (2016). Carbon dots as a trackable drug delivery carrier for localized cancer therapy in

vivo. *Journal of Materials Chemistry B*, *4*(30), 5119–5126. https://doi.org/10.1039/c6tb01259k

38. Xiong, Y., Schneider, J., Ushakova, E. V., & Rogach, A. L. (2018). Influence of molecular fluorophores on the research field of chemically synthesized carbon dots. *Nano Today*, *23*, 124–139. https://doi.org/10.1016/j.nantod.2018.10.010
39. Kasprzyk, W., ŚWiergosz, T., Bednarz, S., Walas, K., Bashmakova, N. V., & Bogdał, D. (2018). Luminescence phenomena of carbon dots derived from citric acid and urea – a molecular insight. *Nanoscale*, *10*(29), 13889–13894. https://doi.org/10.1039/c8nr03602k
40. Moon, B. J., Oh, Y., Shin, D. H., Kim, S. J., Lee, S. H., Kim, T. W., Park, M., & Bae, S. (2016). Facile and Purification-Free Synthesis of Nitrogenated Amphiphilic Graphitic Carbon Dots. *Chemistry of Materials*, *28*(5), 1481–1488. https://doi.org/10.1021/acs.chemmater.5b04915
41. Mondal, S., Yucknovsky, A., Akulov, K., Ghorai, N., Schwartz, T., Ghosh, H. N., & Amdursky, N. (2019). Efficient Photosensitizing Capabilities and Ultrafast Carrier Dynamics of Doped Carbon Dots. *Journal of the American Chemical Society*, *141*(38), 15413–15422. https://doi.org/10.1021/jacs.9b08071
42. Devi, S., Kaur, A., Sarkar, S., Vohra, S., & Tyagi, S. (2018). Synthesis and characterization of highly luminescent N-doped carbon quantum dots for metal ion sensing. *Integrated Ferroelectrics*, *186*(1), 32–39. https://doi.org/10.1080/10584587.2017.1369322
43. Sendão, R. M. S., Crista, D. M. A., Afonso, A. C. P., Martínez De Yuso, M. D. V., Algarra, M., Esteves Da Silva, J. C. G., & Pinto Da Silva, L. (2019). Insight into the hybrid luminescence showed by carbon dots and molecular fluorophores in solution. *Physical Chemistry Chemical Physics*, *21*(37), 20919–20926. https://doi.org/10.1039/c9cp03730f
44. Liang, Y., Zhang, H., Zhang, Y., & Chen, F. (2015). Simple hydrothermal preparation of carbon nanodots and their application in colorimetric and fluorimetric detection of mercury ions. *Analytical Methods*, *7*(18), 7540–7547. https://doi.org/10.1039/c5ay01301a
45. Tao, S., Song, Y., Zhu, S., Shao, J., & Yang, B. (2017). A new type of polymer carbon dots with high quantum yield: From synthesis to investigation on fluorescence mechanism. *Polymer*, *116*, 472–478. https://doi.org/10.1016/j.polymer.2017.02.039
46. Hou, J., Li, H., Tang, Y., Sun, J., Fu, H., Qu, X., Xu, Z., Yin, D., & Zheng, S. (2018). Supported N-doped carbon quantum dots as the highly effective peroxydisulfate catalysts

for bisphenol F degradation. *Applied Catalysis B: Environmental*, *238*, 225–235. https://doi.org/10.1016/j.apcatb.2018.07.032

47. Yang, J., Frøseth, V., Chen, D., & Holmen, A. (2016). Particle size effect for cobalt Fischer–Tropsch catalysts based on in situ CO chemisorption. *Surface Science*, *648*, 67–73. https://doi.org/10.1016/j.susc.2015.10.029
48. Pinna, N. (2007). The "benzyl alcohol route": an elegant approach towards organic–inorganic hybrid nanomaterials. *J. Mater. Chem.*, *17*(27), 2769–2774. https://doi.org/10.1039/b702854g
49. Peng, S., Fan, X., Li, S., & Zhang, J. (2013). Green synthesis and characterization of graphite oxide by orthogonal experiment. *Journal of the Chilean Chemical Society*, *58*(4), 2213–2217. https://doi.org/10.4067/s0717-97072013000400067
50. Qian, W., Sun, F., Xu, Y., Qiu, L., Liu, C., Wang, S., & Yan, F. (2014). Human hair-derived carbon flakes for electrochemical supercapacitors. *Energy Environ. Sci.*, *7*(1), 379–386. https://doi.org/10.1039/c3ee43111h
51. Puvvada, N., Kumar, B. N. P., Konar, S., Kalita, H., Mandal, M., & Pathak, A. (2012). Synthesis of biocompatible multicolor luminescent carbon dots for bioimaging applications. *Science and Technology of Advanced Materials*, *13*(4), 045008. https://doi.org/10.1088/1468-6996/13/4/045008
52. Gao, T., Du, Y., & Li, H. (2019). Preparation of nitrogen-doped graphitic porous carbon towards capacitive deionization with high adsorption capacity and rate capability. *Separation and Purification Technology*, *211*, 233–241. https://doi.org/10.1016/j.seppur.2018.09.085
53. Papaioannou, N., Marinovic, A., Yoshizawa, N., Goode, A. E., Fay, M., Khlobystov, A., Titirici, M. M., & Sapelkin, A. (2018). Structure and solvents effects on the optical properties of sugar-derived carbon nanodots. *Scientific Reports*, *8*(1). https://doi.org/10.1038/s41598-018-25012-8
54. Atchudan, R., Edison, T. N. J. I., & Lee, Y. R. (2016). Nitrogen-doped carbon dots originating from unripe peach for fluorescent bioimaging and electrocatalytic oxygen reduction reaction. *Journal of Colloid and Interface Science*, *482*, 8–18. https://doi.org/10.1016/j.jcis.2016.07.058
55. Safardoust-Hojaghan, H., Salavati-Niasari, M., Amiri, O., & Hassanpour, M. (2017). Preparation of highly luminescent nitrogen doped graphene quantum dots and their application as a probe for detection of Staphylococcus aureus and E. coli. *Journal of Molecular Liquids*, *241*, 1114–1119. https://doi.org/10.1016/j.molliq.2017.06.106

56. Yang, Z., Xu, M., Liu, Y., He, F., Gao, F., Su, Y., Wei, H., & Zhang, Y. (2014). Nitrogen-doped, carbon-rich, highly photoluminescent carbon dots from ammonium citrate. *Nanoscale*, *6*(3), 1890–1895. https://doi.org/10.1039/c3nr05380f
57. Liu, X., Pang, J., Xu, F., & Zhang, X. (2016). Simple Approach to Synthesize Amino-Functionalized Carbon Dots by Carbonization of Chitosan. *Scientific Reports*, *6*(1). https://doi.org/10.1038/srep31100
58. So, R. C., Sanggo, J. E., Jin, L., Diaz, J. M. A., Guerrero, R. A., & He, J. (2017). Gram-Scale Synthesis and Kinetic Study of Bright Carbon Dots from Citric Acid and *Citrus japonica* via a Microwave-Assisted Method. *ACS Omega*, *2*(8), 5196–5208. https://doi.org/10.1021/acsomega.7b00551
59. Rao, L., Tang, Y., Lu, H., Yu, S., Ding, X., Xu, K., Li, Z., & Zhang, J. (2018). Highly Photoluminescent and Stable N-Doped Carbon Dots as Nanoprobes for Hg2+ Detection. *Nanomaterials*, *8*(11), 900. https://doi.org/10.3390/nano8110900
60. Mondal, S., Yucknovsky, A., Akulov, K., Ghorai, N., Schwartz, T., Ghosh, H. N., & Amdursky, N. (2019b). Efficient Photosensitizing Capabilities and Ultrafast Carrier Dynamics of Doped Carbon Dots. *Journal of the American Chemical Society*, *141*(38), 15413–15422. https://doi.org/10.1021/jacs.9b08071
61. Nekoueian, K., Amiri, M., Sillanpää, M., Marken, F., Boukherroub, R., & Szunerits, S. (2019). Carbon-based quantum particles: an electroanalytical and biomedical perspective. *Chemical Society Reviews*, *48*(15), 4281–4316. https://doi.org/10.1039/c8cs00445e
62. Lucchese, M., Stavale, F., Ferreira, E. M., Vilani, C., Moutinho, M., Capaz, R. B., Achete, C., & Jorio, A. (2010). Quantifying ion-induced defects and Raman relaxation length in graphene. *Carbon*, *48*(5), 1592–1597. https://doi.org/10.1016/j.carbon.2009.12.057
63. Jorio, A., Lucchese, M. M., Stavale, F., Martins Ferreira, E. H., Moutinho, M. V. O., Capaz, R. B., & Achete, C. A. (2010). Raman study of ion-induced defects in*N*-layer graphene. *Journal of Physics: Condensed Matter*, *22*(33), 334204. https://doi.org/10.1088/0953-8984/22/33/334204
64. Ferrari, A. C. (2007). Raman spectroscopy of graphene and graphite: Disorder, electron–phonon coupling, doping and nonadiabatic effects. *Solid State Communications*, *143*(1–2), 47–57. https://doi.org/10.1016/j.ssc.2007.03.052
65. Antunes, E., Lobo, A., Corat, E., Trava-Airoldi, V., Martin, A., & Veríssimo, C. (2006). Comparative study of first- and second-order Raman spectra of MWCNT at visible and

infrared laser excitation. *Carbon*, *44*(11), 2202–2211. https://doi.org/10.1016/j.carbon.2006.03.003

66. Bandi, R., Dadigala, R., Gangapuram, B. R., & Guttena, V. (2018). Green synthesis of highly fluorescent nitrogen – Doped carbon dots from Lantana camara berries for effective detection of lead(II) and bioimaging. *Journal of Photochemistry and Photobiology B: Biology*, *178*, 330–338. https://doi.org/10.1016/j.jphotobiol.2017.11.010
67. Wang, X., Cao, L., Yang, S. T., Lu, F., Meziani, M., Tian, L., Sun, K., Bloodgood, M., & Sun, Y. P. (2010). Bandgap-Like Strong Fluorescence in Functionalized Carbon Nanoparticles. *Angewandte Chemie International Edition*, *49*(31), 5310–5314. https://doi.org/10.1002/anie.201000982
68. Liu, R., Wu, D., Liu, S., Koynov, K., Knoll, W., & Li, Q. (2009). An Aqueous Route to Multicolor Photoluminescent Carbon Dots Using Silica Spheres as Carriers. *Angewandte Chemie International Edition*, *48*(25), 4598–4601. https://doi.org/10.1002/anie.200900652
69. Iijima, S. (1991). Helical microtubules of graphitic carbon. *Nature*, *354*(6348), 56–58. https://doi.org/10.1038/354056a0
70. Li, D., Jing, P., Sun, L., An, Y., Shan, X., Lu, X., Zhou, D., Han, D., Shen, D., Zhai, Y., Qu, S., Zbořil, R., & Rogach, A. L. (2018). Carbon Dots: Near-Infrared Excitation/Emission and Multiphoton-Induced Fluorescence of Carbon Dots (Adv. Mater. 13/2018). *Advanced Materials*, *30*(13), 1870092. https://doi.org/10.1002/adma.201870092
71. Liao, J., Cheng, Z., & Zhou, L. (2016b). Nitrogen-Doping Enhanced Fluorescent Carbon Dots: Green Synthesis and Their Applications for Bioimaging and Label-Free Detection of Au^{3+} Ions. *ACS Sustainable Chemistry & Engineering*, *4*(6), 3053–3061. https://doi.org/10.1021/acssuschemeng.6b00018
72. Song, Z., Quan, F., Xu, Y., Liu, M., Cui, L., & Liu, J. (2016). Multifunctional N,S co-doped carbon quantum dots with pH- and thermo-dependent switchable fluorescent properties and highly selective detection of glutathione. *Carbon*, *104*, 169–178. https://doi.org/10.1016/j.carbon.2016.04.003
73. Huang, H., Li, C., Zhu, S., Wang, H., Chen, C., Wang, Z., Bai, T., Shi, Z., & Feng, S. (2014). Histidine-Derived Nontoxic Nitrogen-Doped Carbon Dots for Sensing and Bioimaging Applications. *Langmuir*, *30*(45), 13542–13548. https://doi.org/10.1021/la503969z

74. Wu, J., Wen, C., Zou, X., Jimenez, J., Sun, J., Xia, Y., Fonseca Rodrigues, M. T., Vinod, S., Zhong, J., Chopra, N., Odeh, I. N., Ding, G., Lauterbach, J., & Ajayan, P. M. (2017). Carbon Dioxide Hydrogenation over a Metal-Free Carbon-Based Catalyst. *ACS Catalysis*, *7*(7), 4497–4503. https://doi.org/10.1021/acscatal.7b00729
75. Sciortino, A., Mauro, N., Buscarino, G., Sciortino, L., Popescu, R., Schneider, R., Giammona, G., Gerthsen, D., Cannas, M., & Messina, F. (2018). β-C3N4 Nanocrystals: Carbon Dots with Extraordinary Morphological, Structural, and Optical Homogeneity. *Chemistry of Materials*, *30*(5), 1695–1700. https://doi.org/10.1021/acs.chemmater.7b05178
76. Hu, Y., Yang, J., Tian, J., & Yu, J. S. (2015). How do nitrogen-doped carbon dots generate from molecular precursors? An investigation of the formation mechanism and a solution-based large-scale synthesis. *Journal of Materials Chemistry B*, *3*(27), 5608–5614. https://doi.org/10.1039/c5tb01005e
77. Strauss, V., Margraf, J. T., Dolle, C., Butz, B., Nacken, T. J., Walter, J., Bauer, W., Peukert, W., Spiecker, E., Clark, T., & Guldi, D. M. (2014). Carbon Nanodots: Toward a Comprehensive Understanding of Their Photoluminescence. *Journal of the American Chemical Society*, *136*(49), 17308–17316. https://doi.org/10.1021/ja510183c
78. Auweter, H., Haberkorn, H., Heckmann, W., Horn, D., Lüddecke, E., Rieger, J., & Weiss, H. (1999). Supramolecular Structure of Precipitated Nanosize β-Carotene Particles. *Angewandte Chemie International Edition*, *38*(15), 2188–2191. https://doi.org/10.1002/(sici)1521-3773(19990802)38:15
79. Li, H., Kang, Z., Liu, Y., & Lee, S. T. (2012). Carbon nanodots: synthesis, properties and applications. *Journal of Materials Chemistry*, *22*(46), 24230. https://doi.org/10.1039/c2jm34690g
80. Wang, D., Wang, Z., Zhan, Q., Pu, Y., Wang, J. X., Foster, N. R., & Dai, L. (2017). Facile and Scalable Preparation of Fluorescent Carbon Dots for Multifunctional Applications. *Engineering*, *3*(3), 402–408. https://doi.org/10.1016/j.eng.2017.03.014
81. Sugiarti, S., & Darmawan, N. (2015). Synthesis of Fluorescence Carbon Nanoparticles from Ascorbic Acid. *Indonesian Journal of Chemistry*, *15*(2), 141–145. https://doi.org/10.22146/ijc.21207
82. Liu, Q., Zhang, N., Shi, H., Ji, W., Guo, X., Yuan, W., & Hu, Q. (2018). One-step microwave synthesis of carbon dots for highly sensitive and selective detection of copper ions in aqueous solution. *New Journal of Chemistry*, *42*(4), 3097–3101. https://doi.org/10.1039/c7nj05000c

83. S., T., & D., R. S. (2016). Green synthesis of highly fluorescent carbon quantum dots from sugarcane bagasse pulp. *Applied Surface Science*, *390*, 435–443. https://doi.org/10.1016/j.apsusc.2016.08.106
84. Baker, S., & Baker, G. (2010). Luminescent Carbon Nanodots: Emergent Nanolights. *Angewandte Chemie International Edition*, *49*(38), 6726–6744. https://doi.org/10.1002/anie.200906623
85. Sun, X., He, J., Yang, S., Zheng, M., Wang, Y., Ma, S., & Zheng, H. (2017). Green synthesis of carbon dots originated from Lycii Fructus for effective fluorescent sensing of ferric ion and multicolor cell imaging. *Journal of Photochemistry and Photobiology B: Biology*, *175*, 219–225. https://doi.org/10.1016/j.jphotobiol.2017.08.035
86. Bandi, R., Dadigala, R., Gangapuram, B. R., & Guttena, V. (2018b). Green synthesis of highly fluorescent nitrogen – Doped carbon dots from Lantana camara berries for effective detection of lead(II) and bioimaging. *Journal of Photochemistry and Photobiology B: Biology*, *178*, 330–338. https://doi.org/10.1016/j.jphotobiol.2017.11.010
87. Cao, L., Meziani, M. J., Sahu, S., & Sun, Y. P. (2012). Photoluminescence Properties of Graphene versus Other Carbon Nanomaterials. *Accounts of Chemical Research*, *46*(1), 171–180. https://doi.org/10.1021/ar300128j
88. Zhu, S., Song, Y., Zhao, X., Shao, J., Zhang, J., & Yang, B. (2015). The photoluminescence mechanism in carbon dots (graphene quantum dots, carbon nanodots, and polymer dots): current state and future perspective. *Nano Research*, *8*(2), 355–381. https://doi.org/10.1007/s12274-014-0644-3
89. Mkhari, O., Ntuli, T. D., Coville, N. J., Nxumalo, E. N., & Maubane-Nkadimeng, M. S. (2021). A comparison of fluorescent N-doped carbon dots supported on the surface of hollow and solid carbon spheres, and solid silica spheres. *Diamond and Related Materials*, *118*, 108500. https://doi.org/10.1016/j.diamond.2021.108500
90. Lakowicz, J. R., & Masters, B. R. (2008). Principles of Fluorescence Spectroscopy, Third Edition. *Journal of Biomedical Optics*, *13*(2), 029901. https://doi.org/10.1117/1.2904580
91. Wang, W., Damm, C., Walter, J., Nacken, T. J., & Peukert, W. (2016). Photobleaching and stabilization of carbon nanodots produced by solvothermal synthesis. *Physical Chemistry Chemical Physics*, *18*(1), 466–475. https://doi.org/10.1039/c5cp04942c
92. Qu, S., Wang, X., Lu, Q., Liu, X., & Wang, L. (2012). A Biocompatible Fluorescent Ink Based on Water-Soluble Luminescent Carbon Nanodots. *Angewandte Chemie International Edition*, *51*(49), 12215–12218. https://doi.org/10.1002/anie.201206791

93. Liu, H., Ye, T., & Mao, C. (2007). Fluorescent Carbon Nanoparticles Derived from Candle Soot. *Angewandte Chemie International Edition*, *46*(34), 6473–6475. https://doi.org/10.1002/anie.200701271
94. Sun, D., Ban, R., Zhang, P. H., Wu, G. H., Zhang, J. R., & Zhu, J. J. (2013). Hair fiber as a precursor for synthesizing of sulfur- and nitrogen-co-doped carbon dots with tunable luminescence properties. *Carbon*, *64*, 424–434. https://doi.org/10.1016/j.carbon.2013.07.095
95. Tian, L., Ghosh, D., Chen, W., Pradhan, S., Chang, X., & Chen, S. (2009). Nanosized Carbon Particles From Natural Gas Soot. *Chemistry of Materials*, *21*(13), 2803–2809. https://doi.org/10.1021/cm900709w
96. Yuan, Y. H., Liu, Z. X., Li, R. S., Zou, H. Y., Lin, M., Liu, H., & Huang, C. Z. (2016). Synthesis of nitrogen-doping carbon dots with different photoluminescence properties by controlling the surface states. *Nanoscale*, *8*(12), 6770–6776. https://doi.org/10.1039/c6nr00402d
97. Li, X., Jiang, X., Liu, Q., Liang, A., & Jiang, Z. (2019). Using N-doped Carbon Dots Prepared Rapidly by Microwave Digestion as Nanoprobes and Nanocatalysts for Fluorescence Determination of Ultratrace Isocarbophos with Label-Free Aptamers. *Nanomaterials*, *9*(2), 223. https://doi.org/10.3390/nano9020223
98. Kim, S., Yoo, B. K., Choi, Y., Kim, B. S., & Kwon, O. H. (2018). Time-resolved spectroscopy of the ensembled photoluminescence of nitrogen- and boron/nitrogen-doped carbon dots. *Physical Chemistry Chemical Physics*, *20*(17), 11673–11681. https://doi.org/10.1039/c8cp01619d
99. Miao, X., Qu, D., Yang, D., Nie, B., Zhao, Y., Fan, H., & Sun, Z. (2017). Synthesis of Carbon Dots with Multiple Color Emission by Controlled Graphitization and Surface Functionalization. *Advanced Materials*, *30*(1), 1704740. https://doi.org/10.1002/adma.201704740
100. Zhou, J., Sheng, Z., Han, H., Zou, M., & Li, C. (2012). Facile synthesis of fluorescent carbon dots using watermelon peel as a carbon source. *Materials Letters*, *66*(1), 222–224. https://doi.org/10.1016/j.matlet.2011.08.081
101. Pan, D., Zhang, J., Li, Z., Zhang, Z., Guo, L., & Wu, M. (2011). Blue fluorescent carbon thin films fabricated from dodecylamine-capped carbon nanoparticles. *Journal of Materials Chemistry*, *21*(11), 3565. https://doi.org/10.1039/c0jm03763j
102. Barman, M. K., Jana, B., Bhattacharyya, S., & Patra, A. (2014). Photophysical Properties of Doped Carbon Dots (N, P, and B) and Their Influence on Electron/Hole

Transfer in Carbon Dots–Nickel (II) Phthalocyanine Conjugates. *The Journal of Physical Chemistry C*, *118*(34), 20034–20041. https://doi.org/10.1021/jp507080c

103. Safardoust-Hojaghan, H., Salavati-Niasari, M., Amiri, O., & Hassanpour, M. (2017b). Preparation of highly luminescent nitrogen doped graphene quantum dots and their application as a probe for detection of Staphylococcus aureus and E. coli. *Journal of Molecular Liquids*, *241*, 1114–1119. https://doi.org/10.1016/j.molliq.2017.06.106

104. Wang, D., Wang, Z., Zhan, Q., Pu, Y., Wang, J. X., Foster, N. R., & Dai, L. (2017b). Facile and Scalable Preparation of Fluorescent Carbon Dots for Multifunctional Applications. *Engineering*, *3*(3), 402–408. https://doi.org/10.1016/j.eng.2017.03.014

105. Cailotto, S., Amadio, E., Facchin, M., Selva, M., Pontoglio, E., Rizzolio, F., Riello, P., Toffoli, G., Benedetti, A., & Perosa, A. (2018). Carbon Dots from Sugars and Ascorbic Acid: Role of the Precursors on Morphology, Properties, Toxicity, and Drug Uptake. *ACS Medicinal Chemistry Letters*, *9*(8), 832–837. https://doi.org/10.1021/acsmedchemlett.8b00240

106. Hajir Bahrami, S., Bajaj, P., & Sen, K. (2003). Thermal behavior of acrylonitrile carboxylic acid copolymers. *Journal of Applied Polymer Science*, *88*(3), 685–698. https://doi.org/10.1002/app.11637

107. Lim, S. Y., Shen, W., & Gao, Z. (2015). Carbon quantum dots and their applications. *Chemical Society Reviews*, *44*(1), 362–381. https://doi.org/10.1039/c4cs00269e

108. Du, Q., Zheng, J., Wang, J., Yang, Y., & Liu, X. (2018). The synthesis of green fluorescent carbon dots for warm white LEDs. *RSC Advances*, *8*(35), 19585–19595. https://doi.org/10.1039/c8ra02226g

109. Li, X., Jiang, X., Liu, Q., Liang, A., & Jiang, Z. (2019b). Using N-doped Carbon Dots Prepared Rapidly by Microwave Digestion as Nanoprobes and Nanocatalysts for Fluorescence Determination of Ultratrace Isocarbophos with Label-Free Aptamers. *Nanomaterials*, *9*(2), 223. https://doi.org/10.3390/nano9020223

110. Bandi, R., Gangapuram, B. R., Dadigala, R., Eslavath, R., Singh, S. S., & Guttena, V. (2016). Facile and green synthesis of fluorescent carbon dots from onion waste and their potential applications as sensor and multicolour imaging agents. *RSC Advances*, *6*(34), 28633–28639. https://doi.org/10.1039/c6ra01669c

111. Koteswararao, D., Rajkumar, B., Prameela, K., Ashok, K., & Sridevi, G. (2019). Microwave Assisted Synthesis and Optical Properties ofHighly Fluorescent N-Doped

Carbon Dots. *Asian Journal of Chemistry*, *31*(12), 2897–2902. https://doi.org/10.14233/ajchem.2019.22334

112. Codorniu Pujals, Daniel, Rodríguez Garcés, Dairon, Arias de Fuentes, Olimpia, & Desdín García, Luis F. (2018). XPS of carbon nanostructures obtained by underwater arc discharge of graphite electrodes. *Nucleus (Havana), (64)*, 15-18.

113. Qian, Z., Ma, J., Shan, X., Feng, H., Shao, L., & Chen, J. (2014). Highly Luminescent N-Doped Carbon Quantum Dots as an Effective Multifunctional Fluorescence Sensing Platform. *Chemistry - A European Journal*, *20*(8), 2254–2263. https://doi.org/10.1002/chem.201304374

114. Schneider, J., Reckmeier, C. J., Xiong, Y., von Seckendorff, M., Susha, A. S., Kasák, P., & Rogach, A. L. (2017). Molecular Fluorescence in Citric Acid-Based Carbon Dots. *The Journal of Physical Chemistry C*, *121*(3), 2014–2022. https://doi.org/10.1021/acs.jpcc.6b12519

115. Liu, B., Yang, C. M., Liu, Z., & Lai, C. S. (2017). N-Doped Graphene with Low Intrinsic Defect Densities via a Solid Source Doping Technique. *Nanomaterials*, *7*(10), 302. https://doi.org/10.3390/nano7100302

116. Das, S. K., Dickinson, C., Lafir, F., Brougham, D. F., & Marsili, E. (2012). Synthesis, characterization and catalytic activity of gold nanoparticles biosynthesized with Rhizopus oryzae protein extract. *Green Chemistry*, *14*(5), 1322. https://doi.org/10.1039/c2gc16676c

117. Miao, X., Qu, D., Yang, D., Nie, B., Zhao, Y., Fan, H., & Sun, Z. (2017b). Synthesis of Carbon Dots with Multiple Color Emission by Controlled Graphitization and Surface Functionalization. *Advanced Materials*, *30*(1), 1704740. https://doi.org/10.1002/adma.201704740

118. Wei, Y., Chen, L., Wang, J., Liu, X., Yang, Y., & Yu, S. (2020). Rapid synthesis of B-N co-doped yellow emissive carbon quantum dots for cellular imaging. *Optical Materials*, *100*, 109647. https://doi.org/10.1016/j.optmat.2019.109647

119. Sprenger, D., & Anderson, O. (1991). Deconvolution of XPS spectra. *Fresenius' Journal of Analytical Chemistry*, *341*(1–2), 116–120. https://doi.org/10.1007/bf00322120

120. Mewada, A., Pandey, S., Shinde, S., Mishra, N., Oza, G., Thakur, M., Sharon, M., & Sharon, M. (2013). Green synthesis of biocompatible carbon dots using aqueous extract of Trapa bispinosa peel. *Materials Science and Engineering: C*, *33*(5), 2914–2917. https://doi.org/10.1016/j.msec.2013.03.018

121. Nie, H., Li, M., Li, Q., Liang, S., Tan, Y., Sheng, L., Shi, W., & Zhang, S. X. A. (2014). Carbon Dots with Continuously Tunable Full-Color Emission and Their Application in Ratiometric pH Sensing. *Chemistry of Materials*, *26*(10), 3104–3112. https://doi.org/10.1021/cm5003669

122. Sandeep Kumar, G., Roy, R., Sen, D., Ghorai, U. K., Thapa, R., Mazumder, N., Saha, S., & Chattopadhyay, K. K. (2014). Amino-functionalized graphene quantum dots: origin of tunable heterogeneous photoluminescence. *Nanoscale*, *6*(6), 3384. https://doi.org/10.1039/c3nr05376h

Chapter 5

Synthesis and functionalization of onion-like carbon nanomaterials using the flame pyrolysis method

5.1 Introduction

Following the discovery of fullerenes [1-2], the study of carbon-based nanomaterials has sparked a surge of interest that continues to grow year after year. Nanofibers, nanotubes, and spherical carbons such as nano-spheres, nano-dots, and nano-onions are among the newly identified nano-carbon allotropes. These carbon nanostructured materials may be made using well-known techniques such the arc discharge [3], flame pyrolysis [4] and chemical vapour deposition methods [5]. Spherical carbons that include carbon nano-onions (CNOs) and onion-like carbon nanomaterial (OLCNs) or interchangeably, onion-like nanocarbons (OLNCs) are spherical nanostructured materials with good electrical and structural characteristics and have also been widely explored. CNOs and OLCNs have a variety of structural morphologies, ranging from spherical to polyhedral [6]. They resemble concentric multi-layered spheres that can be core-filled, solid, hollow/voided, or any combination of the three. Some of the methods frequently used to prepare CNOs include high temperature annealing of nanodiamond particles [7], implantation of carbon atoms on silver particles [8], and laser vaporization of composite carbon metal targets at low helium pressures and in the presence of C_{60} as a nucleating centre [9].

Pyrolysis is another innovative way for producing OLCNs. One approach is propane pyrolysis, which has been claimed to produce OLCNs at a low-cost, long-term method [10]. OLCNs in gram scale quantities were reported to have been produced using this pyrolysis process. The benefit of this process is that it does not require the use of a catalyst, resulting in carbon compounds that are generally free of contaminants [11]. The open flame pyrolysis approach is an alternative method for producing catalyst-free solid OLCNs in a continuous manner under ambient circumstances [12–16]. The carbon supply is broken down into atomic or radical fragments, which then react to generate OLCN aggregates with primary nucleation sites, which may then be used to form agglomerates [17]. OLCNs layers develop from the inside out, predominantly from carbon particle-nodules that curl on their own [17,18].

Recently, the pyrolysis of oil into OLCNs has attracted many researchers [32]. Different oils are usable and have been in the past. In this work, olive oil was pyrolyzed in a straightforward, inexpensive process to create OLCNs. Olive oil was chosen for this study because of its carbon-rich structure and high content of oleic acid (monosaturated fatty acid), which is less susceptible to heat oxidation than many other vegetable oils. Post doping and surface functionalization were enhanced to change the characteristics of the produced OLCNs. The current study's flame pyrolysis synthesis technique is an alternate way for generating OLCNs under ambient room temperature circumstances by using a carbon-containing liquid (bio-oil) as a carbon source.

5.2 Experimental procedure

In this study, OLCNs were synthesized using the flame pyrolysis of liquid fuels; in particular, olive oil was used, following the procedure reported by Mongwe et al. [20]. See schematic diagram (**Scheme 5.1**) below.

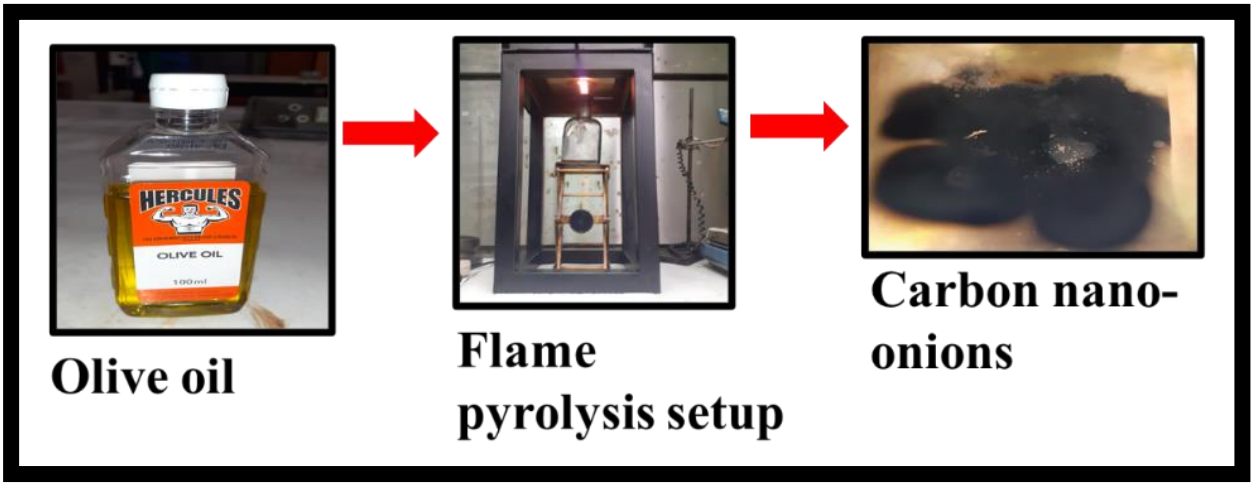

Scheme 5.1: Synthesis procedure for the production of carbon nano-onions.

5.2.1. Starting materials

Table 5.1: Materials and reagents used in this study.

Reagents and materials	Purity and speciation	Supplier
Olive Oil	-	Hercules brand
Ammonia gas,	$NH_{3(g)}$, 99.7 %	Sigma-Alrich
Hydrogen peroxide	H_2O_2	Sigma-Alrich
n-Pentane	*n*-C_5H_{12}	Sigma-Alrich

None of the commercially available, analytical purity-grade compounds needed any further purification before usage. Three types of OLCNs were synthesized; pristine onion-like carbons (p-OLCNs), oxygen functionalized (ox-OLCNs) and nitrogen doped (N-OLCNs) analogues using functionalization and nitrogen doping. This conversion of p-OLCNs was achieved using a reflux method, and a chemical vapour deposition method, respectively.

5.2.2. Synthesis of onion-like carbon nanomaterials using flame pyrolysis

Using the flame pyrolysis technique, OLCNs were effectively created by burning roughly 100 mL of Hercules olive oil with a wick until there was no more oil in the container. A flame was produced by lighting the wick, which was submerged in olive oil. The incomplete combustion of the oil in the flame's centre zone resulted in the production of a deep-black powder by the flame. The product obtained (carbogenic black powder) from the incomplete combustion was collected on a brass plate (see **Scheme 1** above) and labelled as pristine OLCNs (p-OLCNs). The flame assisted process took about ~1 hour and a good yield of ~4g OLCNs was obtained (before purification).

5.2.3. Purification of the as-prepared onion-like carbon nanomaterials

To eliminate the olive oil residue that remained on the OLCNs after synthesis, the OLCNs were moved to a flask with a round bottom and 40 mL of *n*-pentane. To create the pure carbon nano-onions, the OLCNs were refluxed in n-pentane at 80 ºC for six hours. After that, the mixture was rinsed with double-distilled water and centrifuged at a high speed of 15,000

rpm for 15 minutes to separate it. Then the OLCNs were placed in a vacuum oven at 100 ºC until completely dry, to remove all the *n*-pentane and obtain p-OLCNs a dry powder-like soot.

5.2.4. Functionalizing the onion-like carbon nanomaterials

Following Siswana et al [21], 50% hydrogen peroxide (H_2O_2) was used to oxidize the p-OLCNs. Numerous oxidizing agents, including HNO_3, HNO_3/H_2SO_4, $KMnO_4$, HCl, $(NH_4)_2S_2O_8$, and H_2O_2 [27], can add oxygen-containing functional groups to the surface of carbon nanostructures. In effect, these oxidative reactions can produce aldehydes, ketones, esters, alcohols, and carboxylic acid moieties, among other oxygenated functional groups. When carbon materials are oxidized with very aggressive chemicals, their hydrophilicity significantly increases as a result of the increased oxygen atom concentration and distribution on the carbon nano-structures [28].

In this study, 40 mL H_2O_2 was used to functionalize the OLCNs with oxygen groups. During the functionalization, the reaction temperature was set at 80 ºC for 6 hours (**Fig. 1a**), under stirring to introduce carboxylic (COO^-) functional groups. The obtained OLCNs were then rinsed using a Millipore filter (**Fig. 1b**) with distilled water until a pH of about 7 was achieved, or until the filtrate was clear in colour to obtain ox-OLCNs. To obtain a neutral pH, a basic NaOH solution was used.

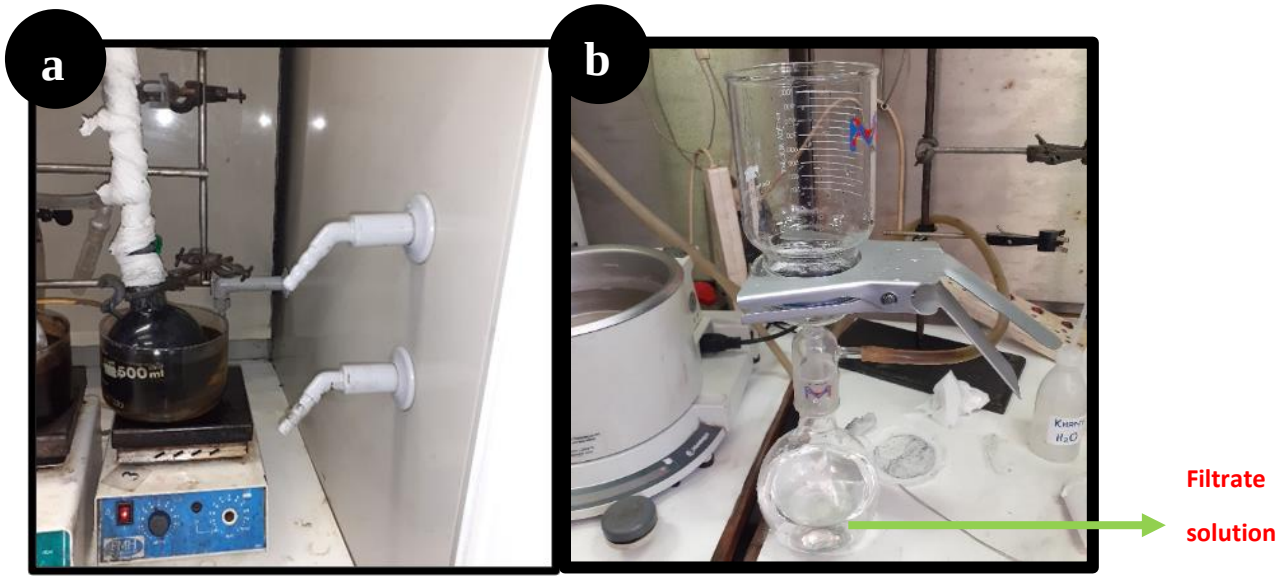

Figure 5.1: a) Reflux system and b) Millipore filter used to rinse OLCNs after functionalizing.

Chemical vapour deposition (CVD) was used to manufacture nitrogen-doped OLCNs in a horizontal tube furnace with argon serving as the nitrogen source and the carrier gas (**Fig. 5.2**) [29]. A quartz boat containing about 0.2 g of the purified p-OLCNs was inserted in the middle of the quartz tube, installed within an electric furnace, and the system was then flushed with argon. The purified p-OLCNs were heated for 60 minutes at 900 ºC under a stream of diluted gases (100 mL/min argon and 150 mL/min ammonia) after the furnace temperature was increased to 900 ºC under argon. Under argon gas, the produced N-OLCNs were allowed to cool to room temperature.

Figure 5.2: CVD reactor system used to dope the OLCNs with ammonia gas.

5.2.5. Characterization techniques

- The synthesized materials were characterized using TEM, FESEM, PXRD spectroscopy, Raman spectroscopy, Uv-vis and PL spectroscopy, FTIR, XPS, CHNS Elemental Analyzer and Branauer-Emmett-Teller (BET) surface area analysis.

5.3 Results and discussion

This section includes both the functionalized OLCNs and the findings and discussions of the synthesized OLCNs. To make OLCNs more catalytically active and to change their overall conductivity for use in dye-sensitized solar cells, OLCNs were doped with O and N atoms (see **Chapter 7**). The results and discussion sections below review the experimental findings and discusses them in the context of literature, while linking characterization techniques to each other and properties to performance, as per application in DSSCs.

5.3.1. Morphological analysis

Transmission electron microscopy (TEM) images of the uniformly dispersed p-OLCNs, ox-OLCNs, and N-OLCNs are shown in **Fig 5.3 a, b and c**. The images of the pristine and functionalized OLCNs do not present an explicitly clear onion-like nanostructure as the multi-shells (concentric multi-layers) expected are not clearly visible due to the low magnification of the images. But it does demonstrate that these substances have quasi-spherical morphologies and chain-like structures that are comparable to those mentioned by Habiba et al [30]. These nanomaterials are mostly connected in an accreted form [30, 31] owing to the chain-like morphology. The circular shell seems to remain intact in the photos below, indicating that the onion-like nanostructure was preserved during the oxidation and nitrogen doping processes (**Fig 5.3 b and c**).

The use of a high resolution TEM (HRTEM) is able to quantify the number of shells and any disordering (if any) in the shells. Particle size distribution histograms for all OLCNs were obtained by measuring approximately 100 particles using ImageJ software. It has been reported that structural morphology, interlayer spacing, the shell layering, and graphitic nature OLCNs can be tuned by doping or functionalization processes [32, 33]. The p-OLCNs formed have particle sizes ranging between 20–60 nm, and an average diameter of 42 nm ± 3.3 nm in comparison, ox-OLCNs exhibited particle diameters varying between 60–200 nm, and an average diameter of 125 nm ± 4.1 nm. N-OLCNs had particle diameters varying between 50–120 nm with an average diameter of 85 nm ± 3.5. The histogram of ox-OLCNs demonstrated a broader size distribution as compared to the other OLCNs. The reason for this is not clear at the moment. This may also be due to the chain-like structure of OLCNs, as the interconnection may distort the particle sizes measurements. These results vary to those found by Sikeyi et al [34], who synthezised and functionalized OLCNs following the same methods used in this current study.

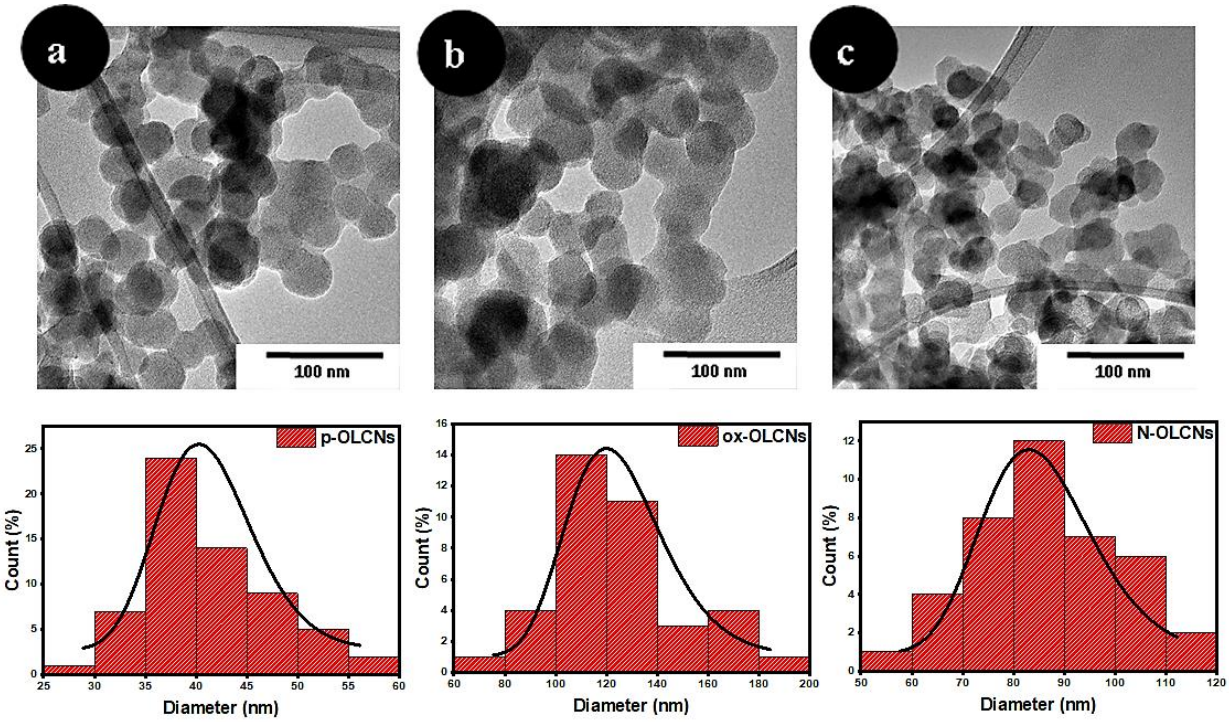

Figure 5.3: TEM images and their corresponding size distribution histograms underneath of a) p-OLCNs, b) ox-OLCNs and c) N-OLCNs.

The quasi-spherical form of the OLCNs is seen in SEM pictures, along with the agglomeration or aggregation of nanoparticles as shown in **Fig 5.4** below. The SEM micrographs of the OLCNs confirm that these nanomaterials are connected in form accreted quasi-spherical shapes. There were no nanomaterials formed other than onion-like carbon. The FESEM micrographs show that the OLCNs retained its surface morphology even after functionalization.

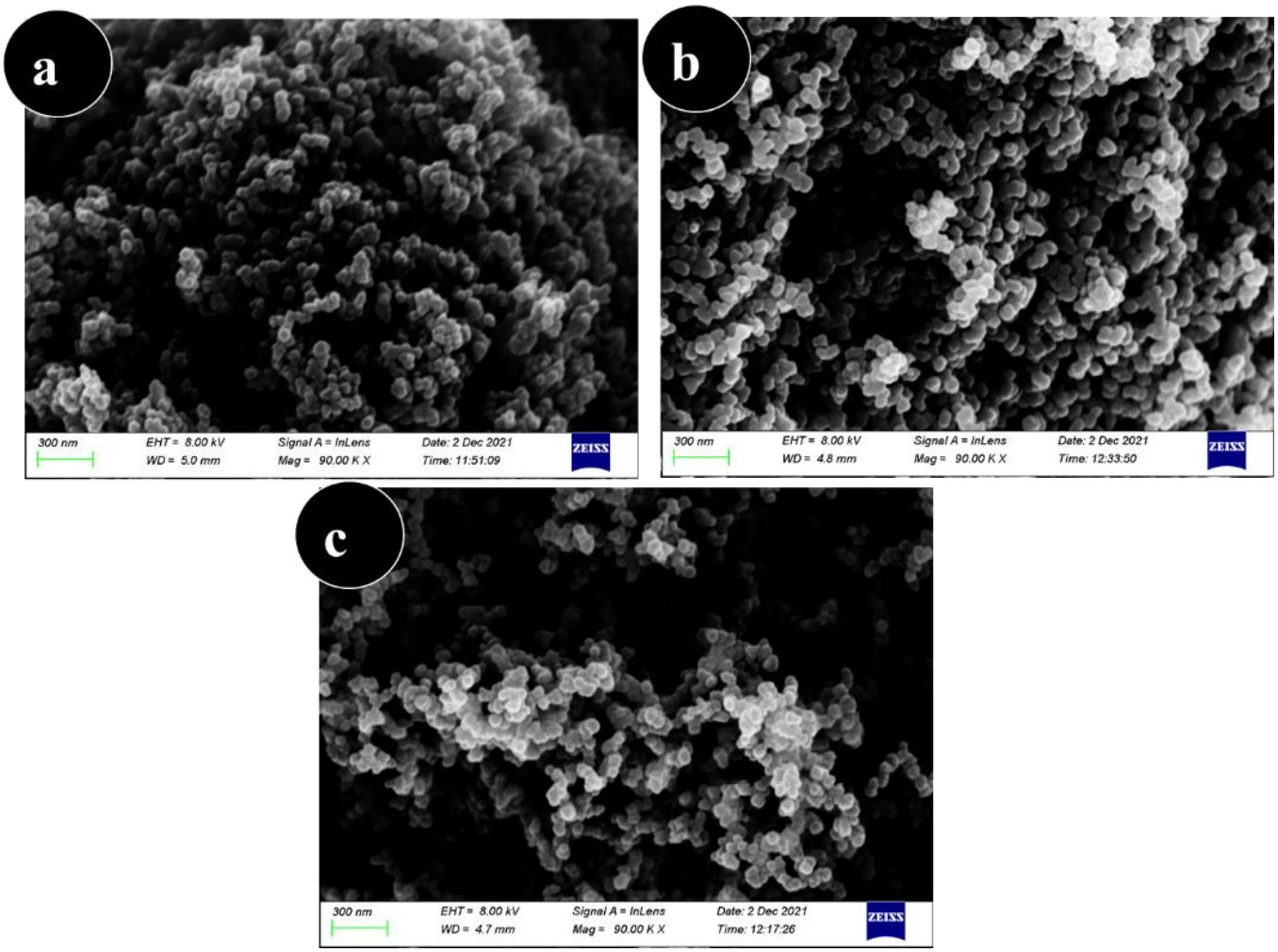

Figure 5.4: SEM images of a) p-OLCNs, b) ox-OLCNs and c) N-OLCNs.

5.3.2. Powder X-ray diffraction (PXRD) spectroscopy analysis

For each and every OLCNs sample, the PXRD analysis was performed. The outcomes for the unmodified and functioning OLCNs are shown in **Fig. 5.5**. The PXRD diffractograms for all OLCNs did not exhibit any appreciable changes, as can be observed from the patterns for p-OLCNs, ox-OLCNs, and the N-OLCNs. However, an extra peak can be seen ca 18º for ox-OLCNs. The substantial asymmetric reflection of all carbon compounds (~ca. $2\theta = 25º$) indicates the existence of sp^2-bonded carbons. This signal is related to the reflection of X-ray radiation from the (002) plane [35-37]. For the ox-OLCNs and N-OLCNs the peak at 2θ of approximately 43º correlate to the carbon's diffraction in the (111) basal plane [38]. This peak was not observed in the pristine material as expected from the low intensity of the 002 peak (**Fig. 5.5**).

According to literature, the size of the nanoparticles is the main source of diffraction widening. Strains and flaws in the crystalline material are also thought to contribute to this phenomenon [39]. For the changed OLCNs, this widening of reflections is more noticeable, which may indicate that the adjustments to the OLCNs were successful. Due to the reduced size, the spreading of the peaks may be a sign of a general disordering of the structure [40] of the OLCNs as observed in the electron micrographs (**Fig. 5.5**). The ox-OLCNs exhibited a less prominent shoulder peak at around 2θ = 18º (corresponding to the 001 plane) which overlaps with the characteristic 002 carbon peak, signifying an increased interlayer spacing upon successful insertion of oxygen groups between the layers [41].

The XRD data from **Figure 5.5** below was used to determine the crystallite size and interplanar d-space on the various OLCNs employing the Scherrer equation (1) and Bragg's law (2), respectively. From the XRD graph, we can calculate the full width and half maximum (FWHM) and utilise the FWHM value obtained to calculate both the crystallite size and d-space.

$$D = \frac{K\lambda}{\beta cos\theta} \quad \ldots\ldots (1)$$

Where D is the average crystallite size (nm), K is the Scherrer constant (also called the shape factor or shape parameter) whose value is ~0.94 for spherical crystallites (with cubic symmetry), λ is the X-ray wavelength for the Cu-K_α X-ray source which has been experimentally deterimed and has value of 1.5406 Å (0.15406 nm), β is the line broadening at FWHM in radians and θ is the peak position/Bragg's angle in degrees at half of 2θ.

$$2dsin\theta = n\lambda \quad \ldots\ldots (2)$$

Here, d is the interplanar spacing (in Å or nm), θ is the Bragg's angle, n is the diffraction order (for first order, n=1) and λ is X-ray wavelength (Cu-K_α = 0.15406 nm).

The calculated (average) crystallite sizes for p-OLCNs, ox-OLCNs and N-OLCNs were found to be 1.84 nm, 1.03 nm and 1.07 nm for respectively. The interplanr spacing values were calculated to be $d_{(200)}$ = 0.36 nm for p-OLCNs. For ox-OLCNs, the calculated d-space values were $d_{(001)}$ = 0.39 nm, $d_{(200)}$ = 0.37 nm and $d_{(111)}$ = 0.20 nm. For N-OLCNs, values were determined to be $d_{(200)}$ = 0.36 nm and $d_{(111)}$ = 0.21 nm.

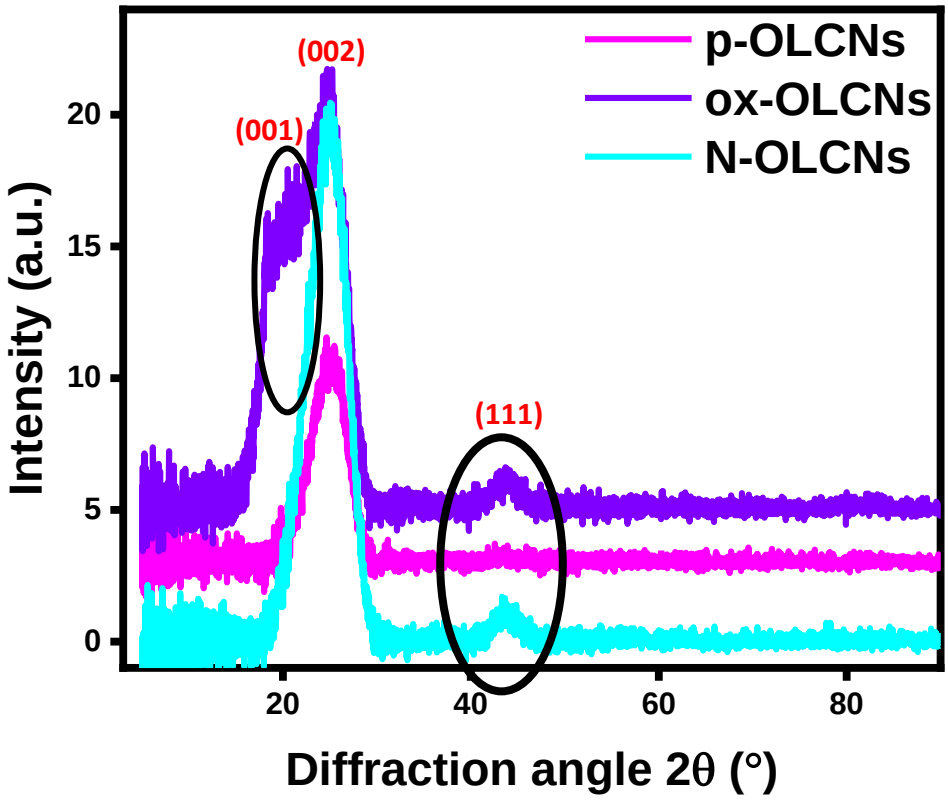

Figure 5.5: PXRD patterns of the as-synthesized OLCNs.

5.3.3. Raman spectroscopic analysis

The graphitization degree of the OLCNs both functionalized and un-functionalized was studied and investigated using Raman spectroscopy. Three bands were of importance in the analysis. The D-band is responsible for the presence of amorphous carbon nanoparticles and structural defects in the graphitic layers of the carbonaceous material (disordered carbon). The tangential vibrations recorded in the graphitic layers of carbon give birth to the G-band (graphitic carbon) [42]. The 2D (D′) peak is extremely responsive to the level of graphitization and structural modifications in carbon materials.

The as-synthesised OLCNs' Raman spectra revealed two peaks that correspond to the D-band and the G-band (**Fig. 5.6**). The Raman spectrum of the p-OLCNs demonstrated two bands at 1353 and 1592 cm^{-1}. Both the doped and the oxidized and modified OLCNs had shifted and widened D and G bands. Specifically, the change in both peaks upon functionalization (**Fig. 5.6**) can be attributed to the symmetry loss brought on by the inclusion of the nitrogen and

carboxylic groups to the unsaturated carbon–carbon bonds, respectively, and the existence of disordered carbon structures. Indicating an electronic influence of both the nitrogen and oxygen incorporation on the carbon structure, the measured peak locations for the p-OLCNs, ox-OLCNs, and N-OLCNs exhibited a little upshift for the D and G bands (ox-OLCNs > N-OLCNs > p-OLCNs) [43].

The D and G ratio was calculated using the peak regions of the D and G bands. (I_D/I_G) [44]. The I_D/I_G ratios of the N-OLCNs, ox-OLCNs, and p-OLCNs were found to be 3.34, 2.65, and 3.09, respectively (see **Table 5.2**). This possibly relates to the defect-rich nature of the OLCNs after N and O addition [45]. See **Supplementary Information** (**SI**, **Fig. S13**) for deconvoluted spectra.

In addition to the G band, another peak is seen at around 4200 cm^{-1} [46]. This band may occasionally be shown as the G band's shoulder [47]. It is classified as a D′ peak [48], is also disorder-induced, and is not seen in highly oriented pyrolytic graphite (HOPG) but is frequently seen in extremely defective graphite [49]. The 2D peak is particularly sensitive to the degree of graphitization and structural changes in carbon materials. As a general rule, the strongest bands are those that are visible at nearly twice the wavenumber of the D and G bands. As a result, when the excitation wavelength is varied, this first-order counterpart operates resonantly.

According to reports, the size of the OLCNs affects the ID/IG ratio seen in the Raman spectra of OLCNs [50]. The peak intensities of the D-band and the G-band cannot be shown to be the same or equal when comparing the peaks of all OLCNs. The p-OLCN, ox-OLCN, and N-OLCN Raman spectra all show a little decrease of the D-band (in cm^{-1}) in comparison to the G-band (in cm^{-1}), indicating purification of the pure OLCNs from carbonaceous material during the process. [51]. This also implies that there was some structural deformation and structural flaws, but the degree of deformity may be assessed by calculating the I_D/I_G ratios. Since the peak intensities are not exactly the same and the peaks do not have exactly the same height, therefore the material does not have equal ratio of sp^3 hybridized: sp^2 hybridized carbon atoms. Thus, the difference in peak intensities can also be attributed the amorphous carbon nanomaterial structure mentioned in **Section 5.3.2** above.

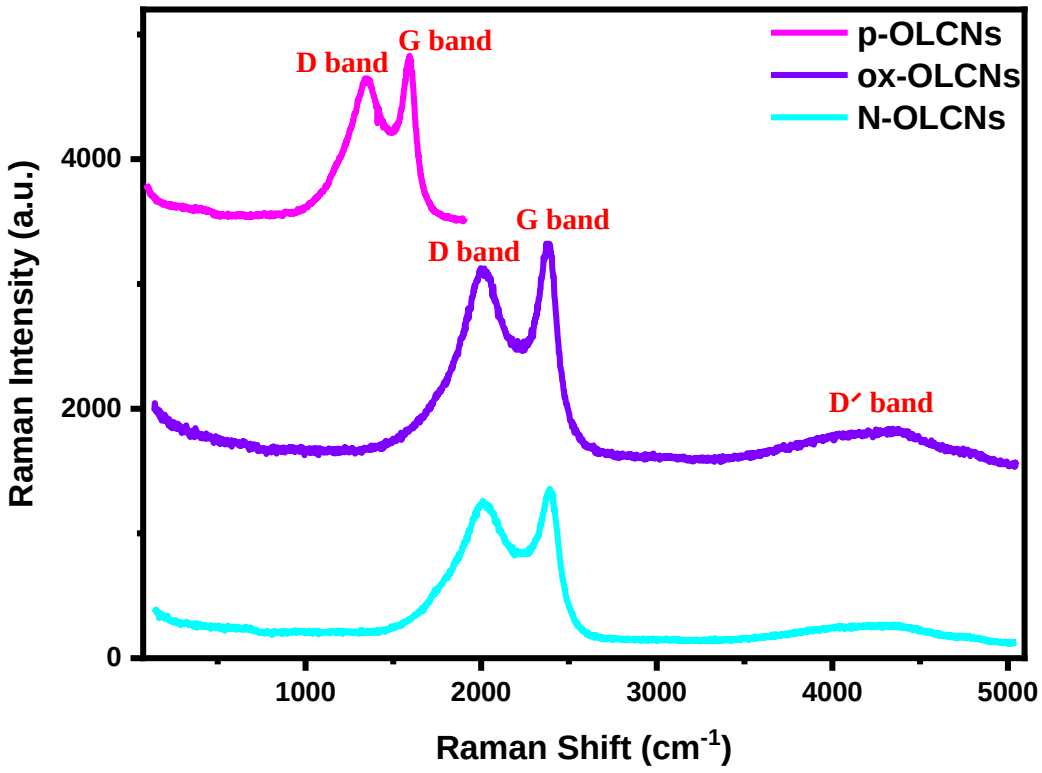

Figure 5.6: Raman spectra patterns of the as-synthesized OLCNs all recorded at λ_{ex} 514nm.

Table 5.2: Summary of the Raman spectroscopy analysis data.

Sample name	D Band (cm^{-1})	Area	G Band (cm^{-1})	Area	I_D/I_G ratio
p-OLCNs	1353	300737	1592	97406	3.09
ox-OLCNs	2005	548380	2386	206560	2.65
N-OLCNs	1999	448408	2393	134445	3.34

5.3.4 Optical properties (absorbance measurement and fluorescence studies analysis)

The typical peaks for OLCNs [52] in UV spectroscopy also exhibit a red shift that gradually developed with the particles' size growth following functionalization: N-OLCNs, p-OLCNs, and ox-OLCNs. The spectra shows that all prepared OLCNs absorb in the ultraviolet region. The absorption band evolves at wavelengths ~400 nm which indicates that the materials synthesized

absorb the ultraviolet light since this peak is below the visible region. These observations can be attributed to the overlapping of aromatic polycyclic hydrocarbons of OLCNs [53, 54].

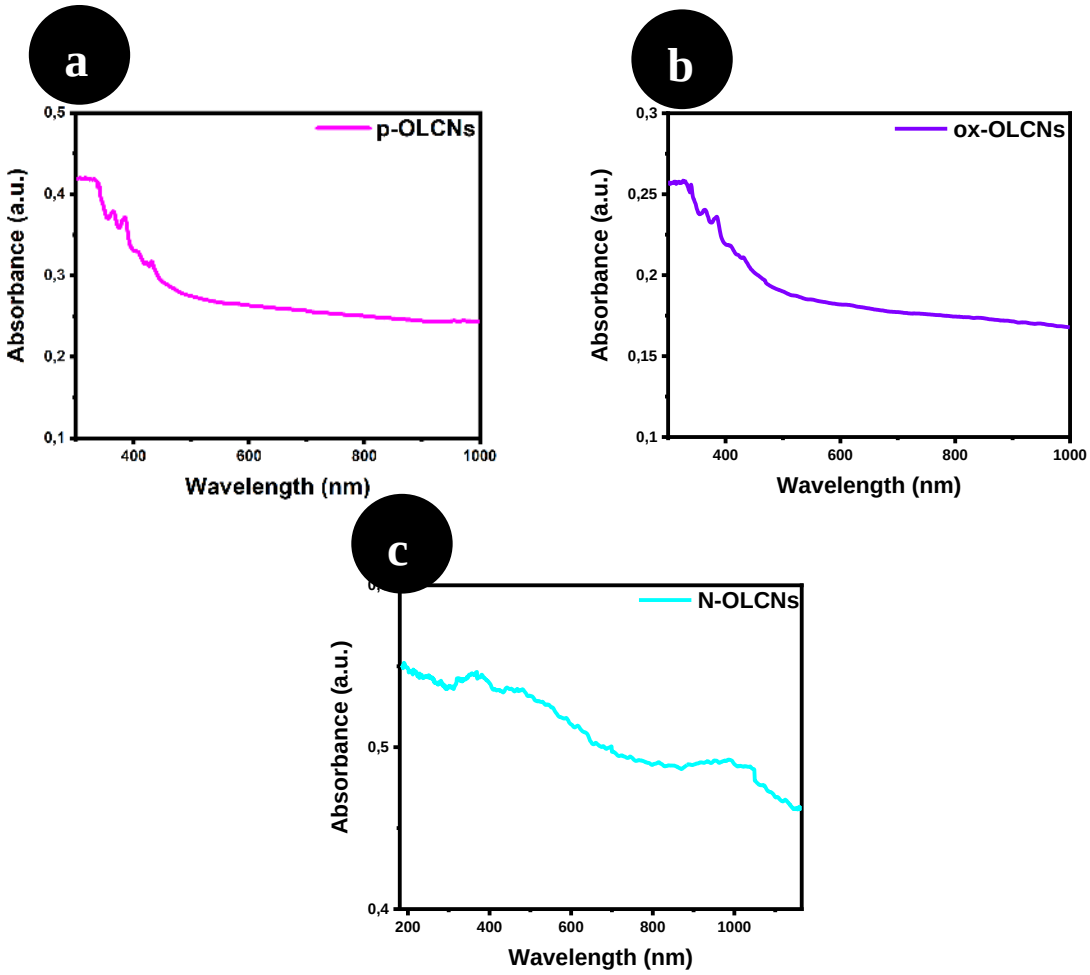

Figure 5.7: UV-vis absorption spectrum of a) p-OLCNs, b) ox-OLCNs and c) N-OLCNs.

All of the OLCNs were dispersed in distilled water and photoexcited at 350 nm, which resulted in powerful emission bands with maximal wavelengths at 465 nm (p-OLCNs), 425 nm (ox-OLCNs), and 390 nm (N-OLCNs), respectively. The various OLCNs' varying maximum emission wavelengths suggest that the fluorophores tethered to their surfaces are surrounded by distinct surroundings. Tauc plots of allowed transitions to determine the bandgap energy can be found in the **SI, Figure. S14**.

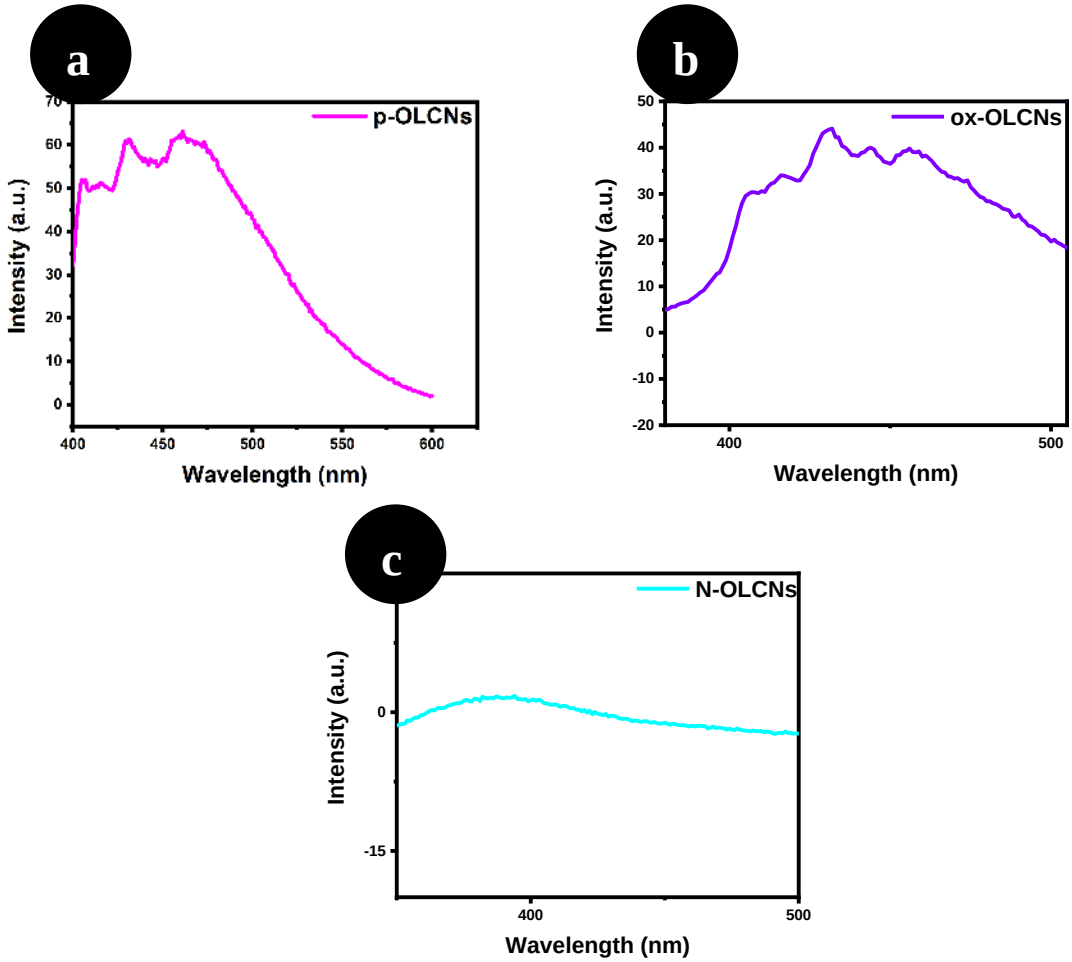

Figure 5.8: PL spectra of the aqueous solution of a) p-OLCNs, b) ox-OLCNs and c) N-OLCNs at λ_{ex} 350 nm.

5.3.5 Thermogravimetric/differential (TGA/DTA) analysis

To examine the thermal stability of the p-OLCNs, ox-OLCNs, and N-OLCNs nanomaterials, thermogravimetric (TGA) and derivative thermogravimetric (DTA) analysis were used. As shown in **Fig. 5.9 a**, p-OLCNs, ox-OLCNs, and N-OLCNs' TGA profiles show a large start decomposition weight loss at T > 500 ºC. The thermal disintegration of the oxygen functional groups and perhaps some of the carbon core of the onion structure can be attributed to the reduction in the weight loss of ox-OLCNs at the three decomposition temperatures [55].

The DTA curves data (**Fig. 5.9 b**) for N-OLCNs showed improved thermal stability (650 ºC) than the p-OLCNs (610 ºC) and the ox-OLCNs (645 ºC). The increased surface area of the N-OLCNs is what is responsible for their improved thermal stability (see below) and presence of N atoms OLCNs [56]. The ox-OLCNs displayed two distinct thermal phases, with the lower peak position for ox-OLCNs being caused by the loss of oxygen-functional groups,

such as the removal of carboxylic groups from the OLCNs' surface (**Fig. 5.9 b**) [57, 58]. The TGA and DTA results are in good agreement with the Raman results as well as absorbance and fluorescence results, as it shows the OLCNs all have different surface functional groups which means they all exhibit different fluorophores.

The TGA plot demonstrates that the washed material, p-OLCNs, and functionalized materials were all pure as no residue remained after the analysis.

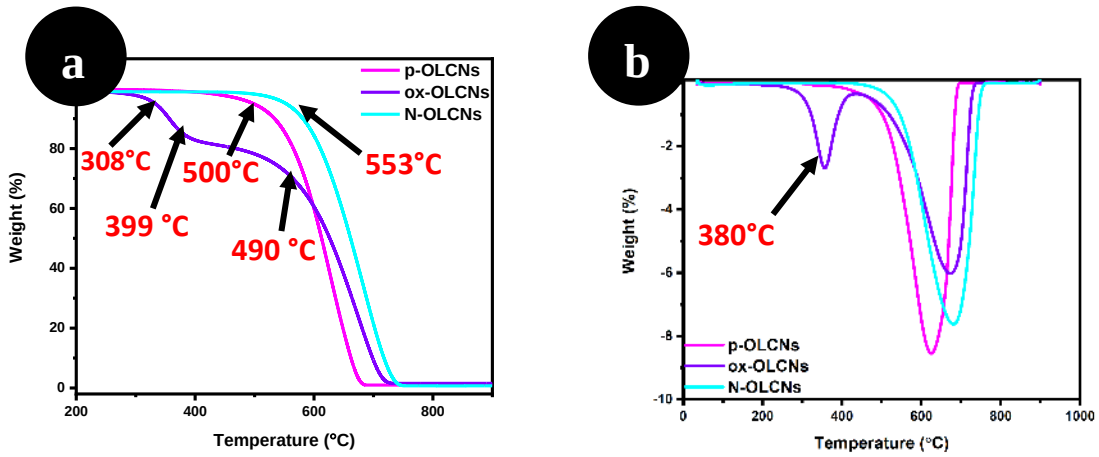

Figure 5.9: The percentage weight loss as a function of temperature; a) TGA profiles for the produced OLCNs, and b) DTA curves for the OLCNs.

5.3.6. Fourier transmission infrared spectroscopy (FTIR) analysis

The spectra of the OLCNs show several peaks (**Fig. 5.10**). Two peaks centred at 3878 and 3842 cm^{-1}, are due to NH^- stretching modes [59]. The OH^- peak usually observed between 3000 and 3500 cm^{-1} is broad, but in this instance the NH peak is divided into two, which is explained by the presence of alcohol OH groups and/or water absorped unto the surface of the OLCNs [34, 60]. The p-OLCNs have an OH- peak that is shifted, and different from the other functionalized OLCNs. This can be attributed to the p-OLCNs not undergoing any surface modification. The peak centred at 1688 cm^{-1} can be due to the C=C stretching mode in aromatic rings.

When oxygenated functional groups were added to the surface of the p-OLCNs using hydrogen peroxide, a new peak at 1795 cm^{-1} that can be connected to the C=O stretching mode of carboxylic groups was formed. The creation of various quantities of oxygen-containing functional groups, such as hydroxyl (-C-OH), carboxyl (-COOH), and carbonyl (-C=O), is reportedly the result of controlled modification that was carried out using a variety of solvents

[61–63] and at various temperatures [64,65]. The peak at 1043 cm^{-1} can be ascribed the C-O group [59].

A new peak for a C=N stretching mode for a nitrile group developed at 2494 cm^{-1} when nitrogen was added to the p-OLCNs [34]. This suggests that nitrogen was incorporated into the structure of p-OLCNs. The spectra of all three materials were similar, demonstrating that they shared a backbone structure and that the p-OLCNs carbon structure was not completely disrupted or harmed by the nitrogen doping and oxidation processes [66].

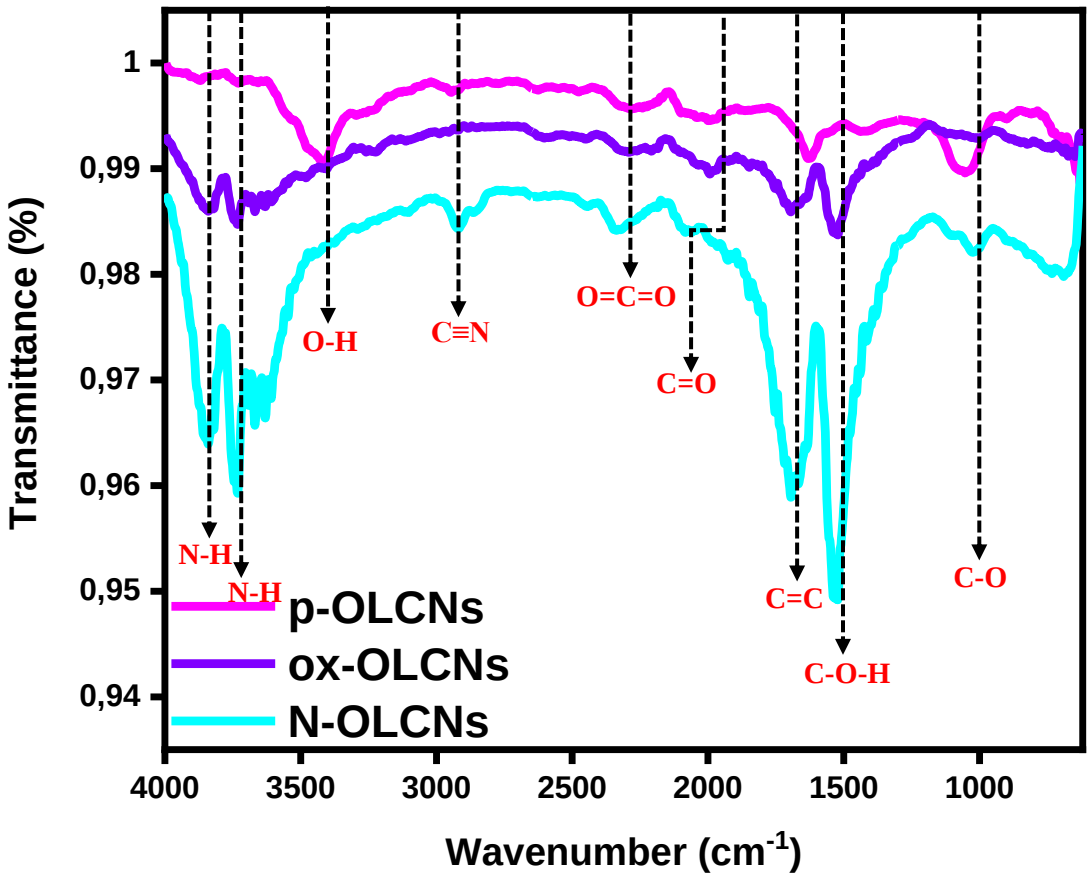

Figure 5.10: FTIR spectra of all as-prepared OLCNs.

5.3.7. X-ray photoelectron spectroscopy (XPS) analysis

The surface of the as-prepared OLCNs was analyzed using XPS to estimate the chemical composition and determine the elemental compositions, potential functional groups, and valence states (at. %). The signals of the nitrogen atoms in the N-OLCNs, as well as the carbon and

oxygen atoms, were all detectable in all survey spectra. From the analysis, it was revealed that all as-prepared OLCNs are composed mostly by C (~74-89 at. %) and O (~10-18 at. %) elements, and only N-OLCNs presented with nitrogen (~0.8 at. %) as shown in **Table 5.3**. Detailed scans for the internal levels of C 1s, O 1s, and N 1s are shown in the figures below. All C 1s peaks were observed to be unsymmetrical for all OLCNs, which is reported to be a characteristic of conducting forms of carbon [67].

Figure 5.11 a show the XPS full scan spectrum of the p-OLCNs as well as the high resolution spectra of C1s and O1s deconvoluted separately into different peaks. The main peak C1s (**Figure 5.11 b**) centred at 284.2 can be assigned to sp^2 hybridized carbon atoms in strained C-C bonds due to the curvature of the onions [68]. The other two peaks at 285.9 and 288.5 eV were assigned to carboxylic groups (C-O) and (O-C=O), respectively [69].

Furthermore, the deconvolution of the high-resolution spectrum of O1s (**Figure 5.11 c**) revealed two signals at 531.8 eV and 533.2 eV which are associated with organic C-O and C=O were determined to have 5.8 % and 5.1 % atomic percentage, respectively. These oxygenated groups originate from the reaction of oxygen with the edges of incomplete graphitic layers containing highly reactive dangling bonds [70] or moisture as the as p-OLCNs are hygroscopic in ambient room temperature.

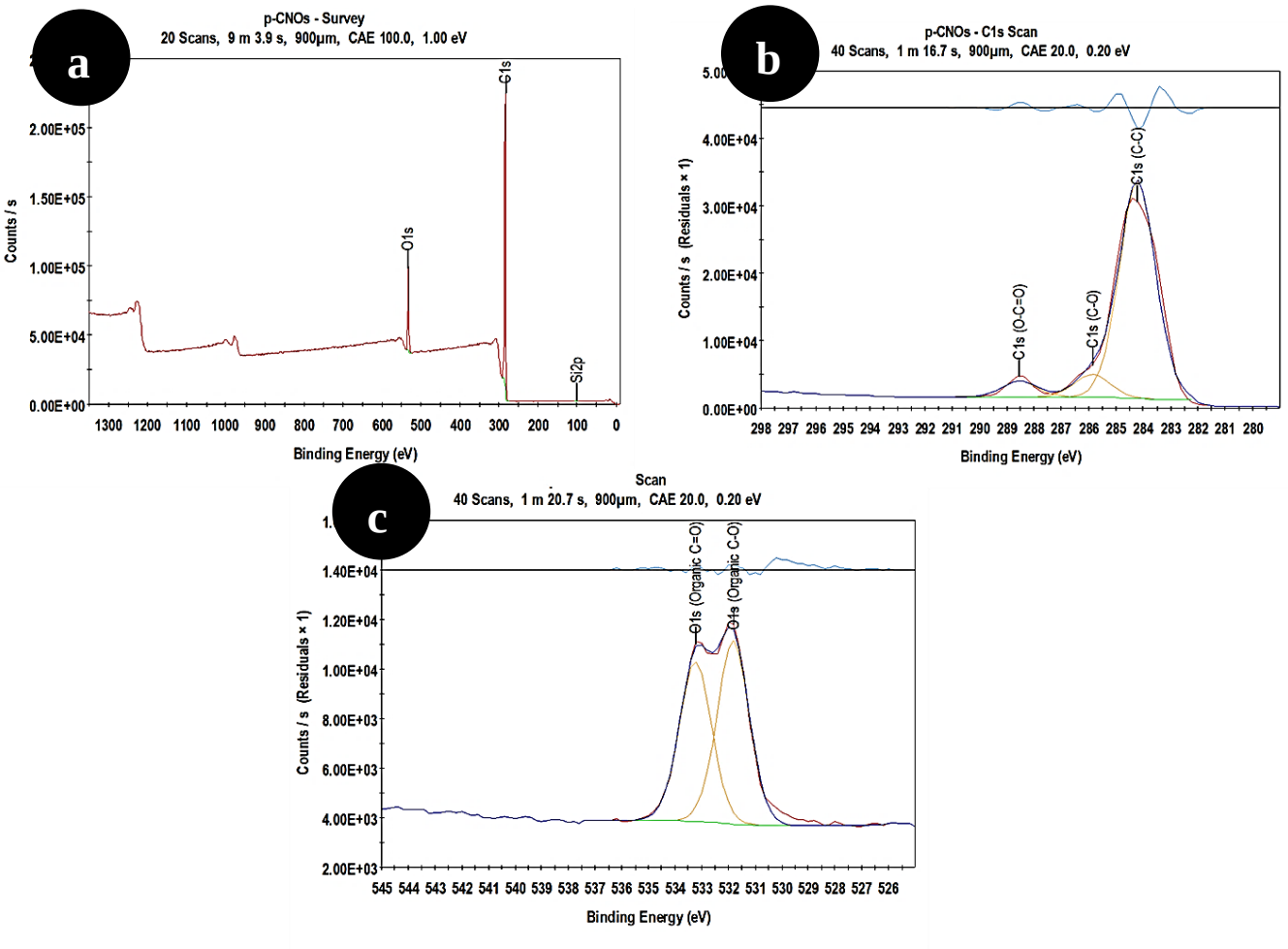

Figure 5.11: a) XPS full scan spectrum, and the corresponding high-resolution spectra of b) C1s and c) O1s of the as-synthesized p-OLCNs.

Figure 5.12 a show the XPS full scan spectrum of ox-OLCNs with two predominant peaks at 284.4 eV and 532.2 eV which are attributed to the first orbital of the carbon (C1s) and oxygen (O1s) with atomic percentages of 74.3 % and 18.6 %, respectively. The high resolution spectra of C1s, and O1s were deconvoluted separately into different peaks. The high-resolution spectrum of C1s (**Figure 5.12 b**) revealed five different peaks at 284.1 eV, 284.9 eV, 286.4 eV, 287.5 eV and 288.7 eV which were assigned to C-C sp^2 hybridization (36.1 %), C-C sp^3 hybridization (27.7 %), C-O (5.8 %), C=O (0.5 %) and O=C-O (5 %), respectively [71].

In addition, deconvolution of the high-resolution spectrum of O1s (**Figure 5.12 c**) revealed two signals at 532.0 eV and 533.4 eV which are associated with C-O and C=O respectively [72]. These findings concur with earlier findings [32].

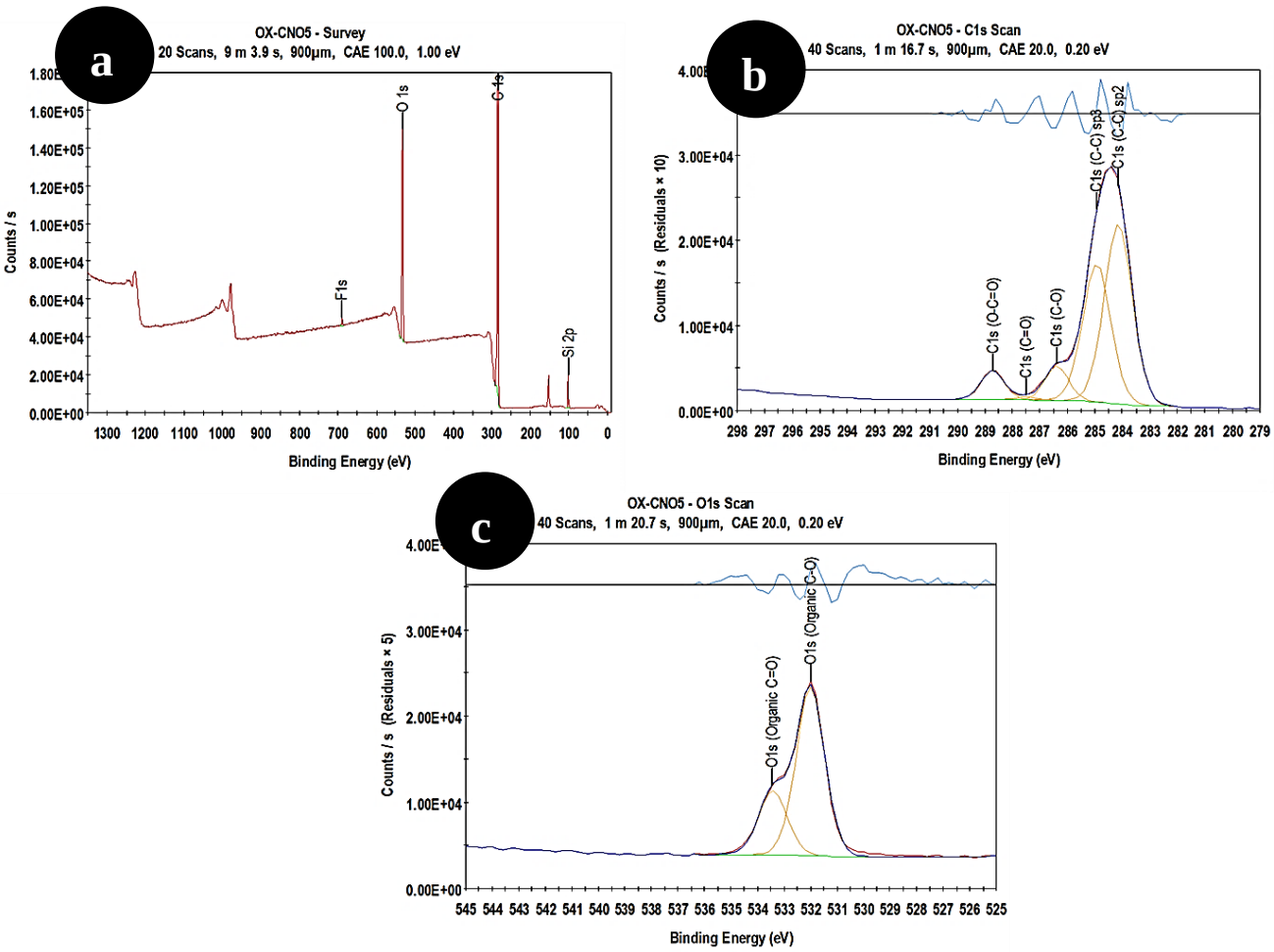

Figure 5.12: a) XPS full scan spectrum, and the corresponding high-resolution spectra of b) C1s and c) O1s of the as-synthesized ox-OLCNs.

N-OLCNs (**Figure 5.13 a**) revealed three peaks at 284.4 eV, 398.8 eV and 532.8 eV which are attributed to the C1s, N1s and O1s respectively. As shown in **Table 5.4**, the atomic percentages of C1s, N1s and O1s in N-OLCNs were 87.4 %, 0.8 % and 11.5 %, respectively. The high-resolution C1s (**Figure 5.13 b**) also showed five different types of carbon at 284.2 eV, 285.0 eV, 286.2 eV, 287.5 eV and 288.8 eV which were assigned to C-C sp^2 hybridization, C-C sp^3 hybridization, C-O, C=O/C=N and O-C=O, respectively [73].

The deconvolution of high-resolution spectrum of N1s (**Figure 5.13 c**) resulted in a single type of nitrogen atoms located at 399.3 eV associated with pyrrolic nitrogen as the dominant nitrogen-doping configuration [72]. The atomic percentage of the N1s nitrogen is 0.8 at. %. This shows that successful N-doping did occur (as also seen from the FTIR spectra).

Lastly, the high resolution spectrum of O1s (**Figure 5.13 d**) revealed two peaks at 532.1 eV and 533.5 eV which are attributed to C-O and C=O, respectively. These O-configuration almost have an equal atomic composition percentage at 6% and 5.78%, respectively.

All C1s showed that multiple types of carbons were formed on the surface [74]. These results are in good agreement with data from FTIR studies.

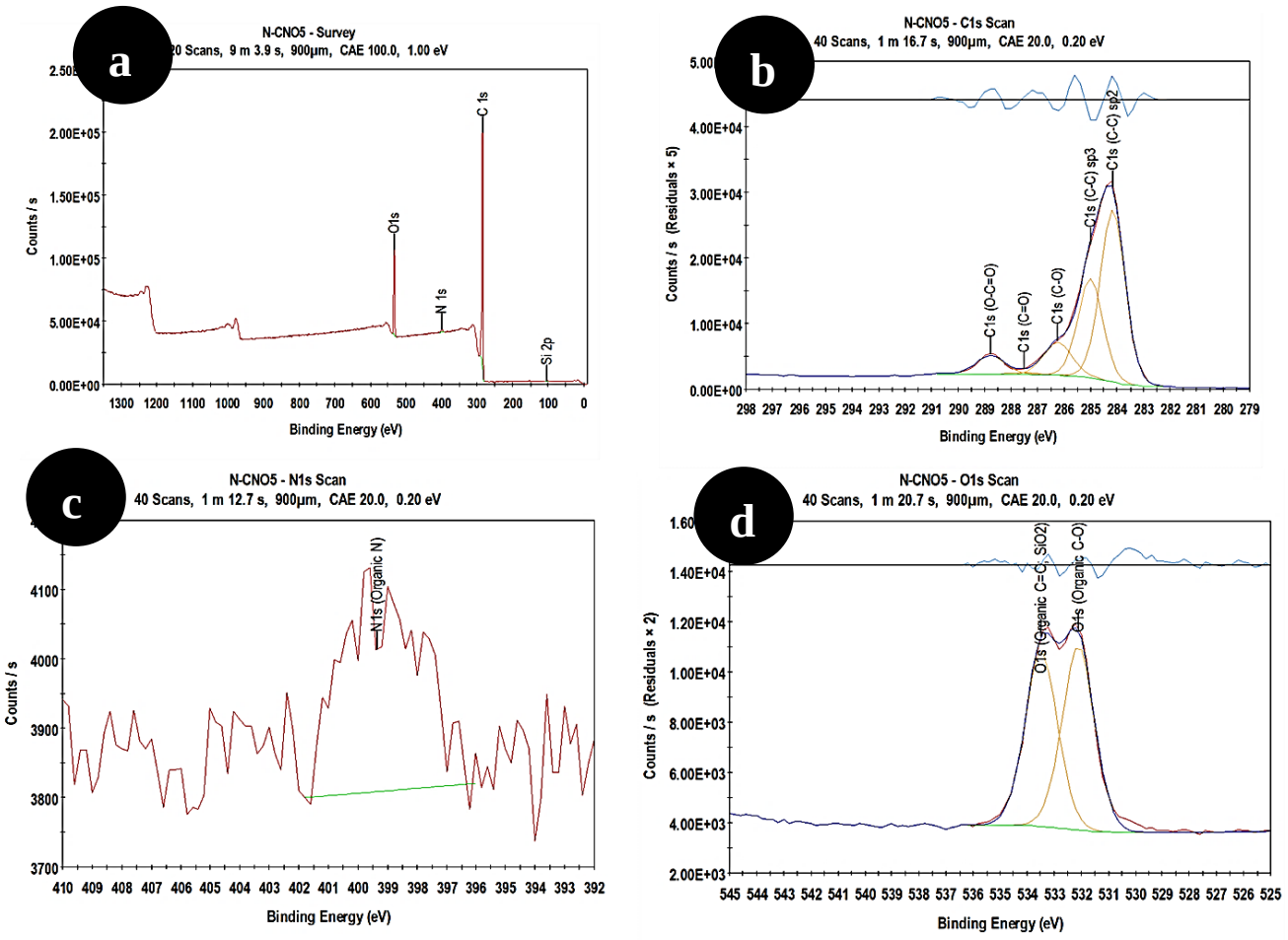

Figure 5.13: a) XPS full scan spectrum, and the corresponding high-resolution spectra of b) C1s, c) N1s, and d) O1s of the as-synthesized N-OLCNs.

Table 5.3: The relative percentage composition of the as-synthesized p-OLCNs, ox-OLCNs and N-OLCNs from XPS spectroscopy.

	Atomic percentage			
Sample name	C (%)	N (%)	O (%)	Impurities (%)
p-OLCNs	89.2	-	10.6	0.2
ox-OLCNs	74.3	-	18.6	7.1
N-OLCNs	87.4	0.8	11.5	0.3

5.3.8. Elemental (CHNS) analysis

The elemental analysis data are reported in **Table 5.5**. The high percentage carbon is consistent with a carbonaceous material with a large carbon backbone, agreeing well with the PXRD, Raman, FTIR, and XPS analysis.

These results further confirm the successful N-doping of N-OLCNs (1.3 %). The p-OLCNs and ox-OLCNs show small percentages of N-atoms possibly due to contamination, as they couldn't be picked up by FTIR and XPS analysis techniques.

Table 5.4: Summary of the CHNS analysis results.

	Results (%)			
Sample name	C	H	N	S
p-OLCNs	95.48	1.822	0.13	-
ox-OLCNs	87.90	3.143	0.15	-
N-OLCNs	92.87	0.962	1.34	-

5.3.9. Brunauer-Emmett-Teller (BET) surface area analysis

Table 5.6 below shows a summary of the BET data. The SSA of p-OLCNs is 61.7 m^2/g, 68.7 m^2/g for ox-OLCNs and 197.7 m^2/g for N-OLCNs. The p- and ox-OLCN surface areas are

comparable, whereas N-OLCN surface areas are much greater. The increase in BET surface area caused by ammonia-induced surface erosion; potential stacking of N atoms on/in the OLCNs [175]. The creation of inter- and intra-particle pores can also be linked to the elimination of surface functional groups [176]. These findings concur with those of TEM, Raman, and TGA analyses. BET plots can be found in th **SI, Figure. S.15**.

Table 5.5: Summary of the BET results.

Sample name	Surface area (m^2/g)	Pore volume (cm^3/g)	Pore size (nm)
p-OLCNs	61.7 ± 0.2	0.31	26.6
ox-OLCNs	68.7 ± 0.1	0.45	36.3
N-OLCNs	197.9 ± 1.1	0.33	16.2

5.3 Conclusion

The synthesis and functionalization of OLCNs were described in this chapter of the study by doping nitrogen atoms into as-produced OLCNs using ammonia gas as a nitrogen source and oxidizing OLCNs using the reflux technique with H_2O_2 resulting in p-, ox- and N-OLCNs. The resulting OLCNs exhibited chain-like quasi-spherical morphology with varying particle sizes. The surface modifications on the OLCNs were successful as the N and O were seen to be present in the N-OLCNs and ox-OLCNs. The PXRD analysis, Raman spectroscopy, FTIR spectroscopy, XPS analysis and CHN-S analysis were well in agreement with each other proving this.

References

1. Leis, J., Perkson, A., Arulepp, M., Käärik, M., & Svensson, G. (2001). Carbon nanostructures produced by chlorinating aluminium carbide. *Carbon*, *39*(13), 2043–2048. https://doi.org/10.1016/s0008-6223(01)00020-3
2. Katcho, N. A., Urones-Garrote, E., Avila-Brande, D., Gomez-Herrero, A., Urbonaite, S., Csillag, S., Lomba, E., Agullo-Rueda, F., Landa-Canovas, A. R., & Otero-Diaz, L. C. (2007). Carbon Hollow Nanospheres from Chlorination of Ferrocene. *ChemInform*, *38*(30). https://doi.org/10.1002/chin.200730192
3. Lian, W., Song, H., Chen, X., Li, L., Huo, J., Zhao, M., & Wang, G. (2008). The transformation of acetylene black into onion-like hollow carbon nanoparticles at 1000°C using an iron catalyst. *Carbon*, *46*(3), 525–530. https://doi.org/10.1016/j.carbon.2007.12.024
4. Ma, Y., Hu, Z., Huo, K., Lu, Y., Hu, Y., Liu, Y., Hu, J., & Chen, Y. (2005). A practical route to the production of carbon nanocages. *Carbon*, *43*(8), 1667–1672. https://doi.org/10.1016/j.carbon.2005.02.004
5. Zhang, C., Li, J., Liu, E., He, C., Shi, C., Du, X., Hauge, R. H., & Zhao, N. (2012). Synthesis of hollow carbon nano-onions and their use for electrochemical hydrogen storage. *Carbon*, *50*(10), 3513–3521. https://doi.org/10.1016/j.carbon.2012.03.019
6. Chen, X., Deng, F., Wang, J., Yang, H., Wu, G., Zhang, X., Peng, J., & Li, W. (2001). New method of carbon onion growth by radio-frequency plasma-enhanced chemical vapor deposition. *Chemical Physics Letters*, *336*(3–4), 201–204. https://doi.org/10.1016/s0009-2614(01)00085-9
7. Kuznetsov, V. L., Chuvilin, A. L., Butenko, Y. V., Mal'kov, I. Y., & Titov, V. M. (1994). Onion-like carbon from ultra-disperse diamond. *Chemical Physics Letters*, *222*(4), 343–348. https://doi.org/10.1016/0009-2614(94)87072-1
8. Cabioc'h, T., Riviere, J. P., & Delafond, J. (1995). A new technique for fullerene onion formation. *Journal of Materials Science*, *30*(19), 4787–4792. https://doi.org/10.1007/bf01154486
9. Mordkovich, V., & Takeuchi, Y. (2002). Multishell fullerenes by laser vaporization of composite carbon–metal targets. *Chemical Physics Letters*, *355*(1–2), 133–138. https://doi.org/10.1016/s0009-2614(02)00196-3
10. Garcia-Martin, T., Rincon-Arevalo, P., & Campos-Martin, G. (2013). Method to obtain carbon nano-onions by pyrolisys of propane. *Open Physics*, *11*(11). https://doi.org/10.2478/s11534-013-0294-1

11. Choucair, M., & Stride, J. A. (2012). The gram-scale synthesis of carbon onions. *Carbon*, *50*(3), 1109–1115. https://doi.org/10.1016/j.carbon.2011.10.023
12. Singh, V. (2018). Natural source derived carbon nano-onions as electrode material for sensing applications. *Diamond and Related Materials*, *87*, 202–207. https://doi.org/10.1016/j.diamond.2018.06.007
13. Tripathi, K. M., Singh, A., Bhati, A., Sarkar, S., & Sonkar, S. K. (2016). Sustainable Feasibility of the Environmental Pollutant Soot to Few-Layer Photoluminescent Graphene Nanosheets for Multifunctional Applications. *ACS Sustainable Chemistry & Engineering*, *4*(12), 6399–6408. https://doi.org/10.1021/acssuschemeng.6b01045
14. Dubey, P., Tripathi, K. M., Mishra, R., Bhati, A., Singh, A., & Sonkar, S. K. (2015). A simple one-step hydrothermal route towards water solubilization of carbon quantum dots from soya-nuggets for imaging applications. *RSC Advances*, *5*(106), 87528–87534. https://doi.org/10.1039/c5ra14536h
15. Mohapatra, D., Badrayyana, S., & Parida, S. (2016). Facile wick-and-oil flame synthesis of high-quality hydrophilic onion-like carbon nanoparticles. *Materials Chemistry and Physics*, *174*, 112–119. https://doi.org/10.1016/j.matchemphys.2016.02.057
16. Mohapatra, J., Ananthoju, B., Nair, V., Mitra, A., Bahadur, D., Medhekar, N., & Aslam, M. (2018). Enzymatic and non-enzymatic electrochemical glucose sensor based on carbon nano-onions. *Applied Surface Science*, *442*, 332–341. https://doi.org/10.1016/j.apsusc.2018.02.124
17. Dhand, V., Prasad, J. S., Rao, M. V., Bharadwaj, S., Anjaneyulu, Y., & Jain, P. K. (2013). Flame synthesis of carbon nano onions using liquefied petroleum gas without catalyst. *Materials Science and Engineering: C*, *33*(2), 758–762. https://doi.org/10.1016/j.msec.2012.10.029
18. Levy, L., Chaudhuri, I. S., Krueger, N., & McCunney, R. J. (2012). Does Carbon Black Disaggregate in Lung Fluid? A Critical Assessment. *Chemical Research in Toxicology*, *25*(10), 2001–2006. https://doi.org/10.1021/tx300160z
19. Dhand, V., Prasad, J. S., Rao, M. V., Bharadwaj, S., Anjaneyulu, Y., & Jain, P. K. (2013b). Flame synthesis of carbon nano onions using liquefied petroleum gas without catalyst. *Materials Science and Engineering: C*, *33*(2), 758–762. https://doi.org/10.1016/j.msec.2012.10.029
20. Mongwe, T. H., Matsoso, B. J., Mutuma, B. K., Coville, N. J., & Maubane, M. S. (2018). Synthesis of chain-like carbon nano-onions by a flame assisted pyrolysis technique using

different collecting plates. *Diamond and Related Materials*, *90*, 135–143. https://doi.org/10.1016/j.diamond.2018.10.002

21. Siswana, M. P., Ozoemena, K. I., & Nyokong, T. (2006). Electrocatalysis of asulam on cobalt phthalocyanine modified multi-walled carbon nanotubes immobilized on a basal plane pyrolytic graphite electrode. *Electrochimica Acta*, *52*(1), 114–122. https://doi.org/10.1016/j.electacta.2006.03.090
22. Yu, H., Jin, Y., Peng, F., Wang, H., & Yang, J. (2008). Kinetically Controlled Side-Wall Functionalization of Carbon Nanotubes by Nitric Acid Oxidation. *The Journal of Physical Chemistry C*, *112*(17), 6758–6763. https://doi.org/10.1021/jp711975a
23. Chou, A., Böcking, T., Liu, R., Singh, N. K., Moran, G., & Gooding, J. J. (2008). Effect of Dialysis on the Electrochemical Properties of Acid-Oxidized Single-Walled Carbon Nanotubes. *The Journal of Physical Chemistry C*, *112*(36), 14131–14138. https://doi.org/10.1021/jp7113785
24. Zhang, J., Zou, H., Qing, Q., Yang, Y., Li, Q., Liu, Z., Guo, X., & Du, Z. (2003). Effect of Chemical Oxidation on the Structure of Single-Walled Carbon Nanotubes. *The Journal of Physical Chemistry B*, *107*(16), 3712–3718. https://doi.org/10.1021/jp027500u
25. Datsyuk, V., Kalyva, M., Papagelis, K., Parthenios, J., Tasis, D., Siokou, A., Kallitsis, I., & Galiotis, C. (2008). Chemical oxidation of multiwalled carbon nanotubes. *Carbon*, *46*(6), 833–840. https://doi.org/10.1016/j.carbon.2008.02.012
26. Ziegler, K. J., Gu, Z., Shaver, J., Chen, Z., Flor, E. L., Schmidt, D. J., Chan, C., Hauge, R. H., & Smalley, R. E. (2005). Cutting single-walled carbon nanotubes. *Nanotechnology*, *16*(7), S539–S544. https://doi.org/10.1088/0957-4484/16/7/031
27. Miyata, Y., Maniwa, Y., & Kataura, H. (2005). Selective Oxidation of Semiconducting Single-Wall Carbon Nanotubes by Hydrogen Peroxide. *The Journal of Physical Chemistry B*, *110*(1), 25–29. https://doi.org/10.1021/jp055692y
28. Zhang, J., Zou, H., Qing, Q., Yang, Y., Li, Q., Liu, Z., Guo, X., & Du, Z. (2003b). Effect of Chemical Oxidation on the Structure of Single-Walled Carbon Nanotubes. *The Journal of Physical Chemistry B*, *107*(16), 3712–3718. https://doi.org/10.1021/jp027500u
29. Shaikh, A., Singh, B. K., Mohapatra, D., & Parida, S. (2019). Nitrogen-Doped Carbon Nano-Onions as a Metal-Free Electrocatalyst. *Electrocatalysis*, *10*(3), 222–231. https://doi.org/10.1007/s12678-019-00514-9
30. Habiba, K., Makarov, V. I., Avalos, J., Guinel, M. J., Weiner, B. R., & Morell, G. (2013). Luminescent graphene quantum dots fabricated by pulsed laser synthesis. *Carbon*, *64*, 341–350. https://doi.org/10.1016/j.carbon.2013.07.084

31. Shen, J., Zhu, Y., Yang, X., & Li, C. (2012). Graphene quantum dots: emergent nanolights for bioimaging, sensors, catalysis and photovoltaic devices. *Chemical Communications*, *48*(31), 3686. https://doi.org/10.1039/c2cc00110a
32. Ewels, C. P., & Glerup, M. (2005). Nitrogen Doping in Carbon Nanotubes. *Journal of Nanoscience and Nanotechnology*, *5*(9), 1345–1363. https://doi.org/10.1166/jnn.2005.304
33. Georgakilas, V., Kordatos, K., Prato, M., Guldi, D. M., Holzinger, M., & Hirsch, A. (2002). Organic Functionalization of Carbon Nanotubes. *Journal of the American Chemical Society*, *124*(5), 760–761. https://doi.org/10.1021/ja016954m
34. Sikeyi, L. L., Ntuli, T. D., Mongwe, T. H., Maxakato, N. W., Carleschi, E., Doyle, B. P., Coville, N. J., & Maubane-Nkadimeng, M. S. (2021). Microwave assisted synthesis of nitrogen doped and oxygen functionalized carbon nano onions supported palladium nanoparticles as hybrid anodic electrocatalysts for direct alkaline ethanol fuel cells. *International Journal of Hydrogen Energy*, *46*(18), 10862–10875. https://doi.org/10.1016/j.ijhydene.2020.12.154
35. Tomita, S., Burian, A., Dore, J. C., LeBolloch, D., Fujii, M., & Hayashi, S. (2002). Diamond nanoparticles to carbon onions transformation: X-ray diffraction studies. *Carbon*, *40*(9), 1469–1474. https://doi.org/10.1016/s0008-6223(01)00311-6
36. Aleksenskii, A. E., Baidakova, M. V., Vul', A. Y., Davydov, V. Y., & Pevtsova, Y. A. (1997). Diamond-graphite phase transition in ultradisperse-diamond clusters. *Physics of the Solid State*, *39*(6), 1007–1015. https://doi.org/10.1134/1.1129989
37. Yang, Q. H., Hou, P. X., Unno, M., Yamauchi, S., Saito, R., & Kyotani, T. (2005). Dual Raman Features of Double Coaxial Carbon Nanotubes with N-Doped and B-Doped Multiwalls. *Nano Letters*, *5*(12), 2465–2469. https://doi.org/10.1021/nl051779j
38. Liu, X. J., Feng, J. K., Ren, A. M., & Zhou, X. (2003). Comparative studies of the spectra and the second-order nonlinear polarizabilities for donor–acceptor ensembles between Zn-porphyrin/fullerene [60] and Zn-porphyrin/naphthalenediimide. *Journal of Molecular Structure: THEOCHEM*, *635*(1–3), 191–202. https://doi.org/10.1016/s0166-1280(03)00420-2
39. Namazian, M., Norouzi, P., & Ranjbar, R. (2003). Corrigendum to "Prediction of electrode potentials of some quinone derivatives in acetonitrile" [J. Mol. Struct. (Theochem) 625 (2003) 235–241)]. *Journal of Molecular Structure: THEOCHEM*, *664–665*, 319. https://doi.org/10.1016/j.theochem.2003.10.047
40. Butsyk, O., Olejnik, P., Romero, E., & Plonska-Brzezinska, M. E. (2019). Postsynthetic treatment of carbon nano-onions: Surface modification by heteroatoms to enhance their

capacitive and electrocatalytic properties. *Carbon*, *147*, 90–104. https://doi.org/10.1016/j.carbon.2019.02.063

41. Han, F. D., Yao, B., & Bai, Y. J. (2011). Preparation of Carbon Nano-Onions and Their Application as Anode Materials for Rechargeable Lithium-Ion Batteries. *The Journal of Physical Chemistry C*, *115*(18), 8923–8927. https://doi.org/10.1021/jp2007599
42. Yap, P. L., Kabiri, S., Auyoong, Y. L., Tran, D. N. H., & Losic, D. (2019). Tuning the Multifunctional Surface Chemistry of Reduced Graphene Oxide via Combined Elemental Doping and Chemical Modifications. *ACS Omega*, *4*(22), 19787–19798. https://doi.org/10.1021/acsomega.9b02642
43. Kyotani, T., Sonobe, N., & Tomita, A. (1988). Formation of highly orientated graphite from polyacrylonitrile by using a two-dimensional space between montmorillonite lamellae. *Nature*, *331*(6154), 331–333. https://doi.org/10.1038/331331a0
44. Zhang, Y., Reed, A., & Kim, D. Y. (2018). Nitrogen doped carbon nano-onions as efficient and robust electrocatalysts for oxygen reduction reactions. *Current Applied Physics*, *18*(4), 417–423. https://doi.org/10.1016/j.cap.2018.02.001
45. Camisasca, A., Sacco, A., Brescia, R., & Giordani, S. (2018). Boron/Nitrogen-Codoped Carbon Nano-Onion Electrocatalysts for the Oxygen Reduction Reaction. *ACS Applied Nano Materials*, *1*(10), 5763–5773. https://doi.org/10.1021/acsanm.8b01430
46. Mykhailiv, O., Zubyk, H., & Plonska-Brzezinska, M. E. (2017). Carbon nano-onions: Unique carbon nanostructures with fascinating properties and their potential applications. *Inorganica Chimica Acta*, *468*, 49–66. https://doi.org/10.1016/j.ica.2017.07.021
47. Plonska-Brzezinska, M. E., Brus, D. M., Breczko, J., & Echegoyen, L. (2013). Carbon Nano-Onions and Biocompatible Polymers for Flavonoid Incorporation. *Chemistry - A European Journal*, *19*(16), 5019–5024. https://doi.org/10.1002/chem.201300009
48. Roy, D., Chhowalla, M., Wang, H., Sano, N., Alexandrou, I., Clyne, T., & Amaratunga, G. (2003). Characterisation of carbon nano-onions using Raman spectroscopy. *Chemical Physics Letters*, *373*(1–2), 52–56. https://doi.org/10.1016/s0009-2614(03)00523-2
49. Rao, A. M., Jorio, A., Pimenta, M. A., Dantas, M. S. S., Saito, R., Dresselhaus, G., & Dresselhaus, M. S. (2000). Polarized Raman Study of Aligned Multiwalled Carbon Nanotubes. *Physical Review Letters*, *84*(8), 1820–1823. https://doi.org/10.1103/physrevlett.84.1820
50. Rettenbacher, A. S., Elliott, B., Hudson, J. S., Amirkhanian, A., & Echegoyen, L. (2006). Preparation and Functionalization of Multilayer Fullerenes (Carbon Nano-Onions).

Chemistry - A European Journal, *12*(2), 376–387. https://doi.org/10.1002/chem.200500517

51. Wajs, E., Molina-Ontoria, A., Nielsen, T. T., Echegoyen, L., & Fragoso, A. (2014). Supramolecular Solubilization of Cyclodextrin-Modified Carbon Nano-Onions by Host–Guest Interactions. *Langmuir*, *31*(1), 535–541. https://doi.org/10.1021/la504065r
52. Frasconi, M., Maffeis, V., Bartelmess, J., Echegoyen, L., & Giordani, S. (2015). Highly surface functionalized carbon nano-onions for bright light bioimaging. *Methods and Applications in Fluorescence*, *3*(4), 044005. https://doi.org/10.1088/2050-6120/3/4/044005
53. Molina-Ontoria, A., Chaur, M. N., Plonska-Brzezinska, M. E., & Echegoyen, L. (2013). Preparation and characterization of soluble carbon nano-onions by covalent functionalization, employing a Na–K alloy. *Chemical Communications*, *49*(24), 2406. https://doi.org/10.1039/c3cc39077b
54. Koudoumas, E., Kokkinaki, O., Konstantaki, M., Couris, S., Korovin, S., Detkov, P., Kuznetsov, V., Pimenov, S., & Pustovoi, V. (2002). Onion-like carbon and diamond nanoparticles for optical limiting. *Chemical Physics Letters*, *357*(5–6), 336–340. https://doi.org/10.1016/s0009-2614(02)00557-2
55. Tripathi, K. M., Tran, T. S., Kim, Y. J., & Kim, T. (2017). Green Fluorescent Onion-Like Carbon Nanoparticles from Flaxseed Oil for Visible Light Induced Photocatalytic Applications and Label-Free Detection of Al(III) Ions. *ACS Sustainable Chemistry & Engineering*, *5*(5), 3982–3992. https://doi.org/10.1021/acssuschemeng.6b03182
56. D'Amora, M., Camisasca, A., Lettieri, S., & Giordani, S. (2017). Toxicity Assessment of Carbon Nanomaterials in Zebrafish during Development. *Nanomaterials*, *7*(12), 414. https://doi.org/10.3390/nano7120414
57. Qiao, Z., Li, J., Zhao, N., Shi, C., & Nash, P. (2006). Graphitization and microstructure transformation of nanodiamond to onion-like carbon. *Scripta Materialia*, *54*(2), 225–229. https://doi.org/10.1016/j.scriptamat.2005.09.037
58. Plonska-Brzezinska, M. E., Lapinski, A., Wilczewska, A. Z., Dubis, A. T., Villalta-Cerdas, A., Winkler, K., & Echegoyen, L. (2011). The synthesis and characterization of carbon nano-onions produced by solution ozonolysis. *Carbon*, *49*(15), 5079–5089. https://doi.org/10.1016/j.carbon.2011.07.027
59. Rani, U. A., Ng, L. Y., Ng, C. Y., & Mahmoudi, E. (2020). A review of carbon quantum dots and their applications in wastewater treatment. *Advances in Colloid and Interface Science*, *278*, 102124. https://doi.org/10.1016/j.cis.2020.102124

60. Croitoru, A., Oprea, O., Nicoara, A., Trusca, R., Radu, M., Neacsu, I., Ficai, D., Ficai, A., & Andronescu, E. (2019). Multifunctional Platforms Based on Graphene Oxide and Natural Products. *Medicina, 55*(6), 230. https://doi.org/10.3390/medicina55060230
61. Gu, W., Peters, N., & Yushin, G. (2013). Functionalized carbon onions, detonation nanodiamond and mesoporous carbon as cathodes in Li-ion electrochemical energy storage devices. Carbon, 53, 292–301. https://doi.org/10.1016/j.carbon.2012.10.061
62. Naeimi, H., Mohajeri, A., Moradi, L., & Rashidi, A. M. (2009). Efficient and facile one pot carboxylation of multiwalled carbon nanotubes by using oxidation with ozone under mild conditions. *Applied Surface Science*, *256*(3), 631–635. https://doi.org/10.1016/j.apsusc.2009.08.094
63. Li, M., Boggs, M., Beebe, T. P., & Huang, C. (2008). Oxidation of single-walled carbon nanotubes in dilute aqueous solutions by ozone as affected by ultrasound. *Carbon*, *46*(3), 466–475. https://doi.org/10.1016/j.carbon.2007.12.012
64. Chen, Z., Ziegler, K. J., Shaver, J., Hauge, R. H., & Smalley, R. E. (2006). Cutting of Single-Walled Carbon Nanotubes by Ozonolysis. *The Journal of Physical Chemistry B*, *110*(24), 11624–11627. https://doi.org/10.1021/jp057494c
65. Banerjee, S., & Wong, S. S. (2002). Rational Sidewall Functionalization and Purification of Single-Walled Carbon Nanotubes by Solution-Phase Ozonolysis. *The Journal of Physical Chemistry B*, *106*(47), 12144–12151. https://doi.org/10.1021/jp026304k
66. Mawhinney, D. B., Naumenko, V., Kuznetsova, A., Yates, J. T., Liu, J., & Smalley, R. E. (2000). Infrared Spectral Evidence for the Etching of Carbon Nanotubes: Ozone Oxidation at 298 K. *Journal of the American Chemical Society*, *122*(10), 2383–2384. https://doi.org/10.1021/ja994094s
67. Butsyk, O., Olejnik, P., Romero, E., & Plonska-Brzezinska, M. E. (2019b). Postsynthetic treatment of carbon nano-onions: Surface modification by heteroatoms to enhance their capacitive and electrocatalytic properties. *Carbon*, *147*, 90–104. https://doi.org/10.1016/j.carbon.2019.02.063
68. Estrade-Szwarckopf, H. (2004). XPS photoemission in carbonaceous materials: A “defect” peak beside the graphitic asymmetric peak. *Carbon*, *42*(8–9), 1713–1721. https://doi.org/10.1016/j.carbon.2004.03.005
69. Pujals, C. (2018). XPS of carbon nanostructures obtained by underwater arc discharge of graphite electrodes. *Nucleus (Havana)*, *64*, 15–18.
70. Estrade-Szwarckopf, H., Rousseau, B., & Jupille, J. (1992). Cesium Surface Atoms: XPS Comparison between GIC Surfaces and Thin Layers Deposited on Graphite. *Materials*

Science Forum, *91–93*, 703–708. https://doi.org/10.4028/www.scientific.net/msf.91-93.703

71. Schlgl, R., Che, M., Clause, O., Marcilly, C., Louis, C., Kninger, H., Teglauer, E., Keim, W., Drieben-Hlscher, B., Geus, J. W., van Dillen, A. J., & Barbier, J. (1997). Preparation of Solid Catalysts: Sections 2.1.9– 2.2.1.6. *Handbook of Heterogeneous Catalysis*, 138–264. https://doi.org/10.1002/9783527619474.ch2b
72. Thomas, J. (2009). Handbook Of Heterogeneous Catalysis. 2., completely revised and enlarged Edition. Vol. 1–8. Edited by G. Ertl, H. Knözinger, F. Schüth, and J. Weitkamp. *Angewandte Chemie International Edition*, *48*(19), 3390–3391. https://doi.org/10.1002/anie.200901598
73. Zuaznabar-Gardona, J. C., & Fragoso, A. (2020). Band structure, work function and interfacial diagrams of oxygen-functionalized carbon nano-onions. *Synthetic Metals*, *266*, 116434. https://doi.org/10.1016/j.synthmet.2020.116434
74. Lesiak, B., Jiricek, P., & Bieloshapka, I. (2017). Chemical and structural properties of Pd nanoparticle-decorated graphene—Electron spectroscopic methods and QUASES. *Applied Surface Science*, *404*, 300–309. https://doi.org/10.1016/j.apsusc.2017.01.183
75. Fujimoto, A., Yamada, Y., Koinuma, M., & Sato, S. (2016). Origins of sp3 C peaks in C 1s X-ray Photoelectron Spectra of Carbon Materials. *Analytical Chemistry*, *88*(12), 6110–6114. https://doi.org/10.1021/acs.analchem.6b01327
76. Estrade-Szwarckopf, H. (2004b). XPS photoemission in carbonaceous materials: A “defect” peak beside the graphitic asymmetric peak. *Carbon*, *42*(8–9), 1713–1721. https://doi.org/10.1016/j.carbon.2004.03.005
77. Zeiger, M., Fleischmann, S., Krüner, B., Tolosa, A., Bechtel, S., Baltes, M., Schreiber, A., Moroni, R., Vierrath, S., Thiele, S., & Presser, V. (2016). Influence of carbon substrate on the electrochemical performance of carbon/manganese oxide hybrids in aqueous and organic electrolytes. *RSC Advances*, *6*(109), 107163–107179. https://doi.org/10.1039/c6ra24181f
78. Ferrari, A. C., & Robertson, J. (2000). Interpretation of Raman spectra of disordered and amorphous carbon. *Physical Review B*, *61*(20), 14095–14107. https://doi.org/10.1103/physrevb.61.14095

Chapter 6
Synthesis of NCdots: OLCNs composites using the refluxing method

6.1 Introduction

Global warming and rising energy consumption are two problematic issues that the world is now grappling with. To assist with providing a solution to these problems, much effort has been spent in producing various types of solar cells. Solar cell technologies have the potential to either improve energy efficiency or assist with the development of renewable energy sources [1] when fossil fuels run out or become too scarce or too expensive. The dye-sensitized solar cell (DSSC), one of the most recent solar cells that has been created to address the aforementioned problems is a low-cost device with an easy manufacturing process [2, 3]. The four crucial parts of a DSSC device's performance are the photoanode, dye, electrolyte, and counter electrode [4, 5]. The counter electrode transports electrons to the electrolyte from the external circuit. Mechanical, chemical, and electrochemical stability, resilience, and excellent catalytic activity are all characteristics of an efficient counter electrode (CE) [6]. Strong electro-catalytic activity for effective electrolyte reduction, outstanding electrical conductivity for low charge-transfer resistance, cheap cost and high stability for large-scale manufacturing, and excellent electro-catalytic activity are all necessary for a good counter electrode [7].

Platinum (Pt) has been employed as a potential CE material due to its excellent electrical conductivity and electro-catalytic activities; nevertheless, the pricey cost and ease of corrosion by I^-/I_3^- based electrolytes have limited the usage of Pt [8]. As an alternative to platinum, carbon has been shown to be quite enticing. Nanoscale carbon compounds have a large surface area and many active sites [9], particularly heteroatom-doped carbon materials [10–16], have been produced and studied as possible replacement for Pt in DSSC devices.

Carbon dots (Cdots) are a new class of nano-carbonaceous materials with photoluminescent (PL) features that have sparked a lot of interest in a variety of fields since their discovery. Due to their low toxicity, great stability, and good photodegradation resistance, these dots have been deemed better than typical semiconductor quantum dots and organic dyes [17].

Electronic transitions in Cdots include σ→π*, π→π*, n→π* and σ→σ*, which are closely connected to Cdots' chemical make-up and optical characteristics [18]. Aromatic sp^2 domains in the carbon core are what give rise to the π -states in Cdots. As the quantity of conjugated carbon atoms increases, the energy gap between the -states, for instance, in graphene quantum dots (GQDs), rapidly decreases [19]. Functionalization may be utilized to change the redox potential of GQDs by covalently adding electron-withdrawing or -donating groups, even though it has little impact on the band gaps of GQDs. Functional groups, such as carbonyls and amines, that are present on the surface of Cdots and contain lone electron pairs can contribute to the N-states in Cdots. Additionally, electronic transitions from n-states in the functional groups to π* states in the sp^2 carbon domains are possible when the functional groups are bound to carbon domains [20]. As a result, the optical properties of Cdots are significantly influenced by electronic structures and related electronic transitions. This can influence their use, such as in optoelectronic cells. However, the electrical structure of Cdots remains a mystery and has to be investigated further.

Onion-like carbon nanomaterials (OLCNs) with a multilayer lamellar structure stand apart from other graphic carbon materials in a variety of ways, including their tiny diameter, structural stability, and possibility for a sizable exterior surface area, all of which are helpful for catalytic processes [21, 22]. The outcome is electrodes composed of carbon nanomaterials have been proposed to have good electrode-electrolyte interface leading to excellent conversion efficiencies. Since it is known that carbon can be used in DSSCs, the question arises as to whether carbon composites could be used to enhance the electrode activity. A composite or hybrid material with improved qualities may be created by combining two carbons with very different and distinct nanostructures. There are a few examples of all-carbon nanocomposites employed as a CE in DSSCs in the literature [7], suggesting this approach has potential. The incorporation of NCdots into a support material introduces functional groups into the support [23].

In this study, N doped and O functionalized OLCNs and pristine OLCNs with NCdots to create a new type of carbon-carbon composite is described. There are instances of the creation and application of composites made of Cdots and other carbon compounds [24, 25]. However, no thorough investigation of the interplay of OLCNs as a support for the Cdots or NCdots in particular has been made to far. According to our knowledge, this research is still in its infancy.

In situ growth, chemical bonding, and physical mixing are the three processes utilized to create Cdot-based composites or hybrids. Cdots and other materials are mixed physically to create composites that exhibit noncovalent interactions including electrostatic adsorption and hydrogen-bond interaction [26-28], or π–π stacking interaction. This occurs after blending the components by stirring or ultrasonication [29, 30]. When chemical bonding occurs between the Cdots and the second component, Cdots and other materials interact covalently. The heterogeneous nucleation and growth of a nanostructure on the surface of another nanomaterial is known as in situ growth [31].

In this study physical mixing was used to create the Cdots: OLCNs interactions via stated, π–π stacking interactions, hydrogen bonding, and/or electrostatic adsorption (**Scheme 6.1**) [32].

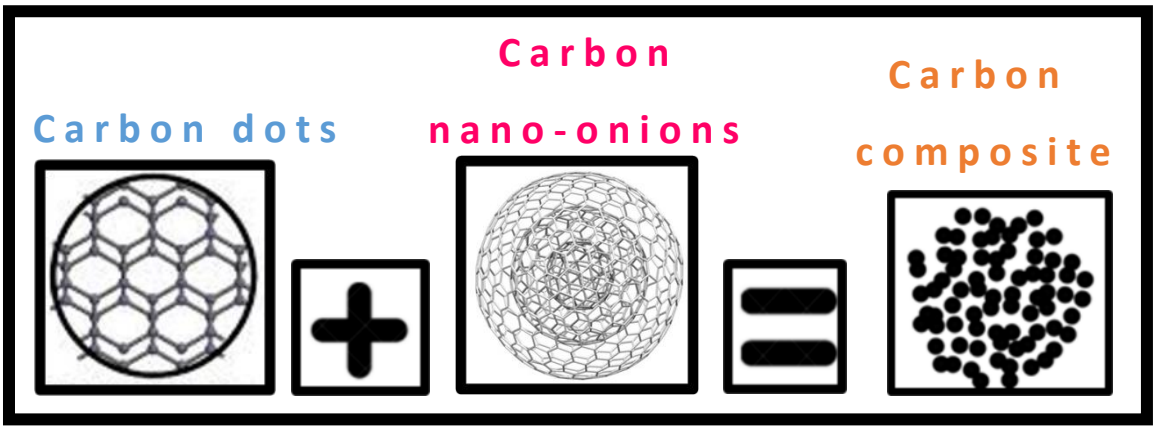

Scheme 6.1: Schematic representation of the formation of NCdots: OLCNs composites.

6.2 Experimental procedure

The synthesis of the NCdots and OLCNs has been reported in **Chapters 4 and 5**, respectively. In this study, the NCdots were loaded on the surface of the p-OLCNs, ox-OLCNs and N-OLCNs (**Scheme 6.1**) to produce a composite material using modified methods reported in literature [33, 34] via physical mixing (**Scheme 6.2**), as explained by Chen et al [31].

6.2.1. Starting materials

Table 6.1: Materials and reagents used in this study.

Reagents and materials	Purity	Supplier/source
NCdots (EDA)	-	Chapter 4
p-/ox-/N- OLCNs	-	Chapter 5
Ethanol	EtOH, 96%	Sigma-Alrich
Ammonium hydroxide	NH_4OH, 98%	Sigma-Alrich

6.2.2. Preparation NCdots: OLCNs composite

20 mL of water and 10 mL of ethanol were combined with the necessary number of NCdots (5 %, 10 %, 15 %, and so on. See **Tables 6.2 and 6.3**) and sonicated for 15 minutes. A required quantity of the support material (p-OLCNs, ox-OLCNs, and N-OLCNs) was added to a solution of 1 mL of NH_4OH and 10 mL of distilled water in a second, independent beaker. The combination was thereafter given a 15-minute sonication. After combining the two mixes, which separately contained the support solution and the NCdots solution, they were further sonicated for five minutes. The resulting mixture was then stirred for 6 hours under reflux at of 80 ºC (**Scheme 6.2**).

To create dry black powder, the product was then dried overnight in a vacuum oven at 80 ºC and a rotating evaporator at 70 ºC. The dispersion of NCdots over the surfaces of the OLCNs support was made easier by the ammonia present in the solution combination [35].

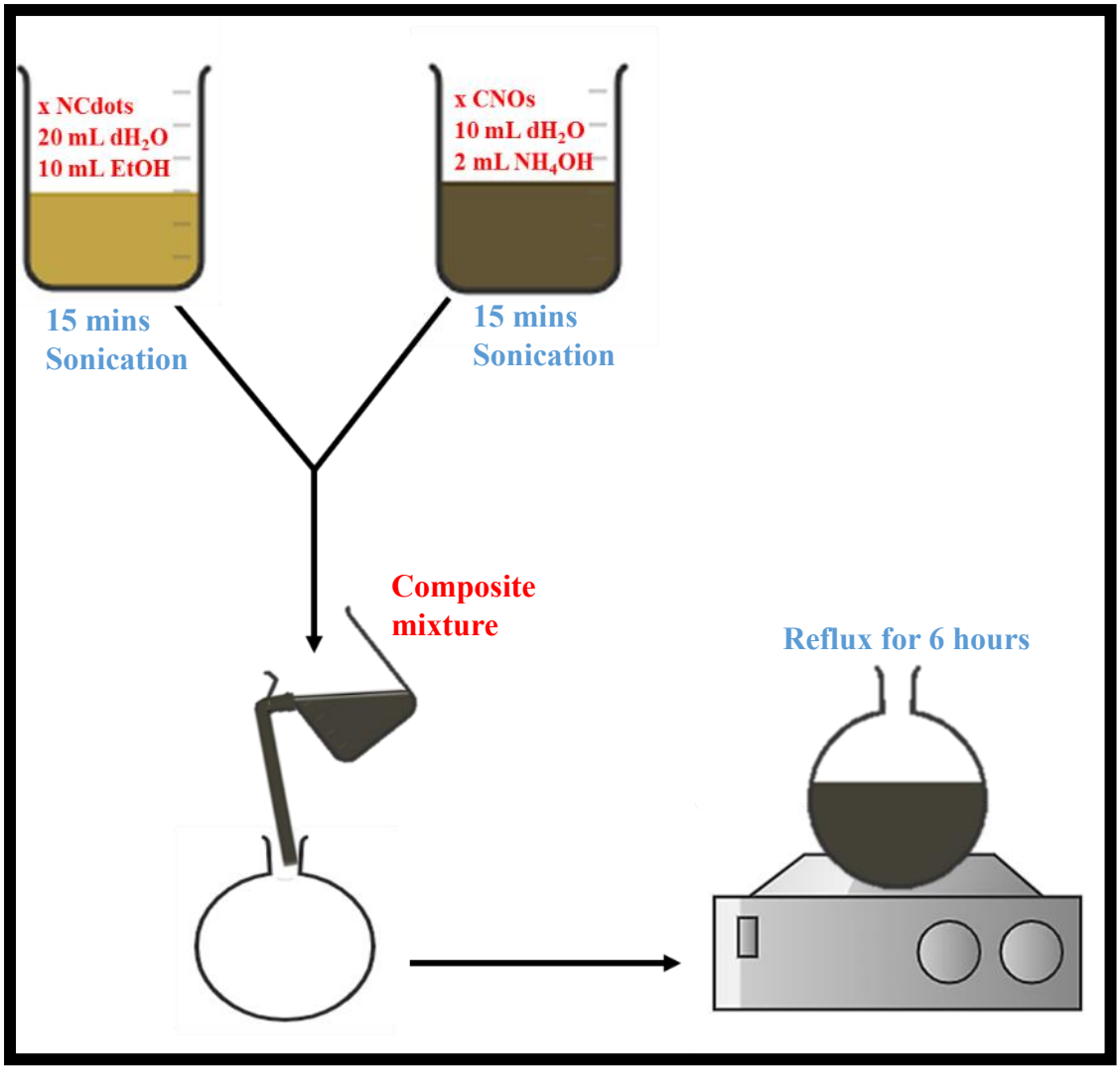

Scheme 6.2: Synthesis procedure for the NCdots: OLCNs composites.

NCdots: OLCNs composites were prepared in varying ratios. Synthesis conditions summarized in **Table 6.2** and **Table 6.3**.

Table 6.2: Summary of composite synthesis, following the standard procedure stated above (Section 6.2.2).

Mass of NCdots	Mass of OLCNs	% weight loading
1 mg	20 mg	5%
2 mg	20 mg	10%
3 mg	20 mg	15%
4 mg	20 mg	20%
6 mg	20 mg	30%
8 mg	20 mg	40%
10 mg	20 mg	50%

Table 6.3: Summary of composite synthesis with a lower support loading weight percentage than the NCdots.

Mass of OLCNs	Mass of NCdots	% weight loading
1 mg	20 mg	5%
2 mg	20 mg	10%

6.2.3. Characterization techniques

- The synthesized composites were characterized using TEM, PXRD, Uv-vis and PL spectroscopy and FTIR spectroscopy.

6.3 Results and discussion

Considering its safety, ease, and dispersibility for both Cdots and OLCNs, water was chosen as the preferred medium in the fabrication of Cdots: OLCNs nanocomposites. When making composites, there are a few pre-existing factors to consider [36-38]:

1) Reaction time: largely has an impact on the size and structure of composites

2) Reaction temperature: the ultimate shape of composite materials is controlled by regulating the pace at which nanostructures form on the surface of another nanomaterial
3) pH of the solution: may change or alter the surface state of the materials

In this study, experiments were carried out to optimize the above parameters. The hydrothermal reflux method was chosen as the appropriate procedure of synthesize for this purpose. This method can cater for long reaction times, low-to-moderate heating temperatures and continuos stirring with minimal manipulation to the reaction contents. Thus, 6 hours was chosen as the optimal reaction time as it allowed sufficient time for slow and steady mixng on the composite constituents into a single component without agglomeration. The optimal reaction temperature was set to be 80 ºC, as this temperature provided moderate heat to the reflux system which is crucial during physical mixing so as to preserve the structural shape of the composite constituents as they mix, and the NCdots embed into the structural matrix of the OLCNs'. High heating temperature have the potential of altering the structural shape and size of the constituents mixing thus altering the structure, function and ultimately properties of the composite being formed. Also, the composite may disintergrate as it forms due to burning from the high temepratured being provided. Continuous stirring at low speed was found to be useful in ensuring a uniform environment in the composite solution, avoid agglomeration in the complex system, and to help in maintaining the pace at which the nanocomposites form. Water was used as the preferred medium for the fabrication of the nanocomposites as it has a neutral pH, providing balance of acidty and basicity in the mixing solution. Thus, the pH of the system was found to be relatively the same before and after synthesis. The difference in pH was neglible, thus this gave evidence that the mixing procedure occurred under consistent and stable reaction conditions. The results and discussion sections below review the experimental findings and discuss them in the context of literature, while linking characterization techniques to each other and properties to performance, as per application in DSSCs.

6.3.1. Morphological analysis

The TEM images (**Figs. 6.1–6.3**) below show the composite material synthesized at different weight percentage loadings. Images of three selected groups of various nanocomposites are reported in this chapter (ranging from low to high loading, namely 5% NCdots: OLCNs, 50%

NCdots: OLCNs and 5% OLCNs: NCdots), information on other composites may be found in the **Supplementary Information (SI, Figs. S16-20)**.

The TEM micrographs revealed that all as-synthesized NCdots: OLCNs composites revealed the concentric turbostatic shells of the OLCNs, but the carbon dots were not clearly visible at the resolution used. The interaction between Cdots and support nanostructures has been shown to be weak and unstable, despite the physical mixing approach being simple and quick [39]. High resolution TEM can be able to provide us with more accurate details about the physical interaction of the NCdots and the surface of the various OLCNs. Furthermore, in **Fig. 6.1** there is no distinct visible morphological difference between the different types of nanocomposites overall (**Figs. 6.1 a, b and c**). It is possible that the Cdots are not visible on the support due to the low quantity of Cdots dispersing in an ethanol and water mixture.

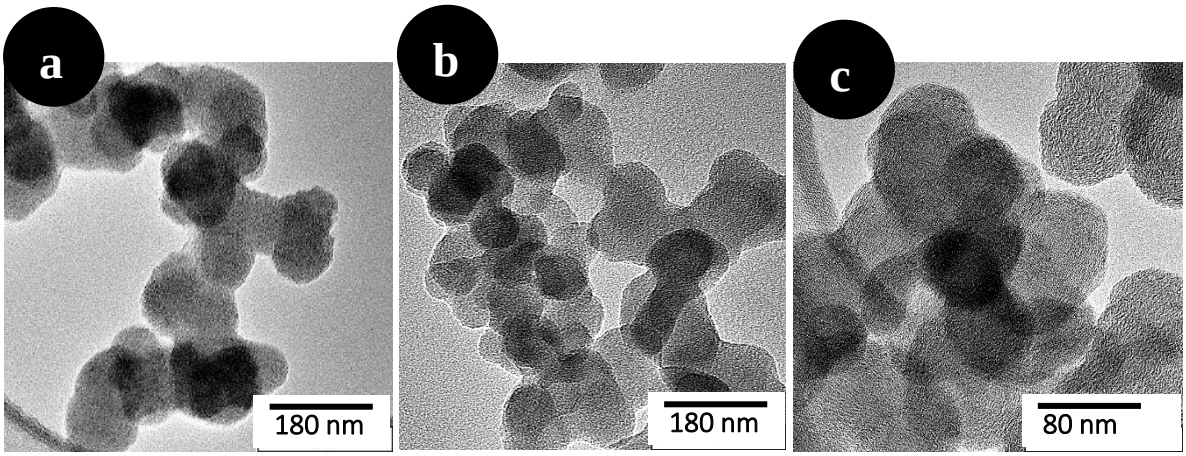

Figure 6.1: TEM images of a) 5%NCdots (EDA): p-OLCNs, b) 5%NCdots (EDA): ox-OLCNs and c) 5%NCdots (EDA): N-OLCNs composites.

The structure of the NCdots: OLCNs nanocomposites was found not to change as the NCdots: OLCNs ratio was varied (see **S16-20**). At very high loadings, **Fig. 6.2 c** it is possible to see NCdots (shown by arrows) on the external surface of N-OLCNs, suggesting that's these nanocomposites are bonded to each other extrinsically. The Derjagin-Laundau-Verwey-Overbeek hypothesis postulates that smaller particles are unstable in the vicinity of bigger particles, hence, the Cdots particles are dispersed throughout the support's surface. As a result, the Cdots adhere to the support material's surface (OLCNs) [40].

.

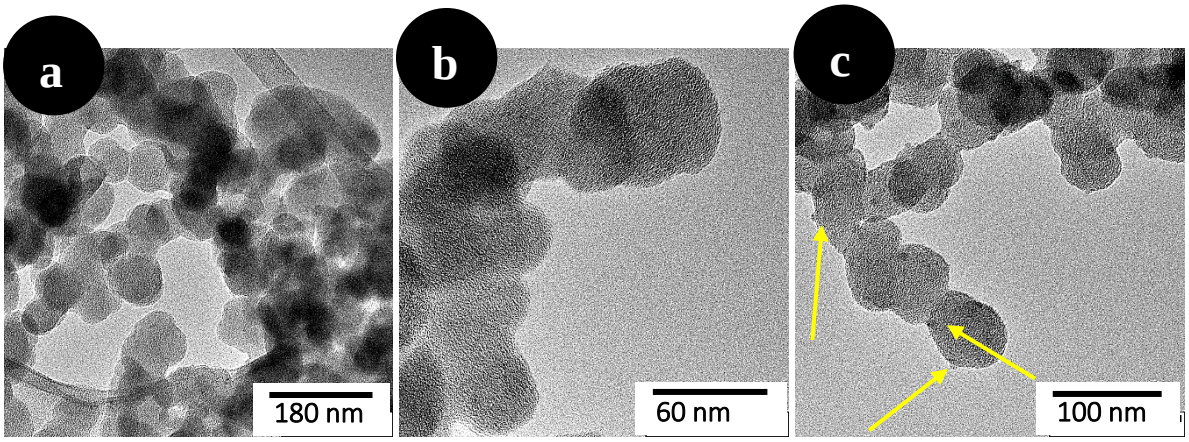

Figure 6.2: TEM images of a) 50%NCdots (EDA): p-OLCNs, b) 50%NCdots (EDA): ox-OLCNs and c) 50%NCdots (EDA): N-OLCNs composites.

The micrographs below were obtained from a composite material made by incorporating a higher ratio of NCdots to OLCNs (**Figs. 6.3 a, b and c**). The NCdots are still not visible on the surface of the various OLCNs. It is possible that Van der Waals forces involved binding Cdots to the OLCNs particles' surfaces, allowed them to stay bonded even during the subsequent drying cycle [40]. However, simple mixing techniques like physical mixing are primarily focused on liquid systems with hard integration modes, which cannot fully utilize and achieve the maximum intrinsic properties of each active material. This results in minimal control over constituent parts and failure to clarify the structural framework relationships between components in nanocomposites [41] which suggests why NCdots could not be visualized in the composite at such low TEM magnifications.

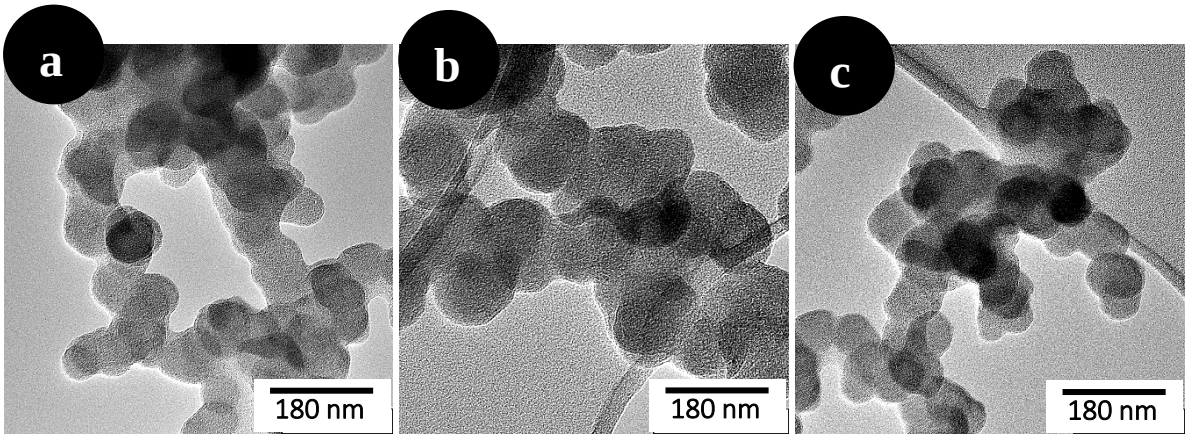

Figure 6.3: TEM images of a) 5% p-OLCNs: NCdots (EDA), b) 5% ox-OLCNs: NCdots (EDA) and c) 5% N-OLCNs: NCdots (EDA) composites.

In the same breath, micrographs of 10% wt. % OLCNs: NCdots composites observed below (**Figs. 6.4 a, b and c**) show the traditional morphology that has been observed in the above figures. Still the presence of NCdots on the surface/matrix of the OLCNs is not visible. Herein the OLCNs were added at 10% wt. % loading unto the NCdots and it was expected to see NCdots in/on the OLCNs or dangling on the edges of the OLCNs nanostructure at least.

To fully comprehend these nanocomposites, however, further knowledge regarding the nature of interaction between the various functional groups found in NCdots and OLCNs is necessary.

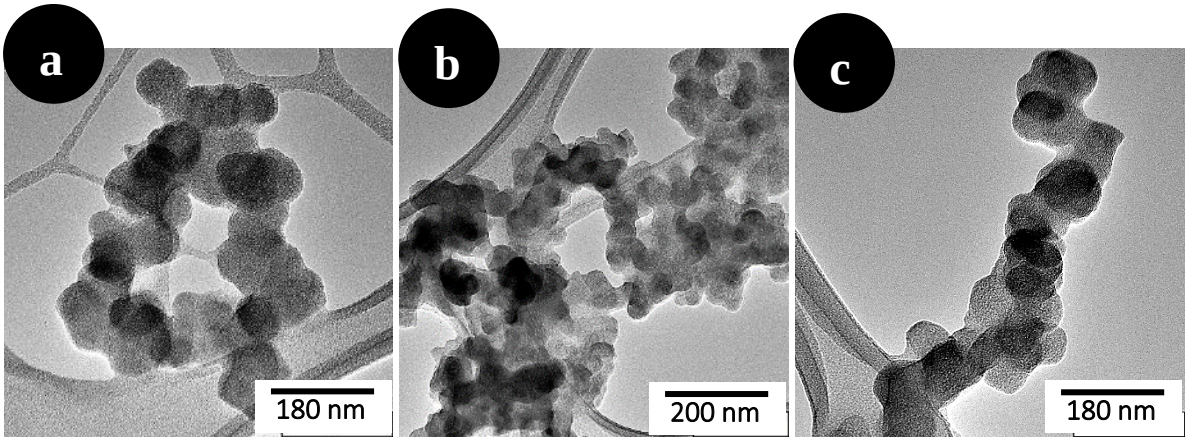

Figure 6.4: TEM images of a) 10% p-OLCNs: NCdots (EDA), b) 10% ox-OLCNs: NCdots (EDA) and c) 10% N-OLCNs: NCdots (EDA) composites.

6.3.2. Powder X-ray diffraction (PXRD) spectroscopy analysis

The PXRD analysis was measured for NCdots (EDA) and the various as-synthesized OLCNs samples and results are shown in **Fig. 6.5 a and b**, respectively. **Fig. 6.5 a**, the diffractogram shows a broad observed peak centred at 2θ = 24.7˚ (**Sec 4.3.2, Ch. 4**) and small peak centred at ~2θ = 61.0˚. The (002) and (100) planes may be used to explain the two peaks, respectively [42]. **Fig. 6.5 b** shows PXRD analysis was computed for all OLCNs samples (**Sec 5.3.2, Ch.5**). All OLCNs presented with a maximum asymmetric broad reflection at ~2θ = 25º, which can also be attributed to the (002) of turbostatic carbon and graphene carbon. The ox- and N-functionalized OLCNs presented with an additional peak at 2θ = 43º not present in the pristine material, which corresponds to the diamond structure observed on the (111) basal plane diffraction [43]. Moreover, ox-OLCNs exhibited a less a prominent shoulder peak at

around ~2θ = 18º (corresponding to the 001 plane) attributed to oxygen groups between the layers [44].

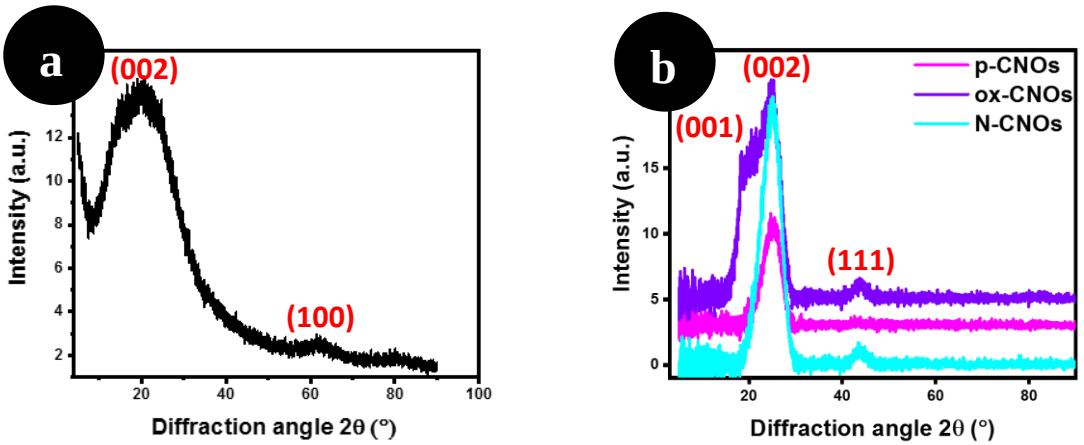

Figure 6.5: PXRD patterns of the as-synthesized precursor material of the composites; a) NCdots (EDA) and b) p-OLCNs, ox-OLCNs and N-OLCNs.

Figure 6.6 a and b shows full spectral patterns of nanocomposites prepared with 5% and 10% NCdots wt. % loadings, respectively. These XRD results further verified the structural properties of these nanomaterials. From both plots, the (002) graphitic plane clearly demonstrates that all NCdots: OLCNs have improved crystallinity at 2θ = ~25º (**Fig. 6.6**) [45]. The outcomes of the nanocomposite experiments show that the OLCNs' pore structure can serve as a basis for evenly dispersing NCdots. The OLCNs (**Fig. 6.5 b**) shows stronger and relatively sharper peak at the same peak position as the nanocomposite precursors could mean that the formed nanocomposites were even less graphitic in structure, after the physical mixing process [46]. The OLCNs diffractogram dominates that of the NCdots.

Figure 6.6 b shows even broader peaks of the (002) diffraction plane upon increase in w/w percentage loading. This also applies to diffractograms in **Fig 6.7**. The considerably larger carbon signal is a marker of little disordering of the structure of carbon in accordance with vivid amorphous broadening [47]. The broadening of the peak can be an indication of a widespread disordering of the structure due to the smaller sized/small quantities of sp^2-hybridized carbon [48]. So, the further broadening could be attributed to incorporation of the NCdots, whereby the XRD instrument picking up the smaller sized dots in the nanocomposite [49]. The peak positions did not change when compared to the nanocomposite precursor material (**Fig. 6.5 a and b**) indicating no change in the size of the carbon domains.

Figure 6.6 a and b both exhibited a small peak which can be attributed to the (100) reflection. This XRD pattern is typical of the as-prepared sample, the sharp diffraction peak (2θ = ~44.38 º) with low peak intensity. This peak is also present in (**Fig. 6.5 a**) and is indexed as graphite peak. Furthermore, 5% NCdots: ox-OLCNs (**Fig. 6.6 a**) presents a very low unresolved intensity peak between 40 and 50°. The chaotic structure of the graphene rings inside the ox-OLCNs in the (111) plane may be responsible for this peak [48, 49]. The weak peak corresponds to the (111) peak of the diamond structure in the XRD diffractogram [50, 51], It seems during OLCNs synthesis, the graphitic carbon peaks grow during formation, with some residual diamond peaks [52].

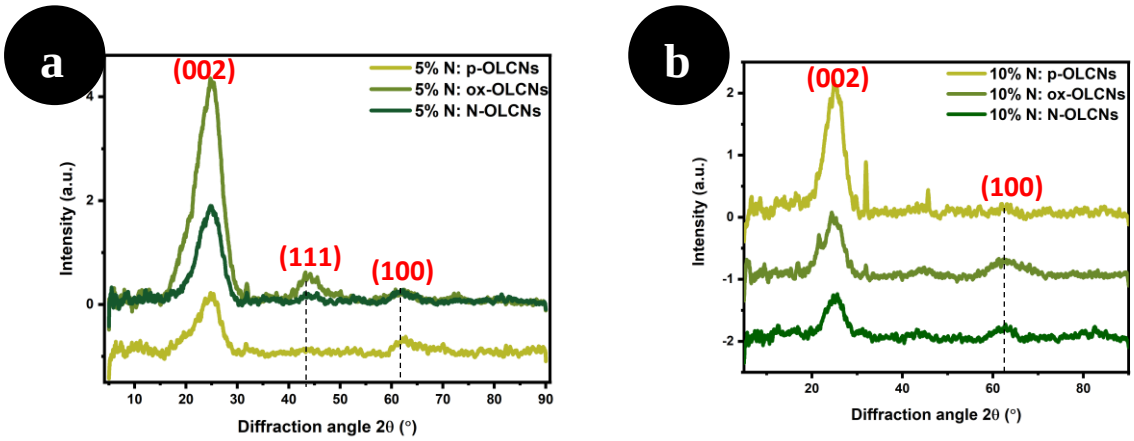

Figure 6.6: PXRD patterns of the NCdots: OLCNs synthesized at a) 5% NCdots wt. % loading and b) 10% NCdots wt. % loading unto support.

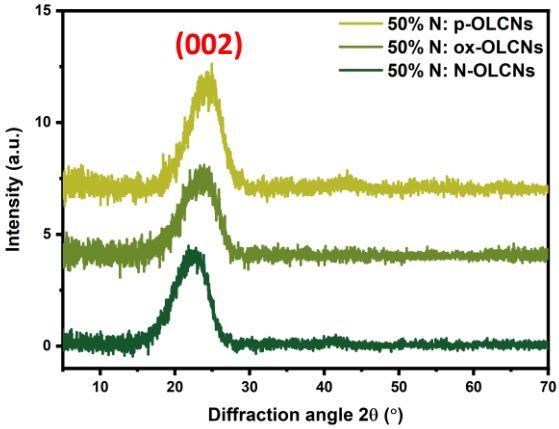

Figure 6.7: PXRD patterns of the NCdots: OLCNs synthesized at 50% NCdots wt. % loading unto support.

The other nanocomposites (not shown here, diffractograms can be found in the **SI, S21 – S22**) all exhibited similar diffractograms. Whereby, the dominant (002) peak that is observed in both the precursor material also reappears in all the X-ray diffraction patterns below, however with broader and weaker peaks than before physical mixing reaction. These peaks appear due to the graphitic carbon being still defective with incomplete shells formed [47]. These results are consistent even for the composites prepared with higher NCdots ratio: OLCNs support (**Fig. 6.8**).

In summary, the various NCdots: OLCNs nanocomposites primarily exhibited diffraction patterns of NCdots contain broadened peaks lying at the angles typical of the 002, 001, and 111 reflections of graphite.

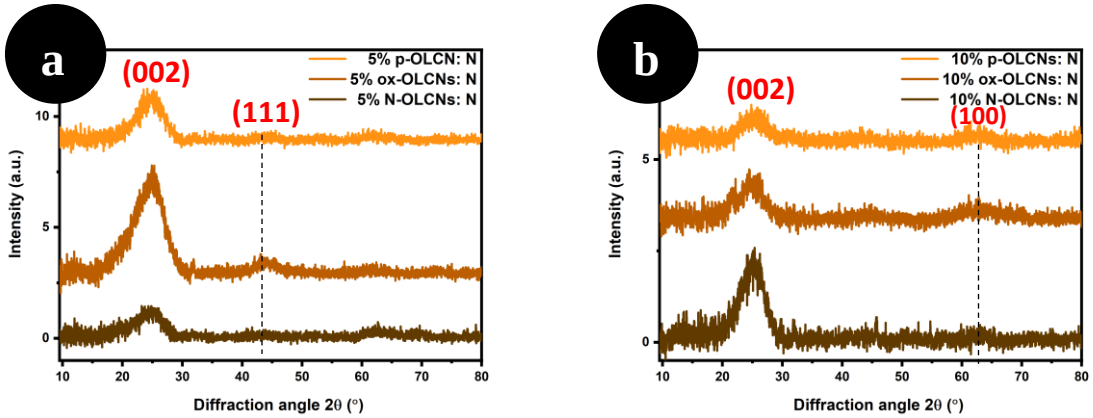

Figure 6.8: PXRD patterns of the OLCNs: NCdots synthesized at a) 5% OLCNs wt. % loading and b) 10% OLCNs wt. % loading unto NCdots.

6.3.4. Optical properties (absorbance measurement and fluorescence studies analysis)

Figure 6.9 below shows the optical properties of the as-synthesized NCdots were studied using both ultraviolet-visible (Uv-vis) absorption and photoluminescence (PL) spectrophotometry. As discussed in **Ch. 4, Sec. 4.3.4**, the NCdots exhibited a single absorption peak at 275 nm and an emission maxima at wavelength 438 nm when excited with energy of λ_{em} 350 nm (**Fig. 6.9 a**). What these results revealed was that the synthesized NCdots have single-emissive center which is believed to be core state rather than surface state, and broad absorption for the PL emission mechanism. **Figure 6.9 b** shows the traditional excitation-dependant emission behaviour of Cdots, with maximum emission reached at excitation wavelength 410 nm.

.

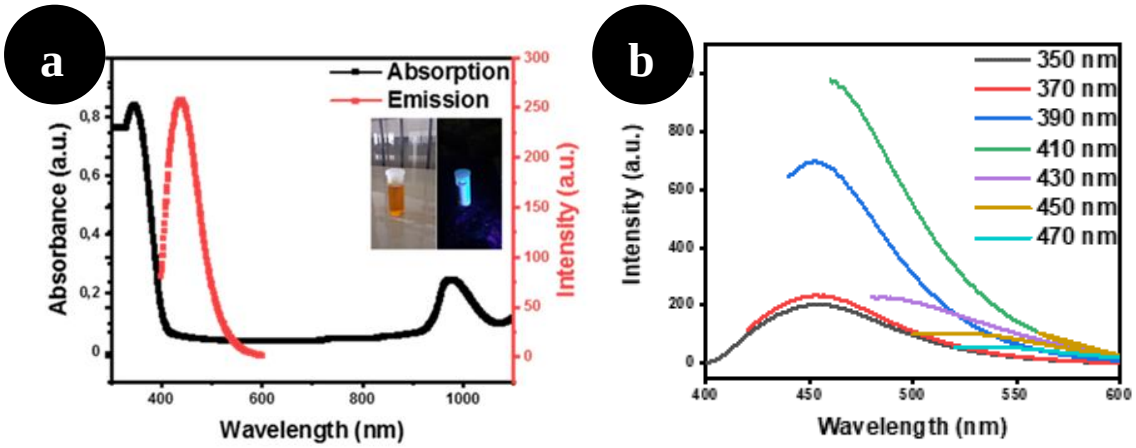

Figure 6.9: a) UV-vis absorption spectrum and PL emission spectrum of NCdots (EDA) recorded at wavelength 350 nm and b) PL spectra of NCdots (EDA) recorded at various excitation wavelengths. The inserts show the photographs of NCdots in water under visible light (brown solutions) and under UV lamp (blue solutions) at 365 nm excitation wavelength under irradiation.

Figures 6.10-12 shows the UV-vis and PL spectra of as prepared p-/ox- and N-OLCNs. The UV-vis spectra (**Figs. 6.10 a - 6.12a**) below presented with red shift characteristic peaks for all OLCNs, as all the OLCNs absorb in the ultraviolet region. The large absorption peaks at ~300 nm are below the visible spectrum (<400 nm) and suggest that the OLCNs absorb UV light. This may be because distinct surface functional groups have introduced varied structural orderliness to the OLCNs. The p- and ox-OLCNs exhibited multiple emission centres. However, the intense emission maxima bands were measured at 465 nm (p-OLCNs), 425 nm (ox-OLCNs) and 390 nm (N-OLCNs), respectively (**Figs. 6.10 b - 6.12b**).

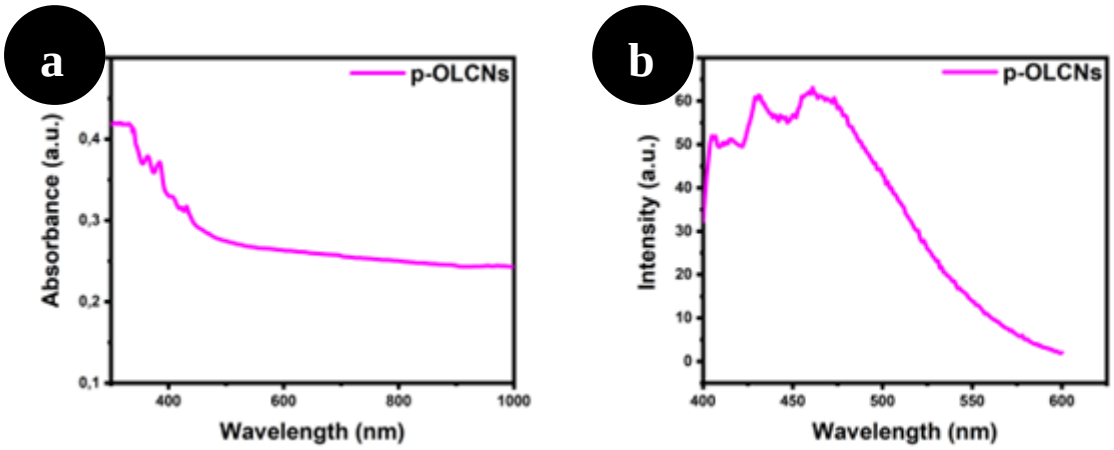

Figure 6.10: a) UV-vis absorption spectrum and b) PL emission spectrum of p-OLCNs recorded at wavelength 350 nm.

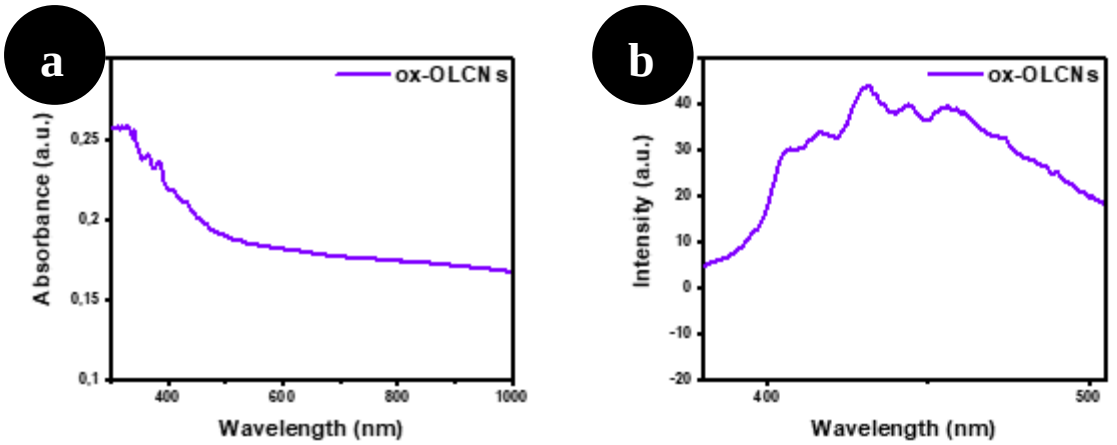

Figure 6.11: a) UV-vis absorption spectrum and b) PL emission spectrum of ox-OLCNs recorded at wavelength 350 nm.

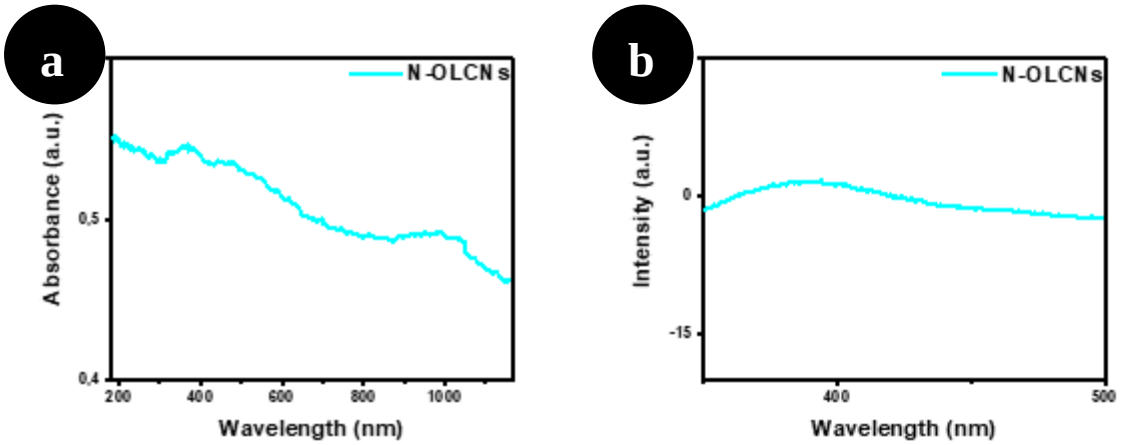

Figure 6.12: a) UV-vis absorption spectrum and b) PL emission spectrum of N-OLCNs recorded at wavelength 350 nm.

UV-vis analysis was used to examine the optical characteristics of the NCdots: OLCNs nanocomposites (**Figs. 6.13a - 6.16a**) and PL spectroscopy (**Figs. 6.13b - 6.16b**), respectively. The UV-vis and PL information of other nanocomposites can be found in the **SI**. It was observed that all the nanocomposites (**Figs. 6.13a – 6.16a**) ran in aqueous solution at ambient conditions had similar absorption peaks at approximately the same peak positions, see summary in **Table 6.5**. The approximate wavelengths of the colours in the visible light areas and their complementary colour to the absorbed colour calculated [53, 54], as well as the light absorption zones at specific transitions and measured wavelengths are also shown in **Table 6.5**.

The nanocomposites present with absorption peaks related to both NCdots and OLCNs. Bands observed at ~242, ~278, ~279 and ~288 nm are poorly defined and can be attributed to the presence of NCdots in the hybrid system (see arrows below; **Figs. 6.13b - 6.16b.** Enlarged inserts of this area can be found in the **SI**). And the more pronounced peaks observed at ~362 - ~636 nm can be from the OLCNs when light passed through the nanocomposite structure. This is deduced from the optical properties provided by the absorbance measurement and fluorescence studies analysis above (**Figs. 6.9-6.12**). The resulting absorbance spectra are a result of delocalized absorptions in the hybrid nanostructure and as such the maximum absorption is moved to a longer wavelength, as the amount of delocalization increases. Tauc plots used to determine the bandgap energy of the nanocomposites can be found in the **SI, Figures. S28 and S29**.

Table 6.4: Absorption measurements wavelength at maximal light absorbance observed in all nanocomposites.

UV-vis absorption wavelength (nm)	Absorbed colour	Reflected colour (Complementary)
~242	-	-
~278	-	-
~279	-	-
~288	-	-
~ 362	Violet	Yellow-green
~ 419	Violet	Yellow-green
~ 446	Violet	Yellow-green
~ 455	Blue	Yellow
~ 463	Blue	Yellow
~ 536	Green	Violet
~ 636	Red	Blue-green

This experiment discovered that the absorption peak intensities between the various nanocomposites had not changed or increased, most likely because each composite included an equal number of n-π* transitions of π systems comprising C-N/C≡ N bonds [55, 56]. The intensity of absorption peaks at ~362-447 nm and ~460-640 nm excitation wavelengths are

similar in the case of all the NCdots: OLCNs composites. This behaviour could be explained by the domain size distribution and carbonization degree analysed from the difference of NCdots: OLCNs nanocomposite (and individual carbon dots) surface composition [57, 58]. The intragap states, which are extra electronic states between the HOMO and LUMO levels, were produced by the N atoms. Since intragap states close the energy gap, NCdots with more N atoms are often able to absorb more photons with lower energy [18].

By creating intragap states, N-doping can boost light absorption and occasionally extend the spectrum sensitivity of NCdots to red and even near-infrared wavelengths. For instance, using a microwave-assisted hydrothermal technique, NCdots with an absorbance peak centered at 650 nm were easily created from citric acid and urea [59]. The NCdots that Qu et al. previously created by solvothermal processing citric acid and diethylenetriamine showed blue, green, or yellow emissions when the reaction solvent was changed from water to DMF or when no solvent was used [60]. The conjugated pyrrole/pyrrolidone groups were used to identify the edge state of NCdots, and as the quantity of pyrrolic N increased, the PL and excitation wavelengths shifted toward the red. This is what is observed in the spectra above.

The wavelengths of molecules containing one chromophore group can fluctuate. The magnitude of the wavelength is affected by the colours in visible light when measuring wavelength [53]. It's critical to remember that the maximal UV absorption of a conjugated molecule is proportional to the degree of conjugation [54].

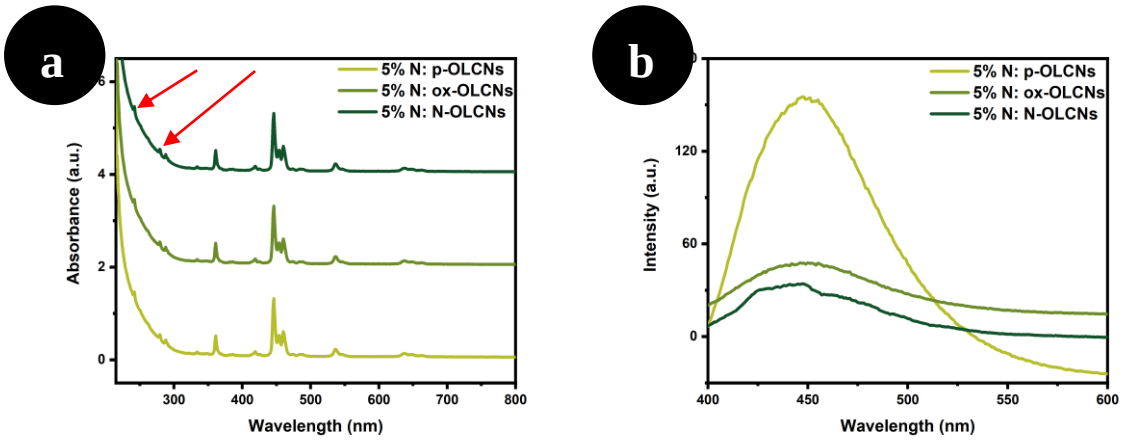

Figure 6.13: a) UV-vis absorption spectrum and b) PL emission spectrum (λ_{em} 350 nm) of NCdots: OLCNs synthesized at 5% NCdots wt. % loading unto support.

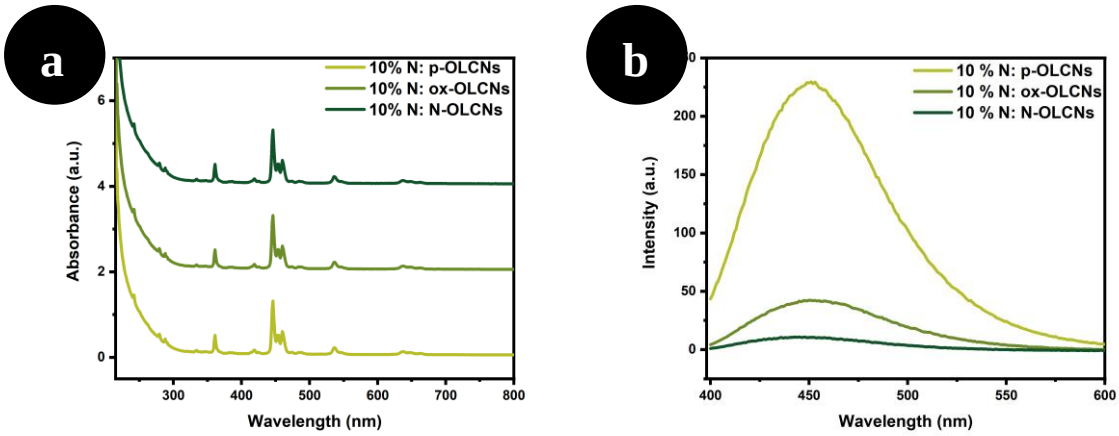

Figure 6.14: a) UV-vis absorption spectrum and b) PL emission spectrum (λ_{em} 350 nm) of NCdots: OLCNs synthesized at 10% NCdots wt. % loading unto support.

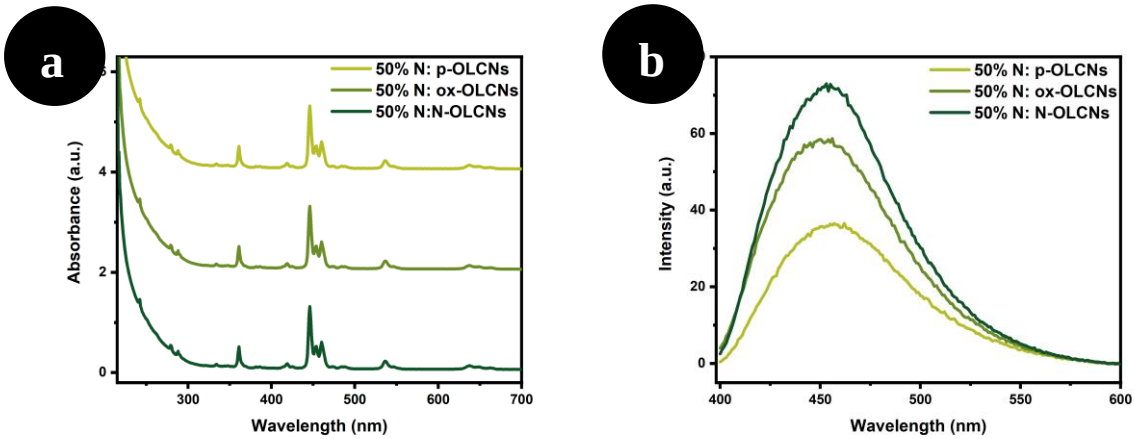

Figure 6.15: a) UV-vis absorption spectrum and b) PL emission spectrum (λ_{em} 350 nm) of NCdots: OLCNs synthesized at 50% NCdots wt. % loading unto support.

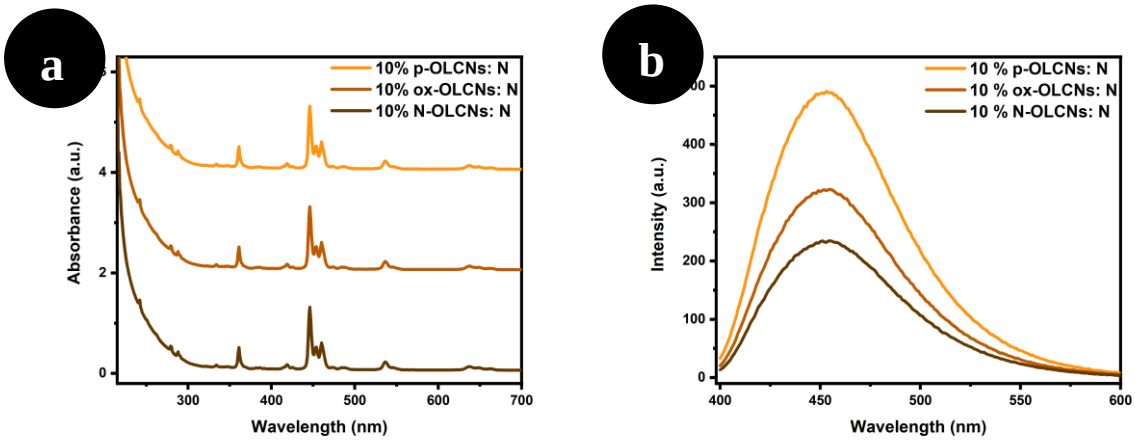

Figure 6.16: a) UV-vis absorption spectrum and b) PL emission spectrum (λ_{em} 350 nm) of OLCNs: NCdots synthesized at 10% OLCNs wt. % loading unto support (NCdots).

As mentioned here in **Figs. 6.13b - 6.16b**, 350 nm excitation wavelength was used to measure PL spectra. The peak maximum at 350 nm excitation wavelength was typically redshifted in the PL spectra for all composites. The maximum emission peaks of the nanocomposites upon incorporation of the NCdots on the surface of the various OLCNs summarised in **Table 6.6** below, information of other nanocomposites can be found in the **SI, S23-27 and Table: S1**. The PL emissions observed in **Figs. 6.13b - 6.16b** emitted in the same range, with variable peak positions. This suggests that the nanocomposite exhibits emissive behaviour from the combination of NCdots and OLCNs fluorophores, thus the hybridization gives off a single emission centre. However, it cannot be adequately quantified at this point from which environment on the nanocomposite the PL emission results from. Thus, the PL data observed might be brought on by a number of circumstances, including the NCdots, or the support (OLCNs), surface-support interactions, nanocomposite made of functional NCdots and support groups, or photoinduced electron transfer (PET) from the NCdots to the support [60].

The optical selection at different defects states, non-radiative recombination of excitons at defects sites, and functional groups found in Cdots are all credited with contributing to the PL emissions data [61]. The variation in size (of the OLCNs) may result in a shift in the maximum emission wavelength. It is probable that the as-prepared nanocomposites exhibit a stronger fluorescence than NCdots because the NCdots modified the arrangement of carbon and nitrogen in the OLCNs (which serve as the composite's support substrate), resulting in surface defect states.

In this research area, it is evident that both precursor concentration and type can impact the production and optical characteristics of the composite material. The electrons of Cdots are not delocalized throughout the particle due to core defects, surface functional groups, and restricted states originating from molecular fluorophores (less-crystalline core structures) [18]. A lone pair of electrons in nitrogen, in particular, is essential for the formation of various nitrogen-induced intragap states (N-states) and for changing photoelectron-related properties such as photo absorbance, photothermal conversion, and photoelectron transfer.

Table 6.5: PL emissions at excitation wavelength of 350 nm of the nanocomposites.

Name of sample	PL emissions (nm)
5% NCdots:p-OLCNs	~448
5% NCdots:ox-OLCNs	~448
5% NCdots:N-OLCNs	~447
10% NCdots:p-OLCNs	~450
10% NCdots:ox-OLCNs	~452
10% NCdots:N-OLCNs	~445
50% NCdots:p-OLCNs	~456
50% NCdots:ox-OLCNs	~451
50% NCdots:N-OLCNs	~454
10% p-OLCNs: NCdots	~452
10% ox-OLCNs: NCdots	~452
10% N-OLCNs: NCdots	~452

6.3.5. Fourier transmission infrared spectroscopy (FTIR) analysis

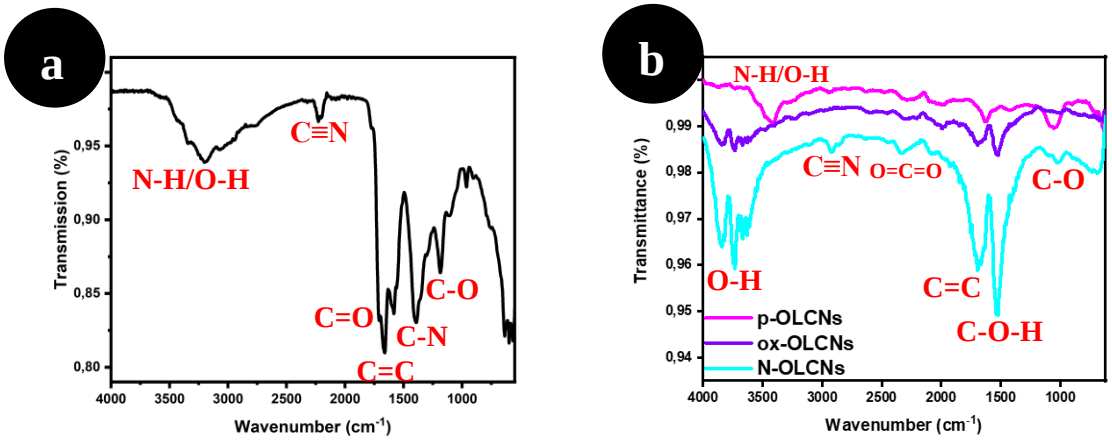

Figure 6.17: FTIR spectra of a) NCdots (EDA) and b) all as-prepared OLCNs.

The surface functional groups of the as-prepared nanocomposites were characterized by FTIR. Spectra are vertically offset for clarity. It was observed that all nanocomposites

produced the same transmittance results for each spectrum (**Figs. 6.18 – 6.20**). The similarity in the infrared spectra could be attributed to the nanocomposites virtually having the same fluorophores (as seen from the UV-vis and PL data). which translates to similar functional groups. The spectra presented with similar peak structure, however the relative peaks were slightly varied in terms of peak position. This is explained by the fact that covalent bonds in molecules selectively absorb light at particular wavelengths, changing the vibrational energy of the bond [62]. As a result, the atoms in the bond determine the type of vibration (stretching or bending) caused by the infrared light.

The spectra below (**Figs. 6.18 – 6.20**) present with eight prominent peaks. The vibration mode at ~1026 cm^{-1} can be attributed to the C-O functional group [63]. This peak presented at 1467 cm^{-1} pertaining to NCdots (EDA) and at 1043 cm^{-1} attributed to OLCNs (see **Fig. 6.17a and b**, respectively). The C=C is observed for the composites at ~1643 cm^{-1} and was seen to be at peak positions 1548 cm^{-1} and 1688 cm^{-1} for the NCdots and various OLCNs, respectively. Another common vibration mode is the C=O which was observed at ~1840 cm^{-1}, 1687 cm^{-1}, and 1795 cm^{-1} for the nanocomposites, NCdots (EDA) and OLCNs, respectively. The O-H/N-H peak, not clearly resolved and visible in the nanocomposites was observed at ~3094 cm^{-1}. This peak has shifted greatly [64]. The peaks observed at ~1500 cm^{-1}, ~2113 cm^{-1}, and ~2997 cm^{-1} can be attributed to the N-O, C≡N, and C-H stretching media, respectively.

An interesting vibration mode at ~2094 cm^{-1} was ascribed to C=C=N ketenimine stretch [65]. It is possible that this functional group could be due to the disruption of the NCdots incorporation which might have caused re-distribution of atoms around the surface of NCdots and the various OLCNs during physical mixing to allow for interaction and bonding to occur. The C≡N peak was observed at 2240 cm^{-1} and 2494 cm^{-1} for the NCdots (EDA) and OLCNs, respectively. Therefore, it is suggested that the formation of the ketenimine may have been caused by some interaction between these two functional groups on the surfaces of the various precursors.

Hence, this suggests that the vibration modes observed in these nanocomposites originate from the composite precursor material, either from the original functional group or partly due to newly formed groups from the NCdots and OLCNs support interactions. **Fig. 6.18 b** was indexed to show the similarity between the different composites. **Fig. 6.19** has asterisks in the

place of the different indexed vibration modes analyzed, again to show the similarity between the different spectra obtained. FTIR spectra of other composites may be found in the **SI, Figs. S30, S31**.

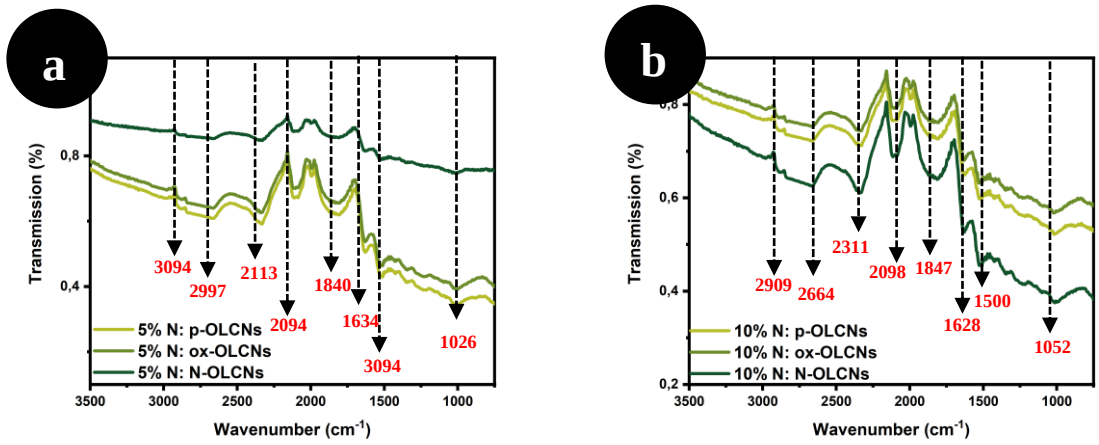

Figure 6.18: FTIR spectra of the NCdots: OLCNs synthesized at a) 5% NCdots wt. % loading and b) 10% NCdots wt. % loading unto support.

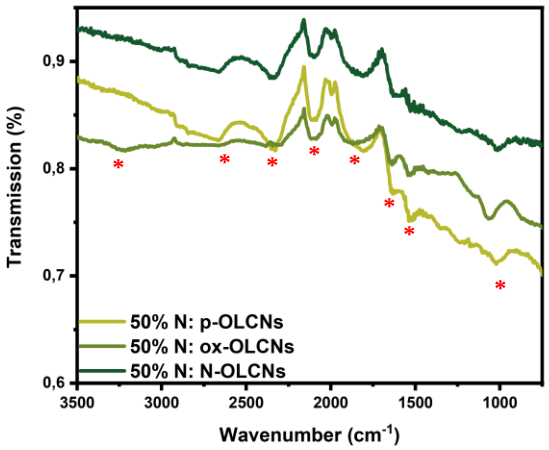

Figure 6.19: FTIR spectra of the NCdots: OLCNs synthesized at 50% NCdots wt. % loading.

The figure below presents the FTIR spectra of the composites prepared with a higher concentration of OLCNs: NCdots. In **Fig. 6.20 a**, the spectra of the 5% p-OLCNs: NCdots (EDA) and 5% N-OLCNs: NCdots (EDA) both did not have clearly defined peaks for characterization. This may be because it's challenging to get the right data and because spectral resolution affects detection sensitivity. Because IR absorption bands have relatively low absorption coefficients compared to Uv-vis spectra, this technique's sensitivity is often low, and the resultant detection limits are rather large [66].

Thus, the spectrum analysed was of 5% ox-OLCNs: NCdots (EDA) (in **Fig. 6.20 a**). As seen, the C-O, C=O and C=C functional groups were ascribed to the vibration modes at peak positions ca. 1052 cm^{-1}, 1912 cm^{-1} and 2114 cm^{-1}, respectively based on the information above. The peaks indexed with asterisks, in this case, were attributed to characteristic molecular environments that could probably be related to multiple compounds overlapping in the chemical structure. The FTIR peaks in **Fig.6.20 b** could be characterized as those in the figures above, due to the similarity in peak positions and spectral shape. Thus, the peaks ca. 1026 cm^{-1}, 1546 cm^{-1}, 1658 cm-1, 1844 cm^{-1}, 2104 cm^{-1}, 2343 cm^{-1}, and 2671 cm^{-1} could be ascribed and attributed to C-O, N-O, C=C, C=O, C≡C, C=C=N and C-H functional groups, respectively.

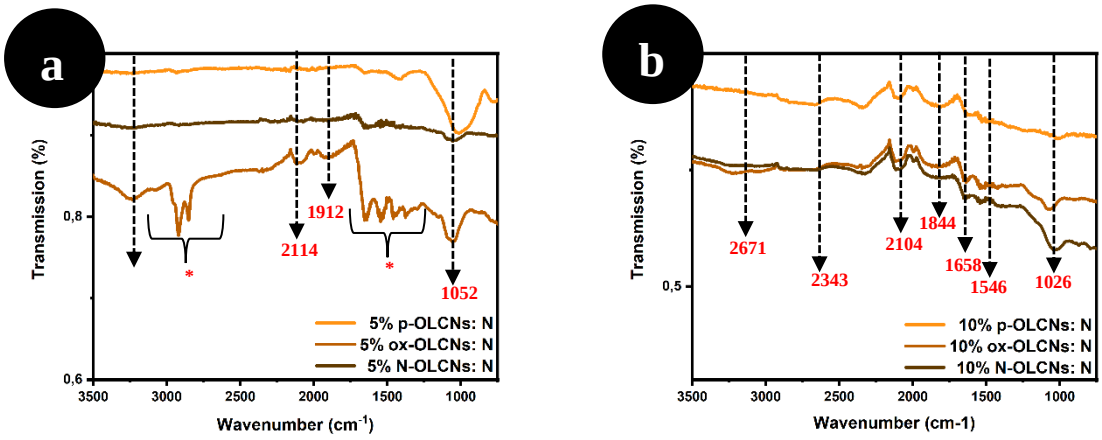

Figure 6.20: FTIR spectra of the OLCNs: NCdots synthesized at a) 5% OLCNs wt. % loading and b) 10% OLCNs wt. % loading unto NCdots.

6.4 Conclusion

This chapter investigated the composite material of two distinct carbon allotropes in this chapter: NCdots and various OLCNs (pristine and functionalized). The interaction of these two materials and the characteristics that resulted in a hybrid nanocomposite. The NCdots: OLCNs composites exhibited properties that were a result of the product of the two starting materials, as seen from the UV-vis, PL, PXRD and FTIR analyses. The X-ray diffraction pattern of the nanocomposites was found to have two distinctive characteristics: i) broadening of the peaks corresponding to the reflections of crystalline graphite, and ii) shift of the first peak (002 plane) to smaller angles in comparison to the 002 reflection of graphite. IR frequencies of the nanocomposites were interpreted in terms of particular structural properties of the chemical group or molecules of interest by investigating these compounds and using

theoretical chemistry for normal modes calculations. This study was challenging since these composites had never been made or studied in terms of their physiochemical and optical characteristics.

References

1. Qiu, X., & Burda, C. (2007). Chemically synthesized nitrogen-doped metal oxide nanoparticles. *Chemical Physics*, *339*(1–3), 1–10. https://doi.org/10.1016/j.chemphys.2007.06.039
2. O'Regan, B., & Grätzel, M. (1991). A low-cost, high-efficiency solar cell based on dye-sensitized colloidal TiO2 films. *Nature*, *353*(6346), 737–740. https://doi.org/10.1038/353737a0
3. Niu, Y., Qian, X., Xu, C., Liu, H., Wu, W., & Hou, L. (2019). Cu-Ni-CoSex quaternary porous nanocubes as enhanced Pt-free electrocatalysts for highly efficient dye-sensitized solar cells and hydrogen evolution in alkaline medium. *Chemical Engineering Journal*, *357*, 11–20. https://doi.org/10.1016/j.cej.2018.09.116
4. Lee, C. P., Lin, C. A., Wei, T. C., Tsai, M. L., Meng, Y., Li, C. T., Ho, K. C., Wu, C. I., Lau, S. P., & He, J. H. (2015). Economical low-light photovoltaics by using the Pt-free dye-sensitized solar cell with graphene dot/PEDOT:PSS counter electrodes. *Nano Energy*, *18*, 109–117. https://doi.org/10.1016/j.nanoen.2015.10.008
5. Hudie, S. M., Lee, C. P., Mathew, R. J., Chien, T. E., Huang, Y. J., Chen, H. T., Ho, K. C., Tseng, C. A., & Chen, Y. T. (2019). Phase-Engineered Weyl Semi-Metallic MoxW1-xTe2 Nanosheets as a Highly Efficient Electrocatalyst for Dye-Sensitized Solar Cells. *Solar RRL*, *3*(3), 1800314. https://doi.org/10.1002/solr.201800314
6. Rahman, G. C. R. (2015). Graphene-incorporated Photoelectrodes for Dye-sensitized Solar Cells. *Bull. Korean Chem. Soc.*, *36*, 762–771.
7. Pang, B., Zhang, M., Zhou, C., Dong, H., Ma, S., Shi, Y., Sun, Q., Li, F., Yu, L., & Dong, L. (2020). Nitrogen-Doped Carbon Nano-Onions Decorated on Graphene Network: A Novel All-Carbon Composite Counter Electrode for Dye-Sensitized Solar Cell with a 10.28% Power Conversion Efficiency. *Solar RRL*, *4*(9), 2000263. https://doi.org/10.1002/solr.202000263
8. Wu, M., & Ma, T. (2012). Platinum-Free Catalysts as Counter Electrodes in Dye-Sensitized Solar Cells. *ChemSusChem*, *5*(8), 1343–1357. https://doi.org/10.1002/cssc.201100676
9. Wang, W., Liu, Y., Zhong, Y. J., Wang, L., Zhou, W., Wang, S., Tadé, M. O., & Shao, Z. (2017). Rational Design of LaNiO3 /Carbon Composites as Outstanding Platinum-Free Photocathodes in Dye-Sensitized Solar Cells With Enhanced Catalysis for the Triiodide Reduction Reaction. *Solar RRL*, *1*(7), 1700074. https://doi.org/10.1002/solr.201700074

10. Bayatsarmadi, B., Zheng, Y., Jaroniec, M., & Qiao, S. Z. (2015). Soft-Templating Synthesis of N-Doped Mesoporous Carbon Nanospheres for Enhanced Oxygen Reduction Reaction. *Chemistry - An Asian Journal*, *10*(7), 1546–1553. https://doi.org/10.1002/asia.201500287
11. Sheng, Z. H., Gao, H. L., Bao, W. J., Wang, F. B., & Xia, X. H. (2012). Synthesis of boron doped graphene for oxygen reduction reaction in fuel cells. *J. Mater. Chem.*, *22*(2), 390–395. https://doi.org/10.1039/c1jm14694g
12. Ma, Z., Dou, S., Shen, A., Tao, L., Dai, L., & Wang, S. (2014). Sulfur-Doped Graphene Derived from Cycled Lithium-Sulfur Batteries as a Metal-Free Electrocatalyst for the Oxygen Reduction Reaction. *Angewandte Chemie International Edition*, *54*(6), 1888–1892. https://doi.org/10.1002/anie.201410258
13. Yang, W., Ma, X., Xu, X., Li, Y., Raj, S. I., Ning, G., Wang, A., & Chen, S. (2015). Sulfur-doped porous carbon as metal-free counter electrode for high-efficiency dye-sensitized solar cells. *Journal of Power Sources*, 282, 228–234. https://doi.org/10.1016/j.jpowsour.2015.02.060
14. Meng, X., Yu, C., Song, X., Liu, Y., Liang, S., Liu, Z., Hao, C., & Qiu, J. (2015). Nitrogen-Doped Graphene Nanoribbons with Surface Enriched Active Sites and Enhanced Performance for Dye-Sensitized Solar Cells. *Advanced Energy Materials*, *5*(11), 1500180. https://doi.org/10.1002/aenm.201500180
15. Fang, H., Yu, C., Ma, T., & Qiu, J. (2014). Boron-doped graphene as a high-efficiency counter electrode for dye-sensitized solar cells. *Chemical Communications*, *50*(25), 3328. https://doi.org/10.1039/c3cc48258h
16. Batmunkh, M., Shrestha, A., Gao, G., Yu, L., Zhao, J., Biggs, M. J., Shearer, C. J., & Shapter, J. G. (2017). Sulfur-Doped Graphene with Iron Pyrite (FeS2) as an Efficient and Stable Electrocatalyst for the Iodine Reduction Reaction in Dye-Sensitized Solar Cells. *Solar RRL*, *1*(3–4), 1700011. https://doi.org/10.1002/solr.201700011
17. Becquerel, E. (1839). Electrod Effect under the Influence of Solar Radiation. *C.R. Acad. Sci., Paris*, *9*, 531.
18. Park, Y., Yoo, J., Lim, B., Kwon, W., & Rhee, S. W. (2016). Improving the functionality of carbon nanodots: doping and surface functionalization. *Journal of Materials Chemistry A*, *4*(30), 11582–11603. https://doi.org/10.1039/c6ta04813g
19. Yan, X., Li, B., Cui, X., Wei, Q., Tajima, K., & Li, L. S. (2011). Independent Tuning of the Band Gap and Redox Potential of Graphene Quantum Dots. *The Journal of Physical Chemistry Letters*, *2*(10), 1119–1124. https://doi.org/10.1021/jz200450r

20. Chen, B. B., Liu, M. L., Li, C. M., & Huang, C. Z. (2019). Fluorescent carbon dots functionalization. *Advances in Colloid and Interface Science*, *270*, 165–190. https://doi.org/10.1016/j.cis.2019.06.008
21. Liu, S., Yang, B., Zhou, J., & Song, H. (2019). Nitrogen-rich carbon-onion-constructed nanosheets: an ultrafast and ultrastable dual anode material for sodium and potassium storage. *Journal of Materials Chemistry A*, *7*(31), 18499–18509. https://doi.org/10.1039/c9ta04699b
22. Gu, D., Bongard, H., Deng, Y., Feng, D., Wu, Z., Fang, Y., Mao, J., Tu, B., Schüth, F., & Zhao, D. (2010). An Aqueous Emulsion Route to Synthesize Mesoporous Carbon Vesicles and Their Nanocomposites. *Advanced Materials*, *22*(7), 833–837. https://doi.org/10.1002/adma.200902550
23. Zhang, M., Yao, Q., Guan, W., Lu, C., & Lin, J. M. (2014). Layered Double Hydroxide-Supported Carbon Dots as an Efficient Heterogeneous Fenton-Like Catalyst for Generation of Hydroxyl Radicals. *The Journal of Physical Chemistry C*, *118*(19), 10441–10447. https://doi.org/10.1021/jp5012268
24. Chowdhuri, A. R., Singh, T., Ghosh, S. K., & Sahu, S. K. (2016). Carbon Dots Embedded Magnetic Nanoparticles @Chitosan @Metal Organic Framework as a Nanoprobe for pH Sensitive Targeted Anticancer Drug Delivery. *ACS Applied Materials & Interfaces*, *8*(26), 16573–16583. https://doi.org/10.1021/acsami.6b03988
25. Lai, C. W., Hsiao, Y. H., Peng, Y. K., & Chou, P. T. (2012). Facile synthesis of highly emissive carbon dots from pyrolysis of glycerol; gram scale production of carbon dots/mSiO2 for cell imaging and drug release. *Journal of Materials Chemistry*, *22*(29), 14403. https://doi.org/10.1039/c2jm32206d
26. Pal, A., Sk, M. P., & Chattopadhyay, A. (2016). Conducting Carbon Dot–Polypyrrole Nanocomposite for Sensitive Detection of Picric acid. *ACS Applied Materials & Interfaces*, *8*(9), 5758–5762. https://doi.org/10.1021/acsami.5b11572
27. He, Y., He, J., Wang, L., Yu, Z., Zhang, H., Liu, Y., & Lei, B. (2017). Synthesis of double carbon dots co-doped mesoporous Al2O3 for ratiometric fluorescent determination of oxygen. *Sensors and Actuators B: Chemical*, *251*, 918–926. https://doi.org/10.1016/j.snb.2017.05.104
28. He, Y., He, J., Yu, Z., Zhang, H., Liu, Y., Hu, G., Zheng, M., Dong, H., Zhuang, J., & Lei, B. (2018). Double carbon dot assembled mesoporous aluminas: solid-state dual-emission photoluminescence and multifunctional applications. *Journal of Materials Chemistry C*, *6*(10), 2495–2501. https://doi.org/10.1039/c8tc00182k

29. Li, G., Liu, Y., Niu, J., Pei, M., & Lin, W. (2018). A ratiometric fluorescent composite nanomaterial for RNA detection based on graphene quantum dots and molecular probes. *Journal of Materials Chemistry B*, *6*(26), 4380–4384. https://doi.org/10.1039/c8tb01125g
30. Ding, H., Zhang, F., Zhao, C., Lv, Y., Ma, G., Wei, W., & Tian, Z. (2017). Beyond a Carrier: Graphene Quantum Dots as a Probe for Programmatically Monitoring Anti-Cancer Drug Delivery, Release, and Response. *ACS Applied Materials & Interfaces*, *9*(33), 27396–27401. https://doi.org/10.1021/acsami.7b08824
31. Chen, B. B., Liu, M. L., & Huang, C. Z. (2020). Carbon dot-based composites for catalytic applications. *Green Chemistry*, *22*(13), 4034–4054. https://doi.org/10.1039/d0gc01014f
32. Gu, J., Li, X., Zhou, Z., Liu, W., Li, K., Gao, J., Zhao, Y., & Wang, Q. (2019). 2D MnO2 nanosheets generated signal transduction with 0D carbon quantum dots: synthesis strategy, dual-mode behavior and glucose detection. *Nanoscale*, *11*(27), 13058–13068. https://doi.org/10.1039/c9nr03583d
33. Zhou, D., Li, D., Jing, P., Zhai, Y., Shen, D., Qu, S., & Rogach, A. L. (2017). Conquering Aggregation-Induced Solid-State Luminescence Quenching of Carbon Dots through a Carbon Dots-Triggered Silica Gelation Process. *Chemistry of Materials*, *29*(4), 1779–1787. https://doi.org/10.1021/acs.chemmater.6b05375
34. Mutuma, B. K., Matsoso, B. J., Ranganathan, K., Keartland, J., Wamwangi, D., & Coville, N. J. (2017). Generation of radical species in CVD grown pristine and N-doped solid carbon spheres using H2 and Ar as carrier gases. *RSC Advances*, *7*(34), 21187–21195. https://doi.org/10.1039/c7ra03142d
35. Zhou, D., Li, D., Jing, P., Zhai, Y., Shen, D., Qu, S., & Rogach, A. L. (2017). Conquering Aggregation-Induced Solid-State Luminescence Quenching of Carbon Dots through a Carbon Dots-Triggered Silica Gelation Process. *Chemistry of Materials*, *29*(4), 1779–1787. https://doi.org/10.1021/acs.chemmater.6b05375
36. Wang, Q., Huang, J., Sun, H., Zhang, K. Q., & Lai, Y. (2017). Uniform carbon dots@TiO2 nanotube arrays with full spectrum wavelength light activation for efficient dye degradation and overall water splitting. *Nanoscale*, *9*(41), 16046–16058. https://doi.org/10.1039/c7nr06809c
37. Krysmann, M. J., Kelarakis, A., Dallas, P., & Giannelis, E. P. (2011). Formation Mechanism of Carbogenic Nanoparticles with Dual Photoluminescence Emission. *Journal of the American Chemical Society*, *134*(2), 747–750. https://doi.org/10.1021/ja204661r

38. Song, Z., Quan, F., Xu, Y., Liu, M., Cui, L., & Liu, J. (2016). Multifunctional N,S co-doped carbon quantum dots with pH- and thermo-dependent switchable fluorescent properties and highly selective detection of glutathione. *Carbon*, *104*, 169–178. https://doi.org/10.1016/j.carbon.2016.04.003
39. S. L. Hu , Y. F. Zhou , C. R. Xue , J. L. Yang and Q. Chang , *Chem. Commun.*, 2017, **53** , 9426 —9429Iijima, S. (1980). Direct observation of the tetrahedral bonding in graphitized carbon black by high resolution electron microscopy. *Journal of Crystal Growth*, *50*(3), 675–683. https://doi.org/10.1016/0022-0248(80)90013-5
40. Eurov, D. A., Stovpiaga, E. Y., Kurdyukov, D. A., Dukin, A. A., Smirnov, A. N., & Golubev, V. G. (2020). Luminescent Properties of Carbon Nanodots Bound to the Surface of Spherical Microresonator. *Physics of the Solid State*, *62*(10), 1898–1904. https://doi.org/10.1134/s1063783420100054
41. Zeng, Z., Xiao, F. X., Phan, H., Chen, S., Yu, Z., Wang, R., Nguyen, T. Q., & Yang Tan, T. T. (2018). Unraveling the cooperative synergy of zero-dimensional graphene quantum dots and metal nanocrystals enabled by layer-by-layer assembly. *Journal of Materials Chemistry A*, *6*(4), 1700–1713. https://doi.org/10.1039/c7ta09119b
42. Liu, X. J., Feng, J. K., Ren, A. M., & Zhou, X. (2003). Comparative studies of the spectra and the second-order nonlinear polarizabilities for donor–acceptor ensembles between Zn-porphyrin/fullerene [60] and Zn-porphyrin/naphthalenediimide. *Journal of Molecular Structure: THEOCHEM*, *635*(1–3), 191–202. https://doi.org/10.1016/s0166-1280(03)00420-2
43. Yap, P. L., Kabiri, S., Auyoong, Y. L., Tran, D. N. H., & Losic, D. (2019). Tuning the Multifunctional Surface Chemistry of Reduced Graphene Oxide via Combined Elemental Doping and Chemical Modifications. *ACS Omega*, *4*(22), 19787–19798. https://doi.org/10.1021/acsomega.9b02642
44. Farivar, F., Yap, P. L., Hassan, K., Tung, T. T., Tran, D. N., Pollard, A. J., & Losic, D. (2021). Unlocking thermogravimetric analysis (TGA) in the fight against "Fake graphene" materials. *Carbon*, *179*, 505–513. https://doi.org/10.1016/j.carbon.2021.04.064
45. Li, Z., Lu, C., Xia, Z., Zhou, Y., & Luo, Z. (2007). X-ray diffraction patterns of graphite and turbostratic carbon. *Carbon*, *45*(8), 1686–1695. https://doi.org/10.1016/j.carbon.2007.03.038
46. McDonough, J. K., & Gogotsi, Y. (2013). Carbon Onions: Synthesis and Electrochemical Applications. *Interface Magazine*, *22*(3), 61–66. https://doi.org/10.1149/2.f05133if

47. Han, F. D., Yao, B., & Bai, Y. J. (2011). Preparation of Carbon Nano-Onions and Their Application as Anode Materials for Rechargeable Lithium-Ion Batteries. *The Journal of Physical Chemistry C*, *115*(18), 8923–8927. https://doi.org/10.1021/jp2007599
48. Dhand, V., Prasad, J. S., Rao, M. V., Bharadwaj, S., Anjaneyulu, Y., & Jain, P. K. (2013). Flame synthesis of carbon nano onions using liquefied petroleum gas without catalyst. *Materials Science and Engineering: C*, *33*(2), 758–762. https://doi.org/10.1016/j.msec.2012.10.029
49. Mykhailiv, O., Zubyk, H., & Plonska-Brzezinska, M. E. (2017). Carbon nano-onions: Unique carbon nanostructures with fascinating properties and their potential applications. *Inorganica Chimica Acta*, *468*, 49–66. https://doi.org/10.1016/j.ica.2017.07.021
50. Hu, Z. P., Li, J., Wu, N. J., & Ignatiev, A. (1989). Surface structure of the C(0001)-(2×2)Cs system: Low-energy electron-diffraction dynamical calculation. *Physical Review B*, *39*(18), 13201–13205. https://doi.org/10.1103/physrevb.39.13201
51. Tomita, S., Burian, A., Dore, J. C., LeBolloch, D., Fujii, M., & Hayashi, S. (2002). Diamond nanoparticles to carbon onions transformation: X-ray diffraction studies. *Carbon*, *40*(9), 1469–1474. https://doi.org/10.1016/s0008-6223(01)00311-6
52. Tomita, S., Sakurai, T., Ohta, H., Fujii, M., & Hayashi, S. (2001). Structure and electronic properties of carbon onions. *The Journal of Chemical Physics*, *114*(17), 7477–7482. https://doi.org/10.1063/1.1360197
53. Pratiwi, R. A., & Nandiyanto, A. B. D. (2022). How to Read and Interpret UV-VIS Spectrophotometric Results in Determining the Structure of Chemical Compounds. *Indonesian Journal of Educational Research and Technology*, *2*(1), 1–20. https://doi.org/10.17509/ijert.v2i1.35171
54. Sandorfy, C. (1976). U.V. absorption of fluorocarbons. *Atmospheric Environment (1967)*, *10*(5), 343–351. https://doi.org/10.1016/0004-6981(76)90001-9
55. Holá, K., Sudolská, M., Kalytchuk, S., Nachtigallová, D., Rogach, A. L., Otyepka, M., & Zbořil, R. (2017). Graphitic Nitrogen Triggers Red Fluorescence in Carbon Dots. *ACS Nano*, *11*(12), 12402–12410. https://doi.org/10.1021/acsnano.7b06399
56. Sarkar, S., Sudolská, M., Dubecký, M., Reckmeier, C. J., Rogach, A. L., Zbořil, R., & Otyepka, M. (2016). Graphitic Nitrogen Doping in Carbon Dots Causes Red-Shifted Absorption. *The Journal of Physical Chemistry C*, *120*(2), 1303–1308. https://doi.org/10.1021/acs.jpcc.5b10186

57. Tuerhong, M., XU, Y., & YIN, X. B. (2017). Review on Carbon Dots and Their Applications. *Chinese Journal of Analytical Chemistry*, *45*(1), 139–150. https://doi.org/10.1016/s1872-2040(16)60990-8
58. Bagheri, Z., Ehtesabi, H., Rahmandoust, M., Ahadian, M. M., Hallaji, Z., Eskandari, F., & Jokar, E. (2017). New Insight into the Concept of Carbonization Degree in Synthesis of Carbon Dots to Achieve Facile Smartphone Based Sensing Platform. *Scientific Reports*, *7*(1). https://doi.org/10.1038/s41598-017-11572-8
59. Permatasari, F. A., Fukazawa, H., Ogi, T., Iskandar, F., & Okuyama, K. (2018). Design of Pyrrolic-N-Rich Carbon Dots with Absorption in the First Near-Infrared Window for Photothermal Therapy. *ACS Applied Nano Materials*, *1*(5), 2368–2375. https://doi.org/10.1021/acsanm.8b00497
60. Pawar, S., Togiti, U. K., Bhattacharya, A., & Nag, A. (2019). Functionalized Chitosan–Carbon Dots: A Fluorescent Probe for Detecting Trace Amount of Water in Organic Solvents. *ACS Omega*, *4*(6), 11301–11311. https://doi.org/10.1021/acsomega.9b01208
61. Mkhari, O., Ntuli, T. D., Coville, N. J., Nxumalo, E. N., & Maubane-Nkadimeng, M. S. (2021). A comparison of fluorescent N-doped carbon dots supported on the surface of hollow and solid carbon spheres, and solid silica spheres. *Diamond and Related Materials*, *118*, 108500. https://doi.org/10.1016/j.diamond.2021.108500
62. Berthomieu, C., & Hienerwadel, R. (2009). Fourier transform infrared (FTIR) spectroscopy. *Photosynthesis Research*, *101*(2–3), 157–170. https://doi.org/10.1007/s11120-009-9439-x
63. Tripathi, K. M., Tran, T. S., Kim, Y. J., & Kim, T. (2017). Green Fluorescent Onion-Like Carbon Nanoparticles from Flaxseed Oil for Visible Light Induced Photocatalytic Applications and Label-Free Detection of Al(III) Ions. *ACS Sustainable Chemistry & Engineering*, *5*(5), 3982–3992. https://doi.org/10.1021/acssuschemeng.6b03182
64. Lim, S. Y., Shen, W., & Gao, Z. (2015). Carbon quantum dots and their applications. *Chemical Society Reviews*, *44*(1), 362–381. https://doi.org/10.1039/c4cs00269e
65. Michael, J. P. (1995). Synthesis: Carbon with One Heteroatom Attached by a Multiple Bond. *Comprehensive Organic Functional Group Transformations*
66. Bacsik, Z., Mink, J., & Keresztury, G. (2004). FTIR Spectroscopy of the Atmosphere. I. Principles and Methods. *Applied Spectroscopy Reviews*, *39*(3), 295–363. https://doi.org/10.1081/asr-200030192.

Chapter 7

Application of the NCdots: OLCNs composites in dye-sensitized solar cells

7.1 Introduction

A great interest in researching alternative renewable energy technologies has arisen in response to an increase in energy demand brought on by industrialization and population development, which is expected to exhaust fossil fuel resources for our contemporary society [1]. One of the most studied alternatives, solar energy is abundant and predominantly employs green technology, making it one of the potential answers to the world's energy problems [2, 3].

Due to its inherent cheap module cost and simplicity of manufacture, dye-sensitized solar cells (DSSCs) have received a lot of interest as a potential alternative for the conventional silicon solar cell since their ground-breaking invention in 1991 [6]. They also have the advantage of being a lightweight and flexible technology. DSSCs are now developing quickly in an effort to create durable, effective, and affordable devices that are suited for usage in real-world applications [7–9]. As opposed to typical semiconductor-based solar cell technologies, DSSCs isolate charge carrier transmission from light absorption. The dye sensitizer takes in the incident sunlight and utilizes the light energy to start a vectorial electron transfer process. As a result, DSSCs are superior to silicon (Si) based photovoltaics in the following ways [10]: 1) resistance to flaws, a common issue with semiconductors like silicon, 2) affordability of production due to the ease of fabrication of the semiconductor-electrolyte interface (SEI), and 3) the capacity to directly convert light into chemical energy.

One of the most important components of the DSSC is the counter electrode [11]. The counter electrode must return electrons from the external circuit to the redox electrolyte in order to decrease the triiodide ion [12, 13]. Because of its extraordinary catalytic conductivity and high remarkable catalytic activity, Pt is frequently used as the catalyst in DSSCs for the triiodide (I_3^-/I^-) redox reaction [14]. Additionally, its high price and scarcity make it impossible to produce on a wide scale for photovoltaic applications [15]. Therefore, readily available and simple to process materials will be preferred for use in big solar energy conversion systems in the future. In order to reduce triiodide ion, it is crucial to develop low-

cost counter electrode materials that also exhibit great electrical conductivity, robust chemical stability, and outstanding catalytic activity.

As of now, the counter electrodes have been made of FTO or ITO (indium tin oxide) glass and have been coated with low-cost carbonaceous materials such as hard carbon spheres, carbon black, fullerene, activated carbon, graphite, carbon nanotubes and graphene, and onion-like carbon nanomaterials (OLCNs). [16–23]. Pt has recently been produced and is being explored as a potential replacement in DSSC devices by nanoscale carbon materials [24]. Their extraordinary qualities, such as their multiple active sites and vast surface area, etc., have served as the main driving force behind these endeavours. Additionally, their utility has been improved by their tunability employing heteroatoms through the doping procedure in carbon materials [25]. The basal layer heteroatoms can create additional active sites, which can increase the inherent catalytic activity of carbon materials. Due to the heterogeneous charge distribution that has been created at nearby sites, this has caused variations in charge density or local spin [26, 27].

Doping nitrogen (N) atoms on the edge or basal carbon planes is one way to encourage the delocalization of -electron domains [28]. Additionally, the addition of N can increase the number of catalytic active sites for I_3^-/I^- redox processes by incorporating lone pair electrons into the large π-conjugated system [29–31]. Due to their fascinating catalytic capabilities, N-doped carbon materials and carbon materials in the form of balls can provide novel electrode materials for electrochemical energy conversion and storage.

For DSSCs, it is critical to concurrently enhance the following [32–34]: (i) electrical conductivity, while matching the electronic energy states within the constituent components; (ii) electrocatalytic activity; and (iii) device stability. To improve the electrical structure of carbon materials as-prepared, oxidative treatments in particular have been applied extensively [35, 36].

In this work, we provide a unique NCdots: OLCNs composite that is entirely carbon-based and serves as the counter electrode material for DSSC. Pang et al. developed an all-carbon composite counter electrode for a DSSC with a 10.28 % power conversion efficiency using graphene networks embellished with nitrogen-doped carbon nano-onions [24]. To date, according to our knowledge, there are not many reports on the use of NCdots, despite the fact that there are a few publications on the application of all carbon-based materials as counter electrode materials. composite OLCNs. Cdots have become a popular new form of light-

harvesting material as a result of its remarkable benefits [37-45]. Cdots can work as both effective catalysts and multifunctional catalyst design elements, promoting a broader spectrum of electron and hole absorption and separation while stabilizing photolysis semiconductors [46].

OLCNs have been successfully used as electrode materials because of their multilayer lamellar structure, which reveals a number of appealing qualities, including a small graphitic layer, improved structural stability, and a highly accessible external surface area, which is helpful for catalytic reactions [47, 48]. Because of their better ion adsorption in electrolyte and higher corrosion resistance, OLCNs have become a more prominent choice for a catalyst [49, 50].

To prevent NCdot particle aggregation in the DSSC system, the high surface area of OLCNs (as a support material) will allow dispersion, while NCdots produced by citric acid and EDA can act as catalytic sites to increase electrocatalytic activity. Following that, the combined network of NCdots and OLCNs will provide a useful path for the transportation of electrolyte as well as electrical conducting channels for the rapid charge transfer of electrons. According to our hypothesis, the novel composite will be a more affordable counter electrode than Pt, creating new prospects for a range of electrochemical device applications.

7.2 Experimental procedure

The electrochemical characteristics of the NCdots: OLCNs composites were examined in an attempt to investigate the effectiveness of the nanocomposites as electrode materials in DSSCs, it is necessary to evaluate their electro-catalytic activity, charge-transfer resistance, and electrochemical stability. Following that, various concentrations and ratios of these materials were used as a counter electrode in the DSSC. A overview of the photovoltaic effect as seen in the current density to voltage properties of NCdots: OLCNs based DSSCs is given in this chapter.

7.2.1 Starting materials

Table 7.1: Materials and reagents.

Reagents and materials	Purity and speciation	Supplier
Acetone	CH_3COCH_3, ≥ 99.5%	Sigma-Alrich
Ethanol	CH_3CH_2OH, 96%	Sigma-Alrich
Acetic acid	CH3COOH, 99.85%	Sigma-Alrich
Acetyl acetone	$CH_3COCH_2COCH_3$, 99.3%	Sigma-Alrich
Fluorene-doped tin oxide (FTO) glasses	-	Sigma-Alrich
N719 dye-sensitizer		Sigma-Alrich
Titania (Degusa, P25) powder	TiO_2	Sigma-Alrich
Sunlight dish washing soap	-	Local supermarket
Aluminium foil	-	Local supermarket
1-hexyl-3-methylimidazolium iodide	$C_{10}H_{19}IN_{2,\geq}$ 98%	Sigma-Alrich
Iodine	$I_{2,\geq}$ 98%	Sigma-Alrich
4-tert butylpyridine	$C_9H_{13}N$, ≥ 96%	Sigma-Alrich
3-methoxypropionitrile	$CH_3OCH_2CH_2CN$, ≥ 98%	Sigma-Alrich
Lithium iodide	LiI, ≥ 99%	Sigma-Alrich
Lithium perchlorate	$LiClO_4$, ≥ 95%	Sigma-Alrich
Acetonitrile	CH_3CN, 99.5%	Sigma-Alrich
Polyethylene glycol	$H(OCH_2CH_2)_nOH$, (PEG,	Sigma-Alrich

Mn 6000)

7.2.2 Preparation of the photoanode and deposition of the dye-sensitizer

A slurry paste was made with Degussa P25 TiO_2 powder. A beaker containing 1.0 g of TiO_2 was filled with the powder, and 0.3 mL of acetyl acetone was added. 12 mL of d-H_2O was then added, and the slurry was continuously heated and stirred for 24 hours at 60 °C (to prevent re-aggregation of TiO_2 nanoparticles). Thereafter, the obtained granulated powder was ground to a fine powder. 0. 2 mL of acetic acid and 3 mL of ethanol were dropwise added to the powdered powder. The slurry paste was further continuously stirred for another 3 hours. FTO glass substrates of dimensions 20 mm x 20 mm were cleaned with d-H_2O, acetone and ethanol sequentially by ultra-sonication for 30 minutes with each solution. Then the paste was deposited onto the conducting sides of the clean FTOs which served as TCOs for each cell as shown in **Fig. 7.1 a**. Following paste deposition, the TiO2 coated FTOs were left to remain at room temperature for ten to fifteen minutes before being sintered for thirty minutes on a hot plate in air at 450 °C. Sintering was used as a substitute for annealing, which is done in a furnace at 450 °C to get rid of any organic materials and enhance contact between the paste and the dye-sensitizer. The ruthenium complex dye-sensitizer (N719) was added to the cooled TiO_2 coated FTOs via drop casting and allowed to dry at room temperature as shown in **Fig. 7.1 b.**

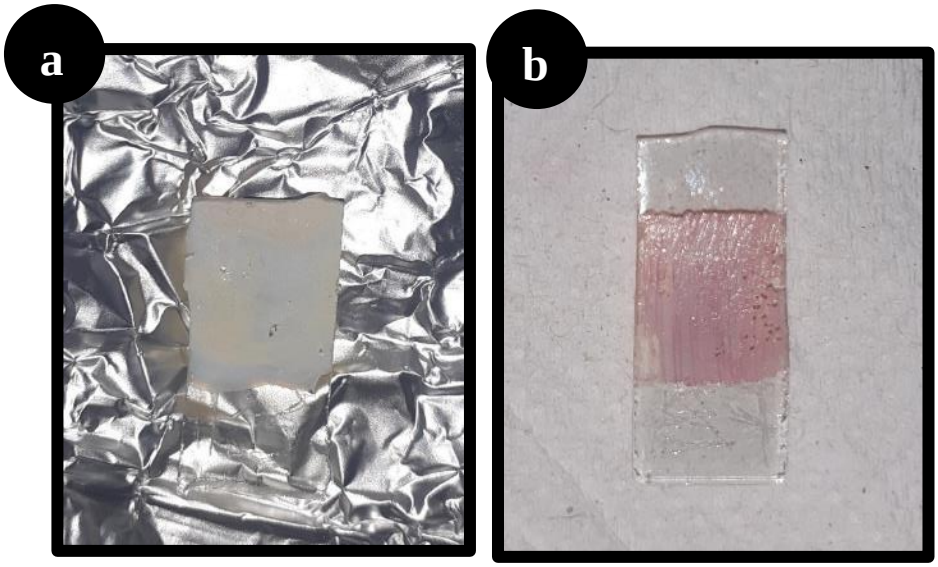

Figure 7.1: a) FTO coated with the TiO_2 paste alone and b) TiO_2 coated FTO with N719 dye-sensitizer deposited.

7.2.3 Preparation of the counter electrode

The DSSCs counter electrodes were prepared using the various as-prepared NCdots: OLCNs composites, in the different variation of the NCdots: OLCNs weight percentage (wt. %) loading, for comparison purposes of their catalytic properties. Firstly, NCdots: OLCNs composites were dispersed in dH_2O and ultra-sonicated for 15 minutes. The binder solution was then agitated for 15 minutes while 7.4g of PEG was dispersed in 20 mL of dH_2O to create a sol-like mixture. In order to create a homogenous mixture, 0.5 mL of the NCdots: OLCNs combination was combined with 0.5 mL of the PEG solution. The mixture was then further sonicated for 5 minutes to create a viscous sol. To prepare each electrode to be tested, the viscous sol was drop-casted onto clean FTO glasses while heating the glass on a hot plate at 60 °C until a fairly uniform coated FTO was obtained as shown in **Fig. 7.2**. The coated FTOs were then re-sintered in air for 30 minutes at 250 °C to eliminate PEG organic molecules from the electrode.

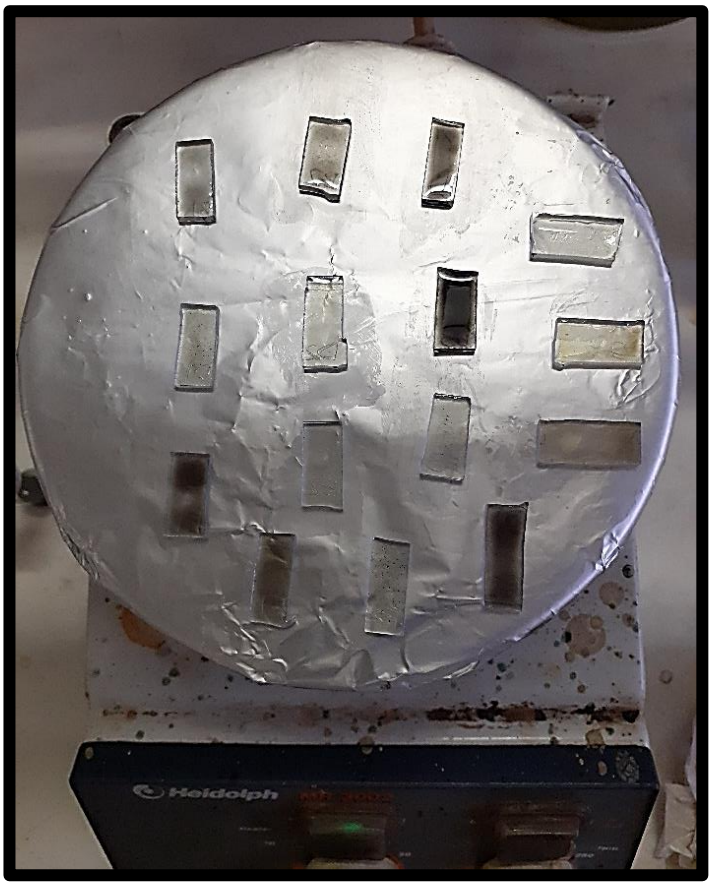

Figure 7.2: Various FTO glass substrates being coated on a hot plate. The colour and transparency of the films also varies according to type of NCdots: OLCNs composite applied.

7.2.4 Device assembly (fabrication)

The photoanode and counter electrodes were combined to complete each cell. Both electrodes were combined using clamps before the electrical conductivity test (see **Fig 7.3** below). The counter electrode was put on top of the photoanode, which was laid face up on a level surface, permitting each electrode's non-coated offset position. The area of each cell exposed to light was ~25 mm^2 (5 mm x 5 mm). Since each electrode was placed offset from the other counter electrode, the exposed non-coated part of the FTOs gave allowance for the solar cells connectors to have access to the electrodes for testing, and this allowed both electrode electrical contact and elimination of cell shorting.

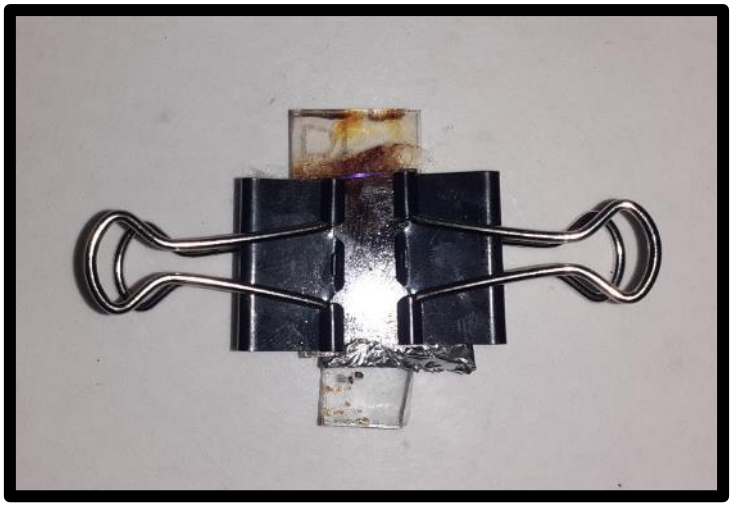

Figure 7.3: Fabricated dye-sensitized cell connected using clip binders.

7.2.5 Electrochemical measurements

An effective method for examining processes involving electron transfers is electrochemistry. It links chemical changes to electron flow [51]. The ensuing chemical change in inorganic chemistry frequently involves the oxidation or reduction (redox) of a metal complex. Tafel polarization analysis, electrochemical impedance spectroscopy, and cyclic voltammetry (CV) were used to examine the electrocatalytic properties of several counter electrodes for triiodide reductions. In a standard procedure, cyclic voltammetry samples were measured in a three-electrode electrochemical cell using glassy carbon as the working electrode (WE), an Ag/AgCl (with 3M KCl) as the reference electrode (RE) and NCdots: OLCNs on FTO as the counter electrode (CE) all dipped in a 40 mL acetonitrile solution of 0.05 M LiL, 0.001 M I_2 and 0.5 M $LiClO_4$. The scan rate conditions were varied between 40-200 mV s^{-1} and the tests for all composite samples were ran at 50 mV s^{-1}. Before measurements with the composite commenced, all electrochemical experiments were conducted using the Pt wire electrode as a reference. This allowed for the evaluation of the composite's catalytic activity. A metallic rod with a 2 mm diameter and a 0.03142 cm^2 surface area was enclosed in glassy carbon. The glassy carbon was first polished to eliminate any impurities using a polishing pad and ultra-pure water. The reference electrode is used to properly measure the applied potential in respect to a trustworthy reference response as the current flows between the working and counter electrodes.

Assembling the three-electrode setup for this study's CV, EIS, and LSV measurements using the BioLogic SP -300 electrochemical workstation and EC Lab software is shown in **Figure 7.4**. The electrochemical impedance spectroscopy measurements were carried out at ambient room temperature with an AC sinus signal amplitude of 10 mV (Vrms ~ 7.07 mV) in the frequency range 100 KHz to 100 MHz at 0 V DC bias. Tafel polarization voltammograms were plotted using LSV data at a scan rate of 100 mV s^{-1}.

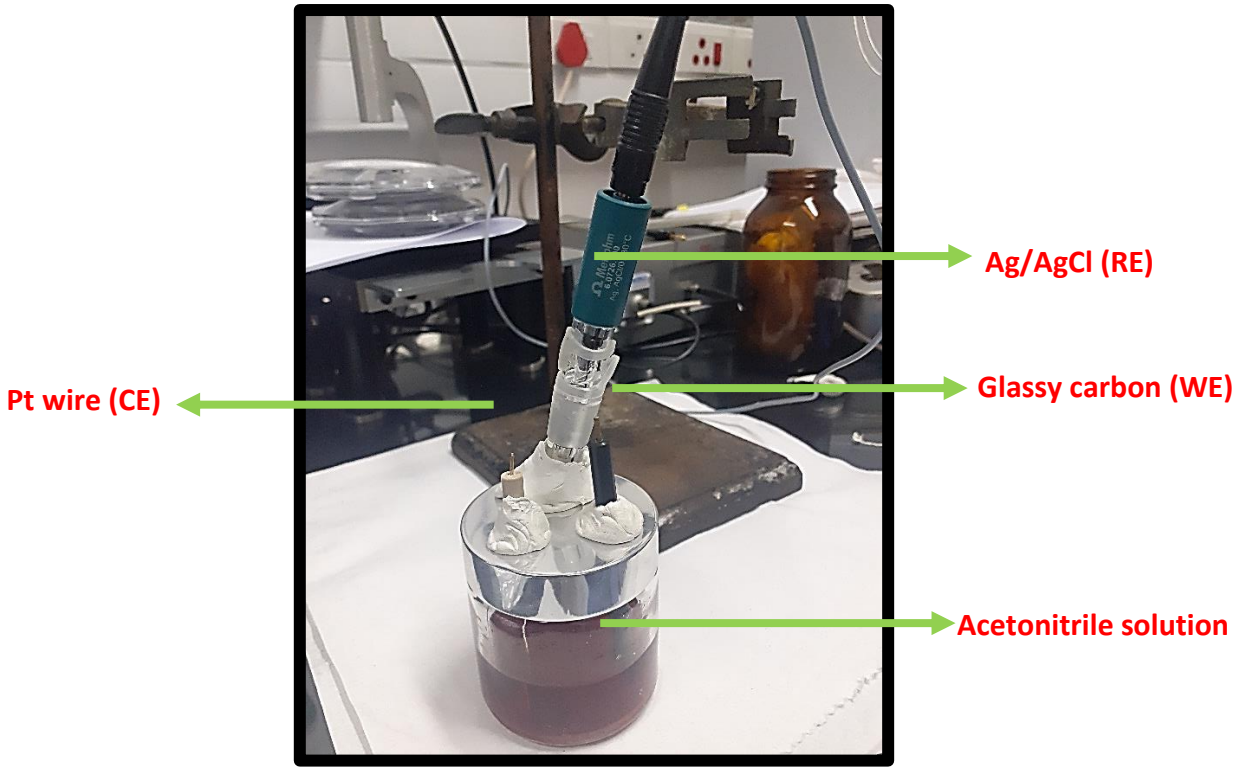

Figure 7.4: Three-electrode electrochemical cell employing the Ag/AgCl reference electrode, glass carbon (working electrode) and Pt wire (counter electrode) used in this study.

7.2.6 Current density-voltage characteristics of the DSSCs

By examining the current-density vs. photovoltage (J-V) characteristic curves under white light corresponding to AM 1.5 and in the dark, the DSSCs' photovoltaic performance was evaluated. These measurements were performed in a natural setting using computer-

controlled HP 4141B source-meter equipment (SMU). The active cell area and incident light intensity were each 25 mm^2 and 100 mW cm^{-2}, respectively.

All of the manufactured devices were put to the test with a liquid electrolyte. 0.6 M methylhexylimidazolium iodide, 0.1 M iodine, 0.5 M tert-butyl pyridine, and 0.1 M lithium iodide were used to create the electrolyte solution [51]. The margins of the offset electrodes were then covered with the redox electrolyte solution. Capillary action then brought the fluid into the area between the electrodes.

7.3 Characterization techniques

By using CV, the electrocatalytic characteristics of several CEs for triiodide reductions were comprehensively examined (**Fig 7.5 a**), EIS (**Fig 7.5 b**), and Tafel polarization experiments (**Fig 7.5 c and d**). These images also provide a basic understanding of what kind of information each plot can provide. A three-electrode cell coupled to a potentiostat was used for all electrochemical voltammogram measurements (BioLogic SP-300). As reference, counter, and working electrodes, respectively, saturated calomel electrode, platinum wire electrode, and glassy carbon electrode were utilized. Using the solar simulator (150 W xenon (Xe) lamp) with 1.5 air mass filters and a source/measure unit HP 4141B under 100 mW cm^{-2} illumination, the photocurrent density-voltage (J-V) characteristics of each cell were measured. Every experiment or measurement was conducted in a controlled environment at room temperature.

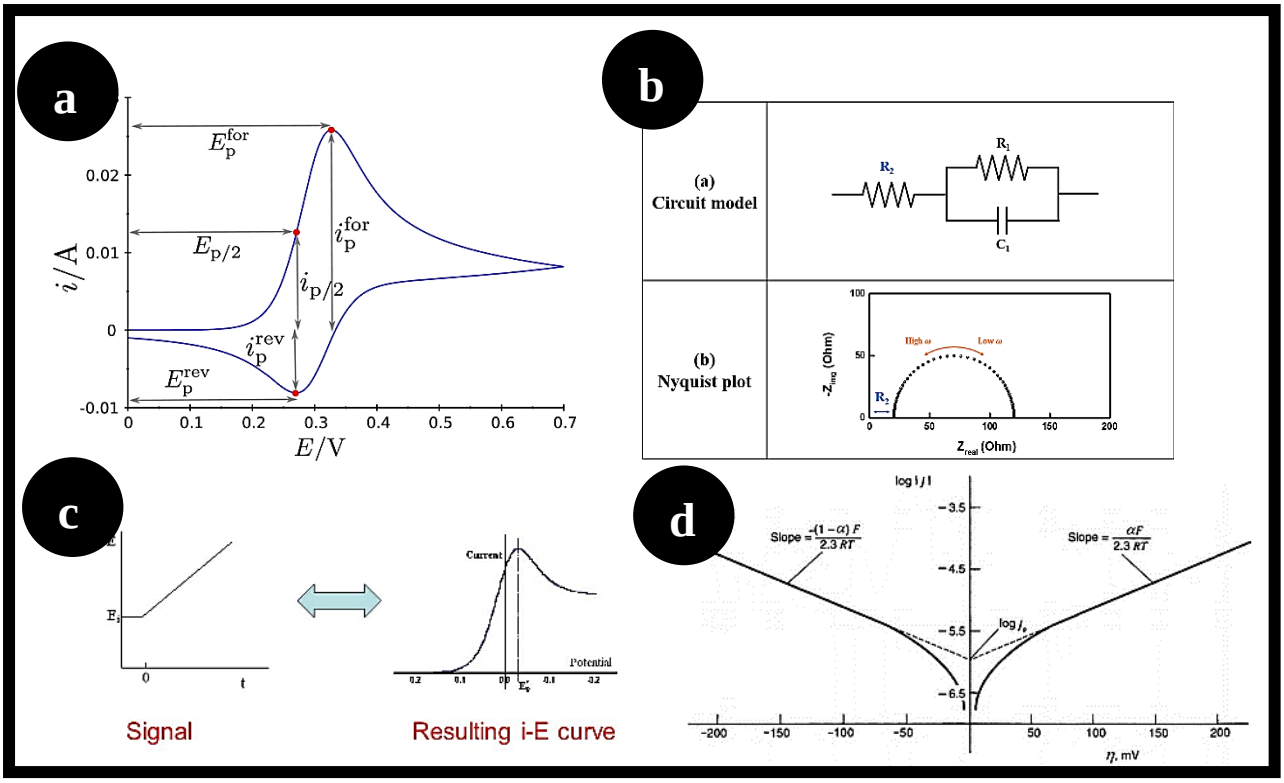

Figure 7.5: Images of standard a) CV plot [52], b) EIS plot [53], c) LSV plot and d) Tafel voltammogram [54].

7.4. Results and discussions

7.4.1 Electrochemical properties of NCdots: OLCNs electrode using CV scans

In the CV study, the electric potential was varied at the speed (scan rate) of 50 mV s^{-1}. **Figure 7.6** shows the CV voltammogram of the Pt electrode that was used in this study for the conduction of the experimental testing showing the direction of the CV scan. In the forward scan (see red arrow), the potential is swept negatively from the starting potential (E_i = 0.9 V) to the switching potential (E_f = -0.58 V) [55, 56]. This is referred to as the cathodic trace (labelled reduction on the graph). The scan direction is then reversed, and the potential is swept positively back to E_i, referred to as the anodic trace (labelled oxidation on the graph) [57−59]. The counter electrode's job is to complete the circuit while the current is being measured as an electron flow between the WE and CE. As a result, while investigating a reduction at the WE, an oxidation takes place at the CE.

There were found to be two common pairings of redox waves (**Fig. 7.6**). Redox reaction (1) is attributed to the more negative pair, while redox reaction (2) is assigned to the more positive pair [60, 61]. The Pt CE presents peak current densities -3.91 mA/cm^2 at 0V

(reduction) and 5.43 mA/cm^2 at 0.28V (oxidation) for the I_3^- redox. In order for DSSCs to function, I^- is first oxidized to I_3^- by the oxidized sensitizing dye in the photoanode, and then I_3^- is diffused to CE to absorb the electrons from the external circuit while being catalytically reduced to I^- by CE, which completes the system cycle.

$I_3^- + 2e^- = 3I^-$ ..... (1)

$3I_2 + 2e^- = 2I_3^-$ ..... (2)

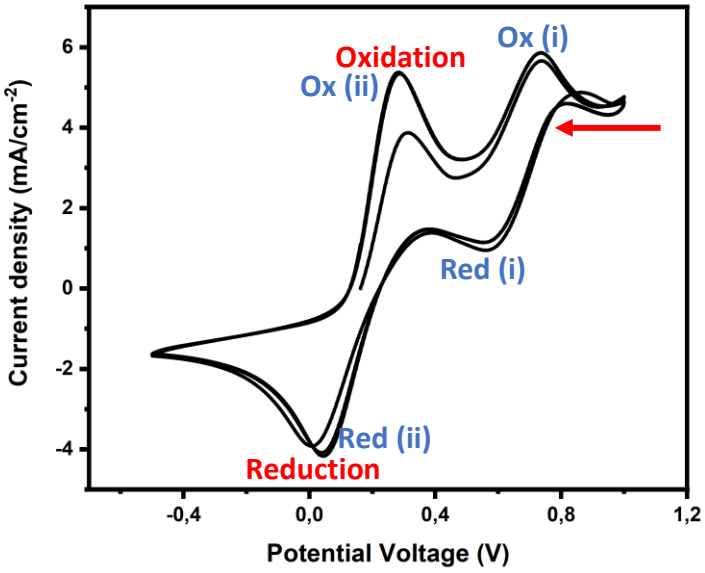

Figure 7.6: CV Voltammogram for the Pt electrode at a scan rate of 50 mV s^{-1}.

In order to distinguish between the differences in catalytic activity of the various NCdot: OLCNs, the CV curves of the nanocomposite electrodes with varying weight percentages were investigated: On the FTO counter electrode, there are NCdot: OLCN composites. The matched curves of the Pt CV and the examined carbon material showed the typical "duck shape" [62].

Figures 7.7 a, b and c show voltammograms from the 5% NCdots on p-/ox-/N-OLCNs, respectively. The peak current densities for each counter electrode material were found to be [-152.24 mA/cm^2 at -0.26 V]; [839.13 mA/cm^2 at -0.03 V] (**Fig 7.7 a**), [-57.85 mA/cm^2 at -0.55 V]; [65.95 mA/cm^2 at 0.024] (**Fig 7.7 b**) and [-5.81 mA/cm^2 at -0.24 V]; [80.84 mA/cm^2 at 0.04 V] (**Fig 7.7 c**). See **Table 7.2** for a detailed tabulated summary. These peak current measurements demonstrate that, under the same circumstances, all of these nanocomposite electrodes had better conductivity and lower resistance than the Pt electrode [63-65].

According to literature, a DSSC's performance may be improved with reduced resistance and better conductivity [62]. In comparison to the Pt electrode or the other nanocomposites, composites made with 5% NCdots: p-OLCNs had a significantly greater current density at the I_3^- reduction peak and a larger I_2 oxidation peak for the carbon electrode. However, it is evident that the 5% NCdots: p-OLCNs electrode's electric potential changed to a more positive and higher oxidation-reduction current density than the Pt electrode. The peak current density values for 5% NCdots: ox-OLCNs and 5% NCdots: N-OLCNs both showed comparable results. Compared to the Pt electrode, they too displayed larger current densities.

Thus, the nanocomposite electrodes can be said to have higher electrocatalytic activity in the I_3^-/ I_2 redox reaction than that of the Pt particles. However, the reduction peak for all the composites was not clearly defined, which may be due to the restrain of the catalytic reaction on the electrodes [66].

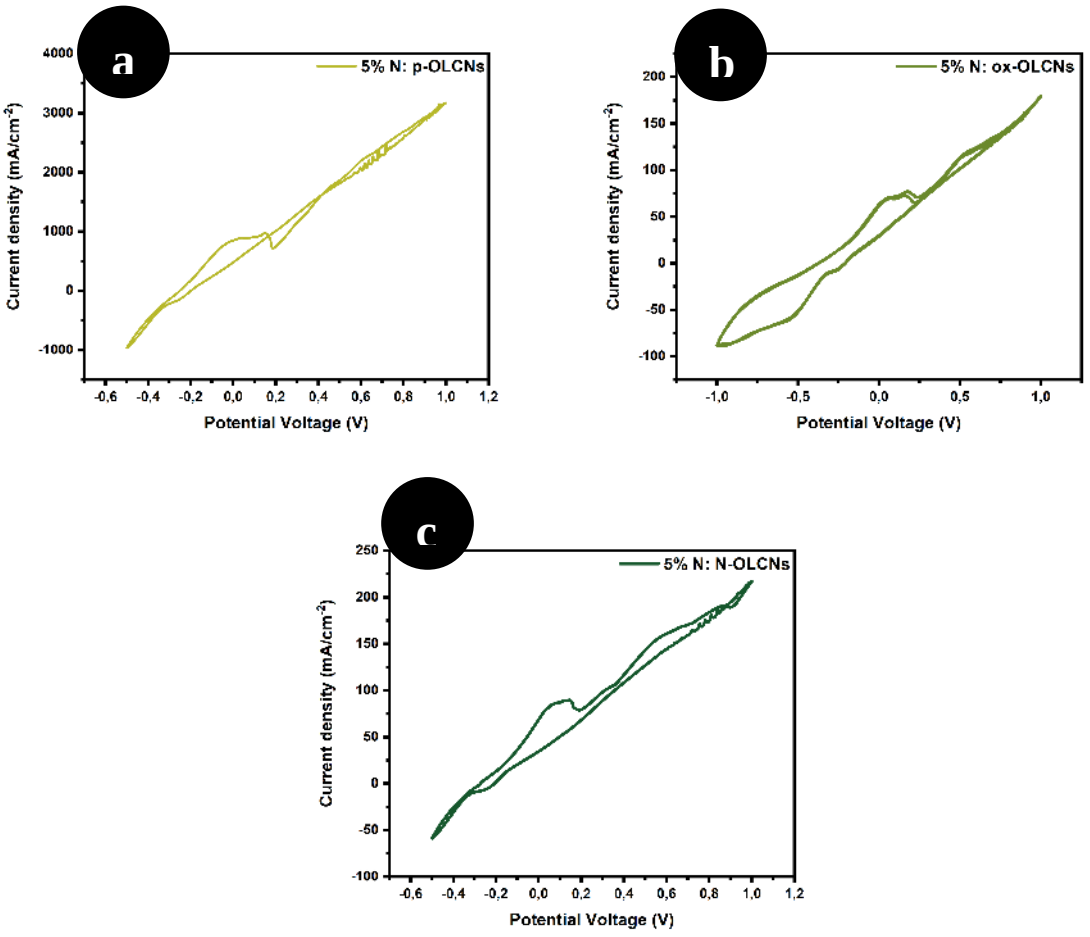

Figure 7.7: CV Voltammogram for CE made of a) 5%NCdots (EDA): p-OLCNs, b) 5%NCdots (EDA): ox-OLCNs and c) 5%NCdots (EDA): N-OLCNs at a scan rate of 50 mV s^{-1}.

The cyclic voltammograms show variable change in the peak currents with the different nanocomposite films (see **Supplementary Information, (SI) Figs. S32-35**). Data with increasing NCdots weight percentage (10–50%) indicate erratic results, suggesting that all nanocomposite films may not be adequately electrocatalytic, and that the process may be constrained by diffusion and the electrocatalytic activity of the electrodes made of NCdots and OLCNs [67]. It was anticipated that the electrochemical study of the nanocomposite films would reveal a linear rise in electrochemical activity with increasing amounts of NCdots deposited on the OLCNs. For example, **Fig 7.8 c, and 7.9 a, b and c,** all show no electrocatalytic activity towards this redox couple.

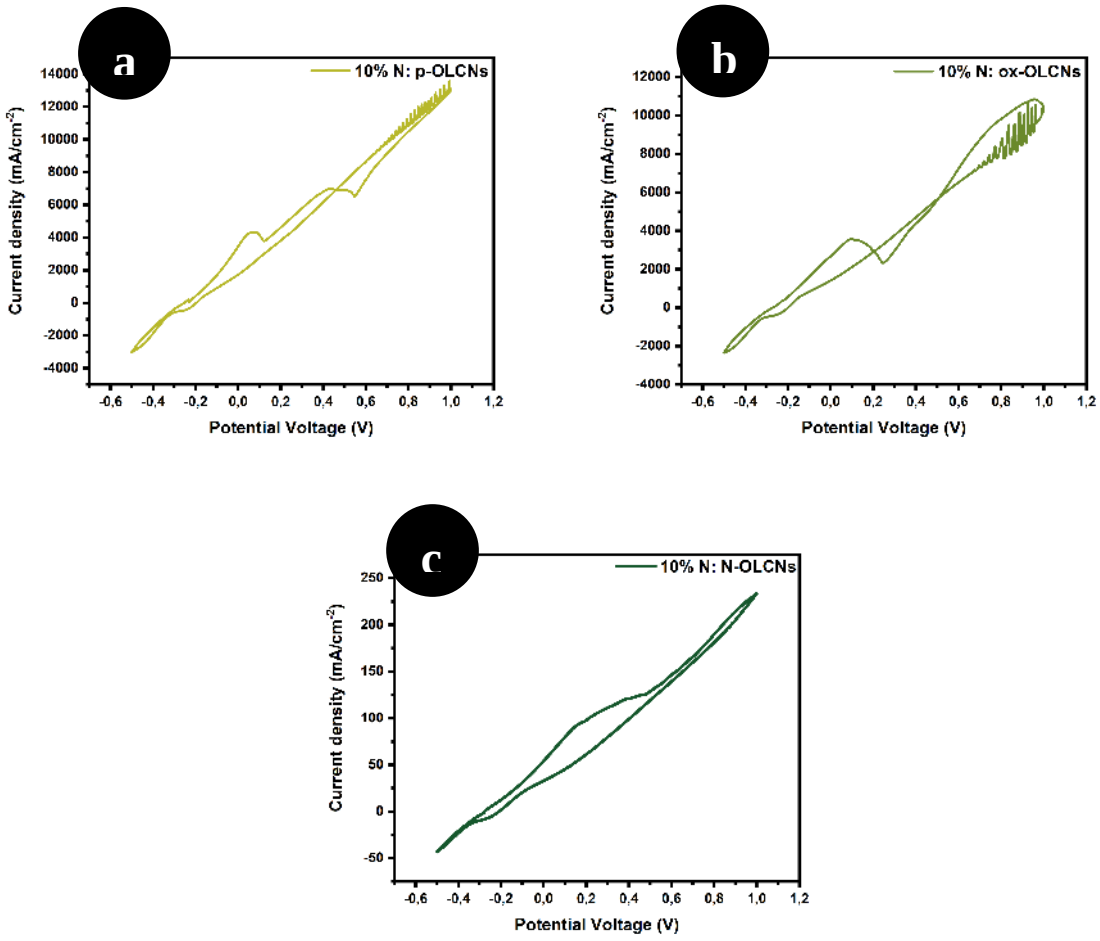

Figure 7.8: CV Voltammogram for CE made of a) 10%NCdots (EDA): p-OLCNs, b) 10%NCdots (EDA): ox-OLCNs and c) 10%NCdots (EDA): N-OLCNs at a scan rate of 50 mV s^{-1}.

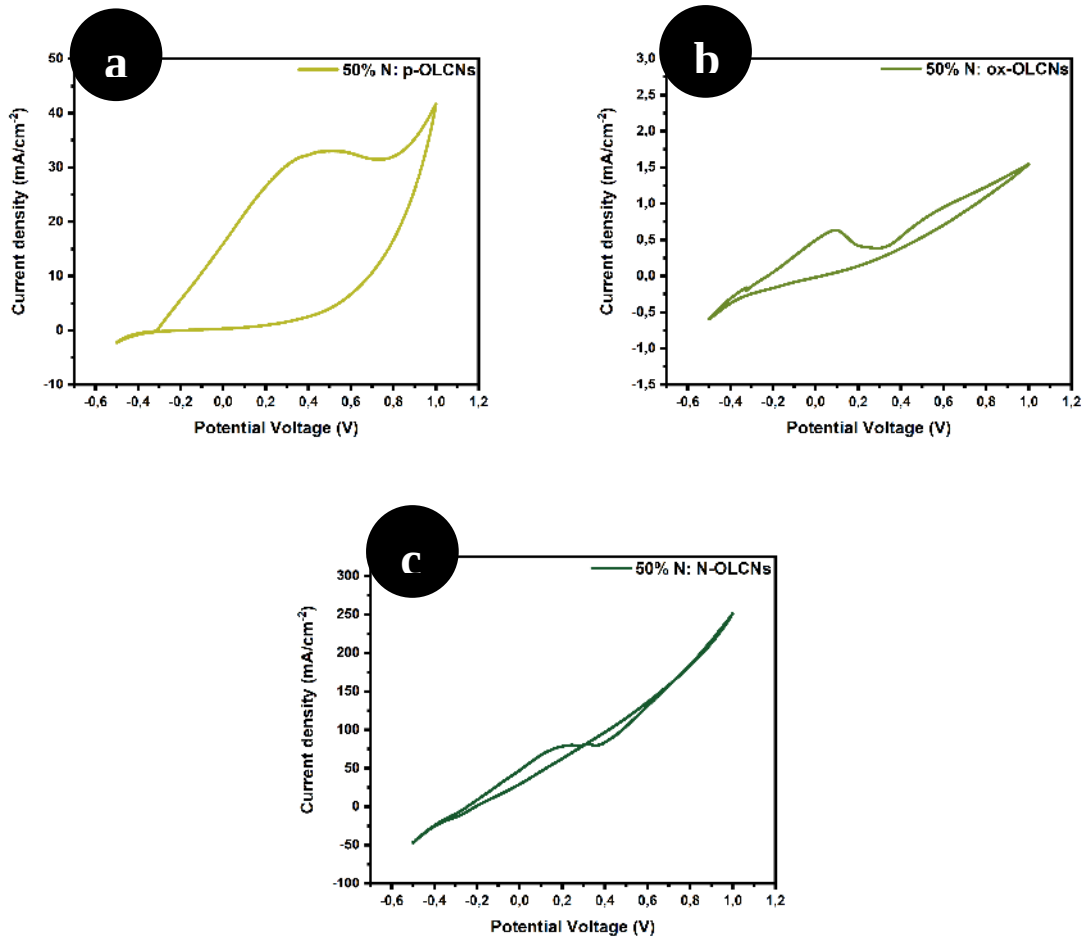

Figure 7.9: CV Voltammogram for CE made of a) 50%NCdots (EDA): p-OLCNs, b) 50%NCdots (EDA): ox-OLCNs and c) 50%NCdots (EDA): N-OLCNs at a scan rate of 50 mV s^{-1}**.**

Figures. 7.10 and 7.11 below both show CV plots of composites prepared with higher NCdots concentration ratio to the various OLCNs. **Fig 7.10 a, b and c** show little to no electrocatalytic activity due to the relatively insignificant values obtained of the peak densities, for both the forward and reverse reactions. Moreover, the cathodic peak for the reduction reaction of I_3^- ions, which is a very important reaction on the counter electrode was hardly observed.

However, **Fig 7.11 a, b and c** shows some electrochemical activity. The peak current densities for each counter electrode material were found to be [-12.90 mA/cm^2 at -0.27 V]; [76.43 mA/cm^2 at 0.11 V] (**Fig 7.11 a**), [-11.82 mA/cm^2 at -0.27 V]; [78.12 mA/cm^2 at 0.14] (**Fig 7.11 b**) and [-8.69 mA/cm^2 at -0.27 V]; [85.11 mA/cm^2 at 0.21 V] (**Fig 7.11 c**). Once more, these peak current figures demonstrate that all of the nanocomposite electrodes are more conductive and have lower resistance than the Pt electrode. A greater electrocatalytic activity toward the reduction process is therefore shown by the nanocomposite electrodes

[68]. If the analyte is stable following reduction and may afterwards be re-oxidized, it is said to be chemically reversible.

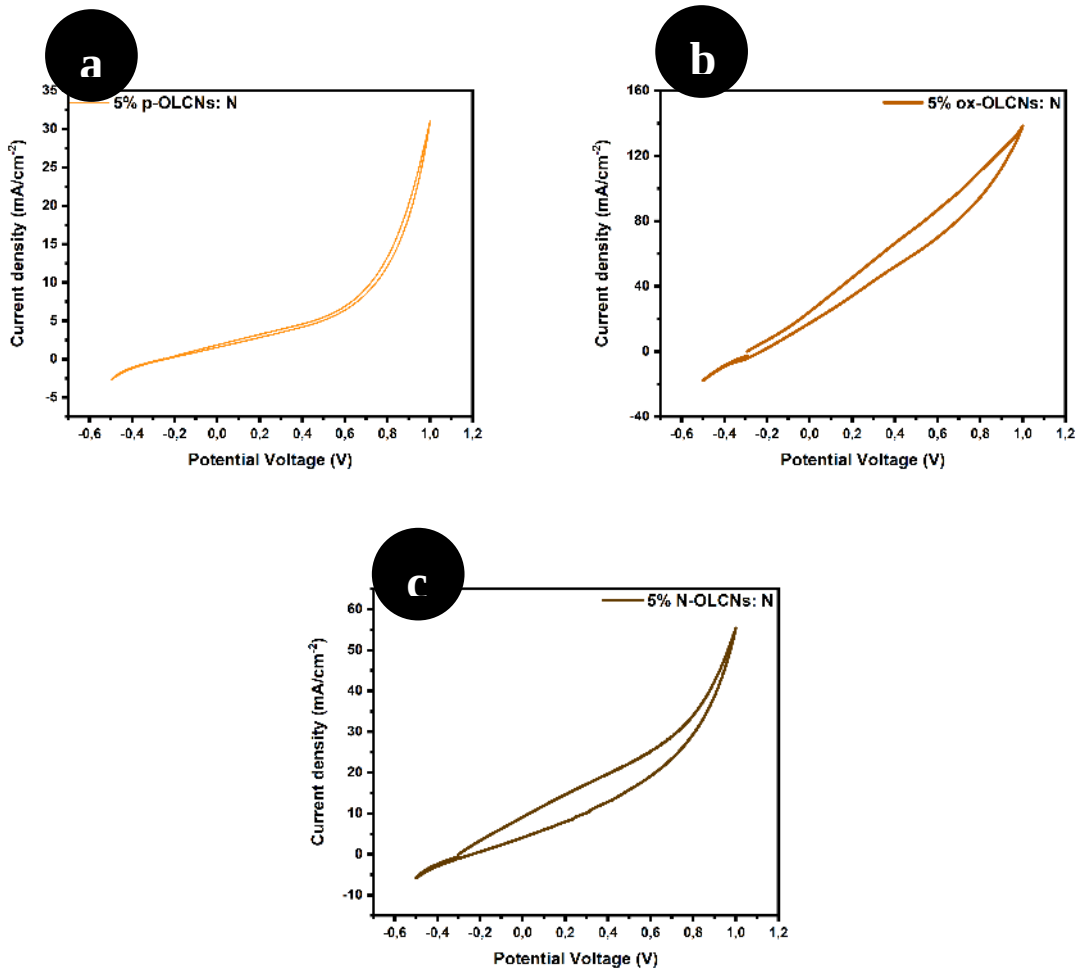

Figure 7.10: CV Voltammogram for CE made of 5% p-OLCNs: NCdots (EDA), b) 5% ox-OLCNs: NCdots (EDA) and c) 5% N-OLCNs: NCdots (EDA) at a scan rate of 50 mV s^{-1}.

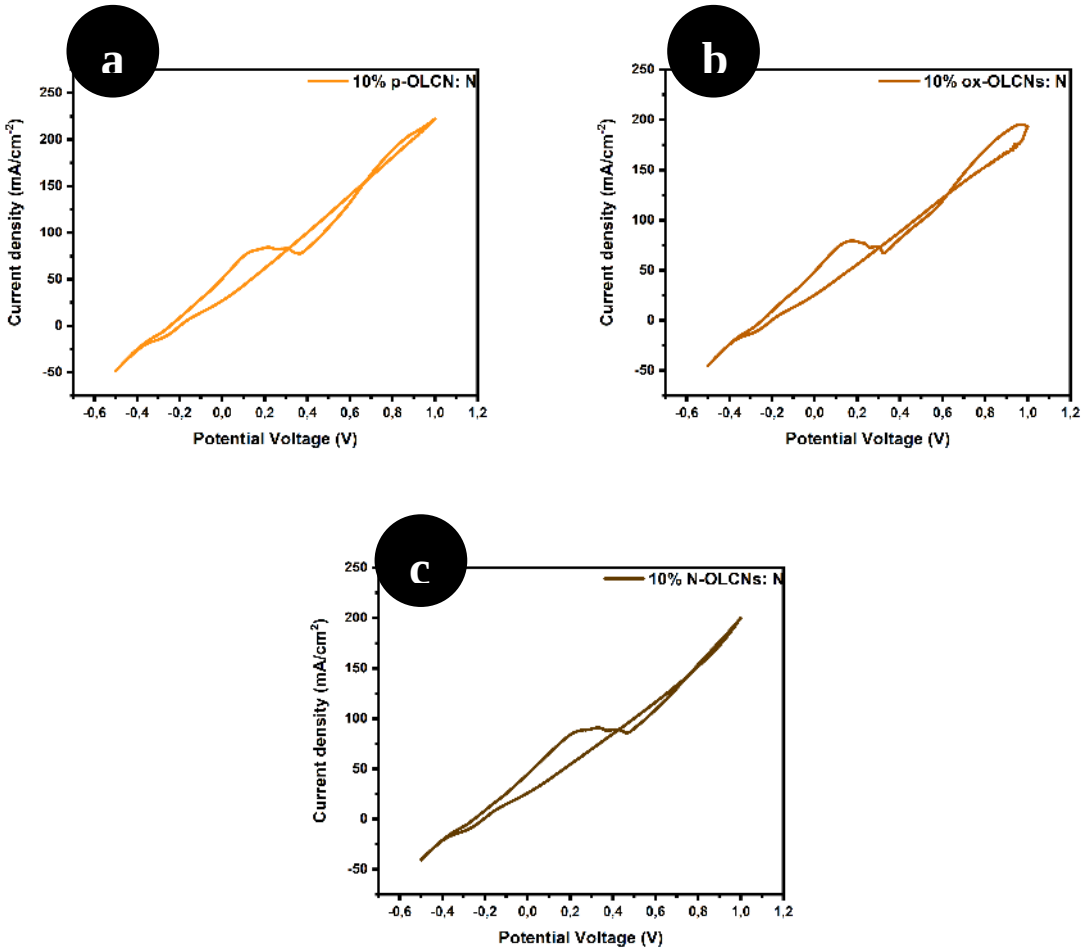

Figure 7.11: CV Voltammogram for CE made of a) 10% p-OLCNs: NCdots (EDA), b) 10% ox-OLCNs: NCdots (EDA) and c) 10% N-OLCNs: NCdots (EDA) at a scan rate of 50 mV s^{-1}.

Peak-to-peak separation (E_{pp}) and absolute reduction peak current density (J_{pc}) reflected from the CV curves typically give details on the counter electrode's electrocatalytic capacity for the triiodide reduction [68, 69]. Thus, commonly a smaller E_{pp} and higher $|J_{pc}|$ values indicate better performance for the I_3^- reduction [70, 71]. **Table 7.2** summarises these values for two chosen composite types: with lower NCdots concentration (5% loading) to the support and with higher NCdots ratio to the various OLCNs (10% loading). Moreover, J_{pc} is the reduction peak current density, as already mentioned, and J_{pa} is the oxidation peak current density, E_{pc} is the reduction peak applied potential and likewise E_{pa} is the oxidation peak applied potential [72].

NCdots loaded unto p-OLCNs at 5% weight percentage are hereby seen to having the lowest peak-to-peak separation for the redox reaction (**Table 7.2**), demonstrating that the effects of doping have significantly improved the decrease of I_3^- to I^-. Furthermore, apparently the 5%

NCdots: OLCNs composites shows the optimal performance for the reduction of I_3^- compared to Pt and the other nanocomposites

Table 7.2: Cyclic Voltammetry analysis results.

	Reduction		Oxidation		
Sample name	J_{pc} (mA/cm^{-2})	E_{pa} (mV)	J_{pc} (mA/cm^{-2})	E_{pa} (mV)	$\Delta Ep/E_{pp}$ (mV)
Pt	-3.91	0	5.34	0.28	0.28
5% NCdots:p-OLCNs	-152.24	-0.26	839.13	-0.03	0.23
5% NCdots:ox-OLCNs	-57.85	-0.55	65.95	0.024	0.57
5% NCdots:N-OLCNs	-5.81	-0.24	80.84	0.040	0.28
10% p-OLCNs:NCdots	-12.90	-0.27	76.43	0.11	0.38
10% ox-OLCNs:NCdots	-11.82	-0.27	78.12	0.14	0.41
10% N-OLCNs:NCdots	-8.69	-0.27	85.11	0.21	0.48

The results reported above imply that the p-OLCNs and NCdots have the potential to improve the electrocatalytic performance of DSSCs. According to the general pattern seen above, composites with co-doping performed worse than those with doped carbon dots put onto virgin OLCNs (in either ratio or concentration). Furthermore, compared to NCdots loaded onto far-fetched N-OLCNs, NCdots loaded onto ox-OLCNs exhibited substantially comparable behavior. The doped surface's passivation and functionalization prevent photogenerated electron-hole pairs from freely moving. Therefore, the bound excitons may grab carriers and produce photoinduced charge traps when exposed to light [73]. Finally, when carriers move through the nanocomposites, they will become stuck, producing the observed photo reaction.

These findings unequivocally show that the addition of lower weight percent (< 10 %) of NCdots to the various OLCNs presents with potential achieve a higher electrical conductivity compared to those with higher wt. % (> 15 %). The most likely explanation for this behaviour is that NCdots are well dispersed in the composite at lower weight percent levels, and as a

result, NCdots and OLCNs are well connected. As a consequence, the hybrid nanocomposite's electrical conductivity is greater than that of the other composites made in this work. The same is valid for composites with increased OLCN content (10% loading). However, samples with 5% loading (10%) also included samples with greater concentrations of conductive NCdots (OLCNs), which improved the conductivity of the composite [74]. The triiodide ions are becoming harder to decrease, as seen by the red(i) shift seen near the lower potential. a surface with cracks that has low lateral conductivity.

In summary, these materials don't conduct electricity well. The efficiency of the co-doped nanocomposites, however, was noticeably significantly lower. This may be because photogenerated charge carriers recombined extremely quickly. Creating better composite nanostructures is one technique to increase charge separation. It may be anticipated that improving composite preparation efficiency may increase the carbon-carbon system's conversion efficiency. The electrode with a 5% loading of NCdots then displayed the maximum current density.

When the proportion of NCdots in mesoscopic carbon film was loaded onto the functionalized, the current density drastically decreased due to the deterioration in catalytic activity, specifically the reduction in total electrochemical active surface area. This might be explained by the functionalized nanoparticles obstructing some of the pores in the carbon template or by the decrease in the catalytic active site exposed in the electrolyte with an increase in carbon concentration [75, 76].

7.4.2 Electrochemical impedance analysis

The cell was biased with open-circuit voltage under sinusoidal perturbation of 0 V with the frequency scanning range of 100 KHz - 100 MHz during the impedance measurement. A separate analysis of the impedance behaviour of the counter electrode might provide further information because numerous operational circuit components will contribute to the DSSC's impedance [77]. **Figure 7.17,** which describes the resistance-to-mass transfer/diffusion rate of the ions across the electrode-electrolyte matrix, shows the diameter of the semicircle impedance loop in the high frequency region. Between the carbon electrodes, the electrolyte was identical to that used in CV testing. Under standard conditions, it is possible to distinguish clearly between charge transfer at the counter electrode, diffusion of the redox species in the electrolyte, electron transport in the mesoscopic TiO_2 film, and electron

recombination at the TiO_2-electrolyte interface by looking at the spectral shapes of the impedance response as a function of frequency [78].

Figure 7.16 shows the EIS plot of the Pt electrode that was used in this study as reference for the nanocomposites of interest in this study. The plot consists of two semicircles, the first one showing an incomplete semicircle – these circles allow extraction of the real part of the impedance corresponding to the R_p = electrode resistance; R_∞ = electrolyte resistance; R_{ct} = charge transfer resistance (Stern layer) and R_{mt} = mass transfer resistance (diffuse layer) [79], respectively. The charge transfer resistance corresponding to the charge exchange between the nanocomposites, Pt counter electrodes, and the triiodide electrolyte was calculated using the semi-arcs in the Nyquist plots. A decrease in R_{ct} signifies an increase in the electrocatalytic activity of the CE relative to Pt by reflecting an acceleration of the electron transfer process at the electrolyte-CE interface [80].

At high frequencies corresponding to 100 kHz and a phase of zero, the Ohmic series resistance (R_s) of the electrode/total series resistance can be determined. The semicircles on the low frequency side of the semicircle indicate the diffusion impedance of the electrolyte, and the charge-transfer resistance of the electrodes may be calculated as half the value of the actual semicircle on the high frequency side [81, 82]. The R_s primarily defines the resistance of the substrates, whereas the Rct gauges the catalytic activity of the electrodes in reducing triiodide ions. For the Pt electrode, it was determined that the R_p = 97.71 Ωcm^2, R_∞ = 40.02 Ωcm^2 and $R_{ct} + R_{mt}$ = 227.43 Ωcm^2. **Table 7.3** summarizes the findings of nanocomposites.

The **SI (Figs. S36-42)** contains the values of various synthetic nanocomposites. In all nanocomposites, the constant phase element (CPE) and R_{ct} nanocomposite network at the electrode and electrolyte interface dominate the impedance in the middle frequency range, between 100 Hz and 10 kHz. The CPE measures the interfacial capacitance while accounting for the electrodes' roughness, which results in a sinking of the semicircle into an ellipse.

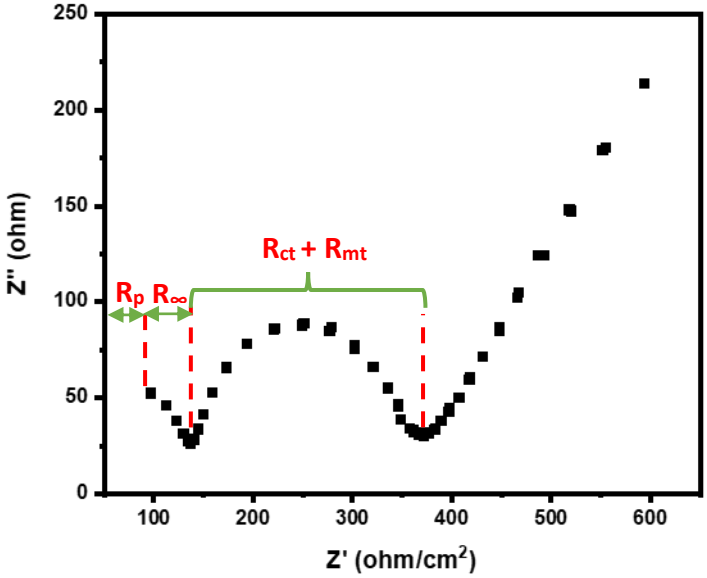

Figure 7.16: EIS Voltammogram for the Pt electrode.

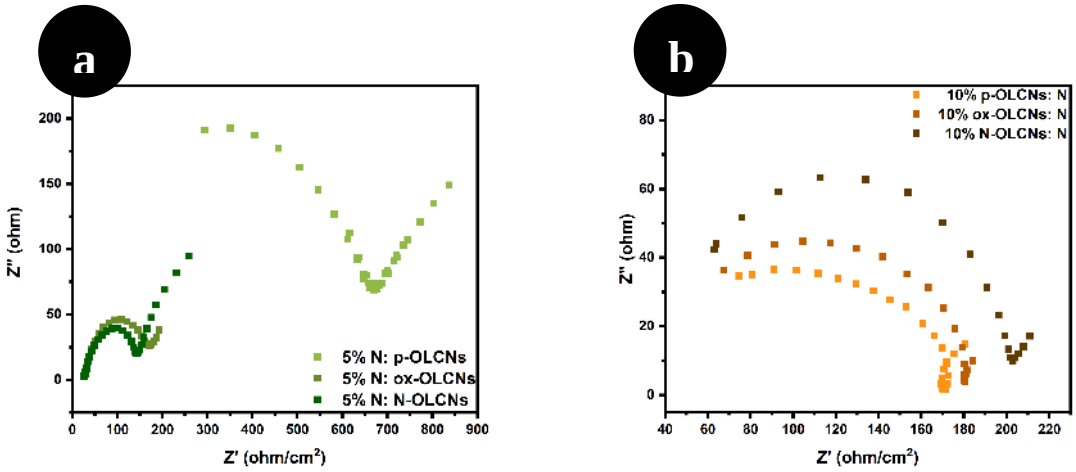

Figure 7.17: EIS Voltammograms for composites prepared with a) 5% NCdots wt. % loading and b) 10% OLCNs wt. % loading unto NCdots.

Looking at the **Fig. 7.17** above, it can be noticed that all nanocomposite electrodes exhibit variable semi arc widths and shapes. This implies that the resistivity values of the various analysis electrodes are variable. This is most likely a result of the hybrid nanocomposite materials' having bad electrical contact and charge transfer to Pt compared to the TCO. It's also possible that the high concentration of NCdots in the composite matrix structure is not evenly distributed, which would explain why the NCdots are not properly coupled to the different OLCNs and TCO substrate [71]. This is true for all examined nanocomposites. This is also consistent with the conductivity findings from CV given above. Additionally, we

previously covered how adding doped carbon dots to functionalized OLCNs increases the contact resistance between the composites of NCdots and OLCNs. Therefore, the higher the co-doping content of the nanocomposites leads to higher resistance of the composite in overall.

From **Fig. 7.17** above and **Table 7.3** below, the response at medium frequencies is related to a high capacitance that strongly depends on light intensity and can be attributed to the NCdots: p-OLCNs/electrolyte interface, because an accumulation of electrons and redox species is expected at this interface under open circuit conditions. The response at low frequencies is connected to electrolyte diffusion mechanisms [82].

From all nanocomposites, three different types of electrochemical reactions were seen. First, there is the Wagner-Traud (corrosion) process, which is applicable to redox reactions without transport restriction. The charge transfer and semi-infinite diffusion process, which is relevant for redox reactions or corrosion with mass-transport restriction (electrode in a quiescent electrolyte, aerobic corrosion), is followed by the charge transfer and adsorption (Volmer- Heyrovsk mechanism), which is relevant for reactions that result in acidic corrosion, electrocatalysis, and/or electrolyzers [83].

Table 7.3: EIS analysis results.

Name of sample	R_p (Ω cm^2)	R_∞ (Ω cm^2)	$R_{ct} + R_{mt}$ (Ω cm^2)
5% NCdots:p-OLCNs	-	-	376.34
5% NCdots:ox-OLCNs	-	-	127.88
5% NCdots:N-OLCNs	-	-	117.91
10% p-OLCNs: NCdots	-	-	96.0
10% ox-OLCNs: NCdots	-	-	113.04
10% N-OLCNs: NCdots	-	-	139.89

The primary need for a substance to be used as a catalyst in a DSSC is the decrease of the charge mediator's oxidized state, which calls for low charge-transfer resistance and high exchange current densities [81]. In order to understand the impacts of sheet resistance, the catalytic properties of the CEs, and to lessen the impact of the photoanode, the EIS study was

carried out. According to the EIS results, increasing NCdots doping increased the semicircle's diameter. This indicates that increasing the number of NCdot loadings does not increase the charge transfer rate throughout the whole composite film [82]. This means, in terms of DSSC application, that increasing of NCdots loadings in the composite material may not necessarily affect the reaction rate across the entire composite electrode. Thus, the overall performance of the DSSC is not affected all-round the surface of the counter electrode.results of other composites can be found in the SI page.

7.4.3 Potentiodynamic polarization curves for Tafel analysis

Linear Sweep Voltammetry is another name for linear polarization (LSV). It is an electrochemical approach where the potential is linearly increased or lowered over time while the current in the circuit is being measured. The current (J) vs potential (V) curve represents the measurement's plot. The Linear Sweep Voltammogram and Polarization Curve are other names for this curve [84]. In corrosion studies, the corrosion potential is surrounded by linear polarization. The polarization curve is then subjected to the Tafel Analysis to provide the corrosion potential, corrosion current, and corrosion rate. Results for the various composites can be found in the **SI** (**Figs. S43-47**).

The three-electrode setup for LSV measurements utilizing the Pt electrode is similar to the one used in the EIS measurement, **Fig. 7.24** shows the measured Tafel results.

From the Tafel polarization plot (**Fig. 7.24 b**), the semi-log arithmic plot presents with non-linearity and no identical symmetry (also see **Fig. 7.24 a**) within the exponential regime. The Pt electrode's slope on the curve's cathodic branch is greater and steeper, suggesting a higher and quicker exchange current density (J_o) on the electrode's surface [4]. A greater J_o value translates into a lower R_{ct} value (as values are inversely proportional) [4, 45], which is consistent with the CV and EIS results above indicating that the Pt electrode has strong catalytic activity of the CE. Good catalytic activity of a CE results in enhanced performance of the DSSC.

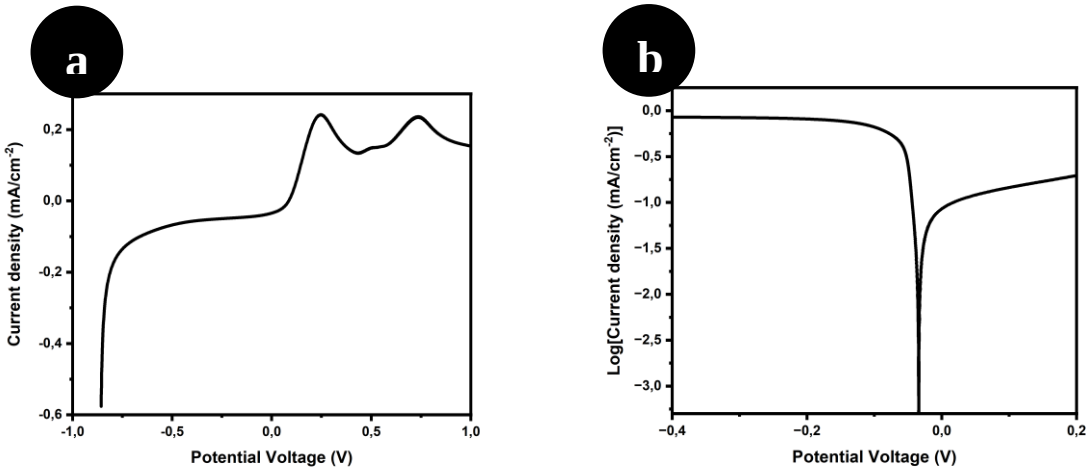

Figure 7.24: a) LSV plot and b) Tafel polarization for the Pt electrode.

7.4.4 Current density - voltage (J-V) characteristic of the DSSCs under illumination

By evaluating the current-voltage (I-V) characteristics in the dark and with AM 1.5G spectral distribution, the cell performance was evaluated. A 150 W Oriel solar simulator outfitted with neutral filters (F1-F6) and AM 1.5 was used for these tests. A silicon photo-detector that was calibrated and operated at 1 Sun was used to calculate the radiance. For certain samples, the brightness of the samples was modified using neutral filters after the samples were lit using the FTO glass substrate (see **Fig. 7.25**). The DSSC device with NCdots's J-V characteristics are shown here: OLCN electrodes were gathered using a 2-point probe configuration HP 4141B SMU operated by a relay box. Here, we talk about the unique hybrid carbon-based nanomaterials we studied that are employed as CEs in DSSCs. Approximately <1 ml of electrolyte was used.

The power conversion efficiency is the ratio of electrical output to radiation power incident on the solar cell surface (PCE/η). The equation provided as Equation (3) is used to determine it. The fill factor, abbreviated as FF, is a measurement of how ideal or square the J-V characteristics are under light in any solar cell technology. Equation (4), where V_{max} = voltage at maximum power; J_{max} = current at maximum power; and V_{oc} = voltage at the contacts of the circuit when there is no load, analytically calculates the fill factor. It is open circuit circumstances that are used to measure V_{oc}. The J_{sc} = the maximum current through a load under short circuit conditions and where η (%) = light conversion efficiency; Ac = active area of the cell; L = intensity of the incident light (100 $mW.cm^{-2}$). The fill factor can also be extracted directly from the maximum power operating and the product of J_{sc} and V_{oc}, as seen

in Equation (5). P_{max} = maximum power delivered by the DSSC determined from the plot of Power to the applied voltage in the DSSC device.

η (%) = (V_{oc} x J_{sc} x FF) / (A x L) …….. (3)

FF = (V_{max} x J_{max}) / (V_{oc} x J_{sc}) ……..……...…….... (4)

FF = (P_{max}) / (V_{oc} x J_{sc}) ……...……...…….... (5)

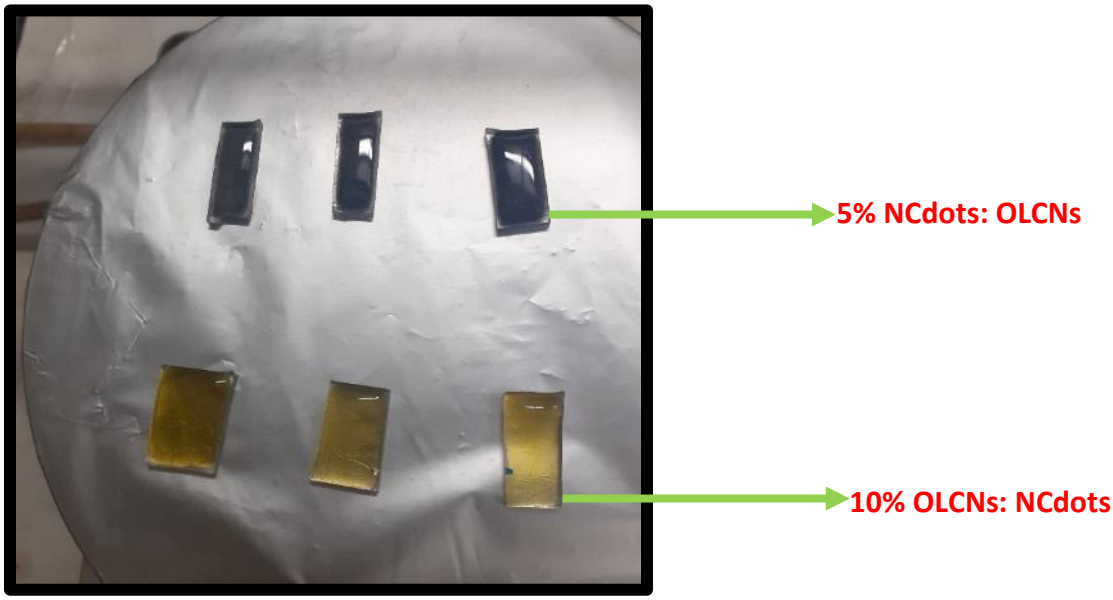

Figure 7.25: Shows various FTO glass substrates being coated on a hot plate.

Resistive effects in solar cells are thought to lower their efficiency by wasting power in internal or series resistance, according to earlier assessments of EIS and the equivalent circuit of DSSCs [85–87]. Internal resistance primarily has two effects: reduced fill factor and photocurrent. The primary variables affecting the internal resistances of the DSSCs are the sheet resistance of the substrates, the charge-transfer processes at the CEs, the electron transfer at the TiO2/dye/electrolyte interface, and the carrier transport by ions inside the electrolyte [85, 86]. The short-circuit current density, open circuit voltage, fill factor, and power conversion efficiency of solar cells (η %) for all counter electrodes used in this work are shown in **Table 6.6**.

Table 7.4: Cell performances of the DSSCs with different nanocomposite electrodes under irradiation of 100 mW/cm^2 simulated AM 1.5.

Name of sample	J_{sc} (A/cm^{-2})	V_{oc} (V)	FF (%)	η (%)	P_{max} (W/cm^{-2})
5% NCdots:p-OLCNs	1.73 x 10^{-5}	0.53	18.43	0.00169	1.69 x 10^{-6}
5% NCdots:ox-OLCNs	9.23 x 10^{-5}	0.02	-	-	2.35 x 10^{-5}
5% NCdots:N-OLCNs	3.37 x 10^{-5}	0.03	-	-	1.40 x 10^{-5}
10% p-OLCNs: NCdots	7.81 x 10^{-5}	0.51	4.07	0.00162	1.62 x 10^{-6}
10% ox-OLCNs: NCdots	6.33 x 10^{-5}	0.55	5.72	0.00199	1.99 x 10^{-6}
10% N-OLCNs: NCdots	7.63 x 10^{-5}	0.8	-	-	-

Figures 7.26 and 7.27 show the J-V curves of the nanocomposites under irradiation and the resulting power-voltage (P-V) curves thereof, respectively. **Figures 7.26 a and b** both have insert graphs which are the enlarged area where the J_{sc} and V_{oc} values could not be clearly visualized. **Table 6.6** summarises the findings. The J-V characteristics show evidence of photovoltaic effect albeit with low performance. The low J_{sc} values are ascribed to the high series resistance of the composite which contributes to losses in electron transfer needed for regeneration of the dye. Additionally, it is evident that the incorporation of NCdots produces long afterglow that reduced or damps the photocurrent making the device photoactive in the dark.

After the simulation experiments, the composites prepared with 10% p-OLCNs: NCdots showed the highest cell efficiency. This DSSC achieved a low light-to-electric conversion efficiency of 0.00199 %, which is significantly lower than that of a Pt electrode (7.78%) recorded in literature under the same conditions [4]. It was expected that the 5% NCdots: p-OLCNs composite would exhibit the highest cell efficiency seeing the good electrode performance characteristics of the film from CV data, however that is not the case.

The reason is that the FF of the DSSC with the 10% p-OLCNs: NCdots electrode is smaller than that of the 5% NCdots: p-OLCNs electrode, even though the 5% NCdots: p-OLCNs showed better performance in terms of both CV and EIS. According to PXRD data, these

observations may be explained by the functionalization of the graphite surface using oxidizing chemicals, which only causes intercalation if there are numerous surface flaws (**Fig. 6.11, Ch. 6**). Therefore, it is possible that a single donor or acceptor material in the composite offers acceptable qualities as a single donor or acceptor, but they are not matched in terms of energy band diagram to complete the energy needs to create enough photo-current to make a workable solar cell [88].

The other composites prepared using higher OLCNs concentration (10% loading) had inadequate photovoltaic parameters. The photoconversion of these devices are very poor and so the performance characteristics as well. Looking at **Fig. 7.27**, the P-V curves of the 10% ox-OLCNs: NCdots show several steps are present which could be due to the material behaving as activated bypass diodes [89]. Hence the P-V curves presented with a "kink" (see arrow in **Fig. 7.27**), of which indicate a mismatch between different areas of the array of module under test. This might result from partial shadowing of the PV array or damage to the PV cells, which would activate materials like bypass diodes. Rapid photo-corrosion of the NCdots: OLCNs composites occurs in the presence of the iodide/triiodide redox electrolyte, leading to low efficiency and brief lifetimes [89].

The charge transfer from CE to oxidized redox species is expected to account for a substantial fill factor and outstanding power conversion efficiency. There is a considerable overpotential for the reduction of oxidized redox species because the poisoning effect's poor charge transfer rate at the Pt CE causes reverse electron transfer at the photoanode [90], reducing the effectiveness of nanocomposites. The degree of the active electrocatalytic materials' adhesion to the FTO when used as a CE is a significant factor in determining the PCE [91]. The sheet resistance of the device layers should be an order of magnitude lower than that of the device's shunt resistance, even though higher values of sheet resistance of the counter electrode in DSSC will contribute to reduction of the FF parameter through either recombination losses or hindered charge transfer, which determines the shape of the current-voltage characteristics and the maximum power output of the device. The counter electrode's resistance has to be as low as feasible to get high FF.

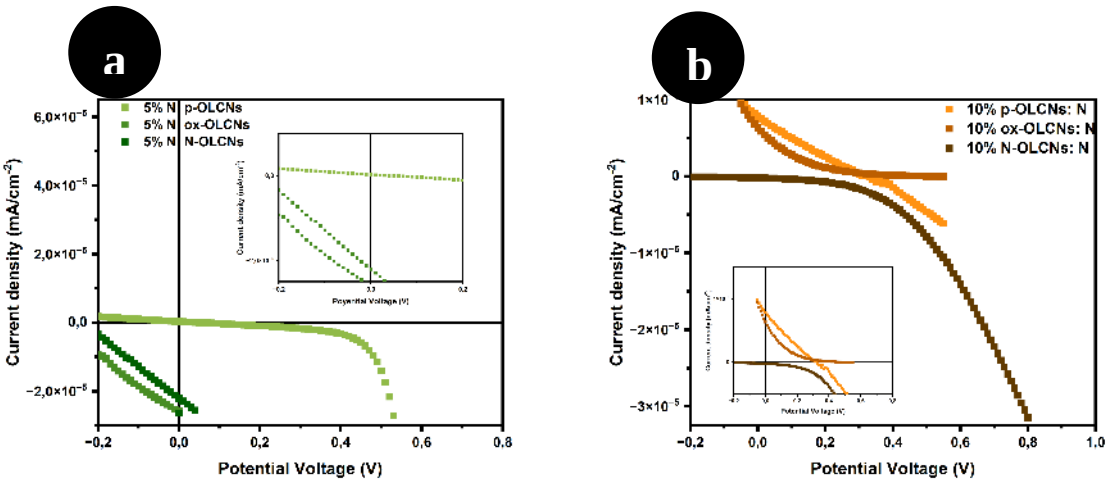

Figure 7.26: Characteristic J–V curves of DSSCs measured under irradiation of 100 mW/cm^2 a) 5% NCdots wt. % loading and b) 10% OLCNs wt. % loading.

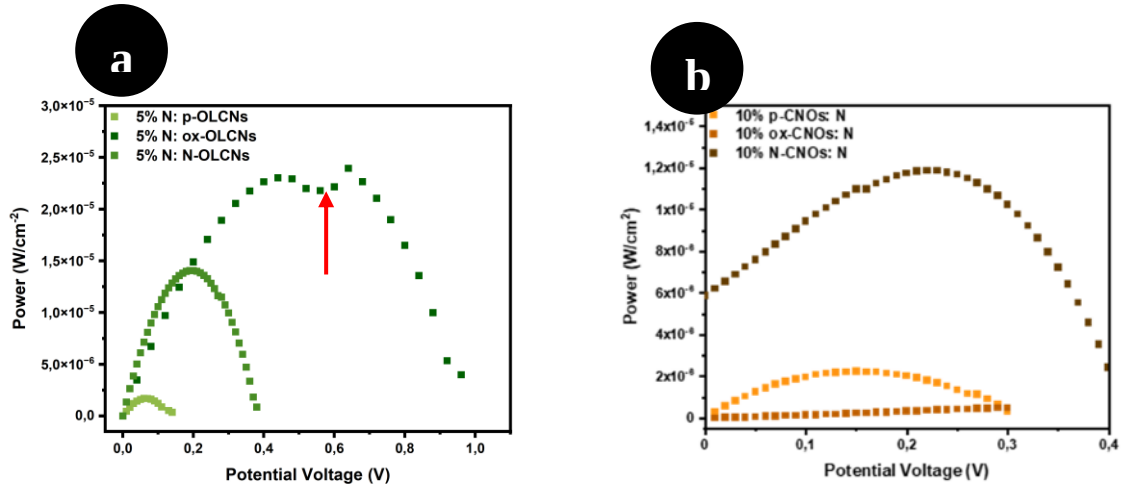

Figure 7.27: Characteristic P–V curves of DSSCs measured under irradiation of 100 mW/cm^2 a) 5% NCdots wt. % loading and b) 10% OLCNs wt. % loading.

Figures 7.28 and 7.29 show the J-V and P-J characteristics of a 25 mm^2 DSSC device under no illumination, respectively. It is evident that J_{sc}, V_{oc} and FF of this device increase with decreasing light intensity. The fact that the device displays a photovoltaic effect in the dark may be due to the long-lasting glow of carbon nanodots in particular, which are directly activated by the solar cell simulator's spectrum radiation. NCdots offer remarkable advantages to be developed as a new class of metal-free afterglow materials because of their high optical capabilities and relative innocuity [92]. In order to encourage intersystem crossover (ISC) and enhance spin-orbit coupling, effective heteroatom doping was used to gradually boost the room temperature phosphorescence emission in bare Cdots [93, 94]. In

addition, Cdots have been given superior room temperature phosphorescence performances by being embedded in a variety of matrices, including polyvinyl alcohol [95-97], potash alum [98], aluminum sulfate [99], zeolites [100, 101], silica gel [102], urea/biuret [103], and polyurethane [104]. These matrices were seen to effectively provide rigidified conditions for fixing emissive species.

This work is very intriguing since it is the first to describe the visible-light-excited afterglow produced by NCdots-carbon composite materials. Thermally triggered delayed fluorescence and phosphorescence were obtained by distributing NCdots in the matrix of pristine and functionalized OLCNs. Although the causes of afterglow emission in Cdots are still not fully understood, mounting evidence suggests that the excitons on the triplet states are the source of the long-lasting emission [105]. According to **Chapter 4**, NCdots have a long lifespan and a high fluorescence quantum yield. According to earlier studies, the C=O/C=N associated functional groups are mostly responsible for the afterglow emission of Cdots because they have high spin-orbit interaction and effectively create triplet excitons [106, 107]. Both of these functional groups were seen on the synthesized NCdots in this investigation (see **Fig. 4.9, Ch.4**).

The fact that the item still shines in the dark after the lighting has been switched off proves that it can still provide electricity. In order to estimate J_{sc} and V_{oc}, we have determined the device's performance characteristics in low light. The device performance characteristics are summarized in **Table 6.7**. The maximum power output could not be used to estimate the fill factor for the dark-operated devices (**Figure 7.29**). These results show that the DSSC device conducts more effectively in the dark than in the illuminated situation, as seen by the low V_{oc} and J_{sc} values in the dark compared to the outcomes achieved under illumination. These NCdots (or mixtures thereof) can therefore be categorized as smart nanomaterials because of their essential sensitivity to light stimuli and their memory properties, which permit their afterglow.

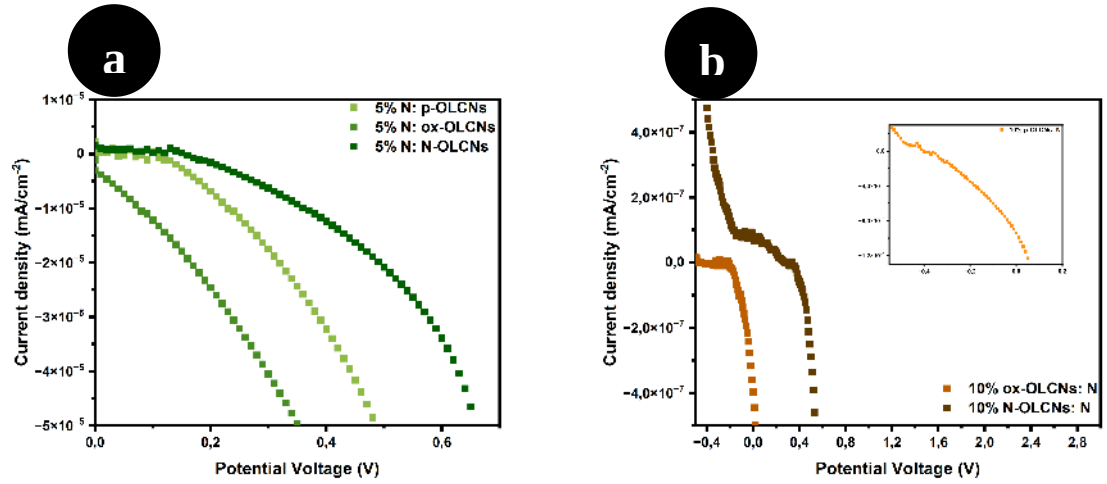

Figure 7.28: Characteristic J–V curves of DSSCs measured under no irradiation of a) 5% NCdots wt. % loading and b) 10% OLCNs wt. % loading.

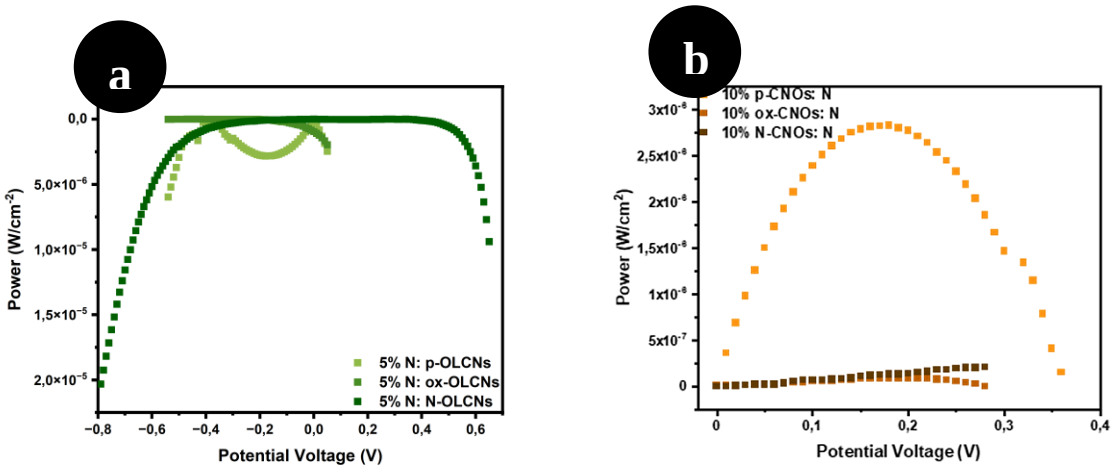

Figure 7.29: Characteristic P–V curves of DSSCs measured under no irradiation of a) 5% NCdots wt. % loading and b) 10% OLCNs wt. % loading.

Table 7.5: Cell performances of the DSSCs with different nanocomposite electrodes in the dark under no irradiation.

Name of sample	J_{sc} (mA/cm^{-2})	V_{oc} (V)	P_{max} (mW/cm^{-2})
5% NCdots:p-OLCNs	1.03 x 10^{-6}	0.48	3.30 x 10^{-9}
5% NCdots:ox-OLCNs	3.04 x 10^{-6}	0.35	2.89 x 10^{-8}
5% NCdots:N-OLCNs	1.02 x 10^{-6}	0.65	-
10% p-OLCNs: NCdots	2.76 x 10^{-6}	0.05	2.83 x 10^{-6}
10% ox-OLCNs: NCdots	4.57 x 10^{-9}	0.02	-
10% N-OLCNs: NCdots	3.06 x 10^{-8}	0.53	-

Dark characteristics for a 25 mm^2 device composed of 10% p-OLCNs: NCdots were investigated in order to better investigate and research this afterglow effect. In the absence of light, the device's asymmetric behavior is visible. It is clear that the instrument conducts with a forward bias. In order to conduct this experiment, the device was first illuminated, as has been done before, and its conductivity was then determined. The cell was then kept in complete darkness for the following five minutes, with no exposure to light. After the allotted time had passed, measurements were made in the dark. Thus, it is evident that these NCdots have a strong memory impact and a consistent afterglow. The J_{sc} and V_{oc} of this cell were determined to be 3.31 x 10^{-5} A/cm^2 and 60 V, respectively. These values are somewhat similar to the values obtained in the dark before the 5 minutes rest time. Thus, this tells us that even after the cells have been kept away from a light source for 5 minutes still produces comparable afterglow efficiency.

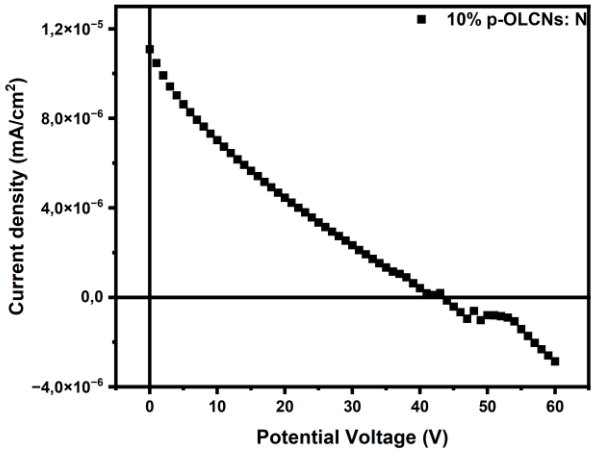

Figure 7.30: Characteristic J–V curves of DSSCs measured under no irradiation of a 10% OLCNs wt. % loading composite after 5 minutes.

Mie scattering [108] brought on by the inclusion of NCdots has been proven to be particularly efficient at increasing light harvesting. However, in terms of solar cell technology, silicon and compound semiconductor-based devices predominate [109]. It is vital to boost the carbon counter electrode's catalytic activity and lateral conductivity since it is employed for both the redox of the electrolyte and the conduction of charge inside the liquid monolithic DSSC. Further, achieving long-term stability requires a quick sensitizer recovery. Also crucial to the performance of solar cells is long-lasting charge separation.

Dark current in DSSC may also result from the injected electron's loss to I_3 from a nanostructured wide bandgap semiconductor, such as TiO_2 (the hole carrier in solution electrolyte). Therefore, in solar cells, this reverse reaction must be prevented or minimized. A drop in dark current results in an increase in the solar cell's open circuit voltage, according to the fundamental equation of a solar cell that links the two variables.

7.5 Conclusion

The all-carbon materials, or DSSCs, that make up NCdots: OLCNs CE nanocomposites all showed very low PCEs of less than 1%, which is far lower than Pt CE reported in the literature. The NCdots network topology provides multidirectional channels to aid electron transport in the NCdots: OLCNs nano composite. In contrast to the functionalized ox- and N-OLCNs, which were thought to be involved in the recombination effects seen in the composites of these materials, it was shown that NCdots had superior surface contact with p-

OLCNs. The afterglow effect seen in these cells, which makes the DSSCs act like diodes, may also be to blame for the reduced PCE. The extremely fluorescent NCdots that were seen to have a lengthy, persistent decay during lifespan investigations are what cause this afterglow. However, because of their superior and reliable memory effect, which produces this afterglow, these composites are deemed smart materials by virtue of this property. The evident rise in R_{ct} suggests that the catalytic activity has decreased as the ratio of graphite has increased.

\

References

1. Qiu, X., & Burda, C. (2007). Chemically synthesized nitrogen-doped metal oxide nanoparticles. *Chemical Physics*, *339*(1–3), 1–10. https://doi.org/10.1016/j.chemphys.2007.06.039.

2. Ranabhat, K., Patrikeev, L., Antal'evna-Revina, A., Andrianov, K., Lapshinsky, V., & Sofronova, E. (2016). An introduction to solar cell technology. *Istrazivanja i Projektovanja Za Privredu*, *14*(4), 481–491. https://doi.org/10.5937/jaes14-10879

3. Wöhrle, D. and Meissner, D., 1991. Organic Solar Cells. Advanced Materials, 3(3), pp.129-138.

4. Yue, G., Wu, J., Xiao, Y., Lin, J., & Huang, M. (2012). Low cost poly(3,4 ethylenedioxythiophene):polystyrenesulfonate/carbon black counter electrode for dye-sensitized solar cells. *Electrochimica Acta*, *67*, 113–118. https://doi.org/10.1016/j.electacta.2012.02.009

5. Gong, J., Liang, J., & Sumathy, K. (2012). Review on dye-sensitized solar cells (DSSCs): Fundamental concepts and novel materials. *Renewable and Sustainable Energy Reviews*, *16*(8), 5848–5860. https://doi.org/10.1016/j.rser.2012.04.044

6. O'Regan, B., & Grätzel, M. (1991). A low-cost, high-efficiency solar cell based on dye-sensitized colloidal TiO2 films. *Nature*, *353*(6346), 737–740. https://doi.org/10.1038/353737a0

7. Garnovskii, A. D., & Garnovskii, D. A. (2006). New edition of "Comprehensive Coordination Chemistry II", McCleverty, J.A. and Meyer, T.J., eds., Amsterdam-Oxford-New York-San Diego: Elsevier-Pergamon, 2003, 10 vols., 8419 pp. *Russian Journal of Coordination Chemistry*, *32*(8), 614–615. https://doi.org/10.1134/s1070328406080148

8. Mishra, A. (2004). Special Issue: Scalability Issues in Wireless Networks—Architectures, Protocols and Services. *Wireless Communications and Mobile Computing*, *4*(3), 247–249. https://doi.org/10.1002/wcm.220

9. Grätzel, M. (2003). Dye-sensitized solar cells. *Journal of Photochemistry and Photobiology C: Photochemistry Reviews*, *4*(2), 145–153. https://doi.org/10.1016/s1389-5567(03)00026-1
10. Wei, D. (2010). Dye Sensitized Solar Cells. *International Journal of Molecular Sciences*, *11*(3), 1103–1113. https://doi.org/10.3390/ijms11031103
11. Liu, G., Wang, H., Li, X., Rong, Y., Ku, Z., Xu, M., Liu, L., Hu, M., Yang, Y., Xiang, P., Shu, T., & Han, H. (2012). A mesoscopic platinized graphite/carbon black counter electrode for a highly efficient monolithic dye-sensitized solar cell. *Electrochimica Acta*, *69*, 334–339. https://doi.org/10.1016/j.electacta.2012.03.012
12. Papageorgiou, N. (2004). Counter-electrode function in nanocrystalline photoelectrochemical cell configurations. *Coordination Chemistry Reviews*, *248*(13–14), 1421–1446. https://doi.org/10.1016/j.ccr.2004.03.028
13. Chen, J., Li, K., Luo, Y., Guo, X., Li, D., Deng, M., Huang, S., & Meng, Q. (2009). A flexible carbon counter electrode for dye-sensitized solar cells. *Carbon*, *47*(11), 2704–2708. https://doi.org/10.1016/j.carbon.2009.05.028
14. Kay, A., & Grätzel, M. (1996). Low cost photovoltaic modules based on dye sensitized nanocrystalline titanium dioxide and carbon powder. *Solar Energy Materials and Solar Cells*, *44*(1), 99–117. https://doi.org/10.1016/0927-0248(96)00063-3
15. Murakami, T. N., Ito, S., Wang, Q., Nazeeruddin, M. K., Bessho, T., Cesar, I., Liska, P., Humphry-Baker, R., Comte, P., PéChy, P., & GräTzel, M. (2006). Highly Efficient Dye-Sensitized Solar Cells Based on Carbon Black Counter Electrodes. *Journal of The Electrochemical Society*, *153*(12), A2255. https://doi.org/10.1149/1.2358087
16. Imoto, K., Takahashi, K., Yamaguchi, T., Komura, T., Nakamura, J. I., & Murata, K. (2003). High-performance carbon counter electrode for dye-sensitized solar cells. *Solar*

Energy Materials and Solar Cells, *79*(4), 459–469. https://doi.org/10.1016/s0927-0248(03)00021-7

17. Huang, Z., Liu, X., Li, K., Li, D., Luo, Y., Li, H., Song, W., Chen, L., & Meng, Q. (2007). Application of carbon materials as counter electrodes of dye-sensitized solar cells. *Electrochemistry Communications*, *9*(4), 596–598. https://doi.org/10.1016/j.elecom.2006.10.028
18. Li, K., Lou, Y., Li, D., & Meng, Q. (2007). Recent Progress of Counter Electrodes in Nanocrystalline Dye-sensitized Solar Cells. *J Mater Sci Technol*, *23*(05), 577–582. https://www.jmst.org/EN/Y2007/V23/I05/577
19. Suzuki, K., Yamaguchi, M., Kumagai, M., & Yanagida, S. (2003). Application of Carbon Nanotubes to Counter Electrodes of Dye-sensitized Solar Cells. *Chemistry Letters*, *32*(1), 28–29. https://doi.org/10.1246/cl.2003.28
20. Trancik, J. E., Barton, S. C., & Hone, J. (2008). Transparent and Catalytic Carbon Nanotube Films. *Nano Letters*, *8*(4), 982–987. https://doi.org/10.1021/nl071945i
21. Hino, T., Ogawa, Y., & Kuramoto, N. (2006). Preparation of functionalized and non-functionalized fullerene thin films on ITO glasses and the application to a counter electrode in a dye-sensitized solar cell. *Carbon*, *44*(5), 880–887. https://doi.org/10.1016/j.carbon.2005.10.027
22. Hong, W., Xu, Y., Lu, G., Li, C., & Shi, G. (2008). Transparent graphene/PEDOT–PSS composite films as counter electrodes of dye-sensitized solar cells. *Electrochemistry Communications*, *10*(10), 1555–1558. https://doi.org/10.1016/j.elecom.2008.08.007
23. Wang, W., Liu, Y., Zhong, Y. J., Wang, L., Zhou, W., Wang, S., Tadé, M. O., & Shao, Z. (2017). Rational Design of $LaNiO_3$ /Carbon Composites as Outstanding Platinum-Free Photocathodes in Dye-Sensitized Solar Cells With Enhanced Catalysis for the Triiodide Reduction Reaction. *Solar RRL*, *1*(7), 1700074. https://doi.org/10.1002/solr.201700074

24. Pang, B., Zhang, M., Zhou, C., Dong, H., Ma, S., Shi, Y., Sun, Q., Li, F., Yu, L., & Dong, L. (2020). Nitrogen-Doped Carbon Nano-Onions Decorated on Graphene Network: A Novel All-Carbon Composite Counter Electrode for Dye-Sensitized Solar Cell with a 10.28% Power Conversion Efficiency. *Solar RRL*, *4*(9), 2000263. https://doi.org/10.1002/solr.202000263

25. Zhao, Y., Yang, L., Chen, S., Wang, X., Ma, Y., Wu, Q., Jiang, Y., Qian, W., & Hu, Z. (2013). Can Boron and Nitrogen Co-doping Improve Oxygen Reduction Reaction Activity of Carbon Nanotubes? *Journal of the American Chemical Society*, *135*(4), 1201–1204. https://doi.org/10.1021/ja310566z

26. Fei, H., Ye, R., Ye, G., Gong, Y., Peng, Z., Fan, X., Samuel, E. L. G., Ajayan, P. M., & Tour, J. M. (2014). Boron- and Nitrogen-Doped Graphene Quantum Dots/Graphene Hybrid Nanoplatelets as Efficient Electrocatalysts for Oxygen Reduction. *ACS Nano*, *8*(10), 10837–10843. https://doi.org/10.1021/nn504637y

27. Yu, D., Nagelli, E., Du, F., & Dai, L. (2010). Metal-Free Carbon Nanomaterials Become More Active than Metal Catalysts and Last Longer. *The Journal of Physical Chemistry Letters*, *1*(14), 2165–2173. https://doi.org/10.1021/jz100533t

28. Huang, J., Qian, X., Yang, J., Niu, Y., Xu, C., & Hou, L. (2020). Construction of Pt-free electrocatalysts based on hierarchical CoS2/N-doped C@Co-WS2 yolk-shell nano-polyhedrons for dye-sensitized solar cells. *Electrochimica Acta*, *340*, 135949. https://doi.org/10.1016/j.electacta.2020.135949.

29. Xue, Y., Liu, J., Chen, H., Wang, R., Li, D., Qu, J., & Dai, L. (2012). Nitrogen-Doped Graphene Foams as Metal-Free Counter Electrodes in High-Performance Dye-Sensitized Solar Cells. *Angewandte Chemie International Edition*, *51*(48), 12124–12127. https://doi.org/10.1002/anie.201207277

30. Chen, M., Shao, L. L., Lv, X. W., Wang, G. C., Yang, W. Q., Yuan, Z. Y., Qian, X., Han, Y. Y., & Ding, A. X. (2020). In situ growth of Ni-encapsulated and N-doped carbon nanotubes on N-doped ordered mesoporous carbon for high-efficiency triiodide reduction in dye-sensitized solar cells. *Chemical Engineering Journal*, *390*, 124633. https://doi.org/10.1016/j.cej.2020.124633
31. Meng, X., Yu, C., Zhang, X., Huang, L., Rager, M., Hong, J., Qiu, J., & Lin, Z. (2018). Active sites-enriched carbon matrix enables efficient triiodide reduction in dye-sensitized solar cells: An understanding of the active centers. *Nano Energy*, *54*, 138–147. https://doi.org/10.1016/j.nanoen.2018.09.070
32. Yu, F., Shi, Y., Yao, W., Han, S., & Ma, J. (2019). A new breakthrough for graphene/carbon nanotubes as counter electrodes of dye-sensitized solar cells with up to a 10.69% power conversion efficiency. *Journal of Power Sources*, *412*, 366–373. https://doi.org/10.1016/j.jpowsour.2018.11.066
33. Kim, C. K., Zhou, H., Kowalewski, T., Matyjaszewski, K., & Kim, H. K. (2018). Soft-Templated Tellurium-Doped Mesoporous Carbon as a Pt-Free Electrocatalyst for High-Performance Dye-Sensitized Solar Cells. *ACS Applied Materials & Interfaces*, *11*(2), 2093–2102. https://doi.org/10.1021/acsami.8b19223
34. Butsyk, O., Olejnik, P., Romero, E., & Plonska-Brzezinska, M. E. (2019). Postsynthetic treatment of carbon nano-onions: Surface modification by heteroatoms to enhance their capacitive and electrocatalytic properties. *Carbon*, *147*, 90–104. https://doi.org/10.1016/j.carbon.2019.02.063
35. Zuaznabar-Gardona, J. C., & Fragoso, A. (2020). Band structure, work function and interfacial diagrams of oxygen-functionalized carbon nano-onions. *Synthetic Metals*, *266*, 116434. https://doi.org/10.1016/j.synthmet.2020.116434

36. Han, Y., Huang, H., Zhang, H., Liu, Y., Han, X., Liu, R., Li, H., & Kang, Z. (2014). Carbon Quantum Dots with Photoenhanced Hydrogen-Bond Catalytic Activity in Aldol Condensations. *ACS Catalysis*, *4*(3), 781–787. https://doi.org/10.1021/cs401118x

37. Liu, Z. X., Chen, B. B., Liu, M. L., Zou, H. Y., & Huang, C. Z. (2017). Cu(i)-Doped carbon quantum dots with zigzag edge structures for highly efficient catalysis of azide–alkyne cycloadditions. *Green Chemistry*, *19*(6), 1494–1498. https://doi.org/10.1039/c6gc03288e

38. Liu, H., Li, R. S., Zhou, J., & Huang, C. Z. (2017). Branched polyethylenimine-functionalized carbon dots as sensitive and selective fluorescent probes for N-acetylcysteine via an off–on mechanism. *The Analyst*, *142*(22), 4221–4227. https://doi.org/10.1039/c7an01136a

39. Wang, J., Sheng Li, R., Zhi Zhang, H., Wang, N., Zhang, Z., & Huang, C. Z. (2017). Highly fluorescent carbon dots as selective and visual probes for sensing copper ions in living cells via an electron transfer process. *Biosensors and Bioelectronics*, *97*, 157–163. https://doi.org/10.1016/j.bios.2017.05.035

40. Liu, Z., Zou, H., Wang, N., Yang, T., Peng, Z., Wang, J., Li, N., & Huang, C. (2018). Photoluminescence of carbon quantum dots: coarsely adjusted by quantum confinement effects and finely by surface trap states. *Science China Chemistry*, *61*(4), 490–496. https://doi.org/10.1007/s11426-017-9172-0

41. Wang, A., Xiao, X., Zhou, C., Lyu, F., Fu, L., Wang, C., & Ruan, S. (2019). Large-scale synthesis of carbon dots/TiO_2 nanocomposites for the photocatalytic color switching system. *Nanoscale Advances*, *1*(5), 1819–1825. https://doi.org/10.1039/c9na00054b

42. Zhang, J., Wu, S., Lu, X., Wu, P., & Liu, J. (2019). Lanthanide-Boosted Singlet Oxygen from Diverse Photosensitizers along with Potent Photocatalytic Oxidation. *ACS Nano*, *13*(12), 14152–14161. https://doi.org/10.1021/acsnano.9b06840

43. Lai, S., Jin, Y., Shi, L., Zhou, R., Zhou, Y., & An, D. (2020). Mechanisms behind excitation- and concentration-dependent multicolor photoluminescence in graphene quantum dots. *Nanoscale*, *12*(2), 591–601. https://doi.org/10.1039/c9nr08461d

44. Liu, R., Huang, H., Li, H., Liu, Y., Zhong, J., Li, Y., Zhang, S., & Kang, Z. (2013). Metal Nanoparticle/Carbon Quantum Dot Composite as a Photocatalyst for High-Efficiency Cyclohexane Oxidation. *ACS Catalysis*, *4*(1), 328–336. https://doi.org/10.1021/cs400913h

45. Yue, G., Wu, J., Xiao, Y., Lin, J., Huang, M., Fan, L., & Yao, Y. (2013). A dye-sensitized solar cell based on PEDOT:PSS counter electrode. *Chinese Science Bulletin*, *58*(4–5), 559–566. https://doi.org/10.1007/s11434-012-5352-3

46. Bogdan, M., Brugger, D., Rosenstiel, W., & Speiser, B. (2014). Estimation of diffusion coefficients from voltammetric signals by support vector and gaussian process regression. *Journal of Cheminformatics*, *6*(1). https://doi.org/10.1186/1758-2946-6-30

47. Liu, S., Yang, B., Zhou, J., & Song, H. (2019). Nitrogen-rich carbon-onion-constructed nanosheets: an ultrafast and ultrastable dual anode material for sodium and potassium storage. *Journal of Materials Chemistry A*, *7*(31), 18499–18509. https://doi.org/10.1039/c9ta04699b

48. Gu, D., Bongard, H., Deng, Y., Feng, D., Wu, Z., Fang, Y., Mao, J., Tu, B., Schüth, F., & Zhao, D. (2010). An Aqueous Emulsion Route to Synthesize Mesoporous Carbon Vesicles and Their Nanocomposites. *Advanced Materials*, *22*(7), 833–837. https://doi.org/10.1002/adma.200902550

49. Pech, D., Brunet, M., Durou, H., Huang, P., Mochalin, V., Gogotsi, Y., Taberna, P. L., & Simon, P. (2010). Ultrahigh-power micrometre-sized supercapacitors based on onion-like carbon. *Nature Nanotechnology*, *5*(9), 651–654. https://doi.org/10.1038/nnano.2010.162

50. Wu, G., Dai, C., Wang, D., Li, D., & Li, N. (2010). Nitrogen-doped magnetic onion-like carbon as support for Pt particles in a hybrid cathode catalyst for fuel cells. *Journal of Materials Chemistry*, *20*(15), 3059. https://doi.org/10.1039/b924010a

51. Choi, W., Shin, H. C., Kim, J. M., Choi, J. Y., & Yoon, W. S. (2020). Modeling and Applications of Electrochemical Impedance Spectroscopy (EIS) for Lithium-ion Batteries. *Journal of Electrochemical Science and Technology*, *11*(1), 1–13. https://doi.org/10.33961/jecst.2019.00528

52. Seeber, R., Zanardi, C., & Inzelt, G. (2015). Links between electrochemical thermodynamics and kinetics. *ChemTexts*, *1*(4). https://doi.org/10.1007/s40828-015-0018-9

53. Elgrishi, N., Rountree, K. J., McCarthy, B. D., Rountree, E. S., Eisenhart, T. T., & Dempsey, J. L. (2017). A Practical Beginner's Guide to Cyclic Voltammetry. *Journal of Chemical Education*, *95*(2), 197–206. https://doi.org/10.1021/acs.jchemed.7b00361

54. Mabbott, G. A. (1983). An introduction to cyclic voltammetry. *Journal of Chemical Education*, *60*(9), 697. https://doi.org/10.1021/ed060p697

55. Bard, A. J. (2002). Electrochemistry in Nonaqueous Solutions By Kosuke Izutsu (Matsumoto, Japan). Wiley-VCH: Weinheim. 2002. xiv + 346 pp. $110.00. ISBN 3–527-30516-5. *Journal of the American Chemical Society*, *124*(50), 15142–15143. https://doi.org/10.1021/ja025265n

56. Kissinger, P. T., & Heineman, W. R. (1983). Cyclic voltammetry. *Journal of Chemical Education*, *60*(9), 702. https://doi.org/10.1021/ed060p702

57. Liu, G., Wang, H., Li, X., Rong, Y., Ku, Z., Xu, M., Liu, L., Hu, M., Yang, Y., Xiang, P., Shu, T., & Han, H. (2012b). A mesoscopic platinized graphite/carbon black counter electrode for a highly efficient monolithic dye-sensitized solar cell. *Electrochimica Acta*, *69*, 334–339. https://doi.org/10.1016/j.electacta.2012.03.012

58. Popov, A. I., & Geske, D. H. (1958). Studies on the Chemistry of Halogen and of Polyhalides. XIII. Voltammetry of Iodine Species in Acetonitrile. *Journal of the American Chemical Society*, *80*(6), 1340–1352. https://doi.org/10.1021/ja01539a018

59. Elgrishi, N., Rountree, K. J., McCarthy, B. D., Rountree, E. S., Eisenhart, T. T., & Dempsey, J. L. (2017b). A Practical Beginner's Guide to Cyclic Voltammetry. *Journal of Chemical Education*, *95*(2), 197–206. https://doi.org/10.1021/acs.jchemed.7b00361

60. Imoto, K., Takahashi, K., Yamaguchi, T., Komura, T., Nakamura, J. I., & Murata, K. (2003b). High-performance carbon counter electrode for dye-sensitized solar cells. *Solar Energy Materials and Solar Cells*, *79*(4), 459–469. https://doi.org/10.1016/s0927-0248(03)00021-7

61. Wu, J., Li, Q., Fan, L., Lan, Z., Li, P., Lin, J., & Hao, S. (2008). High-performance polypyrrole nanoparticles counter electrode for dye-sensitized solar cells. *Journal of Power Sources*, *181*(1), 172–176. https://doi.org/10.1016/j.jpowsour.2008.03.029

62. Pringle, J. M., Armel, V., & MacFarlane, D. R. (2010). Electrodeposited PEDOT-on-plastic cathodes for dye-sensitized solar cells. *Chemical Communications*, *46*(29), 5367. https://doi.org/10.1039/c0cc01400a

63. Mei, X., Cho, S. J., Fan, B., & Ouyang, J. (2010). High-performance dye-sensitized solar cells with gel-coated binder-free carbon nanotube films as counter electrode. *Nanotechnology*, *21*(39), 395202. https://doi.org/10.1088/0957-4484/21/39/395202

64. Wu, J., Li, Q., Fan, L., Lan, Z., Li, P., Lin, J., & Hao, S. (2008). High-performance polypyrrole nanoparticles counter electrode for dye-sensitized solar cells. *Journal of Power Sources*, *181*(1), 172–176. https://doi.org/10.1016/j.jpowsour.2008.03.029

65. Pringle, J. M., Armel, V., & MacFarlane, D. R. (2010b). Electrodeposited PEDOT-on-plastic cathodes for dye-sensitized solar cells. *Chemical Communications*, *46*(29), 5367. https://doi.org/10.1039/c0cc01400a

66. Muto, T., Ikegami, M., Kobayashi, K., & Miyasaka, T. (2007). Conductive Polymer-based Mesoscopic Counterelectrodes for Plastic Dye-sensitized Solar Cells. *Chemistry Letters*, *36*(6), 804–805. https://doi.org/10.1246/cl.2007.804

67. Wang, Y., Guo, Y., Chen, W., Luo, Q., Lu, W., Xu, P., Chen, D., Yin, X., & He, M. (2018). Sulfur-doped reduced graphene oxide/MoS2 composite with exposed active sites as efficient Pt-free counter electrode for dye-sensitized solar cell. *Applied Surface Science*, *452*, 232–238. https://doi.org/10.1016/j.apsusc.2018.04.276

68. Miao, X., Pan, K., Wang, G., Liao, Y., Wang, L., Zhou, W., Jiang, B., Pan, Q., & Tian, G. (2013). Well-Dispersed CoS Nanoparticles on a Functionalized Graphene Nanosheet Surface: A Counter Electrode of Dye-Sensitized Solar Cells. *Chemistry - A European Journal*, *20*(2), 474–482. https://doi.org/10.1002/chem.201303558

69. Batmunkh, M., Shrestha, A., Bat-Erdene, M., Nine, M. J., Shearer, C. J., Gibson, C. T., Slattery, A. D., Tawfik, S. A., Ford, M. J., Dai, S., Qiao, S., & Shapter, J. G. (2018). Electrocatalytic Activity of a 2D Phosphorene-Based Heteroelectrocatalyst for Photoelectrochemical Cells. *Angewandte Chemie International Edition*, *57*(10), 2644–2647. https://doi.org/10.1002/anie.201712280

70. Rountree, E. S., McCarthy, B. D., Eisenhart, T. T., & Dempsey, J. L. (2014). Evaluation of Homogeneous Electrocatalysts by Cyclic Voltammetry. *Inorganic Chemistry*, *53*(19), 9983–10002. https://doi.org/10.1021/ic500658x

71. Li, X., Rui, M., Song, J., Shen, Z., & Zeng, H. (2015). Carbon and Graphene Quantum Dots for Optoelectronic and Energy Devices: A Review. *Advanced Functional Materials*, *25*(31), 4929–4947. https://doi.org/10.1002/adfm.201501250

72. Ahmad, I., McCarthy, J. E., Bari, M., & Gun'ko, Y. K. (2014). Carbon nanomaterial based counter electrodes for dye sensitized solar cells. *Solar Energy*, *102*, 152–161. https://doi.org/10.1016/j.solener.2014.01.012

73. Chen, J., Li, K., Luo, Y., Guo, X., Li, D., Deng, M., Huang, S., & Meng, Q. (2009b). A flexible carbon counter electrode for dye-sensitized solar cells. *Carbon*, *47*(11), 2704–2708. https://doi.org/10.1016/j.carbon.2009.05.028

74. Brown, P., Takechi, K., & Kamat, P. V. (2008). Single-Walled Carbon Nanotube Scaffolds for Dye-Sensitized Solar Cells. *The Journal of Physical Chemistry C*, *112*(12), 4776–4782. https://doi.org/10.1021/jp7107472

75. Wang, Q., Moser, J. E., & Grätzel, M. (2005). Electrochemical Impedance Spectroscopic Analysis of Dye-Sensitized Solar Cells. *The Journal of Physical Chemistry B*, *109*(31), 14945–14953. https://doi.org/10.1021/jp052768h

76. Wang, Q., Ito, S., Grätzel, M., Fabregat-Santiago, F., Mora-Seró, I., Bisquert, J., Bessho, T., & Imai, H. (2006). Characteristics of High Efficiency Dye-Sensitized Solar Cells. *The Journal of Physical Chemistry B*, *110*(50), 25210–25221. https://doi.org/10.1021/jp064256o

77. Mei, B. A., Lau, J., Lin, T., Tolbert, S. H., Dunn, B. S., & Pilon, L. (2018). Physical Interpretations of Electrochemical Impedance Spectroscopy of Redox Active Electrodes for Electrical Energy Storage. *The Journal of Physical Chemistry C*, *122*(43), 24499–24511. https://doi.org/10.1021/acs.jpcc.8b05241

78. Hauch, A., & Georg, A. (2001). Diffusion in the electrolyte and charge-transfer reaction at the platinum electrode in dye-sensitized solar cells. *Electrochimica Acta*, *46*(22), 3457–3466. https://doi.org/10.1016/s0013-4686(01)00540-0

79. Papageorgiou, N., Maier, W. F., & Grätzel, M. (1997). An Iodine/Triiodide Reduction Electrocatalyst for Aqueous and Organic Media. *Journal of The Electrochemical Society*, *144*(3), 876–884. https://doi.org/10.1149/1.1837502

80. Hauch, A., & Georg, A. (2001b). Diffusion in the electrolyte and charge-transfer reaction at the platinum electrode in dye-sensitized solar cells. *Electrochimica Acta*, *46*(22), 3457–3466. https://doi.org/10.1016/s0013-4686(01)00540-0

81. Nogueira, A., Longo, C., & de Paoli, M. A. (2004). Polymers in dye sensitized solar cells: overview and perspectives. *Coordination Chemistry Reviews*, *248*(13–14), 1455–1468. https://doi.org/10.1016/j.ccr.2004.05.018

82. Longo, C., & de Paoli, M. A. (2003). Dye-sensitized solar cells: a successful combination of materials. *Journal of the Brazilian Chemical Society*, *14*(6). https://doi.org/10.1590/s0103-50532003000600005

83. Essner, J. B., & Baker, G. A. (2017). The emerging roles of carbon dots in solar photovoltaics: a critical review. *Environmental Science: Nano*, *4*(6), 1216–1263. https://doi.org/10.1039/c7en00179g

84. Anantharaj, S., Noda, S., Driess, M., & Menezes, P. W. (2021). The Pitfalls of Using Potentiodynamic Polarization Curves for Tafel Analysis in Electrocatalytic Water Splitting. *ACS Energy Letters*, 1607–1611. https://doi.org/10.1021/acsenergylett.1c00608

85. Murer, N., Diard, J. P., & Petrescu, B. (2020). The effects of time-variance on impedance measurements: examples of a corroding electrode and a battery cell. *Journal of Electrochemical Science and Engineering*, *10*(2), 127–140. https://doi.org/10.5599/jese.725

86. Han, L., Koide, N., Chiba, Y., Islam, A., Komiya, R., Fuke, N., Fukui, A., & Yamanaka, R. (2005). Improvement of efficiency of dye-sensitized solar cells by reduction of internal resistance. *Applied Physics Letters*, *86*(21), 213501. https://doi.org/10.1063/1.1925773

87. Koide, N., Islam, A., Chiba, Y., & Han, L. (2006). Improvement of efficiency of dye-sensitized solar cells based on analysis of equivalent circuit. *Journal of Photochemistry*

and Photobiology A: Chemistry, *182*(3), 296–305. https://doi.org/10.1016/j.jphotochem.2006.04.030

88. Kietzke, T. (2007). Recent Advances in Organic Solar Cells. *Advances in OptoElectronics*, *2007*, 1–15. https://doi.org/10.1155/2007/40285
89. Silvestre, S., Boronat, A., & Chouder, A. (2009). Study of bypass diodes configuration on PV modules. *Applied Energy*, *86*(9), 1632–1640. https://doi.org/10.1016/j.apenergy.2009.01.020
90. Wang, Q., Moser, J. E., & Grätzel, M. (2005). Electrochemical Impedance Spectroscopic Analysis of Dye-Sensitized Solar Cells. *The Journal of Physical Chemistry B*, *109*(31), 14945–14953. https://doi.org/10.1021/jp052768h
91. Lee, Y. L., & Chang, C. H. (2008). Efficient polysulfide electrolyte for CdS quantum dot-sensitized solar cells. *Journal of Power Sources*, *185*(1), 584–588. https://doi.org/10.1016/j.jpowsour.2008.07.014
92. Radich, E. J., Dwyer, R., & Kamat, P. V. (2011). Cu_2S Reduced Graphene Oxide Composite for High-Efficiency Quantum Dot Solar Cells. Overcoming the Redox Limitations of S_2^-/S_n^{2-} at the Counter Electrode. *The Journal of Physical Chemistry Letters*, *2*(19), 2453–2460. https://doi.org/10.1021/jz201064k
93. Hauch, A., & Georg, A. (2001). Diffusion in the electrolyte and charge-transfer reaction at the platinum electrode in dye-sensitized solar cells. *Electrochimica Acta*, *46*(22), 3457–3466. https://doi.org/10.1016/s0013-4686(01)00540-0
94. Xu, Z., Sun, X., Ma, P., Chen, Y., Pan, W., & Wang, J. (2020). A visible-light-excited afterglow achieved by carbon dots from rhodamine B fixed in boron oxide. *Journal of Materials Chemistry C*, *8*(13), 4557–4563. https://doi.org/10.1039/c9tc05992j
95. Long, P., Feng, Y., Cao, C., Li, Y., Han, J., Li, S., Peng, C., Li, Z., & Feng, W. (2018). Self-Protective Room-Temperature Phosphorescence of Fluorine and Nitrogen Codoped

Carbon Dots. *Advanced Functional Materials*, *28*(37), 1800791. https://doi.org/10.1002/adfm.201800791

96. Li, H., Ye, S., Guo, J. Q., Kong, J. T., Song, J., Kang, Z. H., & Qu, J. L. (2019). The design of room-temperature-phosphorescent carbon dots and their application as a security ink. *Journal of Materials Chemistry C*, *7*(34), 10605–10612. https://doi.org/10.1039/c9tc03481a
97. Jiang, K., Wang, Y., Cai, C., & Lin, H. (2017). Activating Room Temperature Long Afterglow of Carbon Dots via Covalent Fixation. *Chemistry of Materials*, *29*(11), 4866–4873. https://doi.org/10.1021/acs.chemmater.7b00831
98. He, J., He, Y., Chen, Y., Zhang, X., Hu, C., Zhuang, J., Lei, B., & Liu, Y. (2018). Construction and multifunctional applications of carbon dots/PVA nanofibers with phosphorescence and thermally activated delayed fluorescence. *Chemical Engineering Journal*, *347*, 505–513. https://doi.org/10.1016/j.cej.2018.04.110
99. Tian, Z., Li, D., Ushakova, E. V., Maslov, V. G., Zhou, D., Jing, P., Shen, D., Qu, S., & Rogach, A. L. (2018). Multilevel Data Encryption Using Thermal-Treatment Controlled Room Temperature Phosphorescence of Carbon Dot/Polyvinylalcohol Composites. *Advanced Science*, *5*(9), 1800795. https://doi.org/10.1002/advs.201800795
100. Dong, X., Wei, L., Su, Y., Li, Z., Geng, H., Yang, C., & Zhang, Y. (2015). Efficient long lifetime room temperature phosphorescence of carbon dots in a potash alum matrix. *Journal of Materials Chemistry C*, *3*(12), 2798–2801. https://doi.org/10.1039/c5tc00126a
101. Joseph, J., & Anappara, A. A. (2017). Long Life-time Room-temperature Phosphorescence of Carbon Dots in Aluminum Sulfate. *ChemistrySelect*, *2*(14), 4058–4062. https://doi.org/10.1002/slct.201700786
102. Wang, B., Mu, Y., Zhang, H., Shi, H., Chen, G., Yu, Y., Yang, Z., Li, J., & Yu, J. (2019). Red Room-Temperature Phosphorescence of CDs@Zeolite Composites Triggered

by Heteroatoms in Zeolite Frameworks. *ACS Central Science*, *5*(2), 349–356. https://doi.org/10.1021/acscentsci.8b00844

103. Liu, J., Zhang, H., Wang, N., Yu, Y., Cui, Y., Li, J., & Yu, J. (2019). Template-Modulated Afterglow of Carbon Dots in Zeolites: Room-Temperature Phosphorescence and Thermally Activated Delayed Fluorescence. *ACS Materials Letters*, *1*(1), 58–63. https://doi.org/10.1021/acsmaterialslett.9b00073

104. Joseph, J., & Anappara, A. A. (2017). Cool white, persistent room-temperature phosphorescence in carbon dots embedded in a silica gel matrix. *Physical Chemistry Chemical Physics*, *19*(23), 15137–15144. https://doi.org/10.1039/c7cp02731a

105. Lin, C., Zhuang, Y., Li, W., Zhou, T. L., & Xie, R. J. (2019). Blue, green, and red full-color ultralong afterglow in nitrogen-doped carbon dots. *Nanoscale*, *11*(14), 6584–6590. https://doi.org/10.1039/c8nr09672d

106. Tan, J., Zou, R., Zhang, J., Li, W., Zhang, L., & Yue, D. (2016). Large-scale synthesis of N-doped carbon quantum dots and their phosphorescence properties in a polyurethane matrix. *Nanoscale*, *8*(8), 4742–4747. https://doi.org/10.1039/c5nr08516k

107. Deng, Y., Zhao, D., Chen, X., Wang, F., Song, H., & Shen, D. (2013). Long lifetime pure organic phosphorescence based on water soluble carbon dots. *Chemical Communications*, *49*(51), 5751. https://doi.o rg/10.1039/c3cc42600a

108. Sun, Y., Zhang, X., Zhuang, J., Zhang, H., Hu, C., Zheng, M., Lei, B., & Liu, Y. (2020). The room temperature afterglow mechanism in carbon dots: Current state and further guidance perspective. *Carbon*, *165*, 306–316. https://doi.org/10.1016/j.carbon.2020.04.030

109. Koo, H. J., Park, J., Yoo, B., Yoo, K., Kim, K., & Park, N. G. (2008). Size-dependent scattering efficiency in dye-sensitized solar cell. *Inorganica Chimica Acta*, *361*(3), 677–683. https://doi.org/10.1016/j.ica.2007.05.017

Chapter 8
General conclusions and recommendations

8.1. Introduction

This dissertation's last chapter offers broad findings about the whole study along with suggestions for future work.

8.2. Conclusions

The objective of this study was to produce nitrogen-doped carbon dots (NCdots) and onion-like carbon nanomaterials (OLCNs), and then combine these two different carbon allotropes to produce an all-carbon nanocomposite for use as a counter electrode (CE) material in dye-sensitized solar cells (DSSCs). The following conclusions were formed from the findings of this research effort.

The quality of human existence is significantly influenced by the availability of energy. If renewable energy sources cannot be created swiftly, this is in peril. Chemistry is predicted to play a significant role in identifying ecologically acceptable energy solutions. The simplicity with which the driving force of a reaction may be regulated, as well as the convenience with which thermodynamic and kinetic parameters can be monitored, lies at the heart of electrochemistry's power. Therefore, in order for DSSCs to be commercialized and widely used, they must have sufficient performance [1-3].

8.2.1. Synthesis of NCdots using the microwave-assisted and their properties

NCdots were effectively produced using several nitrogen-containing precursors (ethylenediamine, urea, and fumaronitrile). The distinct NCdots had varying particle sizes, and more curiously, particle sizes > 10 nm, which is an unusual particle size for standard Cdots. This was due to the reaction conditions used in this study. Of the three nitrogen precursors studied, NCdots made with ethylenediamine had the highest fluorescence quantum yield; as a result, they were chosen for use in making NCdots. As a counter electrode material in DSSCs, OLCNs composites. The general conclusion gained from this section of the study was that high-quality NCdots may be synthesized using selective precursors.

8.2.2. Synthesis of OLCNs using flame pyrolysis method and their properties

Using flame pyrolysis of olive oil, OLCNs were successfully synthesized. Even though the many graphitic layers that allow these materials to be called "onions" could not be properly detected due to the low magnification of the TEM instrument. The carbon materials were successfully classified as chain-like and quasi-spherical in shape. According to the various types of functionalization procedures, the functionalized OLCNs were effectively identified as nitrogen-doped and oxygenated. Functionalization of the OLCNs resulted in structural defects as seen from TEM, PXRD spectroscopy, and Raman spectroscopy analyses. The OLCNs synthesized for this study presented prepared with various structural morphologies. To ascertain the amount and kind of heteroatoms present in the functionalized OLCNs structural matrix as well as the effects of surface modification on the OLCNs, additional study is necessary.

8.2.3. Synthesis of NCdot: OLCNs composites using physical mixing and their properties

Physical mixing of the NCdots and OLCNs as precursors via mild refluxing, moderate reaction time, and low temperature produced the nanocomposites. In one set of nanocomposites, different low quantities of NCdots were placed into the surface of the OLCNs, which served as the supporting framework. Another set of composites was made in which the concentration of NCdots was higher than that of OLCNs. Thus, OLCNs were mixed with NCdots using different percentage loadings. The hybrid composites produced different outcomes in terms of diffraction spectroscopy study, however their absorbance analysis produced consistent results for all nanocomposites. Their photoluminescence data revealed that combining NCdots and different CNOs produced material with comparable fluorophores, since the nanocomposites had similar emission wavelengths when excited with the same wavelength. These findings call for much further investigation and characterisation of these composites, including Raman spectroscopy, TGA/DTA, XPS analysis, and HRTEM. There is a lot of room for more research into these new composites.

8.2.4. NCdots: OLCNs composites application in DSSCs

The introduction of NCdots: OLCNs nanocomposites into DSSCs was accomplished effectively. In DSSCs, the selected nanocomposites performed poorly as catalytic materials.

However, not all NCdots: OLCNs-based cells exhibited promising qualities as good solar cells, therefore only six different types of nanocomposites (out of the 27 made) were chosen for testing based on cyclic voltammetry catalytic activity data. When compared to commercially available standard Pt electrodes, the evaluated cells showed poor power cell efficiencies (<1%).

However, due to their smart memory effect, the cells were discovered to be able to exhibit photovoltaic activity in the dark. After spending 5 minutes of no light stimulated after irradiation tests, these cells continued to show after-dark activity. Although it was not expected of these cells to continue delivering this activity in the dark, 5 minutes was randomly chosen as the cooling time period after irradiation. It's possible that these cells might continue to release light in the dark for longer than 5 minutes; further study and analysis is strongly suggested. To the best of our knowledge, visible-light-excited afterglow NCdots: OLCNs nanocomposites have never been reported until now.

8.3. Recommendations

With additional advancements in electrolytes, catalytic carbon nano-onions, organic dye sensitizers, and nanoporous semiconducting electrodes, DSSCs will be able to compete with standard thin film solar technologies.

Future research is advised to concentrate on creating structures with a higher level of order than the fractal-like assembly of random nanoparticles. For an appropriate form of the films, the mesoporous channels or nanorods should be positioned parallel to one another and vertically with respect to the TCO glass current collector. Faster pore diffusion, simpler access to the film surface and grain boundaries, and a more regulated junction creation would all be possible as a result. According to a study by Adachi et al., one technique for creating such oxide structures is to use surfactant templates to help in the synthesis of TiO_2 nanotubes [4]. According to Wang and Hu, functional groups and structural flaws/defects on the surface of graphitic carbon nanomaterials may be crucial to the electrocatalytic sites in DSSC counter electrodes [5]. Tuning defects and looking for different useful functional groups for NCdots, OLCNs, and NCdot: OLCNs might be a viable study field for producing high-performance all-carbon DSSCs.

A photovoltaic device must be functional for at least 20 years without considerable performance degradation ideally. Thus, careful consideration has been given to the

conductivity of each component of nanocrystalline injection solar cells, such as the conducting glass, TiO_2 layer, sensitizer, electrolyte, counter electrode, and sealant [6]. However, other carbon nanostructures have received a lot of attention in a number of sectors, these as-prepared nanocomposites are still regarded a niche in carbon nanostructure research.

8.4. Future work and considerations

The lack of sufficient device characterisation is a last issue affecting the industry, which affects not only carbon-incorporated PVs but the whole PV field. That is to say, one cannot simply construct and analyse a single architectural device and safely assert that the addition of new material resulted in a significant improvement. As a result, without many trials (e.g., device data), it is impossible to determine that the minor performance increases are due to the carbon material.

In next investigations, conducting polymers and carbon materials may be combined to increase solar cell efficiency. Combining carbonaceous nanoparticles with conjugated polymers may result in percolation pathways as well as electron acceptors that may successfully transport the transferred electrons along their length [7-9].

How closely the dye's absorption window covers the spectrum of sunlight determines the maximum current density in dye-sensitized solar cells. Numerous dyes have poor low-energy photon absorption, which is commensurate with how poorly the cells' function. As a result, it's critical to learn more about the nanostructure of nanomaterials (such as Cdots and OLCNs) and their interactions with semiconductor materials, as well as the kinetics of the charge-exchange process at the material interface.

References

1. Zhu, H., Wei, J., Wang, K., & Wu, D. (2009). Applications of carbon materials in photovoltaic solar cells. *Solar Energy Materials and Solar Cells*, *93*(9), 1461–1470. https://doi.org/10.1016/j.solmat.2009.04.006
2. Li, B., Wang, L., Kang, B., Wang, P., & Qiu, Y. (2006). Review of recent progress in solid-state dye-sensitized solar cells. *Solar Energy Materials and Solar Cells*, *90*(5), 549–573. https://doi.org/10.1016/j.solmat.2005.04.039
3. Armel, V., Pringle, J. M., Forsyth, M., MacFarlane, D. R., Officer, D. L., & Wagner, P. (2010). Ionic liquid electrolyte porphyrin dye sensitised solar cells. *Chemical Communications*, *46*(18), 3146. https://doi.org/10.1039/b926087k
4. Adachi, M., Murata, Y., Okada, I., & Yoshikawa, S. (2003). Formation of Titania Nanotubes and Applications for Dye-Sensitized Solar Cells. *Journal of The Electrochemical Society*, *150*(8), G488. https://doi.org/10.1149/1.1589763
5. Wang, H., & Hu, Y. H. (2012). Graphene as a counter electrode material for dye-sensitized solar cells. *Energy & Environmental Science*, *5*(8), 8182. https://doi.org/10.1039/c2ee21905k
6. Grätzel, M. (2003). Dye-sensitized solar cells. *Journal of Photochemistry and Photobiology C: Photochemistry Reviews*, *4*(2), 145–153. https://doi.org/10.1016/s1389-5567(03)00026-1
7. Sandler, J., Kirk, J., Kinloch, I., Shaffer, M., & Windle, A. (2003). Ultra-low electrical percolation threshold in carbon-nanotube-epoxy composites. *Polymer*, *44*(19), 5893–5899. https://doi.org/10.1016/s0032-3861(03)00539-1
8. Allaoui, A. (2002). Mechanical and electrical properties of a MWNT/epoxy composite. *Composites Science and Technology*, *62*(15), 1993–1998. https://doi.org/10.1016/s0266-3538(02)00129-x
9. Bai, J., & Allaoui, A. (2003). Effect of the length and the aggregate size of MWNTs on the improvement efficiency of the mechanical and electrical properties of nanocomposites—experimental investigation. *Composites Part A: Applied Science and Manufacturing*, *34*(8), 689–694. https://doi.org/10.1016/s1359-835x(03)00140-4

Appendix A:

Supplementary information

S1. Optimization of the NCdots synthesis procedure

NCdots were prepared using the microwave-assisted irradiation method. Synthesis varied reaction time: 5-, 7-, and 10-minutes microwave holding time. Various results were obtained as the products had mixed results ranging from obtaining different colours of final products after synthesis, to the liquid-solid constituency of the same products. Some other parameters were kept constant while varying time only viz. solvent volume, precursor mass used, microwave power and conditions (i.e., all samples were synthesized while stirring).

Synthesis of nitrogen-doped carbon dots (Trial 1):

In the initial effort to synthesize NCdots, 20 mL of distilled water was added to about 1.0 g of fumaronitrile (a precursor for carbon and nitrogen). The mixture was transferred as is into Teflon microwave tubes. Fumaronitrile (FN) does not dissolve completely in water therefore during the synthesis procedure a stirrer bar was added to the microwave tube as well, so that the mixture can stir as the NCdots. This was also to allow a uniform mixture to be obtained at the end. In another microwave tube, the same contents of the same quantity were added and both tubes were placed in the microwave rotor in preparation for synthesis.

The rotor was then placed back into the microwave oven and synthesis began. To balance the microwave rotor (as it uses a minimum of 4 tubes and maximum of 8 tubes at a time), two more tubes were used. However, they were only filled with the reaction solvent (distilled water in this case) and stirrer bars as well. All 4 reaction vessels were well balanced in mass and weight. The microwave power was set to stay constant for the duration of the synthesis at 700 W. Reaction (holding) time for the synthesis was set for 10 minutes running time and the ramping time was set to 7 minutes (100 W/per min). The microwave reaction system running a synthesis for the formation of N-Cdots is shown below in **Fig. S1**.

Figure S1: Picture of the microwave oven reaction system used for synthesis.

The reaction ran well until the microwave machine abruptly stopped the synthesis at 14:49 minutes (7:49 minutes after ramping) due to high rise/increase in pressure in the rotor beyond the machine's set power rate increase per second. Therefore, the synthesis procedure was unsuccessful as the reaction couldn't run for the set 10 minutes as expected. The resultant products were two differently coloured solutions. One solution was a very dark brown liquid and the other a very bright orange colour (see **Fig. S2** below). From the microwave reaction system, the reaction tubes had two different final reaction temperatures: one noted temperature was 145 °C and the other 166 °C. There was no particular smell detected from the solutions, however, the dark brown solution had somewhat a soft pungent scent.

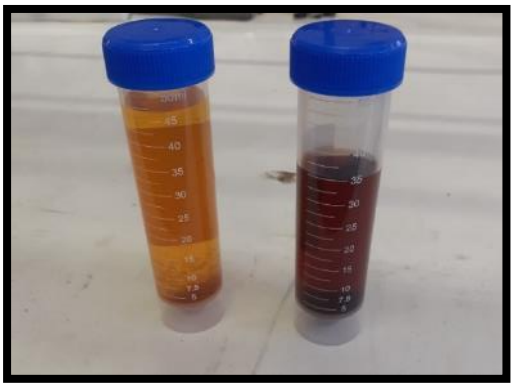

Figure S2: Differently coloured solutions obtained from the first microwave synthesis of NCdots (FN).

The solutions were taken out of the microwave tubes after synthesis and put into 50 mL centrifuge tubes in order to filter out big particles and separate the microwave solid waste from the NCdots supernatant solution. A 0.22 m filter membrane was then used to separate

the supernatant solution from the solid waste at the bottom of the centrifuge after the solutions were spun at 5000 rpm for 20 minutes (**Fig. S3**). The collected solution was then dried for about 24 hours at 100 °C in a vacuum oven.

Figure S3: Picture of the centrifuge machine used with the settings displayed.

A second synthesis was attempted following the same synthesis procedure as above, however the only difference now was that the reaction ran for 5 minutes, instead of 10 minutes. Under the same microwave and precursor preparation conditions, the reaction this time ran successfully to completion. After synthesizing NCdots (FN) for 5 minutes, the obtained products were again different coloured solutions (see **Fig. S4**). The solutions were again centrifuged under the same conditions (as above) and the two differently coloured supernatant solutions were collected and dried in a vacuum oven at 100 °C for 24hrs.

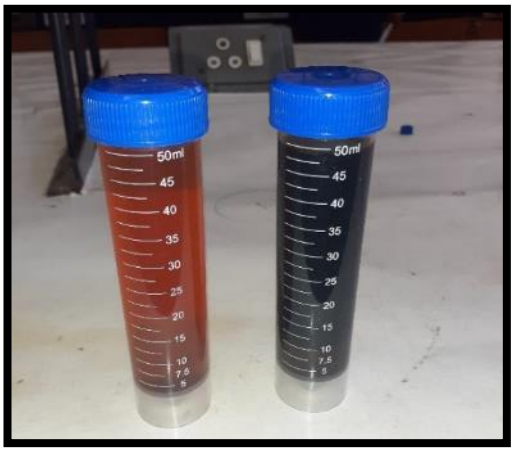

Figure S4: Resultant solutions from the second attempt of NCdots (FN) after microwave synthesis for 5 mins.

Synthesis of nitrogen-doped carbon dots (Trial 2):

After realizing that synthesis using only two microwave reaction vessels was not successful (due to the unsuccessful synthesis in the first attempt and the differently coloured solutions obtained in both the first and the second attempt in Trial 1) the next option was to try synthesize again however this time filling all four reaction tubes with the precursor and reaction solvent.

In the first attempt of Trial 2, about 1.0 g of FN was placed in a 100 mL beaker as before. 20 mL of distilled water was then added into the beaker and the mixture was poured into a microwave reaction vessel. A stirrer bar was then added to the tube as well. This was done for all four reaction vessels to be used for synthesis. All four stirrer bars were of the size and mass relatively, and all four microwave tubes were balanced (on a scale balance instrument) so that they could all have the same mass and weigh the same, before going into the microwave rotor.

Using the same reaction conditions for microwave synthesis as above (same microwave power, same ramping time, mass of solvent and precursor), the reaction was set to run for 10 minutes of synthesis for all four reaction tubes. Unfortunately, again, the reaction could not run to completion. This time, the microwave machine abruptly stopped synthesis at 12:49 minutes (5:49 minutes after ramping) due to high rise/increase in pressure in the rotor. The resultant products obtained were four differently coloured solutions: three of the were all alike, bright orange in colour and the other solution was dark brown in colour. All four samples had the same volume of solvent after synthesis. Four different temperatures were noted from the microwave reaction system after synthesis stopped and the final temperatures observed on the machine screen were at 167 °C, 138 °C, 137 °C, 134 °C. After that, the four solutions were centrifuged. This time at 4000 rpm for 20 minutes as that is the greatest speed the machine can spin at when four tubes are centrifuged as opposed to two (**Fig. S5** below).

Figure S5: Centrifuge machine used for the second trial with the settings displayed.

The supernatant solutions were then collected and separated from the bottom waste. The collected solutions were placed in new centrifuge tubes for drying (**Fig. S6**) and the centrifuge waste (precipitate/sediment waste) in the glass vials. Once more, all solutions were dried in an overnight vacuum oven experiment at a temperature of 100 °C (~24hrs).

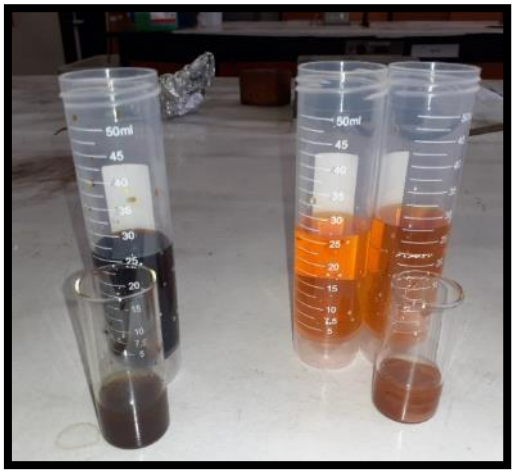

Figure S6: Resultant solutions from the first microwave synthesis of NCdots (FN) ran for 10 mins using 4 vessels.

The second attempt of Trial 2 followed suit to the first one, however this time all four reaction vessels filled with precursor and reaction solvent were run for 5 minutes in the microwave oven. Under the same microwave and precursor preparation conditions as above, the reaction this time ran successfully to completion. After synthesizing NCdots for 5 minutes, the obtained products this time had the same-coloured solutions (see **Fig. S7**) for all four reaction vessels, unlike any of the syntheses before. The final temperature noted for

these solutions was ~145 ± 1.0 °C. The four similarly coloured supernatant solutions were collected and dried in a vacuum oven at 100 °C for 24 hours after the solutions were centrifuged once more under the same circumstances (as above).

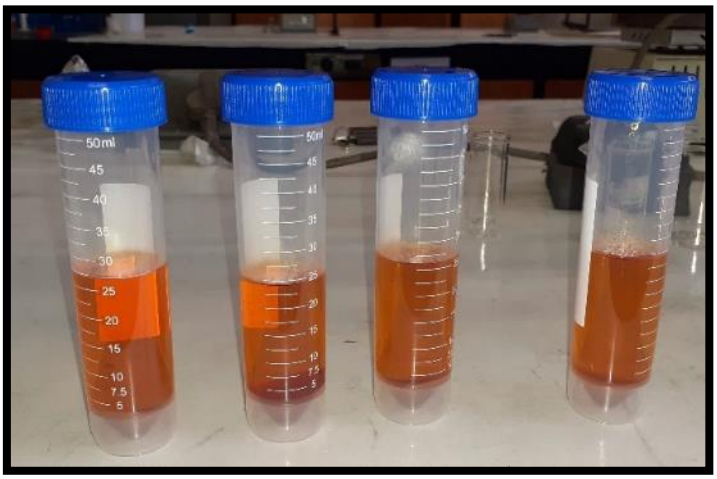

Figure S7: Resultant solutions from microwave synthesis of NCdots (FN) ran for 5 mins using 4 vessels.

The third attempt at synthesizing NCdots followed the same preparation and synthesis procedure as has been used before. However, this attempt was to try and see what the optimal reaction time for getting the expected results was before conclusively proving that using characterization techniques, since all syntheses before gave us variable and somewhat unreliable results to believe that indeed NCdots were synthesized. Therefore, a reaction was run in the microwave reaction system, using the same reaction conditions as prior however the reaction was run for 7 minutes this time. Unfortunately, again, the reaction could not run to completion. Again, the microwave machine abruptly stopped synthesis at 13:48 minutes (6:48 minutes after ramping, which was very close to the 7 minutes reaction time set). The resultant products obtained were four differently coloured solutions, they were labeled as follows: dark-brown solution, red-brown, black-brown, and bright-orange solution (see **Fig. S8**). The obtained solutions were centrifuges and their supernatants collected and dried in a 100 °C vacuum oven until dry.

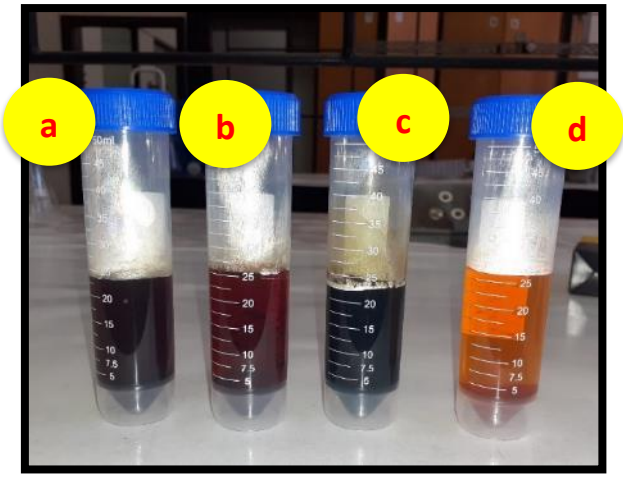

Figure S8: Resultant solutions from microwave synthesis ran for 7 mins with differently coloured solutions labelled: a) dark brown, b) red brown, c) black brown, and d) bright orange solutions.

All dried powders were collected from the vacuum oven (from Trial 2 attempts) and characterized using TEM, FTIR and UV-vis analysis to try and see if indeed NCdots were synthesized or at least get an idea of which reaction time used actually synthesized NCdots.

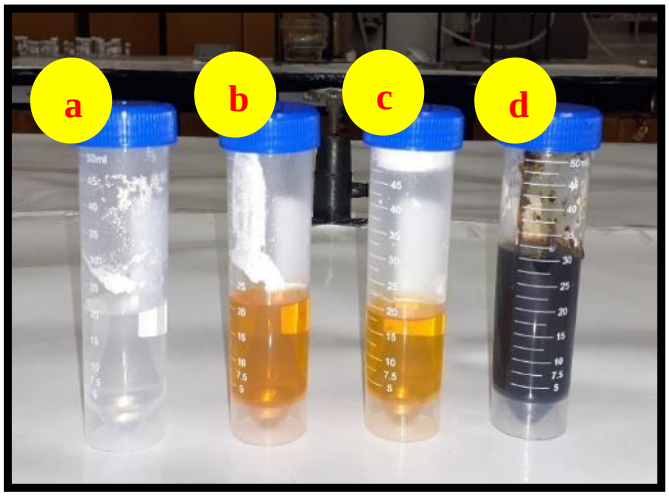

Figure S9: Various synthesized carbon dots a) Cdots, b) NCdots (EDA), c) NCdots (Urea) and d) NCdots (FN).

Finally, after characterization the optimal synthesis reaction time was decided to be 5 minutes for al NCdots (**Fig. S9**). Thus, all Cdots obtained were synthesized under the following microwave conditions; **ramp time:** 5 minutes, **reaction/holding time:** 5 minutes, **microwave power:** 700 W and **reaction temperature reaching:** ~170 ºC. The same amount of precursor was used for all reactions, as well as the same volume and type of solvent. Pristine Cdots were synthesized using 1g citric acid and 20 mL of distilled water to obtain a

cream white/yellowish product labelled as Cdots. The reaction mixture (**Fig. S9 a**) was *colourless* after synthesis. It was a clear liquid with no precipitate, and no observable particles in suspension. The same transparent solution was obtained from NCdots made from precursors 1g ethylenediamine + 1g citric acid, and 1g urea + 1g citric acid both mixed with 20 mL distilled, respectively (**Fig. S9 b and c**) however the observed final mixture colour in **b** was a light orange and that for **c** was a bright yellow.

The opposite is true about NCdots made from 1g fumaronitrile (**Fig. S9 d**). The obtained solution after synthesis was a thick, liquid slurry which was black in colour. Fumaronitrile is very reactive, and the mixture started carbonizing during the 3 mins of ramping, therefore by the end of 5 mins reaction time, the mixture had already "over-carbonised" so to speak.

S1.1 Optimization of the NCdots purification procedure

A great challenge encountered was purifying the carbon dots. The NCdots escaped through the dialysis membrane (14 000 kDa) and was lost in solution, as seen below (**Fig. S10 a and b**). The resulting products obtained were too low for any analysis to be made, literally <5 % of the product could be recovered after dialysis (**Fig. S11**). Therefore, dialysis was not used in the progression of this study.

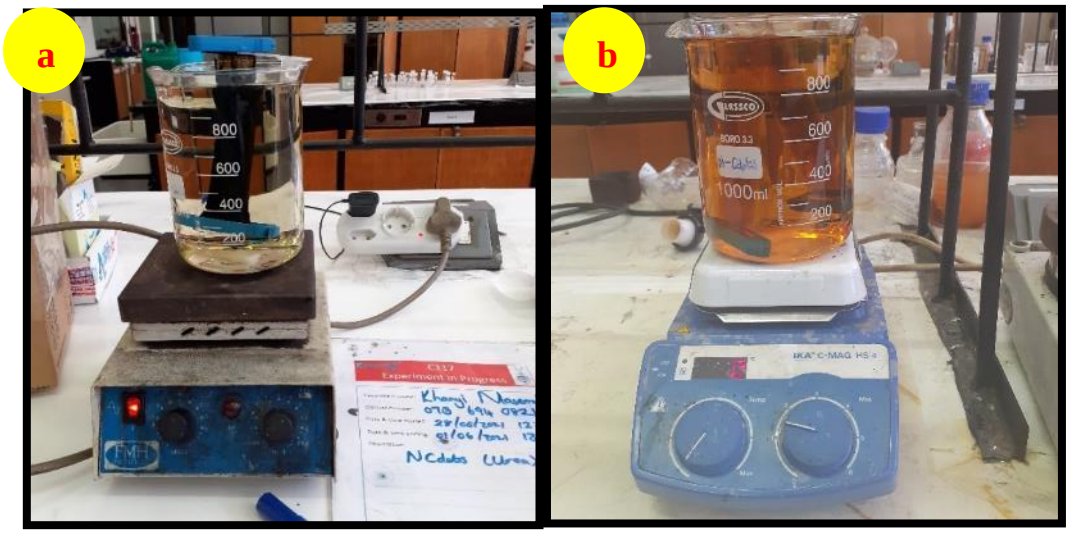

Figure S10: Dialysis of the various synthesized carbon dots a) NCdots (Urea) and b) NCdots (FN).

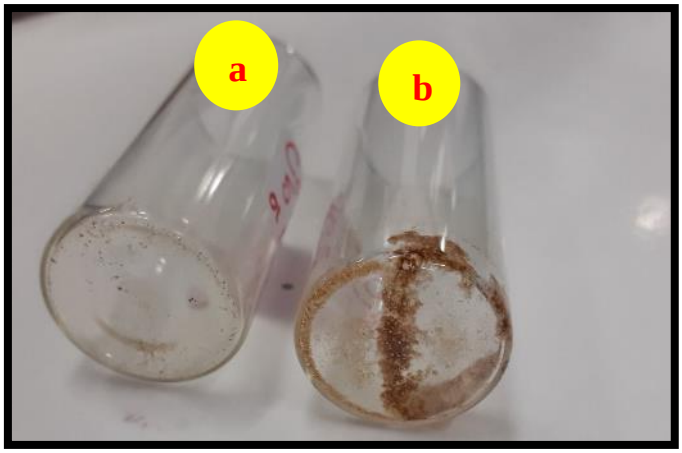

Figure S11: Product obtained from carbon dots after dialysis – a) NCdots (Urea) and b) NCdots (FN).

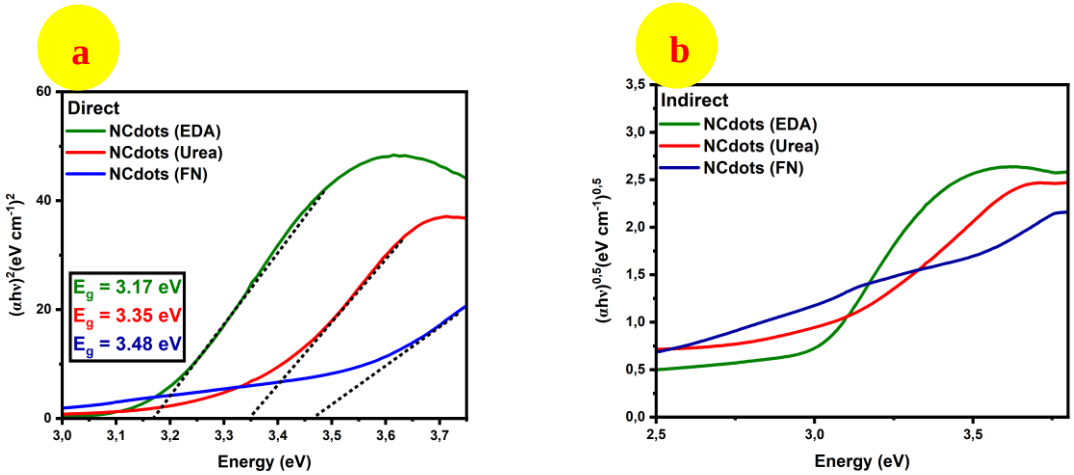

Figure S12: Tauc plots of a) direct and b) indirect allowed transitions to determine the bandgap energy of the various NCdots.

S2. Deconvoluted Raman analysis spectra of OLCNs

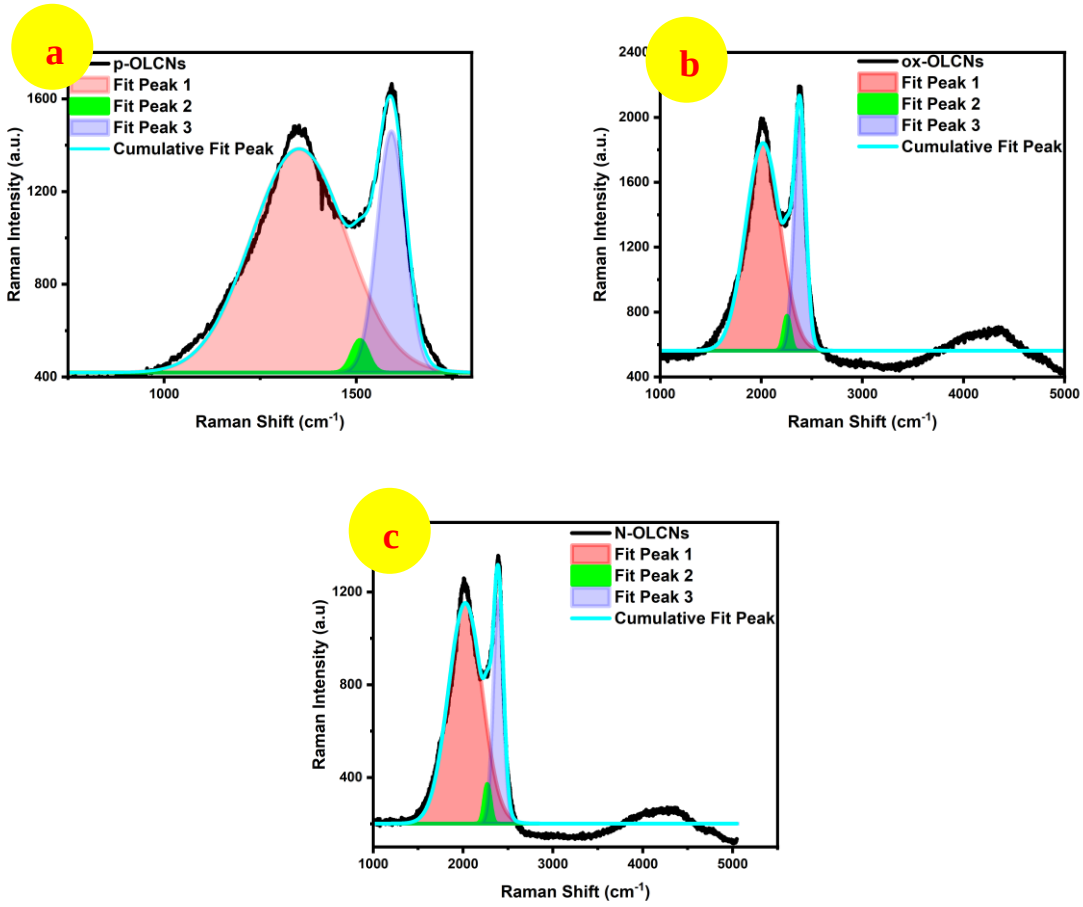

Figure S13: Deconvoluted Raman spectra patterns of the as-synthesized a) p-OLCNs, b) ox-OLCNs and c) N-OLCNs all recorded at λ_{ex} 514nm.

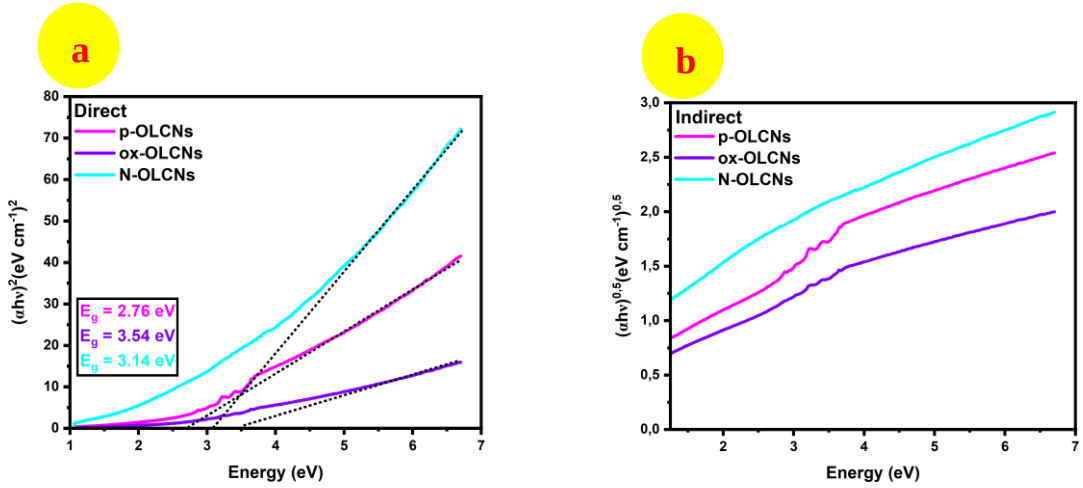

Figure S14: Tauc plots of a) direct and b) indirect allowed transitions to determine the bandgap energy of the various OLCNs.

S3. Brunauer-Emmett-Teller (BET) surface area analysis

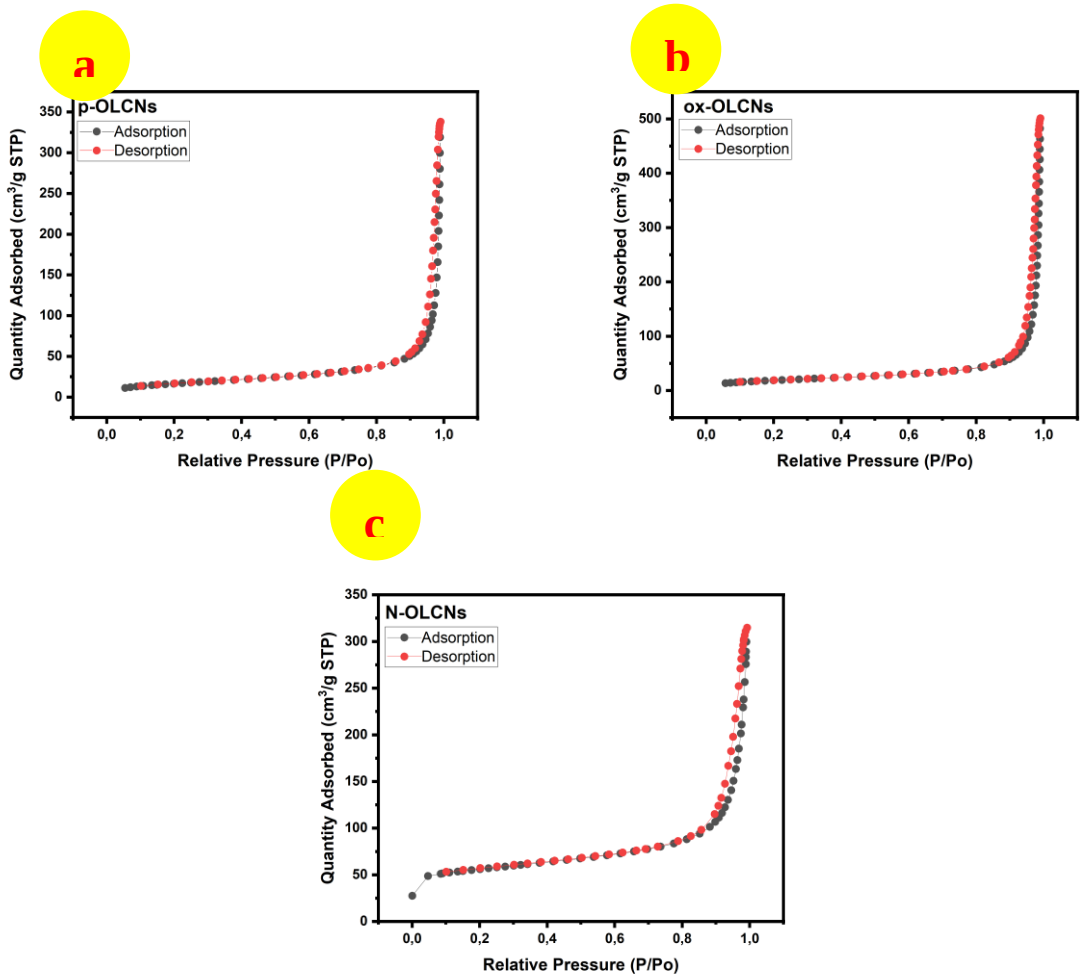

Figure S15: BET surface area isotherms of the as-synthesized a) p-OLCNs, b) ox-OLCNs and c) N-OLCNs.

S4. Morphological analysis of the prepared NCdots: OLCNs

Upon increase in percentage w/w loading of NCdots onto OLCNs, no distinct morphological changes can be observed different from **Fig 6.1 (Ch. 6, Sec 6.3.1**) micrographs. However, **Fig. S16 b** shows the accretion process more clearly. The "onions" almost look interconnected, and this suggests that as they form chain-like structures, the individual fragments form and coalesce unto each other before the previous onion-structure has completely formed complete multi-shells. Again, upon physical mixing there are no differences in morphological structure in comparison to the OLCNs synthesized in (**Sec. 5.3.1**, **Ch. 5**). Thus, this shows that the composite-making process has no structural effects on the OLCNs, and hopefully the NCdots which are not currently visible in the micrographs.

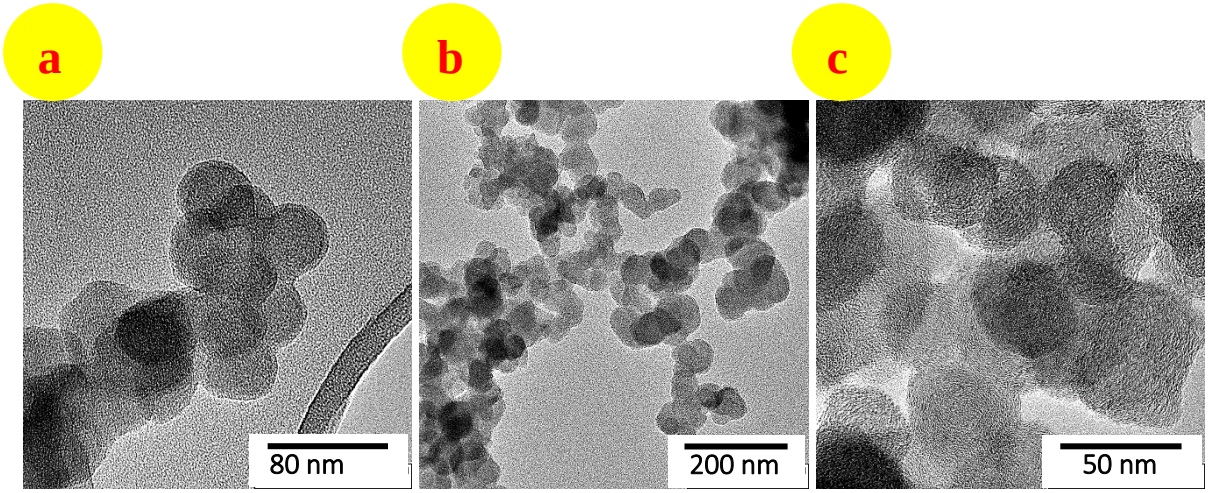

Figure S16: TEM images of a) 10%NCdots (EDA): p-OLCNs, b) 10%NCdots (EDA): ox-OLCNs and c) 10%NCdots (EDA): N-OLCNs composites.

Figure S17 shows that these OLCNs all had varying shapes, however, most of them were quasi-spherical in shape. It is well known in chemistry that lumps/agglomeration do not have a sufficient enough surface area to allow chemical reaction to occur, let alone interaction with other elements/material. Thus, it can be observed that upon increase in NCdots weight percentage loading, the bulk OLCNs structures still retained their chain-like morphology (**Figs. S17 a, b and c**) and without conglomeration sites in sight. However, effects of coalition from the accretion procedure are still visible on the material (see **Fig. S17 c** for example).

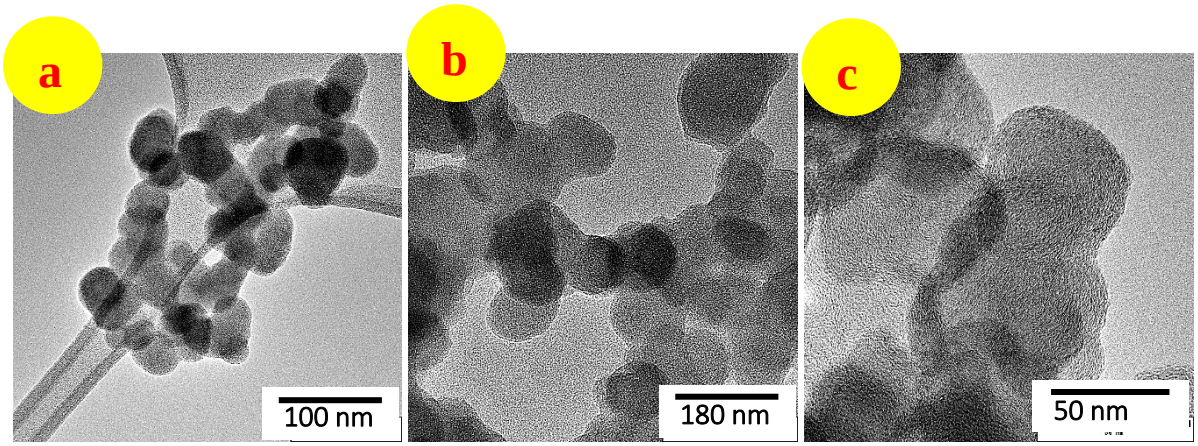

Figure S17: TEM images of a) 15%NCdots (EDA): p-OLCNs, b) 15%NCdots (EDA): ox-OLCNs and c) 15%NCdots (EDA): N-OLCNs composites.

Figure S18 shows the nanocomposite material showing the external morphology of composites. Here it is visualized that these material are still connected in accreted form (**Figs. S18 a, b and c**). The dark spot (herein circled) present with areas of dense distribution of

CNOs. This is where CNOs are gathered in large numbers, yet still no NCdots are visible or the effect of their incorporation physically unto the surface of the various CNOs.

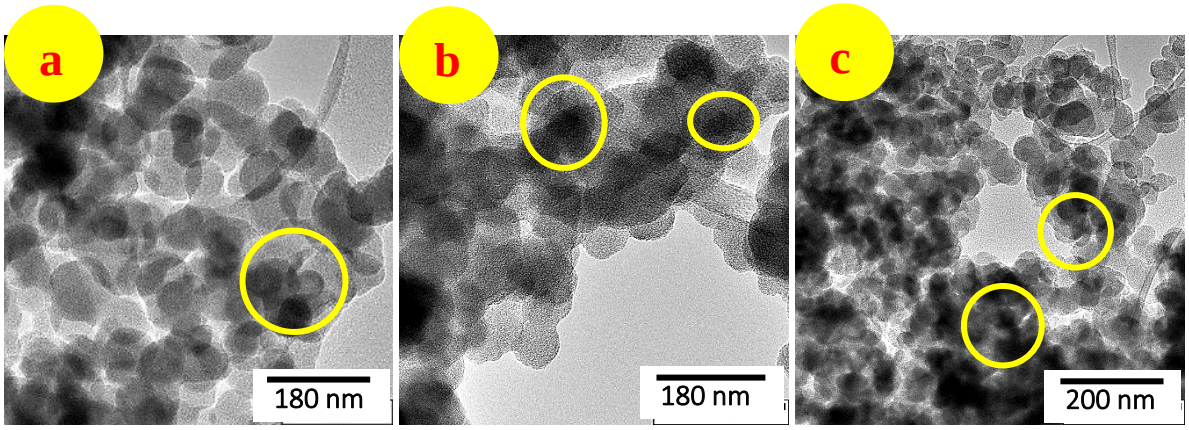

Figure S18: TEM images of a) 20%NCdots (EDA): p-OLCNs, b) 20%NCdots (EDA): ox-OLCNs and c) 20%NCdots (EDA): N-OLCNs composites.

Herein, the morphology of the composites at 30% wt. % loading is observed (**Figs. S19 a, b and c**). It seen that chain-like composites exhibit polyhedral as well quasi-spherical shapes. The micrographs have noticeable dark regions, and these could result from the synthesis procedure of formation. Sill no distinct physical changes are observable upon composite synthesis.

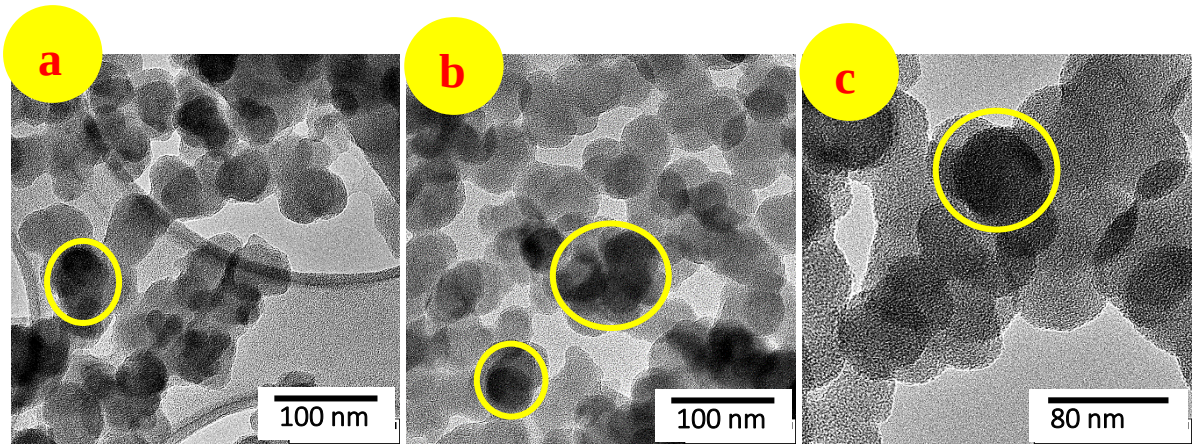

Figure S19: TEM images of a) 30%NCdots (EDA): p-OLCNs, b) 30%NCdots (EDA): ox-OLCNs and c) 30%NCdots (EDA): N-OLCNs composites**.**

The micrographs observed below (**Figs. S20 a, b and c**) present nanocomposites prepared at 40% wt. % loading of NCdots: OLCNs. **Figs. S20 a and b** show the regular conventional morphology that has been experienced in previous figures above. Whereby, the morphology of the composites still maintains the chain-like form. However, looking at **Figs. S20 c**, the N-

CNOs are presenting with small dense-like quasi-spherical structures (see arrows below). This can be ascribed to being clusters of NCdots bonded unto the surface, or individual NCdots.

The image at higher magnification shows these nanostructures to be somewhat bonded unto the surface of the N-OLCNs. It is difficult at this point to determine the type of interaction with which these nanoparticles are having together in their bond. However, N-OLCNs were seen to having the largest specific surface area and the lowest pore size between all three types of as-synthesized OLCNs (**Sec 5.3.9**). Moreover, since we know the types of functional groups of NCdots and N-OLCNs, we can postulate what the proposed noncovalent interactions within the composite material of the two materials could be. Based on the explanation given in **Ch. 6, Sec. 6.1**, these two carbonaceous materials could be said to be bonding via π–π stacking interactions from aromatic rings and electrostatic adsorption due to the N-N atoms on each material via lone pairs.

This postulation comes from the fact that these smaller dense nanoparticles (NCdots) are bonded on the ridges of the N-OLCNs structure, mostly bonded on the edges of the onion structure. Thus, these nanostructures can be said to be dangling on the surface of the N-OLCNs, rather than being bonded intrinsically and being embedded into the structural matrix of the multi-shells of N-OLCNs.

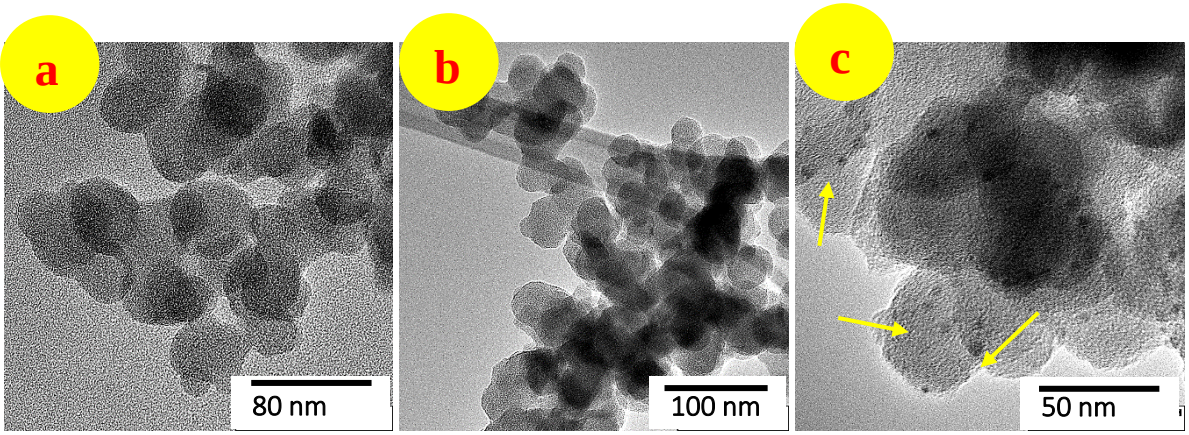

Figure S20: TEM images of a) 40%NCdots (EDA): p-CNOs, b) 40%NCdots (EDA): ox-CNOs and c) 40%NCdots (EDA): N-CNOs composites.

Once more, the OLCNs are joined in a chain-like fashion and their quasi-spherical and polyhedral forms can be seen. In some areas, there is not distinct delineation between two

carbon-onion fragments which make up the bulk structure. Hence, interconnection via accretion as has been observed before (**Figs S16-20** above).

S5. Powder X-ray diffraction (PXRD) spectroscopy analysis of the prepared NCdots: OLCNs

Figure S21 a and b below present XRD spectrums of nanocomposites synthesized at 15% and 20% w/w loading of NCdots unto the OLCNs support. The diffractograms show the conventional (002) graphitic carbon peak and diamond (111) peak. However, the 20% NCdots: ox-OLCNs presented with a small, overlapping peak ca. 2θ = ~14.28 º. The functionalization using oxidising agents on the graphite surface results in intercalation only if a large number of surface defects are present which can be attributed to the (001) plane (see circled area).

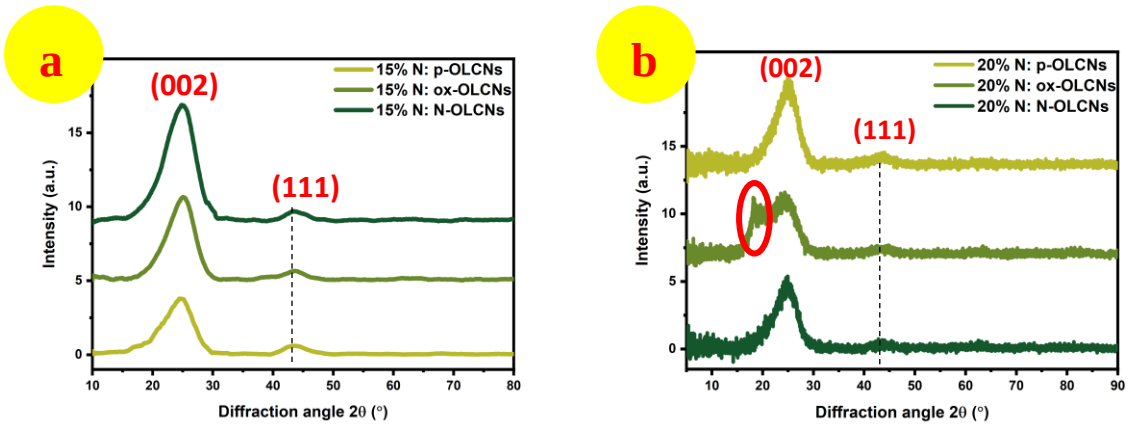

Figure S21: PXRD patterns of the NCdots: OLCNs synthesized at a) 15% NCdots wt. % loading and b) 20 % NCdots wt. % loading unto support.

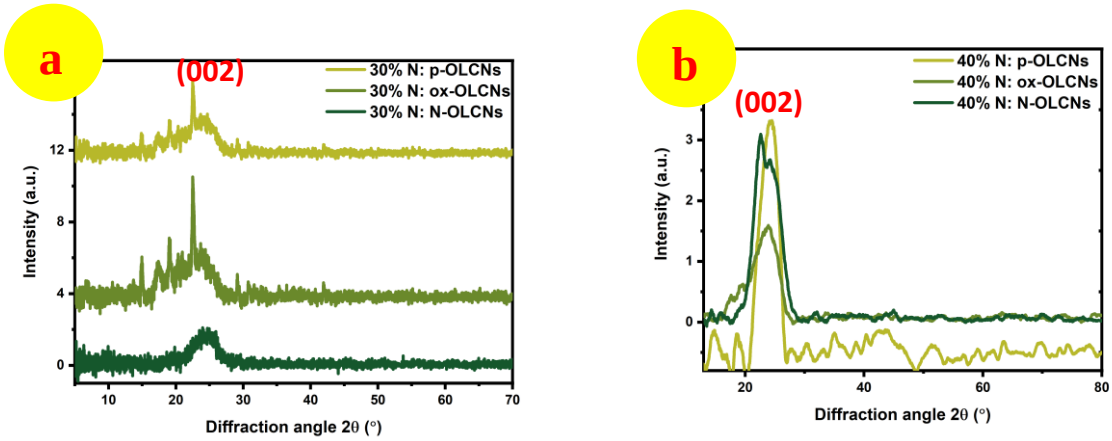

Figure S22: PXRD patterns of the NCdots: OLCNs synthesized at a) 30% NCdots wt. % loading and b) 40% NCdots wt. % loading unto support.

S6. Optical properties (absorbance measurement and fluorescence studies analysis) of the prepared NCdots: OLCNs

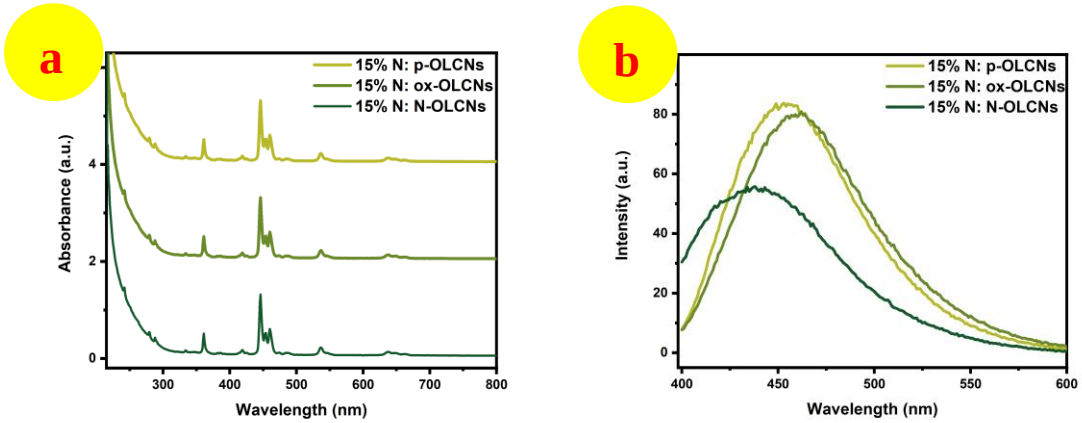

Figure S23: Shows a) UV-vis absorption spectrum and b) PL emission spectrum (λ_{em} 350 nm) of NCdots: OLCNs synthesized at 15% NCdots wt. % loading unto support.

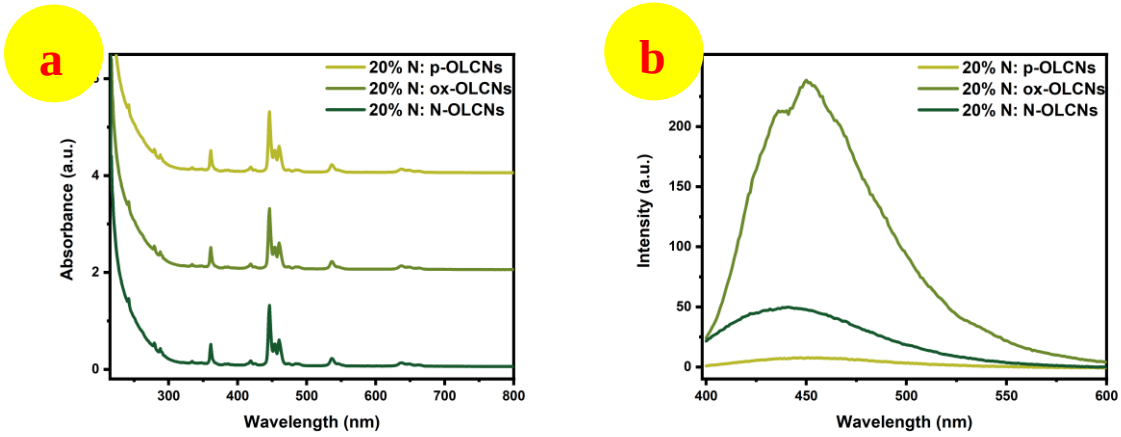

Figure S24: Shows a) UV-vis absorption spectrum and b) PL emission spectrum (λ_{em} 350 nm) of NCdots: OLCNs synthesized at 20% NCdots wt. % loading unto support.

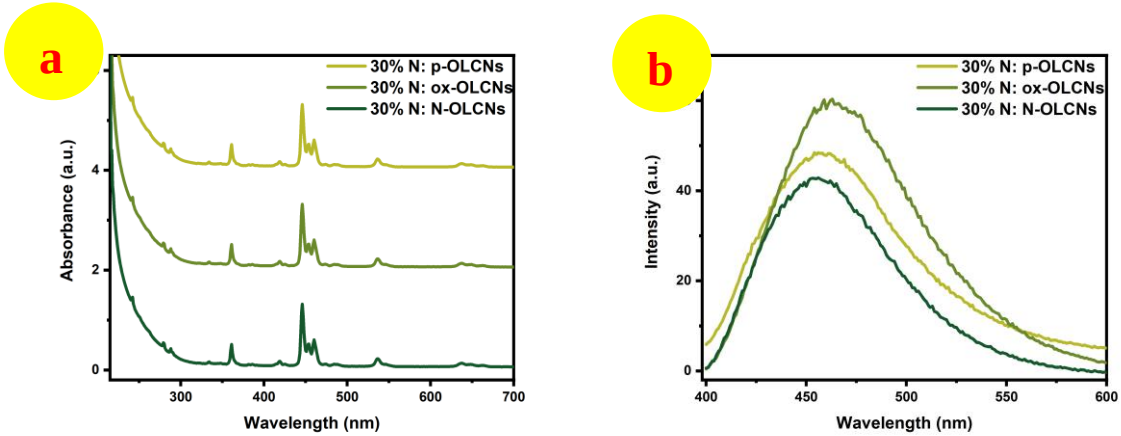

Figure S25: Shows a) UV-vis absorption spectrum and b) PL emission spectrum (λ_{em} 350 nm) of NCdots: OLCNs synthesized at 30% NCdots wt. % loading unto support.

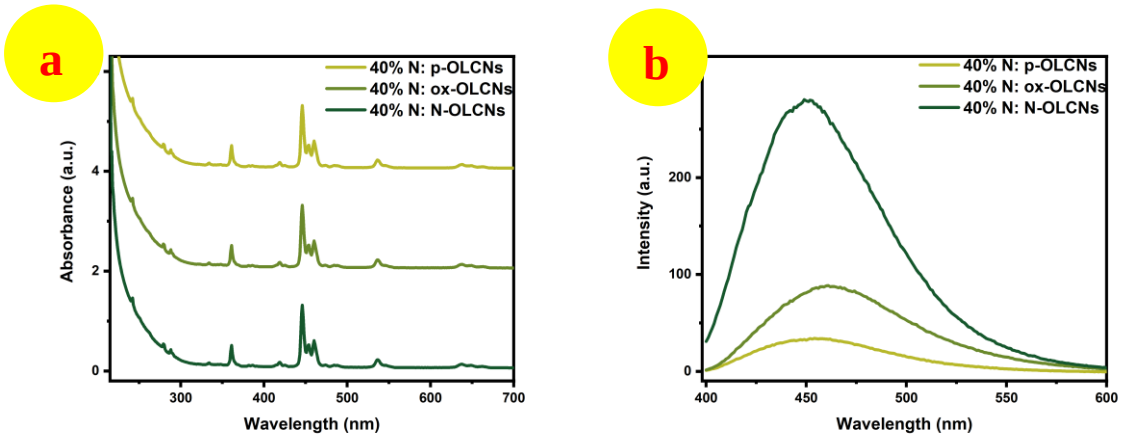

Figure S26: Shows a) UV-vis absorption spectrum and b) PL emission spectrum (λ_{em} 350 nm) of NCdots: OLCNs synthesized at 40% NCdots wt. % loading unto support.

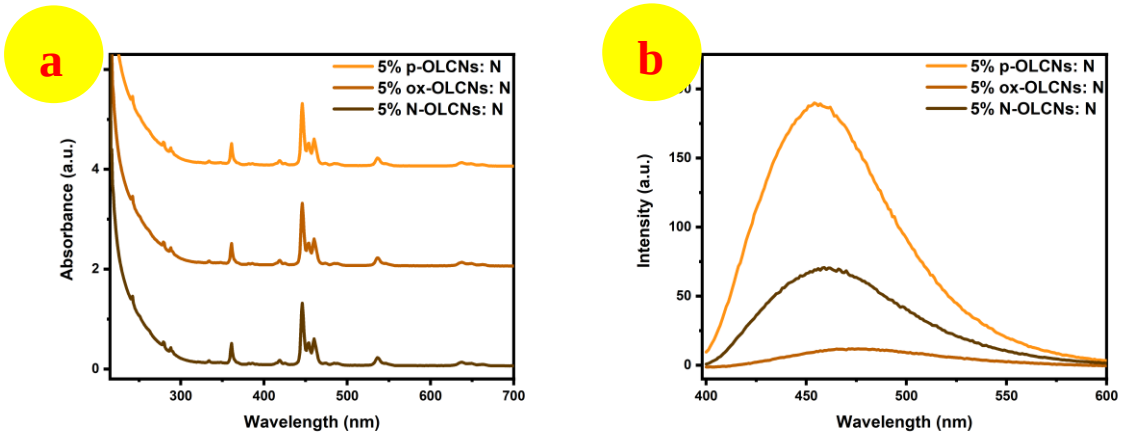

Figure S27: Shows a) UV-vis absorption spectrum and b) PL emission spectrum (λ_{em} 350 nm) of NCdots: OLCNs synthesized at 5% OLCNs wt. % loading.

Table S1: PL emissions at excitation wavelength of 350 nm.

Name of sample	PL emissions (nm)
15% NCdots:p-OLCNs	455
15% NCdots:ox-OLCNs	463
15% NCdots:N-OLCNs	438
20% NCdots:p-OLCNs	447
20% NCdots:ox-OLCNs	436
20% NCdots:N-OLCNs	440

30% NCdots:p-OLCNs	459
30% Ncdots:ox-OLCNs	464
30% NCdots:N-OLCNs	457
40% NCdots:p-OLCNs	454
40% NCdots:ox-OLCNs	462
40% NCdots:N-OLCNs	451
5% p-OLCNs: NCdots	456
5% ox-OLCNs: NCdots	472
5% N-OLCNs: NCdots	460

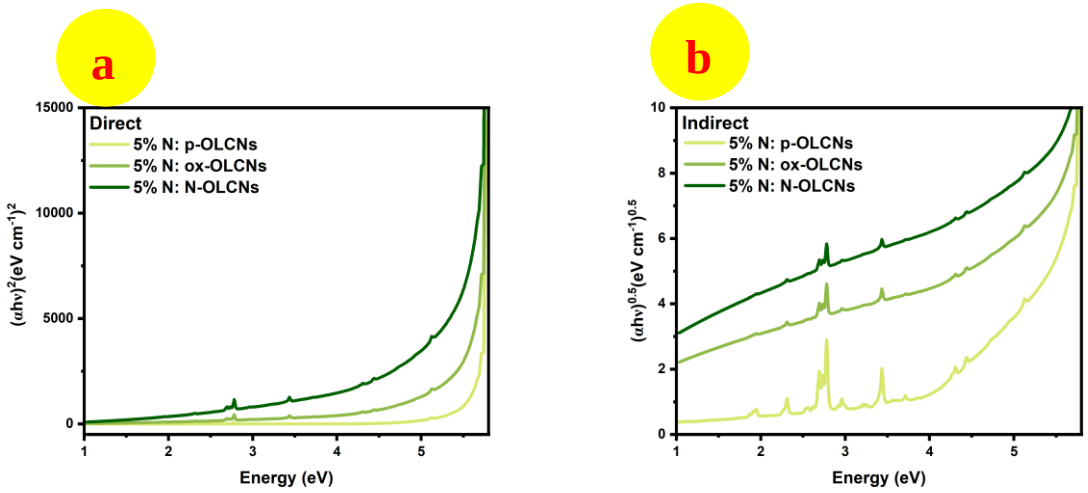

Figure S28: Tauc plots of a) direct and b) indirect allowed transitions to determine the bandgap energy of the various 5% NCdots: OLCNs composites.

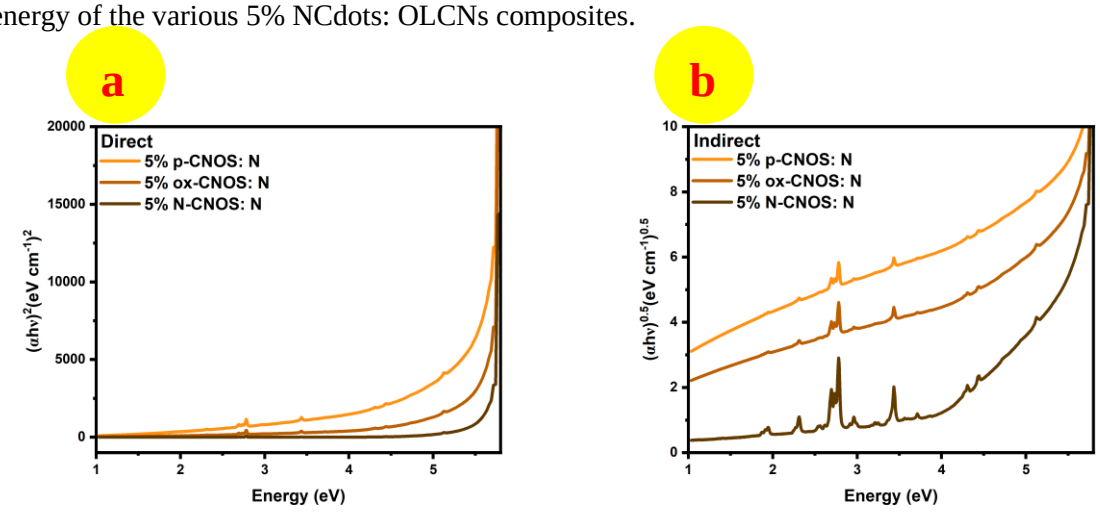

Figure S29: Tauc plots of a) direct and b) indirect allowed transitions to determine the bandgap energy of the various 5% OLCNs: NCdots composites.

S7. Fourier transmission infrared spectroscopy (FTIR) analysis of the prepared NCdots: OLCNs

Again**, Figs. S230 and S31** have asterisks in the place of the different indexed vibration modes analyzed, again to show the similarity between the different spectra obtained.

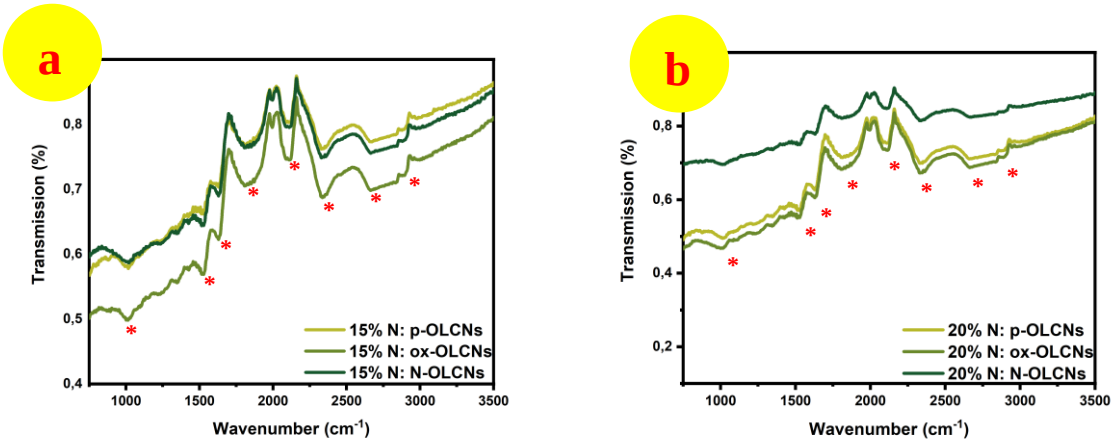

Figure S30: FTIR spectra of the NCdots: OLCNs synthesized at a) 15% NCdots wt. % loading and b) 20% NCdots wt. % loading unto support.

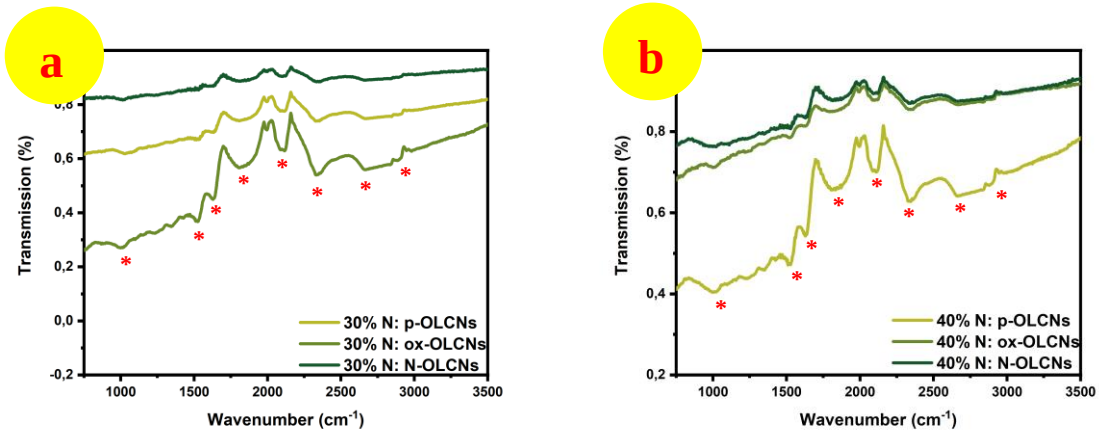

Figure S31: FTIR spectra of the NCdots: OLCNs synthesized at a) 30% NCdots wt. % loading and b) 40% NCdots wt. % loading unto support.

S8. Electrochemical properties of NCdots: OLCNs electrode using CV scans

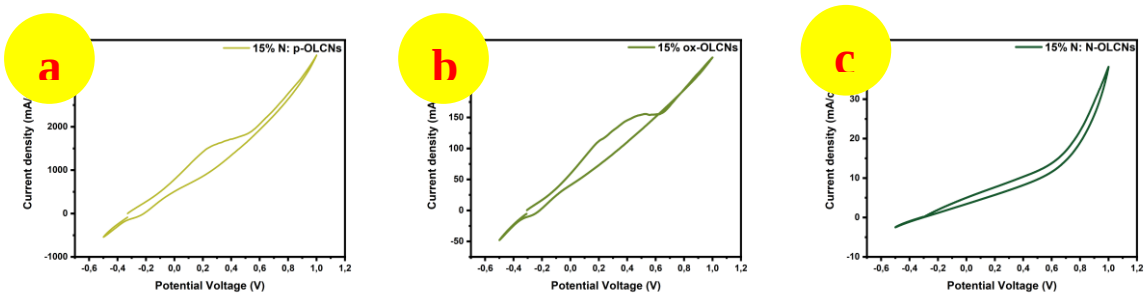

Figure S32: CV Voltammogram for CE made of a) 15%NCdots (EDA): p-OLCNs, b) 15%NCdots (EDA): ox-OLCNs and c) 15%NCdots (EDA): N-OLCNs at a scan rate of 50 mV s^{-1}.

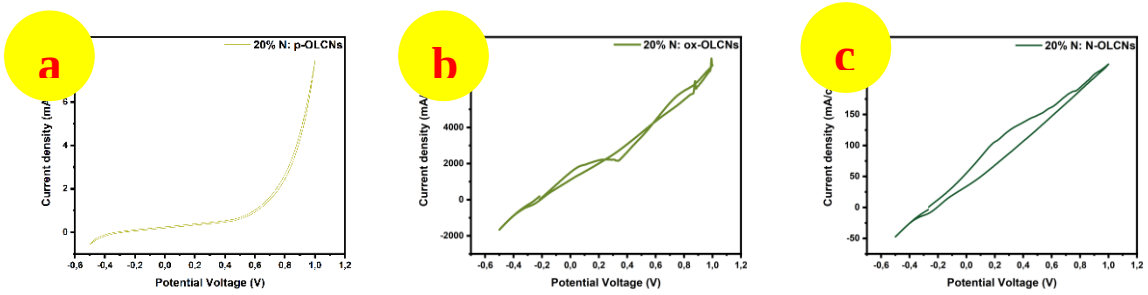

Figure S33: CV Voltammogram for CE made of a) 20%NCdots (EDA): p-OLCNs, b) 20%NCdots (EDA): ox-OLCNs and c) 20%NCdots (EDA): N-OLCNs at a scan rate of 50 mV s^{-1}.

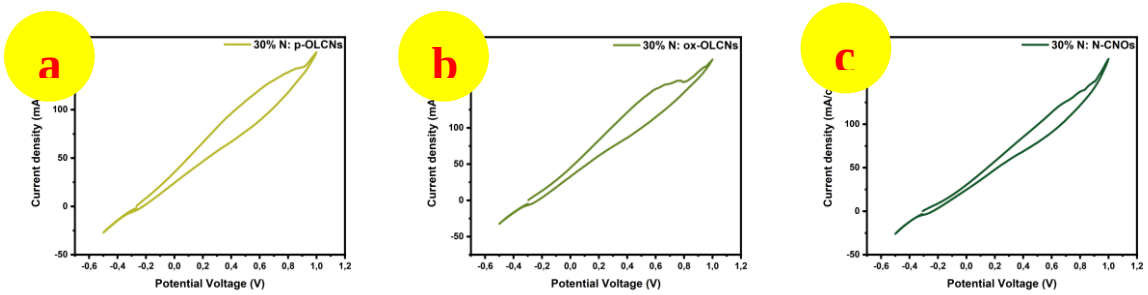

Figure S34: CV Voltammogram for CE made of a) 30%NCdots (EDA): p-OLCNs, b) 30%NCdots (EDA): ox-OLCNs and c) 30%NCdots (EDA): N-OLCNs at a scan rate of 50 mV s^{-1}.

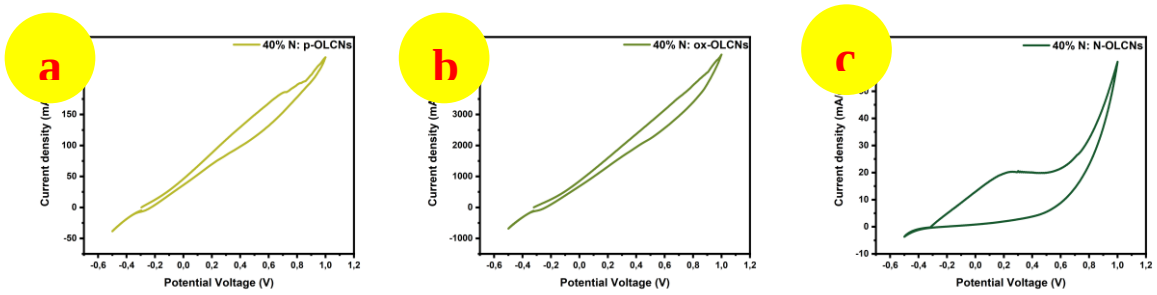

Figure S35: CV Voltammogram for CE made of a) 40%NCdots (EDA): p-OLCNs, b) 40%NCdots (EDA): ox-OLCNs and c) 40%NCdots (EDA): N-OLCNs at a scan rate of 50 mV s^{-1}.

S8. Electrochemical impedance analysis of the prepared NCdots: OLCNs

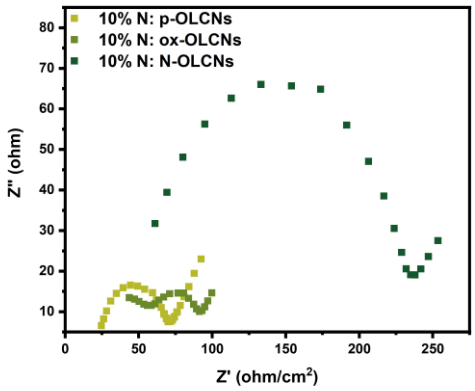

Figure S36: EIS Voltammogram for composites of 10% NCdots (EDA): OLCNs.

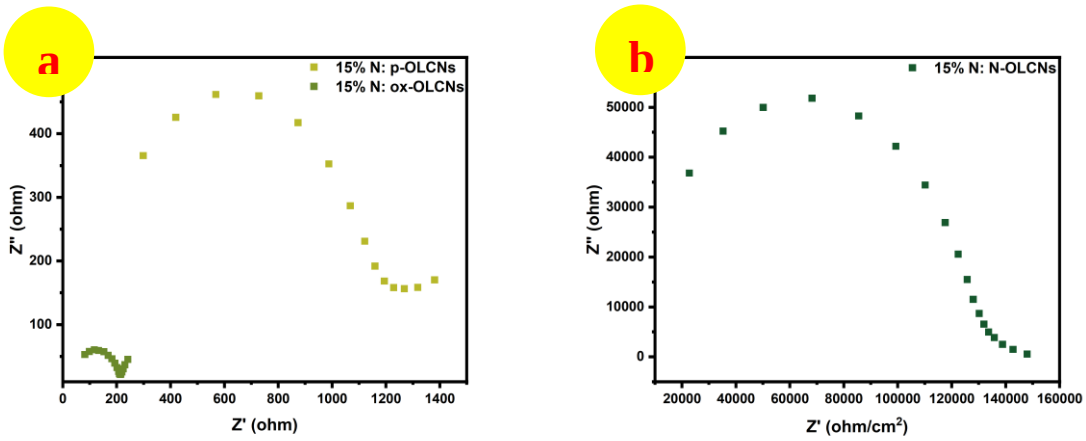

Figure S37: EIS Voltammograms for composites of a) 15% NCdots (EDA): p-OLCNs +10% NCdots (EDA): ox-OLCNs and b) 15% NCdots (EDA): N-CNOs.

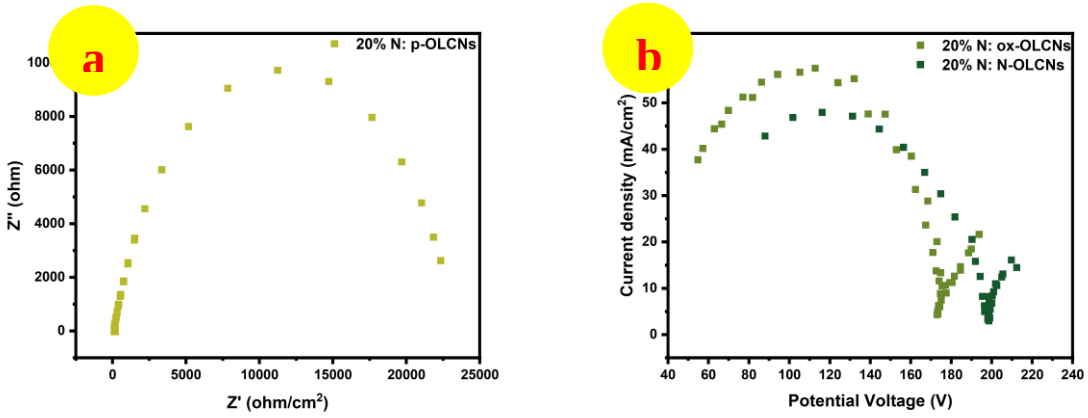

Figure S38: EIS Voltammograms for composites of a) 20% NCdots (EDA): p-OLCNs and b) 20% NCdots (EDA): ox-OLCNs + 20% NCdots (EDA): N-OLCNs.

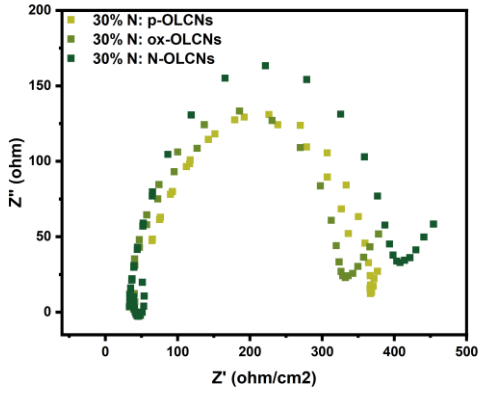

Figure S39: EIS Voltammogram for composites of 30% NCdots wt. % loading unto support.

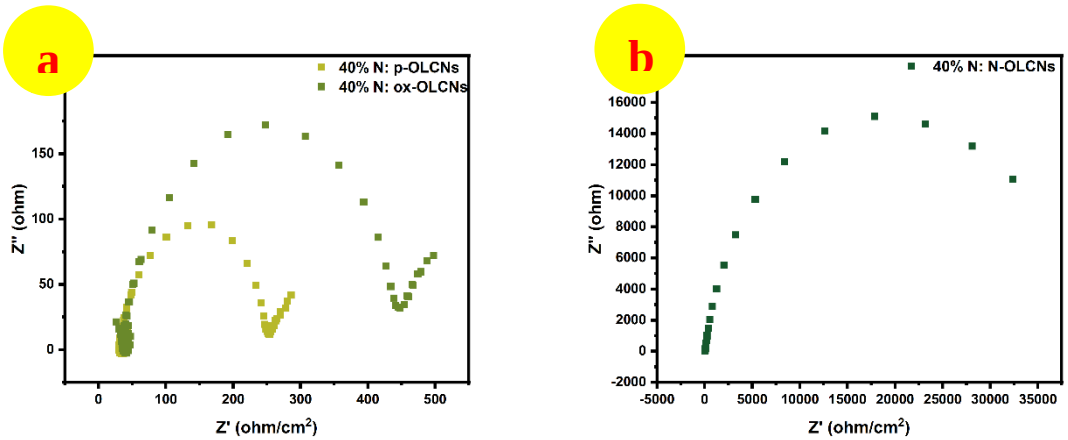

Figure S40: EIS Voltammograms for composites of a) 40% NCdots (EDA): p-OLCNs + 40% NCdots (EDA): ox-OLCNs and b) 40% NCdots (EDA): N-OLCNs.

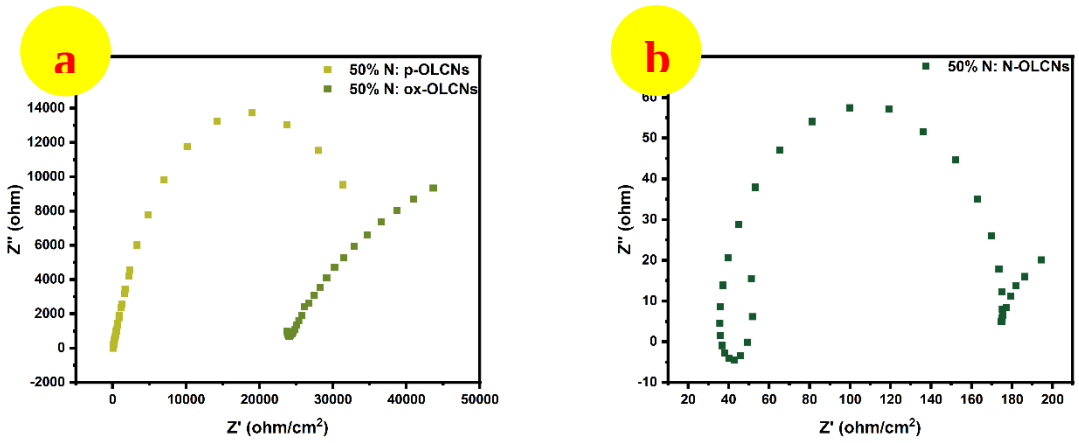

Figure S41: EIS Voltammogram for composites of a) 50% NCdots (EDA): p-OLCNs + 50% NCdots (EDA): ox-OLCNs and b) 50% NCdots (EDA): N-OLCNs.

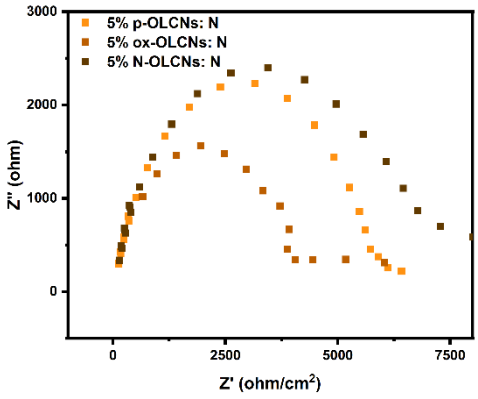

Figure S42: EIS Voltammogram for composites of 5% wt. % OLCNs support.

Table S2: EIS analysis results.

Name of sample	R_p (Ω cm^2)	R_∞ (Ω cm^2)	R_{ct} + R_{mt} (Ω cm^2)
5% NCdots:p-OLCNs	-	-	376.34
5% NCdots:ox-OLCNs	-	-	127.88
5% NCdots:N-OLCNs	-	-	117.91
10% NCdots:p-OLCNs	-	-	45.71
10% NCdots:ox-OLCNs	43.55	9.85	35.29
10% NCdots:N-OLCNs	-	-	173.77

15% NCdots:p-OLCNs	-	-	860.26
15% NCdots:ox-OLCNs	-	-	128.46
15% NCdots:N-OLCNs	-	-	110948.52
20% NCdots:p-OLCNs	-	-	22202.85
20% NCdots:ox-OLCNs	-	-	118.22
20% NCdots:N-OLCNs	-	-	110.66
30% NCdots:p-OLCNs	-	-	302.16
30% Ncdots:ox-OLCNs	-	-	286.09
30% NCdots:N-OLCNs	-	-	357.19
40% NCdots:p-OLCNs	-	-	211.46
40% NCdots:ox-OLCNs	-	-	406.40
40% NCdots:N-OLCNs	-	-	32313.81
50% NCdots:p-OLCNs	-	-	31240.64
50% NCdots:ox-OLCNs	-	300.50	19603.55
50% NCdots:N-OLCNs	-	-	136.73
5% p-OLCNs: NCdots	-	-	6288.15
5% ox-OLCNs: NCdots	-	-	3392.42
5% N-OLCNs: NCdots	-	-	6634.56
10% p-OLCNs: NCdots	-	-	96.0
10% ox-OLCNs: NCdots	-	-	113.04
10% N-OLCNs: NCdots	-	-	139.89

S9. Potentiodynamic polarization curves for Tafel analysis of the prepared NCdots: OLCNs

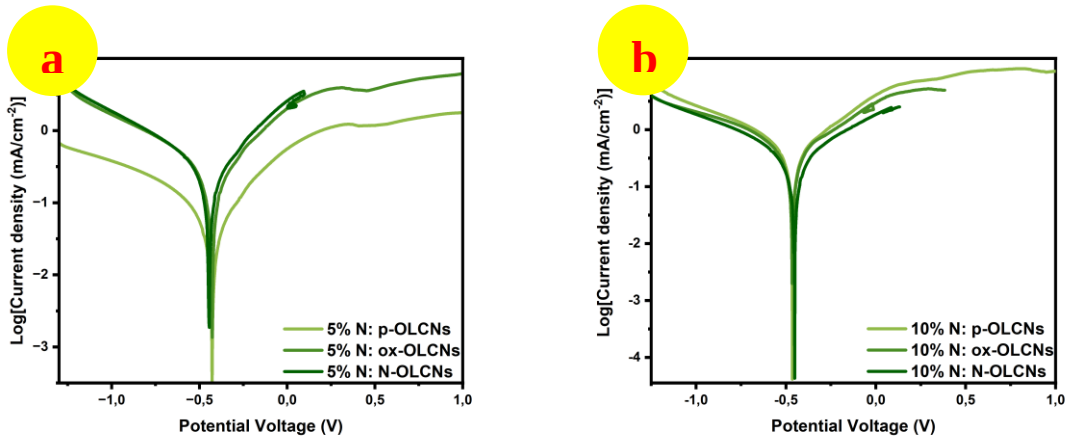

Figure S43: Tafel plots of the NCdots: OLCNs synthesized at a) 5% NCdots wt. % loading and b) 10% NCdots wt. % loading unto support.

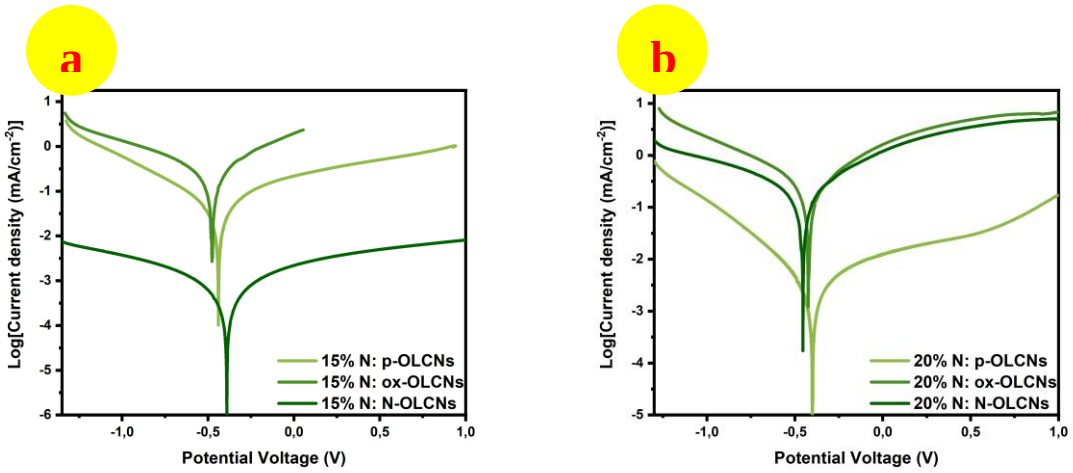

Figure S44: Tafel plots of the NCdots: OLCNs synthesized at a) 15% NCdots wt. % loading and b) 20% NCdots wt. % loading unto support.

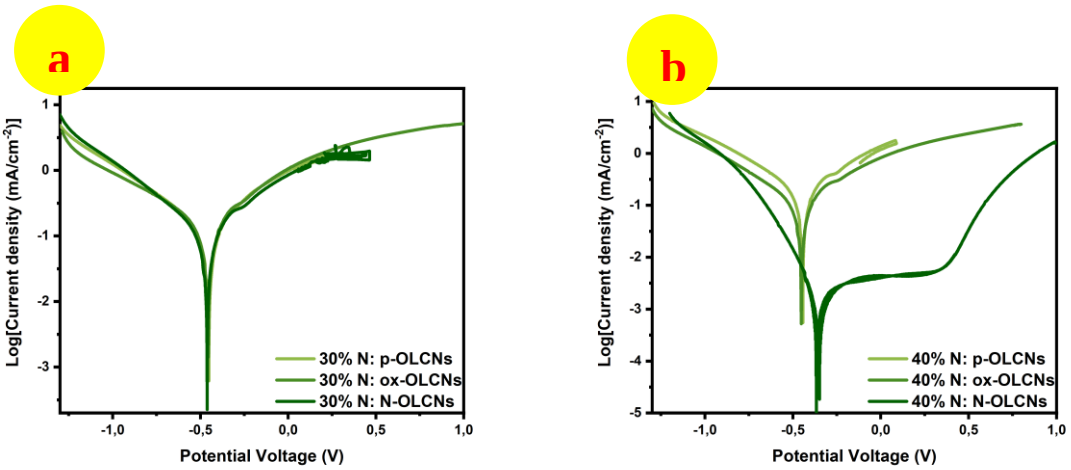

Figure S45: Tafel plots of the NCdots: OLCNs synthesized at a) 30% NCdots wt. % loading and b) 40% NCdots wt. % loading unto support.

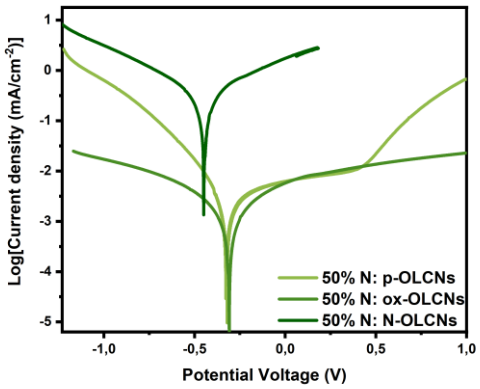

Figure S46: Tafel plots of the NCdots: OLCNs synthesized at 50% NCdots wt. % loading unto support.

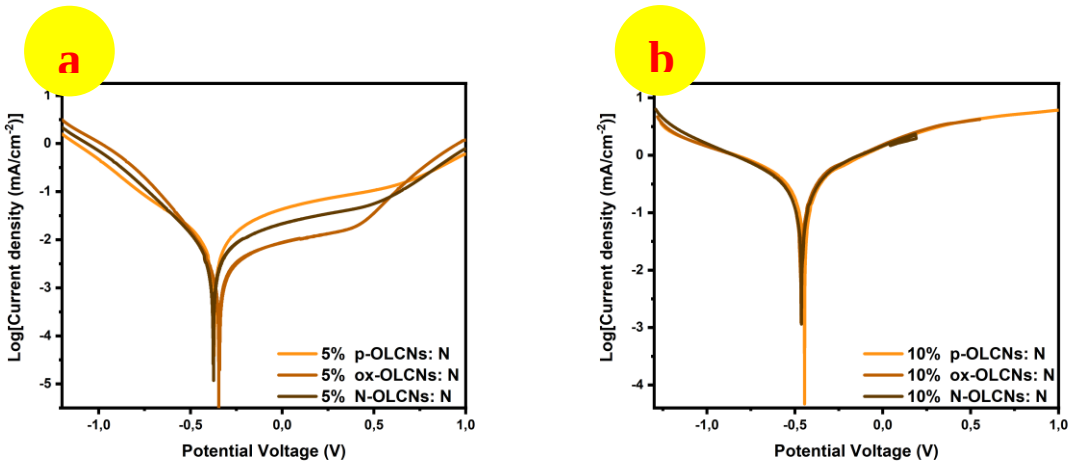

Figure S47: Tafel plots of the OLCNs: NCdots synthesized at a) 5% OLCNs wt. % loading and b) 10% OLCNs wt. % loading unto NCdots